Coherent Two-Dimensional Optical Spectroscopy

Minhaeng Cho

Chem. Rev., **2008**, 108 (4), 1331-1418 • DOI: 10.1021/cr078377b

Coherent Two-Dimensional Optical Spectroscopy

Minhaeng Cho*

Department of Chemistry and Center for Multidimensional Spectroscopy, Korea University, Seoul 136-701, Korea, and Multidimensional Spectroscopy Laboratory, Korea Basic Science Institute, Seoul 136-713, Korea

Received October 16, 2007

Contents

* Electronic mail: mcho@korea.ac.kr. Telephone: +82-2-3290-3133. Fax: +82-2-3290-3121.

10.1021/cr078377b CCC: $71.00
Published on Web 03/26/2008

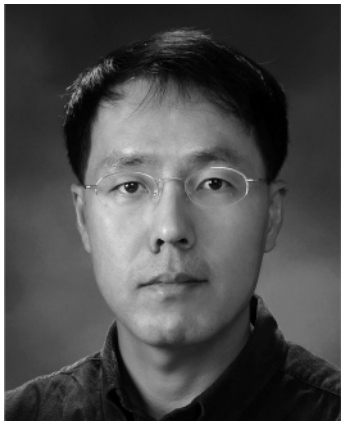

Minhaeng Cho was born in Seoul. He received a B.S. and M.S. in chemistry from Seoul National University in 1987 and 1989 and a Ph.D. from University of Chicago in 1993 under the direction of Graham R. Fleming. After 2 years of postdoctoral training at MIT in Robert J. Silbey's group from 1994 to 1996, he has been on the faculty of Korea University since March 1996, where he is currently a Hyundai-Kia Motor professor and the director of the Center for Multidimensional Spectroscopy. His research interests are theoretical and computational chemistry and ultrafast nonlinear optical spectroscopy. He was elected as a junior member of the Korean Academy of Science and Technology in 2002. He is a recipient of the Nobel Laureate Signatures Award (American Chemical Society) in 1995, the Young Scientist Award (Ministry of Science and Technology, Korea) in 1999, and the British Chevening Award in 2000. He has been married to Junghwa Song since 1993, and he has two children, Sunghak Cho and Sungin Cho.

1. Introduction

Two-dimensional (2D) optical spectroscopy utilizing multiple ultrafast coherent laser pulses in the infrared or UV−vis frequency range has been used to study protein structure and dynamics, hydrogen-bonding dynamics, femtosecond solvation dynamics, solute−solvent complexation, excitation migration process in photosynthetic light harvesting complexes, and coherence transfers in electronically coupled multichromophore systems. Due to a dramatic advent of laser technology, femtosecond laser systems operating in infrared and visible frequency ranges have been commercially available so that we have seen a wide range of applications utilizing such ultrafast nonlinear optical spectroscopic techniques.

Most of the conventional linear spectroscopic methods, though they have been proven to be extremely useful for studying structural and dynamical properties of complex molecules in condensed phases, can only provide highly averaged information. Therefore, novel spectroscopic techniques with much higher information content have been sought and tested continuously. In NMR spectroscopy, such efforts led to developing a variety of 2D NMR techniques such as NOESY (nuclear Overhauser enhancement spectroscopy) and COSY (correlation spectroscopy) methods among many others, and they have been extensively used to study structural and dynamical properties of proteins in solution.[1,2]

Although the optical analogues of 2D NMR do not provide atomic resolution structures of complex molecules, optical domain multidimensional spectroscopy has certain advantages because of the dramatic gain in time resolution (∼subpicosecond scale) possible and because of the ability to directly observe and quantify the couplings between quantum states involved in molecular dynamical processes. An elementary and highly simplified schematic diagram in Figure 1 demonstrates that the 2D vibrational spectroscopic technique can provide detailed information on the 3D structure of a given complex molecule, i.e., proteins. A given pair of vibrational chromophores, e.g., amide I local modes, are coupled to each other via a hydrogen-bonding interaction, which results in cross peaks. As the molecule undergoes a structural transition along the reaction coordinate, which leads to a hydrogen-bond breaking, the cross peaks will disappear in time. Consequently, the transient 2D vibrational spectroscopy will provide information on the local conformational change of the target molecule in this case.

As demonstrated by a number of workers, the existence of cross peaks is direct evidence on the vibrational coupling that is a function of distance between two different vibrational chromophores. Similarly, if two optical chromophores are close to each other, the electronic transition coupling between the two induces an electronic exciton formation and produces cross peaks in the 2D electronic spectrum. Therefore, experimental observation of cross peaks in a measured 2D electronic spectrum and their transient behaviors in time provides invaluable information about the electronic coupling strength between two chromophores and about exciton−exciton coherence and population transfers or even structural changes.

Ultrafast nonlinear optical spectroscopy utilizing an IR and/or visible field has a long history, and an optical analogue of NMR phase coherent multiple pulse spectroscopy was alluded in ref 4, where the acousto-optic modulation technique was used to generate an optical pulse sequence for a photon echo (PE) experiment. Optical PE spectroscopy has been extensively used to study solvation dynamics and ultrafast inertial motions of bath degrees of freedom coupled to an electronic transition of dye molecule in solution.[5] An IR PE experiment with a free electron laser was performed in early 1990s.[6] Since the PE spectroscopy involves two coherence evolutions during τ and t periods that are separated

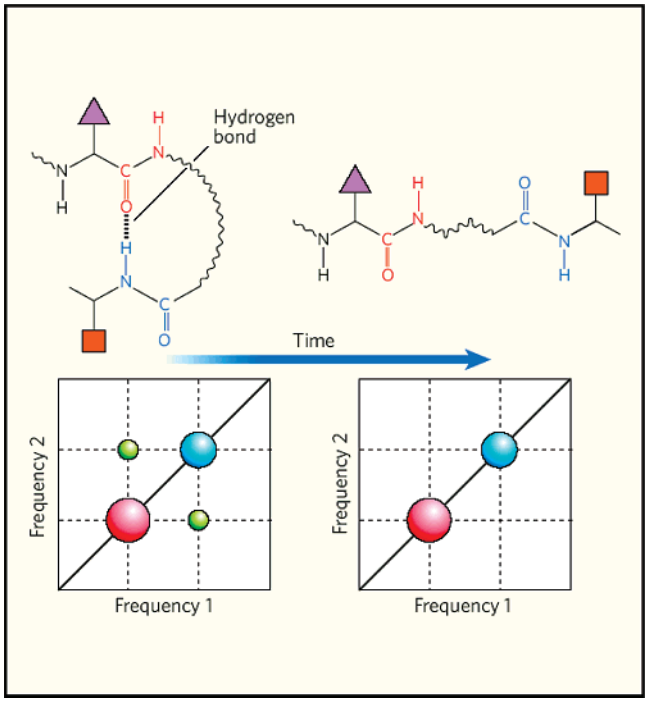

Figure 1. . 2D spectroscopy of changes in molecular structure.[3] The peaks on the diagonal line of this typical two-dimensional infrared spectrum are associated with vibrations of the chemical groups in red and blue in the structures above (the square and the triangle represent amino acid side groups). The cross peaks in green are produced by the coupling of these vibrations. As the molecule unfolds, the length of the hydrogen bond increases and the vibrational coupling decreases, so that the cross peaks become less intense. The cross peaks disappear when the hydrogen bond is broken. By examining the amplitudes of cross peaks from a series of time-resolved spectra, the breaking of a hydrogen bond, and so the structural evolution of a small molecule, can be probed in time.

by another delay time T, the measured echo signal is given as $S(t,T,\tau)$. The two-dimensional spectrum $\tilde{S}(\omega_t,T,\omega_\tau)$ can therefore be obtained by carrying out double Fourier transformations of $S(t,T,\tau)$ with respect to τ and t. T is the so-called waiting time interval during which the system is either on a population state (diagonal density matrix) or a coherence state (off-diagonal density matrix).

A typical coherent two-dimensional spectrum exhibiting a variety of peaks is shown in Figure 2 as an illustrative example. There are diagonal and off-diagonal peaks revealing different dynamics of the complex system. For a two-level system, the two-dimensional line shape of the diagonal peak (see the lower-left diagonal peak in Figure 2) provides information on the relative contributions from the inhomogeneous and homogeneous dephasing processes. The extent of elongation along the diagonal and the slope of the elongation direction are often time-dependent, and their changes were found to be related to the transition frequency−frequency time-correlation function. In the case of an approximately three-level system such as an anharmonic oscillator, the diagonal peak is divided into two parts with positive and negative amplitudes, which reveals overtone anharmonicity. The negative peak corresponds to the excited-state absorption contribution to the signal and the positive peak to the sum of ground-state bleaching and stimulated emission contributions. The cross peaks can also be either antidiagonally or diagonally elongated, which correspond to the cases when the two different transition frequencies are negatively or positively correlated in time. For a coupled homo- or heterodimer, a negative correlation can be induced by modulation of the coupling constant and a positive correlation results from modulation of the transition frequencies of the two monomers. The intensities of the cross peaks can change in time, and their time-dependencies originate from various processes such as excitation transfers between two different excitonic or monomeric states, coherence transfers, chemical exchanges and reactions, and structural transitions, etc., depending on the chemical or physical processes involved.

By using femtosecond IR pulses and the dispersive pump−probe spectroscopic technique, 2D IR spectroscopic measurements of proteins in solution were performed in the late 1990s.[8] Also, it was shown that electronic PE signals from a dye molecule or a photosynthetic light-harvesting protein complex can be experimentally measured by using Fourier transform (FT) spectral interferometry employing the Mach−Zehnder interferometer.[9] In the latter case, it was found that ultrafast excitation relaxation within the manifold of one-exciton states and coherence evolution in electronically coupled multichromophore systems could be studied by examining the time-dependent changes of the 2D PE spectrum and by measuring the cross peak amplitude changes in time.[10,11] A conditional probability of finding the system on a specific quantum state ψ_k at a later time when it was initially on a different state ψ_j was found to be the key factor determining the time-dependency of the associated cross peak amplitude at ($\omega_t = \omega_k$, $\omega_\tau = \omega_j$). In addition, we have seen 2D IR spectroscopic studies of the chemical exchange dynamics[12−16] and hydrogen-bond network in water.[17−19] These works highlighted how such novel spectroscopic methods can be of use in studying fundamental solute−solvent interaction dynamics in real time with an unprecedented time resolution that cannot be reached by any other spectroscopic means. Technically, a femtosecond collinear phase-coherent 2D spectroscopy[20] and a single-shot 2D pump−probe spectroscopy[21,22] were experimentally demonstrated, which will speed up data collection times and extend applications of the technique to a wide variety of problems. In parallel with these experimental efforts, numerous theoretical and computational methods combining molecular dynamics (MD) simulation, quantum chemistry calculation, quantum mechanical/molecular mechanical (QM/MM) simulation, and hybrid QM/MD simulation have been developed to accurately simulate the 2D vibrational and electronic spectra of complex molecular systems such as proteins, nucleic acids, and light-harvesting complexes over the past decade.

2. Hierarchy of Spectroscopic Properties

Linear spectroscopy such as IR absorption and Raman scattering can provide direct information on the distribution of vibrational chromophores in a given polyatomic molecule. There are a variety of marker bands in an IR absorption spectrum of a polyatomic molecule. Analysis of the IR absorption spectrum of an unknown molecule can thus provide information on the constituent chemical groups and bonds included in the molecule. However, if these vibrational chromophores interact or couple to produce delocalized vibrational states, the linear absorption spectrum provides limited information on such coupling strengths that are however keenly dependent on the three-dimensional structure, such as interchromophore distances and orientations.

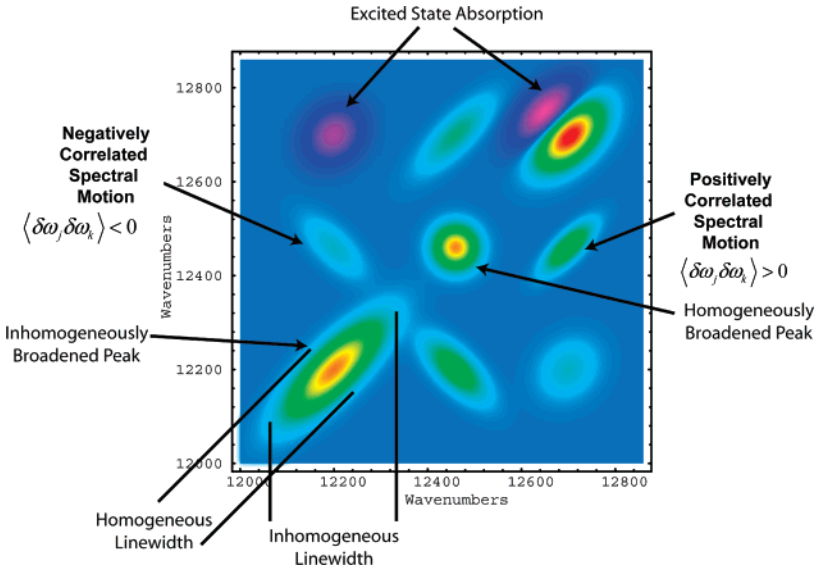

Figure 2. Schematic representation of a 2D spectrum (at a fixed value of the waiting time T) showing cross peaks.[7] In general, both ground-state bleaching and stimulated emission (positive) and excited-state absorption (negative) features appear. Negative features can partially or even wholly cancel positive features. Partial cancellation leads to distortions in the line shapes, as seen in the highest frequency diagonal peak. Note that the 2D spectrum is not symmetric around the diagonal. Cross (off-diagonal) peaks appear (for $T = 0$) only when coupling between chromophores is present. Cross peaks can also be generated by energy transfer, coherence transfer, chemical exchange, physical transformation, and so on for larger values of the waiting time T. Note that the orientation of the cross peaks is controlled by whether the fluctuations of two different transition frequencies are positively or negatively correlated with each other. Modulation of coupling strength by bath or intramolecular degrees of freedom produces an antidiagonally elongated cross peak, whereas any modulation of site energies (monomeric transition frequency) makes the peak diagonally elongated at short time T.

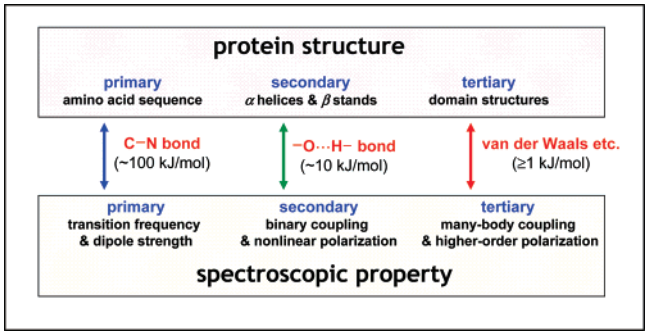

Figure 3. Analogy between hierarchies of spectroscopic properties and protein structures.

Thus, the 2D vibrational spectroscopy capable of measuring such small couplings can be an incisive tool to shed light on the detailed structure and its structural change in time.

In this regard, it is interesting to make an analogy between the the hierarchy of spectroscopic properties and protein structure (see Figure 3). The primary structure of a protein is nothing but a sequence of amino acids encoded in the corresponding gene. The relevant energy associated with the primary protein structure formation is the covalent bond energy, i.e., the peptide bond, of which the magnitude is ~100 kJ/mol. The secondary protein structures such as the α-helix, β-sheet, β-hairpin, etc. are mainly determined by the relatively weak hydrogen bonds with energies of ~10 kJ/mol. The protein tertiary (domain) structure formation involves a variety of interactions such as electrostatic, hydrophobic, van der Waals, disulfide bond interactions, etc. Similarly, one can develop the same hierarchical concept for spectroscopically measurable properties. The primary spectroscopic properties are the fundamental transition frequencies and transition dipole strengths that are the principal quantities extracted from an analysis of an 1D spectrum, and such primary spectroscopic properties are largely determined by the nature of the covalent bond involved in a given vibrational chromophore, e.g., a C═O stretch, a C—H stretch and bend, etc. Most of the 1D spectroscopic means are consequently very useful in delineating the distribution of an individual chromophore in the target molecule, and thus, they can be considered to be a *one-body* spectroscopy identifying each single chromophore. On the other hand, the coupling between two different vibrational chromophores in a molecule is associated with comparatively weak interchromophore interactions such as hydrogen bonds. Consequently, the secondary spectroscopic properties, e.g., vibrational or electronic couplings, nonlinear optical strengths, anharmonic couplings, etc., require nonzero two-body interactions between different chromophores and thus are very sensitive to the detailed configuration, i.e., the 3D structure, of the constituent chromophores in the molecule. As has been shown over the past decade, the coherent 2D optical spectroscopy based on a variety of nonlinear optical spectroscopic techniques is superior to the 1D method in extracting such quantitatively small secondary spectroscopic properties of complicated molecules such as proteins and molecular aggregates via measuring the two-body interaction terms. Extending this analogy further, one can envisage the 3D spectroscopy, which is likely to be of use in measuring tertiary spectroscopic properties such as three-body (three-chromophore) couplings and higher-order nonlinear optical strengths, as a technique that enables determination of higher-order hierarchical molecular structure.

3. Experimental Methods

Coherent 2D optical spectroscopy is a special class of time-domain nonlinear optical spectroscopy,[10,23–36] regardless of the number of laser pulses or of the temporal envelopes of each laser field used. The four-wave-mixing-type nonlinear optical spectroscopy has grown to be a highly developed and thoroughly investigated method, particularly owing to the

dramatic advancement of ultrafast laser technology.[37,38] In the present section, the response function formalism for nonlinear optical polarization and its connection to the measured signal field will be discussed. Numerous coherent multidimensional spectroscopic techniques can be devised by combining a variety of different optical excitation and probing methods.[28] Among them, 2D pump−probe spectroscopy based on dynamic hole-burning and 2D PE spectroscopy employing a FT spectral interferometric phase-and-amplitude measurement method will be discussed.

3.1. Nonlinear Response Function and Signal Field

The radiation−matter interaction is, as usual, treated semiclassically, and the interaction Hamiltonian, when a single particle is at **r**, can be in general written as

$$H_{\text{int}} = -\sum_n \mathbf{V}_n \cdot \mathbf{F}_n(\mathbf{r},t) \tag{3-1}$$

where **V** is the quantum mechanical operator inducing a quantum transition and **F**(**r**,*t*) is the conjugate field that is treated as a classical function.[39,40] A few examples of conjugate pairs of **V** and **F**(**r**,*t*) are given below,

$$\begin{bmatrix} \mu & \leftrightarrow & \mathbf{E}(\mathbf{r},t) \\ \alpha & \leftrightarrow & \mathbf{E}^2(\mathbf{r},t) \\ \beta & \leftrightarrow & \mathbf{E}^3(\mathbf{r},t) \\ \mathbf{m} & \leftrightarrow & \mathbf{B}(\mathbf{r},t) \\ \mathbf{Q} & \leftrightarrow & \nabla\mathbf{E}(\mathbf{r},t) \end{bmatrix} \tag{3-2}$$

where μ, α, β, **m**, and **Q** are the electric dipole, polarizability, first hyperpolarizability, magnetic dipole, and electric quadrupole operators. **E**(**r**,*t*) and **B**(**r**,*t*) are the electric and magnetic fields, respectively. A proper set of $\{\mathbf{V}_j\}$ and $\{\mathbf{F}_j(\mathbf{r},t)\}$ should be chosen for different experimental schemes. The 2D spectroscopy based on a four-wave-mixing scheme within the electric dipole approximation corresponds to the case when $\mathbf{V}_j = \mu$ and $\mathbf{F}_j(\mathbf{r},t) = \mathbf{E}(\mathbf{r},t)$ for all *j*. However, as will be discussed in this paper, one can choose different sets of conjugate pairs to describe other types of coherent multidimensional spectroscopic techniques.

The total Hamiltonian of the system is given as a sum of material and radiation−matter interaction Hamiltonians as

$$H_{\text{total}} = H + H_{\text{int}} \tag{3-3}$$

The dynamics of the system is described by the quantum Liouville equation for density operator $\rho(\mathbf{r},t)$ as

$$\frac{\partial\rho}{\partial t} = -\frac{i}{\hbar}[H,\rho] - \frac{i}{\hbar}[H_{\text{int}},\rho] \tag{3-4}$$

Considering the radiation−matter interaction as the perturbation and the material part as the reference, one can obtain the time-dependent density operator in a power series of the perturbation term and the *n*th-order density operator is given as[37]

$$\rho^{(n)}(\mathbf{r},t) = \left(\frac{i}{\hbar}\right)^n \int_0^\infty dt_n \ldots \int_0^\infty dt_2 \int_0^\infty dt_1 G(t_n)\boldsymbol{V}_n G(t_{n-1})\ldots \boldsymbol{V}_n\rho(-\infty) \otimes \mathbf{F}_n(\mathbf{r},t-t_n)\mathbf{F}_{n-1}(\mathbf{r},t-t_n-t_{n-1}) \times \ldots \times \mathbf{F}_1(\mathbf{r},t-t_n-\ldots-t_2-t_1) \tag{3-5}$$

where ⊗ denotes the tensor product and where the time-evolution operator and the electric dipole operator in the density matrix space are defined as

$$G(t) = \theta(t)\exp\left(-\frac{i}{\hbar}Lt\right) \tag{3-6}$$

$$LA = [H,A] \tag{3-7}$$

$$\boldsymbol{V}A = [\mathbf{V},A] \tag{3-8}$$

Here, $\theta(t)$ is the Heavyside step function, which ensures the causality condition. The experimentally measured quantity is not the *n*th-order density operator but the *n*th-order macroscopic polarization $\mathbf{P}^{(n)}(\mathbf{r},t)$, which is linearly proportional to the expectation value of the electric dipole operator over the *n*th-order density operator, i.e.,

$$\mathbf{P}^{(n)}(\mathbf{r},t) = N\text{Tr}[\mu\rho^{(n)}(\mathbf{r},t)] \tag{3-9}$$

The number density of the chromophore is *N*. Using the *n*th-order density operator and introducing the *n*th-order response function, we have

$$\mathbf{P}^{(n)}(\mathbf{r},t) = N\int_0^\infty dt_n \ldots \int_0^\infty dt_2 \int_0^\infty dt_1 R^{(n)}(t_n,\ldots,t_2,t_1) \otimes \mathbf{F}_n(\mathbf{r},t-t_n)\,\mathbf{F}_{n-1}(\mathbf{r},t-t_n-t_{n-1}) \times \ldots \times \mathbf{F}_1(\mathbf{r},t-t_n-\ldots-t_2-t_1) \tag{3-10}$$

The *n*th-order response function is given as

$$R^{(n)}(t_n,\ldots,t_2,t_1) = \left(\frac{i}{\hbar}\right)^n \prod_{j=1}^n \theta(t_j)\langle[[\ldots[\mu(t_n+\ldots+t_1),\mathbf{V}_n(t_{n-1}+\ldots+t_1)]\ldots\mathbf{V}_2(t_1)],\mathbf{V}_1(0)]\rho_0\rangle \tag{3-11}$$

where the initial canonical density operator was denoted as ρ_0 and the operator in the Heisenberg picture is denoted as $\mathbf{V}(t)$. Detailed expressions for the nonlinear response functions will be discussed later in section 4.

The generalized field of the incoming modes can be written in the following form,

$$\mathbf{F}(\mathbf{r},t) = \sum_{j=1}^n [\mathbf{F}_j(t)\exp(i\mathbf{k}_j\cdot\mathbf{r} - i\omega_j t) + \mathbf{F}_j^*(t)\exp(-i\mathbf{k}_j\cdot\mathbf{r} + i\omega_j t)] \tag{3-12}$$

where $\mathbf{F}_j(t) = \mathbf{f}_j F_j(t)$ and $F_j(t)$ and $\mathbf{f}_j$ are the temporal envelope function and unit vector or *n*th-rank tensor of the *j*th field. Then, the nonlinear polarization $\mathbf{P}^{(n)}(\mathbf{r},t)$ is expanded in the form

$$\mathbf{P}^{(n)}(\mathbf{r},t) = \sum_l \mathbf{P}_l^{(n)}(t)\exp(i\mathbf{k}_l\cdot\mathbf{r} - i\omega_l t) \tag{3-13}$$

where $\mathbf{k}_l$ and ω_l are combinations of the wave vectors and frequencies as

$$\mathbf{k}_l = \pm\mathbf{k}_1 \pm \mathbf{k}_2 \ldots \pm \mathbf{k}_n \tag{3-14}$$

$$\omega_l = \pm\omega_1 \pm \omega_2 \ldots \pm \omega_n \tag{3-15}$$

The spatial amplitude of the electric field generated by one of the *n*th-order induced polarizations should satisfy the following Maxwell equation,[39]

$$\nabla \times \nabla \times \{\mathbf{E}_s^{(n)}(t)\exp(i\mathbf{k}_s'\cdot\mathbf{r})\} - \frac{n_s^2\omega_s^2}{c^2}\mathbf{E}_s^{(n)}(t)\exp(i\mathbf{k}_s'\cdot\mathbf{r}) = \frac{4\pi\omega_s^2}{c^2}\mathbf{P}_s^{(n)}(t)\exp(i\mathbf{k}_s\cdot\mathbf{r}) \quad (3\text{-}16)$$

Here, we look for a solution of the form $\mathbf{E}^{(n)}(\mathbf{r},t) = \mathbf{E}_s^{(n)}(t)\exp(i\mathbf{k}_s'\mathbf{r} - i\omega_s t)$, where $\mathbf{k}_s'$ is different from $\mathbf{k}_s$, which is given by a combination of the incoming wave vectors, due to the frequency dispersion of the refractive index of the optical sample. Within the slowly varying amplitude approximation, the signal field amplitude is given as, when the phase-matching condition is satisfied,[37,39]

$$\mathbf{E}_s^{(n)} = \frac{2\pi i\omega_s L\Phi}{n(\omega_s)c}\mathbf{P}_s^{(n)} \quad (3\text{-}17)$$

where L is the length of the optical sample cell and $n(\omega_s)$ is the index of refraction at the frequency of ω_s. The phase-matching factor Φ is given as $\Phi = [\sin(\Delta kL/2)/(\Delta kL/2)]\exp(i\Delta kL/2)$, where $\Delta k = |\mathbf{k}_s - \mathbf{k}_{s'}|$. Now, the next step toward the complete theoretical description of the coherent multidimensional spectroscopy is to obtain the corresponding nonlinear response function, which is required for the calculation of nonlinear polarization and signal electric field. This will be discussed in section 4.

3.2. Designing Multidimensional Optical Spectroscopy

A number of different coherent multidimensional spectroscopic techniques have been experimentally studied and theoretically proposed over the past 10 years.[10,23−34] It is possible to classify these methods into a few groups by sorting different optical excitation and probing steps and the corresponding nonlinear optical transition pathways. Depending on the center frequencies of pulses used, resonant conditions, and experimental schemes and designs chosen, there are a number of different ways to vibrationally or electronically excite molecules in condensed phases. In particular, there are two classes of experiments, those probing population (diagonal density matrix element) and coherence (off-diagonal density matrix element) relaxations. The former types of experiments are to measure time-dependent changes of excited-state population and to estimate the lifetime of a given quantum state that was resonantly excited. Coherence measurement spectroscopy such as the PE technique was found to be useful in studying the vibrational or electronic decoherence rate directly in time by eliminating the inhomogeneous broadening contribution.

There are a few different ways currently used to create a *vibrational* population or a coherence state: (Ex1) absorption of a resonant IR photon, (Ex2) Raman excitation with an electronically nonresonant pulse, (Ex3) stimulated hyper-Raman excitation with an electronically nonresonant pulse, (Ex4) absorption of a resonant circularly polarized IR photon, (Ex5) stimulated Raman excitation by electronically nonresonant (circularly polarized) optical fields, and so on. One of the most straightforward methods to create a vibrational coherence state is to use a resonant infrared pulse (Ex1), and the corresponding IR-field−matter interaction is, within the electric dipole approximation, $-\mu\cdot\mathbf{E}(t)$. The force exerted on the jth vibrational degree of freedom is then given as $(\partial\mu/\partial Q_j)\cdot\mathbf{E}(t)$. Due to the broad spectral bandwidth of the femtosecond IR pulse, the excitation process involves a range of vibrational excitations of modes whose frequencies are within the envelope of the pulse spectrum, $\tilde{E}(\omega)$. The second method (Ex2) is to use a Raman process to vibrationally excite an electronically ground-state molecule. By using an ultrafast optical pulse whose frequency is electronically nonresonant, Raman-active vibrational modes can be excited when the corresponding vibrational frequencies are within the spectral bandwidth of the incident pulse. In this case, the effective field matter interaction is given as $-\alpha:\mathbf{E}^*(t)\mathbf{E}(t)$, where α is the molecular polarizability operator, so that the force exerted on the jth vibrational degree of freedom is in this case $(\partial\alpha/\partial Q_j):\mathbf{E}^*(t)\mathbf{E}(t)$. The third method (Ex3), involves an inelastic hyper-Raman transition, and the jth mode experiences the force, $(\partial\beta/\partial Q_j):\mathbf{E}_1(t)\mathbf{E}_2(t)\mathbf{E}_3^*(t)$. Since the vibrational selection rules of the hyper-Raman process differ from those of the Raman process, stimulated hyper-Raman spectroscopy will provide complementary information on the vibrational dynamics of complex molecules. Although the first three methods described above utilize linearly polarized lights, with circularly polarized (CP) light, it is possible to measure molecular optical activity that is defined as a differential interaction of the left- and right-CP lights with chiral molecules. As theoretically proposed recently, time-resolved optical activity measurement can be achieved by using CP light beams in sum-frequency-generation or four-wave-mixing spectroscopic schemes.[41−45] These novel spectroscopic methods can be of effective use in studying ultrafast dynamics of chiral molecules in condensed phases.

Once a population or coherence state is created, its time evolution can be probed by employing suitable optical probing methods. Similar to an ultrafast excitation (vibrational coherence state generation) process, one can use the same types of field−matter interaction schemes. The first method (Pr1) is to measure the spontaneously emitted IR or visible field by a homodyne or heterodyne detection method. The second method (Pr2) is based on a stimulated Raman scattering. Suppose that a vibrational coherence state is created on the electronic ground state. Then, an electronically nonresonant optical field can be inelastically scattered by this vibrational transient grating. The measured signal intensity or amplitude contains information on the evolution of the vibrational coherence state, i.e., the linear or nonlinear vibrational response of the molecular system. The third method (Pr3) is to use a higher-order (hyper-Raman) scattering process to probe the dynamic evolution of the vibrational coherence state.

Using a proper set of excitation schemes, one can create a 1D transient grating (TG) in a given optical sample.[46] Depending on the probing method, one can selectively measure different molecular properties such as dipole, polarizability, or hyperpolarizability correlation functions etc. As an example, let us consider the coherent Raman scattering spectroscopy utilizing femtosecond laser pulses. For the jth vibrational coherence, its temporal propagation can be approximately described as a damped oscillator, i.e., $e^{-\gamma_j t}\sin\omega_j t$, where γ_j is the vibrational dephasing constant and ω_j is the oscillation frequency. After a finite delay time, the transient dynamics of this 1D grating can be probed by measuring the stimulated Raman scattering. Typical 1D spectroscopy, such as absorption, Raman scattering, and other related techniques, is therefore useful to measure the oscillation frequency and both the pure and inhomogeneous dephasing rate of the created quantum coherence, which is

Scheme 1

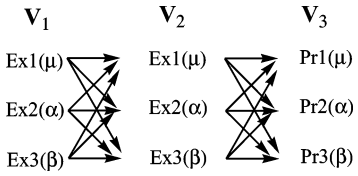

Scheme 2

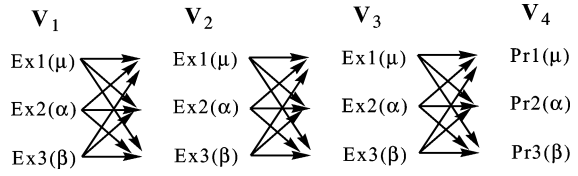

directly related to the corresponding spectrum in the frequency domain via the fluctuation−dissipation theorem.

By combining two or more excitation pulses that are separated in time, it will be possible to create temporally (and/or spatially) multidimensional vibrational or electronic transient gratings. Unlike the 1D case, the signal field generated by the associated nonlinear polarization is then produced by interferences between electric fields created by different nonlinear optical transition pathways. The 2D and 3D spectroscopies are essentially to measure the temporal evolution and relaxation of thus created 2D and 3D transient gratings. In practice, the 2D or 3D signal, $S(t_1,t_2)$ or $S(t_1,t_2,t_3)$, in the time domain is measured as a function of experimentally controlled delay times, and the multidimensional Fourier transformation therefore gives the corresponding 2D or 3D spectrum.

Consequently, combining different sequences of excitation and probing methods, one can devise a number of different ways to create 2D transient gratings, even though only a few of them have been experimentally explored so far. In Scheme 1, some combinations of excitation and probing (Pr1−Pr3) methods are shown. Then, the nonlinear response function associated with two-time-correlation spectroscopy is in general given as

$$R^{(2)}(t_2,t_1) = \left(\frac{i}{\hbar}\right)^2 \langle [[\mathbf{V}_3(t_2+t_1),\mathbf{V}_2(t_1)],\mathbf{V}_1(0)]\rho_0\rangle \qquad (3\text{-}18)$$

In the case of three-time-correlation spectroscopy, there could be 27 different ways to create a 3D transient grating (see Scheme 2) when μ-, α-, and β-induced optical transitions are only considered. The nonlinear response function describing the molecular response to a specific sequence of field−matter interactions in Scheme 2 is defined as

$$R^{(3)}(t_3,t_2,t_1) = \left(\frac{i}{\hbar}\right)^3 \langle [[[\mathbf{V}_4(t_3+t_2+t_1),\mathbf{V}_3(t_2+t_1)],\mathbf{V}_2(t_1)],\mathbf{V}_1(0)]\rho_0\rangle \qquad (3\text{-}19)$$

For example, PE spectroscopy generally involves three laser pulses that are separated in time. Thus, it is one of the 3D experiments in general. However, currently 2D PE experiments have been performed by taking double Fourier transformations with respect to the first and third time variables, and the 2D spectrum as a function of the second delay (waiting or population) time thus obtained was reported. Therefore, it can be viewed as a reduced 2D spectroscopy.

For the sake of simplicity, let us consider the case of an electric-dipole-allowed four-wave-mixing spectroscopy. The third-order nonlinear polarization is given as[37]

$$\mathbf{P}^{(3)}(\mathbf{r},t) \sim N\int_0^\infty dt_3 \int_0^\infty dt_2 \int_0^\infty dt_1\, R^{(3)}(t_n,...,t_2,t_1) \otimes \mathbf{E}(\mathbf{r},t-t_3)\,\mathbf{E}(\mathbf{r},t-t_3-t_2)\,\mathbf{E}(\mathbf{r},t-t_3-t_2-t_1) \qquad (3\text{-}20)$$

In the simple case when the temporal envelopes of the three incident light pulses are approximately Dirac delta functions, we have

$$\mathbf{E}(\mathbf{r},t) = \mathbf{e}_1E_1\delta(t+\tau+T)\exp(i\mathbf{k}_1\cdot\mathbf{r} - i\omega_1 t) + \mathbf{e}_2E_2\delta(t+T)\exp(i\mathbf{k}_2\cdot\mathbf{r} - i\omega_2 t) + \mathbf{e}_3E_3\delta(t)\exp(i\mathbf{k}_3\cdot\mathbf{r} - i\omega_3 t) + c.c. \qquad (3\text{-}21)$$

where the delay times between the first two pulses and between the second and third pulses are denoted as τ and T and E_j is the amplitude of the jth electric field. Suppose that the $(\mathbf{k}_s,\omega_s)$ signal field with $\mathbf{k}_s = (-1)^{m_1}\mathbf{k}_1 + (-1)^{m_2}\mathbf{k}_2 + (-1)^{m_3}\mathbf{k}_3$ and $\omega_s = (-1)^{m_1}\omega_1 + (-1)^{m_2}\omega_2 + (-1)^{m_3}\omega_3$, where m_j can be either 1 or 2 depending on specific nonlinear optical spectroscoscopy experiment and beam configuration, is measured. The $\mathbf{k}_s$-wavevector third-order polarization $\mathbf{P}_s^{(3)}(t,T,\tau)$, which is the coefficient of the $\exp(i\mathbf{k}_s\cdot\mathbf{r} - i\omega_s t)$ Fourier component in the Fourier-expanded $\mathbf{P}^{(3)}(\mathbf{r},t)$, is found to be

$$\mathbf{P}_s^{(3)}(t,T,\tau) = NE_1E_2E_3R^{(3)}(t,T,\tau)\otimes\mathbf{e}_3\mathbf{e}_2\mathbf{e}_1 \qquad (3\text{-}22)$$

From eq 3-17, the electric field emitted by this polarization component is therefore given as

$$\mathbf{E}_s^{(3)}(t,T,\tau) = \frac{2\pi i\omega_s L\Phi NE_1E_2E_3}{n(\omega_s)c}\mathbf{P}_s^{(3)}(t,T,\tau) = \frac{2\pi i\omega_s L\Phi NE_1E_2E_3}{n(\omega_s)c}R^{(3)}(t,T,\tau)\otimes\mathbf{e}_3\mathbf{e}_2\mathbf{e}_1 \qquad (3\text{-}23)$$

Double Fourier transformation of the heterodyne-detected electric field $\mathbf{E}_s^{(3)}(t;m_1,m_2,m_3)$ with respect to τ and t results in the complex 2D spectrum:

$$\tilde{\mathbf{E}}_s^{(3)}(\omega_t,T,\omega_\tau) = \int_{-\infty}^{\infty}dt\int_{-\infty}^{\infty}d\tau\,\mathbf{E}_s^{(3)}(t,T,\tau)e^{i\omega_t t}e^{i\omega_\tau\tau} = \frac{2\pi i\omega_s L\Phi NE_1E_2E_3}{n(\omega_s)c}\int_{-\infty}^{\infty}dt\int_{-\infty}^{\infty}d\tau R^{(3)}(t,T,\tau)\otimes\mathbf{e}_3\mathbf{e}_2\mathbf{e}_1e^{i\omega_t t}e^{i\omega_\tau\tau} \qquad (3\text{-}24)$$

In the case of 3D spectroscopy, the corresponding spectrum is given as

$$\tilde{\mathbf{E}}_s^{(3)}(\omega_t,\omega_T,\omega_\tau) = \frac{2\pi i\omega_s L\Phi NE_1E_2E_3}{n(\omega_s)c}\int_{-\infty}^{\infty}dt\int_{-\infty}^{\infty}dT\int_{-\infty}^{\infty}d\tau\, R^{(3)}(t,T,\tau)\otimes\mathbf{e}_3\mathbf{e}_2\mathbf{e}_1e^{i\omega_t t}e^{i\omega_T T}e^{i\omega_\tau t} \qquad (3\text{-}25)$$

Although an impulsive limit was only considered here, one can easily generalize the argument for the case when the incident pulses have finite temporal widths by using eqs 3-17 and 3-20.

In the above, we considered the electric dipole transition processes only. However, depending on the experimental scheme and the associated nonlinear optical process, the

effective radiation−matter interaction Hamiltonian can be different from $-\mu\cdot\mathbf{E}$, as mentioned above. For instance, in the case of fifth-order Raman scattering spectroscopy, the effective radiation−matter interaction Hamiltonian is given as $H_{\rm int} = -\alpha:\mathbf{E}(\mathbf{r},t)\ \mathbf{E}(\mathbf{r},t)$ (see section 5.1 below for a detailed discussion). Yet, other examples that will be considered in this review are the magnetic dipole−magnetic field interaction and the electric quadrupole−electric field interaction. These interactions are critical in describing nonlinear optical activity measurement spectroscopy for chiral molecules in condensed phases. In any case, one can obtain the corresponding nonlinear response function in terms of multiple time-correlation functions of molecular operators, and the nonlinear polarization is given as convolution integrations over the nonlinear response function and conjugate external fields, as in eq 3-20.

3.3. Phase and Amplitude Detection

There are a number of different ways to detect weak and transient signal electric fields. For instance, one can use a time-gated pulse combined with an upconversion detection technique to measure the temporal amplitude of the signal field.[47−49] A variety of heterodyne detection methods have been developed over the years, such as the time-gated up conversion method mentioned above, FT spectral interferometry,[50−59] and wave packet interferometric detection.[60] In this subsection, we will mainly focus on the spectral interferometry in detail, since it has been extensively used in both 2D IR and 2D electronic spectroscopy, based on a photon echo scheme.

It has been desired to measure both the amplitude and phase of the signal field to fully extract information on nonlinear molecular responses against a train of interrogating pulses. Over the past few years, to achieve the goal, a heterodyne detection method in the frequency domain has been widely used because a fast response array detector became commercially available. In the case when both a reference (local oscillator) field E_0 whose amplitude and phase are fully characterized and the signal field E_s into a dispersive device that is placed prior to an array detector are allowed to interfere with each other, the measured intensity is an absolute square of the sum of the two electric fields

$$I(\omega) = |E_0(\omega) + E_s(\omega)|^2 = |E_0(\omega)|^2 + |E_s(\omega)|^2 + 2\mathrm{Re}[E_0^*(\omega)\, E_s(\omega)] \quad (3\text{-}26)$$

Often the second term on the right-hand side of eq 3-26 is much smaller than the last interference term, since the latter is linearly proportional to the reference field amplitude. Using a chopper properly placed in one of the arms of the Mach−Zehnder interferometer and taking the difference intensity, one can selectively measure the heterodyned signal $I_h = 2\mathrm{Re}[E_0^*(\omega)\, E_s(\omega)]$.[51,52] An experimental setup for the FT spectral interferometry that is based on the Mach−Zehnder interferometer is shown in Figure 4.

In the case when the reference pulse and signal field are temporally overlapped, the interference term is likely to be very large. However, in order to enhance the spectral resolution and to selectively eliminate the contribution from the reference pulse spectrum to the measured heterodyned signal, the reference pulse is deliberately made to precede the signal by a fixed time delay Δ_τ. The delay time Δ_τ is

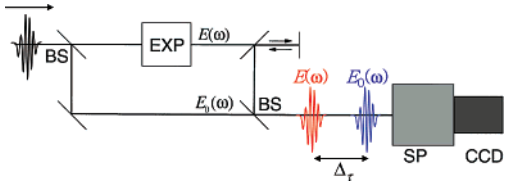

Figure 4. . Mach−Zehnder interferometer for heterodyne-detected Fourier transform spectral interferometry. An unknown electric (signal) field $E(\omega)$ is generated in an experiment (EXP). It interferes in a spectrometer (SP) with a reference beam $E_0(\omega)$. BS's are beam splitters, and CCD represents a charge-coupled device array detector.

chosen to be large enough to ignore the overlap between the reference pulse and the signal field but to be small enough to make the interference signal measurably large. In this case, the interference part of the measured signal has an additional phase-factor originating from the finite delay time Δ_τ as

$$I_h(\omega) = 2\mathrm{Re}[E_0^*(\omega)\, E_s(\omega) e^{i\omega\Delta_\tau}] \quad (3\text{-}27)$$

To obtain the complex spectrum of the signal field, it is necessary to manipulate the heterodyned signal as[52]

$$E_s(\omega) = \frac{F[\theta(t)\, F^{-1}\{I_h(\omega)\}]e^{-i\omega\Delta_\tau}}{E_0^*(\omega)} \quad (3\text{-}28)$$

where $F[...]$ and $F^{-1}[...]$ are the Fourier and inverse Fourier transforms, respectively.

3.4. 2D Pump−Probe

Although a number of different coherent 2D optical spectroscopic methods can be devised by combining a sequence of optical excitation and probing processes, as discussed in section 3.2, one of the early 2D vibrational spectroscopic experiments was based on a pump−probe, i.e., dynamic hole-burning spectroscopy.[8] In a pump−probe experiment, the molecular system is subjected to two light pulses, i.e., pump and probe, of which the center frequencies are $\omega_{\rm pu}$ and $\omega_{\rm pr}$, respectively. The incoming field is therefore given as

$$\mathbf{E}(\mathbf{r},t) = \mathbf{E}_{\rm pu}(t+T)\exp(i\mathbf{k}_{\rm pu}\cdot\mathbf{r} - i\omega_{\rm pu}t) + \mathbf{E}_{\rm pr}(t)\exp(i\mathbf{k}_{\rm pr}\cdot\mathbf{r} - i\omega_{\rm pr}t) + c.c. \quad (3\text{-}29)$$

The time delay of the probe pulse with respect to the pump pulse is T. Then, the probe difference absorption that is defined as the total probe absorption in the presence of the pump minus that in the absence of the pump is detected. In particular, the first two radiation−matter interactions are between a chromophore and the pump pulse. The pump−probe signal field should satisfy the following phase-matching condition, $\mathbf{k}_s = \mathbf{k}_{\rm pu} - \mathbf{k}_{\rm pu} + \mathbf{k}_{\rm pr} = \mathbf{k}_{\rm pr}$.[37] After the first two pump field−matter interactions, not only the ground-state hole but also the excited-state population particle or coherence states can be generated. Note that the first two field−matter interactions occur within the temporal envelope of the pump pulse. After a finite time delay T, the incoming photon stimulates emission of the excited-state particle, is absorbed by the excited-state particle, or is scattered by the ground-state hole. In between the first two field−matter interactions, the system is on an electronic coherence state that is a superposition state of the ground state and one of the excited states. If one uses an ultrafast pump pulse whose

spectral bandwidth is sufficiently broad enough to cover the entire manifold of the excited state, one can simultaneously create an ensemble of ground-state bleaching and excited-state population and coherence states. In such a case, one cannot achieve frequency resolution of the excited states because the measured signal does not depend on the coherence evolution time τ, so that one cannot perform a Fourier transform of the signal with respect to τ. On the other hand, the pump−probe signal can be dispersed by a monochromator, which is analogous to the Fourier transform of the signal with respect to t, the last coherence state evolution time. Therefore, in this case of ultrafast pump−ultrafast probe measurement, the signal can be displayed as a function of the pump−probe delay time T and frequency ω_t, i.e., $\tilde{S}_{PP}(\omega_t,T)$.

To obtain the full 2D pump−probe spectrum, it was therefore necessary to perform a series of dynamic hole burning experiments with a tunable spectrally narrow band pump pulse whose bandwidth should be sufficiently narrow to frequency-resolve the one-quantum excited states or to selectively excite only a subset of the excited states. The frequency tuning of the pump pulse was initially achieved by fine adjustment of the distance between two mirrors in a tunable IR−Fabry−Peror filter, where one of the mirrors was mounted on a stepping motor-controlled translation stage. However, the temporal envelope of the narrow band pump pulse should not be exceedingly broad in comparison to the lifetime of the excited states.

In this case of the mixed frequency−time-resolved pump−probe, the difference absorption signal is given as functions of the center frequency of the pump, the pump−probe delay time T, and the frequency ω_t that is the conjugate frequency of the electronic coherence time t, i.e., $\tilde{S}_{PP}(\omega_t,T,\omega_\tau=\omega_{pu})$. To construct the full 2D pump−probe spectrum, one should scan the pump frequency, ω_{pu}, and assemble the transient difference spectra as a function of the peak frequency ω_{pu}, of the pump pulse.[32] Consequently, this method using a series of dynamic hole burning experiments by tuning the frequency of a spectrally narrow pump pulse is technically not directly analogous to the 2D NMR spectroscopy that utilizes temporally narrow radio frequency pulses and that requires double Fourier transformations to obtain the corresponding 2D NMR spectrum.

Often the frequency scanning of the spectrally narrow pump requires a large amount of data collection time to obtain a single 2D spectrum. One of the experimental breakthroughs was recently achieved by overcoming this low efficiency of currently available methods.[21,22] An essential element of the experimental design is to maximally use a two-dimensional array detector in the visible frequency ranges (see Figure 5). In this case of the so-called single shot 2D electronic spectroscopy (the upper experimental setup in Figure 5), the ultrashort pump pulse whose spectrum is broad enough to excite the entire one-quantum excited states of the coupled multichromophore system is first frequency-dispersed by using a diffraction grating along the x-axis in a space-fixed frame. Here, it is assumed that the pump and probe beams propagate along the z-axis. This frequency dispersed pump pulse, which is spatially encoded in the sample, excites a system. Subsequently, a cylindrically focused probe pulse interrogates the excitation area in the sample. Here, it should be noted that the probe pulse is not frequency-dispersed when it is injected into the sample. Then, the generated pump−probe signal is frequency-dispersed

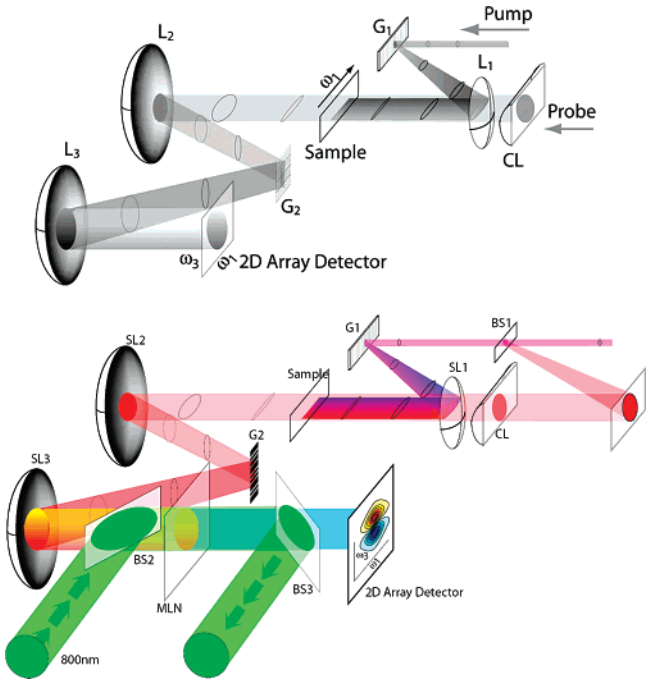

Figure 5. Experimental setups for single-shot 2D electronic (upper)[21] and 2D IR (lower)[22] experiments: G, diffraction grating; L, spherical mirror; CL, cylindrical lens; SL, spherical focusing mirror; BS, beam splitter, and MLN ($MgO:LiNbO_3$), upconversion crystal.

after the sample along the y-axis. Using spherically focusing mirrors, the two-dimensionally (x and y space) spreaded pump−probe signal field is a direct image of the 2D electronic spectrum spatially encoded in the sample, where the spatial dimensions along the x- and y-axes in the recorded image correspond to ω_τ and ω_t, respectively. An experimental demonstration was recently reported for atomic Rb vapor.[21]

Although a 2D array detector in the *visible* spectral range is commercially available, that is not the case in the mid-IR spectral range yet. Therefore, to record the 2D IR spectrum by using the same single shot measurement scheme, an upconversion technique had to be used (see the lower scheme in Figure 5). Using femtosecond mid-IR pump and probe pulses, one can generate a spatially/spectrally two-dimensionally dispersed IR pump−probe field in the mid-IR frequency range. Then, for a frequency upconversion, one can use an 800 nm local osillator field that is spatially overlapped with the above 2D IR pump−probe field. These two beams, the 2D IR pump−probe signal field and the 800 nm local oscillator field, were allowed to interfere by using an upconversion crystal to upconvert the 2D IR spectrum image into the visible spectral range. In this case, the 800 or 400 nm light can be easily removed by using optical filters placed prior to the CCD array. A couple of examples, metal−carbonyl compounds, were chosen to demonstrate the experimental feasibility of this single shot 2D IR spectroscopy.[22]

3.5. 2D Photon Echo

Electronic or vibrational PE is an optical analogue of NMR spin echo. In an optical PE experiment typically utilizing three light pulses, a phase-matching geometry based on momentum conservation of the photons is used to detect the

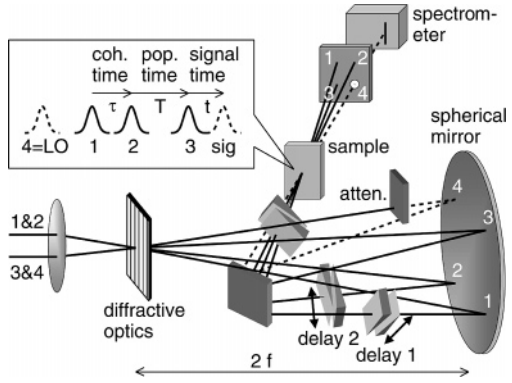

Figure 6. 2D photon echo experimental configuration (see ref 59 for a detailed description of the spectral interfererometric 2D electronic photon echo spectrometer). Two time-delayed parallel beams are focused onto a 30-groove/mm diffractive optics (DO) by a 20 cm lens. The positive and negative first diffraction orders emerge with high efficiency and provide excitation pulses 1−3 as well as the local oscillator (LO) (4 = LO) used for heterodyne detection. A spherical mirror ($2f = 50$ cm) generates a 100-mm beam-diameter ($1/e^2$ intensity level) image of the DO spot via a plane folding mirror inside the sample cell. Time delays (1 and 2) are introduced with interferometric precision by movable glass wedges with the required pulse orders and timing intervals t and T (inset). Spectral interferometry between the attenuated LO and the emitted third-order signal field (dashed curves in the inset and dashed lines in the main figure) fully characterizes the response of the sample in amplitude and phase.

echo signal (see Figure 6).[59] The key idea of PE spectroscopy was to exploit the correlation between the initial excitation frequency and the final detection (emission or probing) frequency in time and to eliminate the static inhomogeneous line broadening contribution by measuring the rephasing echo signal.[5,37,61] In the limiting case when the line shape is dictated by a large inhomogeneous broadening, the echo signal field will peak at $t = \tau$ due to the rephasing process. However, chromophores in solution do not have truly static inhomogeneity due to ultrafast spectral diffusion and solvation processes, so that the echo signal field amplitude varies in time and is a function of the detection time t, which is the delay time after the third pulse in a three-pulse photon echo experiment.

The phase-matched signal field should then satisfy the following wave vector equality, $\mathbf{k}_s = -\mathbf{k}_1 + \mathbf{k}_2 + \mathbf{k}_3$. The corresponding diagrams have been called the rephasing ones. The "mirror image" echoes appear at $\mathbf{k}_s = \mathbf{k}_1 - \mathbf{k}_2 + \mathbf{k}_3$, and the corresponding diagrams are the non-rephasing ones. At short time that is shorter than the correlation time of the solvation dynamics or the relaxation time of the frequency−frequency correlation function, the rephasing echo and the mirror image echo signals with respect to the first coherence period, τ, do not overlap, and the time difference between the two peaks was defined as the three-pulse photon echo peak shift (3PEPS), denoted as $\tau^*(T)$.[62,63] It turned out that the 3PEPS as a function of the second delay time T between the second and third pulses in the three-pulse photon echo, which was called the waiting or population evolution time in the literatures, is directly related to the transition frequency−frequency correlation function and its asymtotic value is related to the static inhomogeneity, directly reflecting unequal environments of chromophores.[5] Although the chromophores in polymers, solids, or protein matrices can have static inhomogeneous environments, those in solutions do not. Nevertheless, one can still interpret the 3PEPS at a finite waiting time T as a *dynamical* inhomogeneity on a time scale of T. If the chemical or physical process of interest is much faster than the solvent correlation time, defined as the time integration of the normalized solvation correlation function, chromophores involved in such a process can be considered to have a broad static inhomogeneous environment because the solvent molecular motions are rather sluggish on such a short time scale. On the other hand, if the time scale of the process of interest is very slow compared to the solvent correlation time, the surrounding solvent molecules will adiabatically follow the process and thus the solvent can be considered to be purely homogeneous for all chromophores.

A femtosecond optical (either visible or infrared) pulse whose spectral bandwidth is sufficiently broad to simultaneously excite a manifold of excited or delocalized excitonic states can create quantum coherence states $\rho_{eg}^{(1)}(\tau)$ between the ground and excited states. The second pulse interacts with the system, and either the ground-state population $\rho_{gg}^{(2)}(\tau,T)$ or the excited-state coherence $\rho_{ee'}^{(2)}(\tau,T)$ (for $e \neq e'$) or population $\rho_{ee}^{(2)}(\tau,T)$ is created. Note that the density matrix $\rho^{(2)}(\tau,T)$ is second-order with respect to the electric field *amplitude*. The third field−matter interaction finally generates the third-order density matrix elements, such as $\rho_{e'g}^{(3)}(\tau,T,t)$, which emits an echo field via a spontaneous emissive interaction with the vaccum field.

The emitted echo field is then put into a spectral interferometer to allow its interference with a local oscillator pulse that temporally precedes the echo by a finite time Δ_τ. In this case of 2D PE, the transient profile of the echo signal field as a function of detection time t is not directly measured but indirectly measured by using the FT spectral interferometry in the frequency domain.[51] Here, the heterodyne-detected interferogram $I_h(\omega_t,T,\tau)$ corresponds to the echo signal depending on the two experimentally controlled delay times τ and T. Therefore, the 2D PE signal field can be extracted from $I_h(\omega_t,T,\tau)$ as

$$E_{echo}(\omega_t,T,\tau) = \frac{F[\theta(t)\, F^{-1}\{I_h(\omega_t,T,\tau)\}]e^{-i\omega_t\Delta_\tau}}{E_0^*(\omega_t)} \quad (3\text{-}30)$$

The 2D PE spectrum is finally obtained by performing a numerical Fourier transformation with respect to the first coherence delay time, τ, as

$$\tilde{E}_{echo}(\omega_t,T,\omega_\tau) = \int_{-\infty}^{\infty} d\tau\, E_{echo}(\omega_t,T,\tau)\exp(i\omega_\tau\tau) \quad (3\text{-}31)$$

This has become the standard procedure for the spectral interferometric heterodyne-detected 2D photon echo experiment.

In the present subsection, we provided a discussion on the experimental method of detecting a 2D PE spectrum by employing FT spectral interferometry. One can of course use a different detection method to characterize the echo field amplitude and phase to collect the entire information on the molecular echo response. Nevertheless, the essential idea is that the double Fourier transformations of the echo signal field $E_{echo}(t,T,\tau)$ with respect to τ and t are required to obtain the complex 2D PE spectrum.

Since the thus obtained 2D PE spectrum is complex and depends on the phase-matching condition used, there exist different ways to present the 2D PE spectra. With the phase-matching condition of $\mathbf{k}_s = -\mathbf{k}_1 + \mathbf{k}_2 + \mathbf{k}_3$, the real and

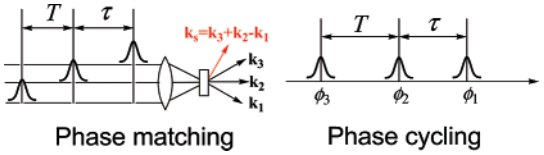

Figure 7. Pulse sequences used in ultrafast 2D spectroscopy with a non-collinear phase-matching geometry (left). Three excitation pulses, separated by delays τ and T and traveling in different directions $\mathbf{k}_1$, $\mathbf{k}_2$, and $\mathbf{k}_3$, respectively, are focused onto the sample. The photon echo signal is emitted in a different direction $\mathbf{k}_s = \mathbf{k}_3 + \mathbf{k}_2 - \mathbf{k}_1$ and hence is spatially isolated. Echo polarization is measured as a function of τ and T. The pulse sequence used in ultrafast 2D spectroscopy with phase cycling (right panel) is also shown. Three collinear pulses, with phases ϕ_1, ϕ_2, and ϕ_3, are separated by delays of τ and T.

imaginary parts of $\tilde{E}_{\mathrm{echo}}(\omega_t,T,\omega_\tau)$ were separately reported. The absolute magnitude spectrum defined as $|\tilde{E}_{\mathrm{echo}}(\omega_t,T,\omega_\tau)|$ was also used and discussed quite often in the literature. An absorptive 2D PE spectrum obtained as the sum of equally weighted rephasing and non-rephasing echo signals was also considered to be of use.

Most of the photon echo spectroscopy experiments were based on a non-collinear four-wave-mixing scheme with a specific phase-matching condition, where incident beams propagate slightly differently (see Figure 7) in space. The phase-matching method has a clear advantage of spatial separation of the desired and undesired signals, as can be seen in Figure 7—note that the signal field propagates in a different direction.

However, the direct optical analogue[4] of 2D NMR utilizing the phase cycling technique was only recently demonstrated to be experimentally feasible.[20] The phases of the three collinearly propagating pulses are controlled so that the echo polarization becomes a function of the input pulse phases $\phi_1 \sim \phi_3$ (see Figure 7). The echo polarization has a unique phase dependence on the input pulses. Then, the photon echo peaks can be selectively measured by combining 16 different phase combinations, i.e., 16-step phase cycling.[20] It should be mentioned that there are certain advantages of the phase cycling technique over phase-matching: (1) coherently averaging away a specific interaction mechanism can enhance the signal intensity;[1,64] (2) the collinear approach decreases the number of required data points; and (3) the phase-matching technique works in extended systems with many chromophores, but the collinear phase cycling technique is not strongly limited by the size of the sample.[20] For the sake of experimental demonstration, rubidium atomic vapor was chosen, where rubidium atom can be considered as a four-level system consisting of the ground state $5S_{1/2}$, two singly excited states $5P_{1/2}$ and $5P_{3/2}$, and one doubly excited state 5D. Despite the success of the optical 2D spectroscopy employing a phase cycling technique, its 2D IR spectroscopy has not been performed yet.

3.6. Two Different Conventions of Plotting 2D Spectra

Unfortunately, there exist a few different notations for the three delay times. In this review, the first, second, and third delay times in a typical heterodyne-detected PE spectroscopy are denoted as τ (or t_1), T (or t_2), and t (or t_3). Since the two-dimensional Fourier transformations were performed for the first and third time variables, the conjugate Fourier frequencies are denoted as ω_τ (or ω_1) and ω_t (or ω_3), respectively. In some of the literature, instead of ω_t, ω_m was used. Also, the waiting time T was often denoted as T_w. However, these are more or less trivial problems, and now more and more workers in this research area use the same notations, either (τ, T, t) or (τ, T_w, t) for time variables and (ω_τ, ω_t) for frequency variables. However, the more serious and quite often very confusing convention is the way of choosing the x- and y-axes for 3D color or contour plots of the 2D spectrum, where the z-axis is reserved for the amplitude or intensity of the spectrum or signal. A group of workers has used the convention that the y-axis is ω_τ and the x-axis is ω_t. Therefore, the frequency spectrum associated with the first coherence state evolution during the τ period is on the y-axis and that with the final coherence state evolution during the t period is on the x-axis. However, the other convention is to choose the ω_τ and ω_t frequency variables as the x- and y-axis labels, respectively. At first sight, this problem seems minor and trivial. However, when one compares two 2D spectra reported by two different groups, even if the two groups took the same molecular system for 2D spectroscopic measurements, the two spectra reported appear to be fairly different due to this plotting convention problem. In this review, a number of 2D spectra reported in the literature will be shown for the sake of completeness. Since it was not possible for the author to replot those 2D spectra obtained by other workers, it is highly recommended that the readers should carefully examine the x- and y-axis labels of each individual 2D plot to follow the discussions.

4. Theory and Computational Method

Both polypeptides and molecular complexes with a number of vibrational or electronic chromophores that are coupled to each other can be successfully modeled by using the Frenkel exciton model,[65−67] where each monomeric chromophore is either a two-level system or an anharmonic oscillator system.[34] In the case of the amide I vibrations, each individual amide I local oscillator can be approximated as an anharmonic oscillator with just three low-lying vibrational states. Note that most of the 2D vibrational spectroscopic techniques based on a four-wave-mixing method such as 2D IR pump−probe and photon echo involve vibrational transitions up to the second excited states that are either overtone or combination states of amide I vibrations. Thus, one can assume that a vibrational chromophore in this case is a three-level system with the overtone anharmonicity correctly taken into consideration.[8,32] On the other hand, for a coupled multichromophore system such as a photosynthetic light-harvesting complex or J-aggregate, where the associated optical transition of an individual chromophore is electronic in nature, one can assume that the monomer is a two-level system.[7,9,10,68−70] However, due to the electronic couplings between two-level monomeric chromophores, the excited states of the entire multichromophore system involve not only one-exciton states but also two-exciton states. Nevertheless, the model Frenkel Hamiltonians for these two different classes of complicated molecular systems are little different from each other. Then, the delocalized excitonic states are given as linear combinations of basis states (or modes). This is in analogy with the LCAO-MO (linear combination of atomic orbitals-molecular orbital) theory, where molecular orbitals are described as linear combinations of atomic orbitals (see Scheme 3). An important issue for developing LCBM-exciton (linear com-

Scheme 3

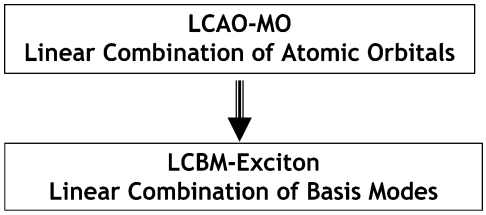

bination of basis modes-exciton) theory is to identify a proper set of basis states or basis modes. Several examples will be discussed in this article.

4.1. Coupled Multichromophore System: Site Representation

Nonlinear optical properties of molecular complexes and aggregates have been described by using the Frenkel exciton theory.[71] Denoting a_m^+ and a_m to be the creation and annihilation operators of an electronic excitation at the mth two-level chromophore, the zero-order Hamiltonian can be written as[10,72]

$$H_0 = \sum_{m=1}^{N} \hbar\omega_m a_m^+ a_m + \sum_{m}^{N}\sum_{n\neq m}^{N} \hbar J_{mn} a_m^+ a_n + H_{ph} \quad (4\text{-}1)$$

where the excited-state energy of the mth chromophore, the electronic coupling constant between the mth and nth chromophores, and the phonon bath Hamiltonian were denoted as $\hbar\omega_m$, J_{mn}, and H_{ph}, respectively (see Figure 8). If each monomeric chromophore is an anharmonic oscillator

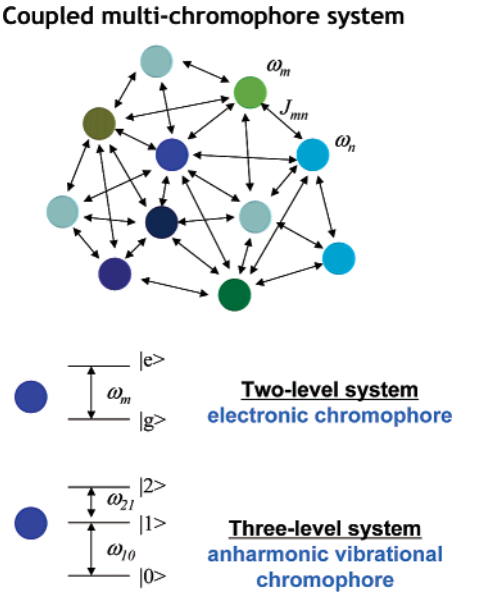

Figure 8. Schematic of a coupled multichromophore system. The transition frequency of the mth monomeric chromophore is denoted as ω_m. The transition frequency can be inhomogeneously distributed due to different local environments for each multichromophore system as well as to variations of chemical structures. The coupling constant between the mth and nth electronic or vibrational transitions is J_{mn}. Although only the arrows representing couplings between nearest neighboring chromophores are drawn in this figure for the sake of simplicity, each monomeric transition is coupled to all other chromophores' transitions in general. Coupling constant amplitude is determined by the relative distance and orientation of a given pair of chromophores. Depending on the molecular system, each chromophore can be modeled as either a two-level system or a three-level system.

instead of a two-level system, the zero-order Hamiltonian should be written as

$$H_0 = \sum_{m=1}^{N} \hbar\omega_m a_m^+ a_m + \sum_{m}^{N}\sum_{n\neq m}^{N} \hbar J_{mn} a_m^+ a_n + \sum_{m}^{N}\sum_{n}^{N} \hbar\Delta_{mn} a_m^+ a_n^+ a_m a_n + H_{ph} \quad (4\text{-}2)$$

Note that the third term on the right-hand side of eq 4-2 describes potential anharmonicities.

The chromophore−bath interaction and the changes of interchromophore distance and orientation induce fluctuations of site energies and coupling constants. Thus, the general system−bath interaction Hamiltonian is written as

$$H_{SB} = \sum_{m}\sum_{n} \hbar q_{mn}(\mathbf{Q}) a_m^+ a_n \quad (4\text{-}3)$$

where $q_{mn}(\mathbf{Q})$ is an operator of bath coordinates, $\mathbf{Q}$, and it is assumed that the expectation values calculated over the bath eigenstates, $\langle q_{mn}(\mathbf{Q})\rangle_0$, are zero—note that if $\langle q_{mn}(\mathbf{Q})\rangle_0$ values are finite, they can be included in the zero-order Hamiltonian. For $m \neq n$, the couplings to bath degrees of freedom can induce excitation transfers between different chromophores in the site representation. The total Hamiltonian can therefore be written as

$$H = H_0 + H_{SB} + H_B \quad (4\text{-}4)$$

4.2. Coupled Multichromophore System: Delocalized Exciton Representation

For any general four-wave-mixing spectroscopy, it is necessary to consider three well-separated quantum state manifolds: the ground state, N one-exciton states, and $\sim N^2$ two-exciton states. The one- and two-exciton eigenvalues and eigenvectors can be obtained by diagonalizing the one- ($\tilde{H}_1$) and two-exciton ($\tilde{H}_2$) Hamiltonian matrices in the site representation as

$$U^{-1}\tilde{H}_1 U = \hbar\tilde{\Omega}$$

$$V^{-1}\tilde{H}_2 V = \hbar\tilde{W} \quad (4\text{-}5)$$

where the one- and two-exciton eigenvalues are the diagonal matrix elements of $\hbar\tilde{\Omega}$ and $\hbar\tilde{W}$, respectively. The one- and two-exciton states are therefore linear combinations of singly or doubly excited-state wave functions, i.e.,

$$|e_j\rangle = \sum_m U_{jm}^{-1} |m\rangle$$

$$|f_k\rangle = \sum_{m=1}^{N-1}\sum_{n=m+1}^{N} v_{mn}^{(k)} |m,n\rangle \quad (4\text{-}6)$$

where $|m\rangle = a_m^+|0\rangle$ and $|m,n\rangle = a_m^+ a_n^+|0\rangle$. The eigenvector elements of the jth one-exciton and the kth two-exciton states were denoted as U_{jm}^{-1} and $v_{mn}^{(k)}$, respectively. The matrix elements of $v^{(k)}$ correspond to the elements of the kth row of the matrix V^{-1}.

Due to the chromophore−bath interaction, the corresponding matrices $H_{SB}^{(1)}$ and $H_{SB}^{(2)}$ in the site representation can be

transformed as, in the delocalized exciton state representation,[10]

$$\hbar\tilde{\Xi}^{(1)}_{SB}(\mathbf{Q}) = U^{-1}\tilde{H}^{(1)}_{SB}(\mathbf{Q})U$$

$$\hbar\tilde{\Xi}^{(2)}_{SB}(\mathbf{Q}) = V^{-1}\tilde{H}^{(2)}_{SB}(\mathbf{Q})V \qquad (4\text{-}7)$$

The diagonal matrix elements, $[\tilde{\Xi}^{(1)}_{SB}(\mathbf{Q})]_{jj}$ and $[\tilde{\Xi}^{(2)}_{SB}(\mathbf{Q})]_{kk}$, describe the energy fluctuations induced by the chromophore−bath interaction of the jth one-exciton and the kth two-exciton states, respectively. The off-diagonal matrix elements of $\tilde{\Xi}^{(1)}_{SB}(\mathbf{Q})$ and $\tilde{\Xi}^{(2)}_{SB}(\mathbf{Q})$ will induce exciton transfers within the one- and two-exciton state manifolds, respectively.

Now, the energy of the jth one-exciton state, fluctuating due to chromophore−bath interactions, can be written as

$$\hbar\Omega_j(\mathbf{Q}) = \hbar\tilde{\Omega}_{jj} + \hbar[\tilde{\Xi}^{(1)}_{SB}(\mathbf{Q})]_{jj} = \hbar\tilde{\Omega}_{jj} + \hbar\sum_m\sum_n U^{-1}_{jm}q_{mn}(\mathbf{Q})U_{nj} \qquad (4\text{-}8)$$

Usually, the fluctuation amplitudes of the coupling constants, q_{mn} (for $m \neq n$), are smaller than the fluctuation amplitudes of the site energies (diagonal elements), i.e.,

$$\langle q_{mm}{}^2\rangle \gg \langle q_{np}{}^2\rangle \qquad \text{for all } m, n, \text{ and } p, \text{ and } n\neq p \qquad (4\text{-}9)$$

Therefore, eq 4-8 can be simplified as

$$\hbar\Omega_j(\mathbf{Q}) \cong \hbar\tilde{\Omega}_{jj} + \hbar\sum_m U_{mj}{}^2 q_{mm}(\mathbf{Q}) \qquad (4\text{-}10)$$

Note that the fluctuation of the jth one-exciton state energy, the second term in eq 4-10, is given by a linear combination of each site energy fluctuation term, $\hbar q_{mm}(\mathbf{Q})$, and the weighting factors are determined by the *square* of the corresponding eigenvector elements. Similarly, the kth two-exciton state energy is written as

$$\hbar W_k(\mathbf{Q}) = \hbar\tilde{W}_{kk} + \hbar[\tilde{\Xi}^{e-p}_2(\mathbf{Q})]_{kk} = \hbar\tilde{W}_{kk} + \hbar\sum_m\sum_n V^{-1}_{jm}[\tilde{H}^{e-p}_2(\mathbf{Q})]_{mn}V_{nj}$$

$$\cong \hbar\tilde{W}_{kk} + \hbar\sum_{m=1}^{N-1}\sum_{n=m+1}^{N}(v^{(k)}_{mn})^2\{q_{mm}(\mathbf{Q}) + q_{nn}(\mathbf{Q})\} \qquad (4\text{-}11)$$

Note that the energy fluctuation at the mth site, described by $\hbar q_{mm}(\mathbf{Q})$, modulates both the one- and two-exciton state energies and that the relative weighting factors are determined by the associated eigenvector elements. From eqs 4-10 and 4-11, one can deduce the fact that the fluctuation of the jth one-exciton transition frequency is intrinsically correlated with the fluctuation of other one- or two-exciton transition frequencies. Because this instantaneous correlation resulted from the electronic couplings, the one- and two-color photon echo peak shifts[68] can be used to study the spatial extent of exciton delocalization as well as the spatial overlap between different one- or two-exciton state probability densities. In addition, the cross peaks in the 2D spectrum at $T = 0$ are spectroscopic signatures of interchromophore couplings.

Once the eigenvectors of the one- and two-exciton states are determined, the exciton transition dipole matrix elements can be expressed as linear combinations of transition dipoles of constituent chromophores, i.e.,

$$\mu_{e_jg} \equiv \langle e_j|\mu|g\rangle = \sum_m U^{-1}_{jm}\mathbf{d}_m$$

$$\mu_{f_ke_j} = \langle f_k|\mu|e_j\rangle = \sum_{m=1}^{N-1}\sum_{n=m+1}^{N} v^{(k)}_{mn}(U^{-1}_{jn}\mathbf{d}_m + U^{-1}_{jm}\mathbf{d}_n)$$

(coupled two-level systems)

$$\mu_{f_ke_j} = \sum_{m=1}^{N}\sum_{n=m}^{N} v^{(k)}_{mn}\{(U^{-1}_{jm}\mathbf{d}_n + U^{-1}_{jn}\mathbf{d}_m)(1-\delta_{mn}) + \sqrt{2}U^{-1}_{jm}\mathbf{d}_m\delta_{mn}\}$$

(coupled anharmonic oscillator systems) (4-12)

where $\mathbf{d}_m$ is the transition dipole vector of the mth chromophore, i.e., $\mathbf{d}_m \equiv \langle m|\mu|0\rangle$. The transition dipole matrix elements in eq 4-12 have been used to calculate various 2D spectroscopic response functions of coupled multichromophore systems, such as polypeptides and light-harvesting complexes.

For a multilevel system considered here, both the autocorrelation and cross-correlation functions of the one- and two-exciton transition frequencies are required to eventually calculate the 2D spectroscopic nonlinear response functions. Using the approximate expressions in eq 4-10, one can obtain the time-correlation between any given two one-exciton transition frequencies as

$$\langle\delta\Omega_j(t)\,\delta\Omega_k(0)\rangle = \sum_m\sum_n U_{mj}{}^2U_{nk}{}^2\langle q_{mm}(t)\,q_{nn}(0)\rangle \qquad (4\text{-}13)$$

where $\delta\Omega_j(\mathbf{Q}) = \Omega_j(\mathbf{Q}) - \tilde{\Omega}_{jj}$ and $\delta\Omega_j(t) = \exp(iH_{ph}t/\hbar)\,\delta\Omega_j(\mathbf{Q})\exp(-iH_{ph}t/\hbar)$. When the transition frequency fluctuation of the mth chromophore can be assumed to be statistically independent of that of the nth chromophore, the following approximation can be used to greatly simplify the theoretical derivation of the nonlinear response function:

$$\langle q_{mm}(t)\,q_{nn}(0)\rangle = \delta_{mn}\langle q_{mm}(t)\,q_{mm}(0)\rangle \qquad (4\text{-}14)$$

Then, eq 4-13 simplifies to

$$\langle\delta\Omega_j(t)\,\delta\Omega_k(0)\rangle = \sum_m U_{mj}{}^2U_{mk}{}^2\langle q_{mm}(t)\,q_{mm}(0)\rangle \qquad (4\text{-}15)$$

Further assuming that the site energy fluctuation correlation functions $\langle q_{mm}(t)\,q_{mm}(0)\rangle$ are all identical, we have

$$\langle q_{mm}(t)\,q_{mm}(0)\rangle = C(t) \quad (\text{for all } m) \qquad (4\text{-}16)$$

In any case, it should be mentioned that the two approximations in eqs 4-14 and 4−16 are not always necessary to calculate the nonlinear response function.

Note that $C(t)$ is a complex function related to the spectral density.[5] Now, $C(t)$ is expressed as a sum of the real and imaginary parts:

$$C(t) = a(t) + ib(t) \qquad (4\text{-}17)$$

Introducing the spectral density $\rho(\omega)$ representing the spectral distribution of the chromophore−bath coupling constants,[5]

one can rewrite the real and imaginary parts, $a(t)$ and $b(t)$, as

$$a(t) = \int_0^\infty d\omega\ \rho(\omega)\coth\left[\frac{\hbar\omega}{2k_BT}\right]\omega^2\cos\omega t \quad (4\text{-}18)$$

$$b(t) = \int_0^\infty d\omega\ \rho(\omega)\omega^2\sin\omega t \quad (4\text{-}19)$$

Note that the absolute magnitude of the spectral density is determined by the solvent reorganization energy associated with the chromophore's excitation as $\lambda = \hbar\int_0^\infty d\omega\ \omega\rho(\omega)$,[5] and λ can be interpreted as a one-quantum energy averaged over the spectral density. Since the initial value of $C(t)$, which is the mean square fluctuation amplitude of the transition frequency of an uncoupled chromophore, is a critical quantity, it is especially denoted as

$$C_0 = C(0) = \langle\omega^2\coth[\hbar\omega/2k_BT]\rangle_\rho = \int_0^\infty d\omega\ \rho(\omega)\coth[\hbar\omega/2k_BT]\omega^2 \quad (4\text{-}20)$$

By using the approximation of eq 4-16, eq 4-13 is further simplified as

$$\langle\delta\Omega_j(t)\ \delta\Omega_k(0)\rangle = (\sum_m U_{mj}{}^2U_{mk}{}^2)C(t) \quad (4\text{-}21)$$

Next, the correlation functions between any given two two-exciton transition frequencies were found to be

$$\langle\delta W_j(t)\ \delta W_k(0)\rangle = \sum_{m=1}^{N-1}\sum_{n=m+1}^{N}\sum_{r=1}^{N-1}\sum_{s=r+1}^{N}(v_{mn}^{(j)})^2(v_{rs}^{(k)})^2\langle\{q_{mm}(t) + q_{nn}(t)\}\{q_{rr}(0)+q_{ss}(0)\}\rangle \cong (\sum_{m=1}^{N-1}\sum_{n=m+1}^{N}(v_{mn}^{(j)})^2\{P_m^{(k)} + P_n^{(k)}\})C(t) \quad (4\text{-}22)$$

where the second equality was obtained by invoking the approximation in eq 4−16, and

$$P_m^{(k)} \equiv \sum_{j=1}^{m-1}(v_{jm}^{(k)})^2 + \sum_{j=m+1}^{N}(v_{mj}^{(k)})^2 \quad (4\text{-}23)$$

In addition to the correlation functions between two one-exciton transition frequencies and between two two-exciton transition frequencies, the cross-correlation functions between $\delta\Omega_j(t)$ and $\delta W_k(0)$ are required in calculating the nonlinear response functions. They are

$$\langle\delta\Omega_j(t)\ \delta W_k(0)\rangle = \sum_{m=1}^{N}\sum_{r=1}^{N-1}\sum_{s=r+1}^{N}U_{mj}{}^2(v_{rs}^{(k)})^2\langle q_{mm}(t)\{q_{rr}(0)+q_{ss}(0)\}\rangle \cong (\sum_{m=1}^{N}U_{mj}{}^2P_m^{(k)})C(t) \quad (4\text{-}24)$$

In this subsection, invoking the two approximations, eqs 4-14 and 4-16, we showed that all autocorrelation and cross-correlation functions of fluctuating one- and two-exciton frequencies can be written in terms of the frequency−frequency correlation function of a single chromophore, $C(t)$. This theory is quite useful for numerical simulations of linear and nonlinear optical spectra of coupled multichromophore systems in general.

4.3. Experimental Signatures of Delocalized Exciton States

Three different correlation functions of one- and two-exciton state frequency fluctuations in eqs 4-21, 4-22, and 4-24 have different physical meanings and are related to either the spatial delocalization of the corresponding excitonic states or the spatial overlap between different excitonic state probability densities. First of all, the mean square fluctuation amplitude of the jth one-exciton transition frequency, $\langle\delta\Omega_j^2\rangle$, is given as

$$\frac{\langle\delta\Omega_j{}^2\rangle}{C_0} = \sum_m U_{mj}{}^4 = \frac{1}{N_j} \quad (4\text{-}25)$$

By noting that the inverse participation ratio (IPR) of the jth one-exciton state denoted as N_j is defined as $N_j = [\sum_m U_{mj}^4]^{-1}$, the ratio $\langle\delta\Omega_j^2\rangle/C_0$ can be of use to obtain the extent of delocalization of the j^{th} exciton state in space. As N_j increases, the associated line width, which is approximately proportional to $\langle\delta\Omega_j{}^2\rangle$, decreases. This is known as an *exchange-narrowing effect* found in a *J*-aggregate.[73] In order to experimentally measure the autocorrelation function, $\langle\delta\Omega_j(T)\ \delta\Omega_j(0)\rangle$, one can use the photon echo peak shift measurement method. It was found that the PE peak shift decays, with respect to T, as[5,62,68]

$$\tau^*(T;\omega_1{=}\omega_3{=}\bar{\omega}_{e_jg}) = \frac{\mathrm{Re}[\langle\delta\Omega_j(T)\ \delta\Omega_j(0)\rangle]}{\sqrt{\pi}\langle\delta\Omega_j{}^2\rangle^{3/2}} \quad (4\text{-}26)$$

where the center frequencies of the femtosecond laser beams, ω_1 and ω_3, are tuned to be identical to the average transition frequency of the jth one-exciton state ($|e_j\rangle$).

Second, the normalized cross-correlation amplitude, $\langle\delta\Omega_j\delta\Omega_k\rangle/C_0$, is written as

$$\frac{\langle\delta\Omega_j\delta\Omega_k\rangle}{C_0} = \sum_m U_{mj}{}^2U_{mk}{}^2 \quad (4\text{-}27)$$

The vector, $\vec{p}_j = (U_{1j}^2, U_{2j}^2, \ldots)$, where each element is the square of an eigenvector element, describes the probability density distribution of the jth exciton state in the site representation. Thus, we have

$$\langle\delta\Omega_j\delta\Omega_k\rangle/C_0 = \vec{p}_j\cdot\vec{p}_k \quad (4\text{-}28)$$

which can be viewed as the *spatial overlap of the two probability density distributions*, $\vec{p}_j$ and $\vec{p}_k$, of the jth and kth exciton states. This suggests that $\langle\delta\Omega_j\delta\Omega_k\rangle/C_0$ is a measure of overlap between $|\psi_j|^2$ and $|\psi_k|^2$, where ψ_j, for example, is the wave function of the jth one-exciton state.[10] Once $\langle\delta\Omega_j\delta\Omega_k\rangle/C_0$ values are experimentally measured, it will provide spatial information about a pair of excitons that have different frequencies. Recently, it was shown that the two-color photon echo peak shift measurement, where the two different frequencies of the incident laser beams are

simultaneously resonant with the jth and kth one-exciton transitions, can be used to measure this particular quantity; i.e.,[7,68]

$$\tau^*_{\mathrm{two}}(T;\omega_1=\bar{\omega}_{e_jg},\omega_3=\bar{\omega}_{e_kg}) = \frac{\mathrm{Re}[\langle \delta\Omega_j(T)\,\delta\Omega_k(0)\rangle]}{\sqrt{\pi}\langle \delta\Omega_j^{\,2}\rangle\langle \delta\Omega_k^{\,2}\rangle^{1/2}} \tag{4-29}$$

Next, let us consider the cross-correlation between the jth one-exciton state frequency fluctuation and the kth two-exciton state frequency fluctuation, $\langle \delta\Omega_j(t)\,\delta W_k(0)\rangle$. It was found that

$$\frac{\langle \delta\Omega_j \delta W_k\rangle}{C_0} = \sum_{m=1}^{N} U_{mj}^{\,2} P_m^{(k)} \tag{4-30}$$

To understand the physical meaning of the quantity, $\sum_{m=1}^{N} U_{mj}^2 P_m^{(k)}$, it is useful to define the projection operator, $\hat{P}_m = |m\rangle\langle m|$, where $|m\rangle$ denotes the singly excited-state of the mth chromophore. Then, one can prove that

$$P_m^{(k)} = \langle f_k|\hat{P}_m|f_k\rangle \tag{4-31}$$

where $|f_k\rangle$ is the kth two-exciton state wave function, i.e.,

$$|f_k\rangle = \sum_{m=1}^{N-1}\sum_{n=m+1}^{N} \upsilon_{mn}^{(k)}|m\rangle|n\rangle \tag{4-32}$$

Therefore, $P_m^{(k)}$ is the expectation value of $\hat{P}_m$ over the probability distribution of the kth two-exciton state and was considered to be the "amount" of the $|m\rangle$ wave function contribution to the kth two-exciton state. In other words, the $\vec{P}_k \equiv (P_1^{(k)},P_2^{(k)},...)$ vector is the *reduced (projected) probability density* of each site in the kth two-exciton state. Therefore, eq 4-30 can be rewritten as

$$\frac{\langle \delta\Omega_j \delta W_k\rangle}{C_0} = \vec{p}_j\cdot\vec{P}_k \tag{4-33}$$

which can be interpreted as the spatial overlap between the probability density of the jth one-exciton and the reduced probability density of the kth two-exciton state.

Finally, the mean square fluctuation amplitude of the kth two-exciton state was found to be

$$\frac{\langle \delta W_k^{\,2}\rangle}{C_0} = \sum_{m=1}^{N-1}\sum_{n=m+1}^{N} (\upsilon_{mn}^{(k)})^2\{P_m^{(k)} + P_n^{(k)}\} \tag{4-34}$$

This suggests that $\langle \delta W_k^2\rangle$ is determined by the overlap of the probability density of the kth two-exciton in the $|m,n\rangle$ basis and the projected (reduced) probability densities.

In the present subsection, the nature of one- and two-exciton states, $|e_j\rangle$ and $|f_k\rangle$, was discussed and also the expressions for transition dipole matrix elements were presented. Then, using the theory for 2D spectroscopic nonlinear response functions given in section 3 and carrying out Fourier transformation of the calculated nonlinear response function, one can obtain the 2D vibrational or electronic spectrum of any coupled multichromophore system, such as proteins and electronically coupled light-harvesting protein complexes.

4.4. Cumulant Expansion Expressions of Linear and Nonlinear Response Functions

Let us denote $|a\rangle$, $|b\rangle$, $|c\rangle$, and $|d\rangle$ to be the eigenstates of the material Hamiltonian. In the present subsection, we will only consider the cases when the field−matter interaction Hamiltonian contains electric dipole−electric field interactions only. If the transition frequency fluctuations of all quantum excited states involved in the nonlinear optical spectroscopy obey Gaussian statistics, one can use the cumulant expansion technique to obtain the linear and nonlinear response functions, which carry information on the time scale and amplitude of the molecular responses with respect to a given sequence of ultrafast external fields.[37] The corresponding expressions for the nth-order response functions,[28,34,37,72,74−78] denoted as $R^{(n)}$, were found to be

$$R^{(1)}(t_1) = \left(\frac{i}{\hbar}\right)\theta(t_1)\sum_{ab} P_a(t_0)\{\mu_{ab}\mu_{ba} \exp(-i\omega_{ba}t_1)F_{ba}(t_1) - c.c.\} \tag{4-35}$$

$$R^{(2)}(t_2,t_1) = \left(\frac{i}{\hbar}\right)^2\theta(t_2)\,\theta(t_1)\sum_{abc} P_a(t_0)[\mu_{ab}\mu_{bc}\mu_{ca} \exp(-i\omega_{ba}t_2 - i\omega_{ca}t_1)G_{bc}^{(1)}(t_2,t_1) - \mu_{ab}\mu_{bc}\mu_{ca} \exp(-i\omega_{cb}t_2 - i\omega_{ca}t_1)G_{bc}^{(2)}(t_2,t_1)] + c.c. \tag{4-36}$$

$$R^{(3)}(t_3,t_2,t_1) = \left(\frac{i}{\hbar}\right)^3\theta(t_1)\,\theta(t_2)\,\theta(t_3)\sum_{\alpha=1}^{4}[H_\alpha(t_3,t_2,t_1) - c.c.] \tag{4-37}$$

where the auxiliary functions are

$$F_{ba}(t_1) = \exp\{-\int_0^{t_1}\mathrm{d}\tau_2\int_0^{\tau_2}\mathrm{d}\tau_1\,\xi_{bb}(\tau_2-\tau_1)\} \tag{4-38}$$

$$G_{bc}^{(1)}(t_2,t_1) = \exp\{-[\int_0^{t_2}\mathrm{d}\tau_1\int_0^{\tau_1}\mathrm{d}\tau_2\,\xi_{bb}(\tau_1-\tau_2) + \int_0^{t_1}\mathrm{d}\tau_1\int_0^{\tau_1}\mathrm{d}\tau_2\,\xi_{cc}(\tau_1-\tau_2) + \int_0^{t_2}\mathrm{d}\tau_1\int_0^{t_1}\mathrm{d}\tau_2\,\xi_{bc}(\tau_1+\tau_2)]\} \tag{4-39}$$

$$G_{bc}^{(2)}(t_2,t_1) = \exp\{-[\int_0^{t_2}\mathrm{d}\tau_1\int_0^{\tau_1}\mathrm{d}\tau_2\,\xi_{bb}^*(\tau_1-\tau_2) + \int_0^{t_1+t_2}\mathrm{d}\tau_1\int_0^{\tau_1}\mathrm{d}\tau_2\,\xi_{cc}(\tau_1-\tau_2) - \int_0^{t_2}\mathrm{d}\tau_1\int_0^{t_1+t_2}\mathrm{d}\tau_2\,\xi_{bc}(\tau_2-\tau_1)]\} \tag{4-40}$$

$$H_1(t_3,t_2,t_1) = \sum_{abcd} P_a(t_0)\mu_{ad}\mu_{dc}\mu_{cb}\mu_{ba}\exp\{i\omega_{cb}t_3 + i\omega_{db}t_2 - i\omega_{ba}t_1\}\exp\{-\int_{t_1}^{t_1+t_2}\mathrm{d}\tau_1\int_{t_1}^{\tau_1}\mathrm{d}\tau_2\,\xi_{dd}^*(\tau_1,\tau_2) - \int_{t_1+t_2}^{t_1+t_2+t_3}\mathrm{d}\tau_1\int_{t_1+t_2}^{\tau_1}\mathrm{d}\tau_2\,\xi_{cc}^*(\tau_1,\tau_2) - \int_0^{t_1+t_2+t_3}\mathrm{d}\tau_1\int_0^{\tau_1}\mathrm{d}\tau_2\,\xi_{bb}(\tau_1,\tau_2) - \int_{t_1}^{t_1+t_2}\mathrm{d}\tau_1\int_{t_1+t_2}^{t_1+t_2+t_3}\mathrm{d}\tau_2\,\xi_{dc}(\tau_1,\tau_2) + \int_{t_1}^{t_1+t_2}\mathrm{d}\tau_1\int_0^{t_1+t_2+t_3}\mathrm{d}\tau_2\,\xi_{db}(\tau_1,\tau_2) + \int_{t_1+t_2}^{t_1+t_2+t_3}\mathrm{d}\tau_1\int_0^{t_1+t_2+t_3}\mathrm{d}\tau_2\,\xi_{cb}(\tau_1,\tau_2)\} \tag{4-41}$$

$$H_2(t_3,t_2,t_1) = \sum_{abcd} P_a(t_0)\mu_{ad}\mu_{dc}\mu_{cb}\mu_{ba} \exp\{i\omega_{cb}t_3 + i\omega_{db}t_2 + i\omega_{da}t_1\} \exp\{-\int_0^{t_1+t_2} d\tau_1 \int_0^{\tau_1} d\tau_2\, \xi^*_{dd}(\tau_1,\tau_2) - \int_{t_1+t_2}^{t_1+t_2+t_3} d\tau_1 \int_{t_1+t_2}^{\tau_2} d\tau_2\, \xi^*_{cc}(\tau_1,\tau_2) - \int_{t_1}^{t_1+t_2+t_3} d\tau_1 \int_{t_1}^{\tau_1} d\tau_2\, \xi_{bb}(\tau_1,\tau_2) - \int_0^{t_1+t_2} d\tau_1 \int_{t_1+t_2}^{t_1+t_2+t_3} d\tau_2\, \xi_{dc}(\tau_1,\tau_2) + \int_0^{t_1+t_2} d\tau_1 \int_{t_1}^{t_1+t_2+t_3} d\tau_2\, \xi_{db}(\tau_1,\tau_2) + \int_{t_1+t_2}^{t_1+t_2+t_3} d\tau_1 \int_{t_1}^{t_1+t_2+t_3} d\tau_2\, \xi_{cb}(\tau_1,\tau_2)\} \quad (4\text{-}42)$$

$$H_3(t_3,t_2,t_1) = \sum_{abcd} P_a(t_0)\mu_{ad}\mu_{dc}\mu_{cb}\mu_{ba} \exp\{i\omega_{cb}t_3 + i\omega_{ca}t_2 + i\omega_{da}t_1\} \exp\{-\int_0^{t_1} d\tau_1 \int_0^{\tau_1} d\tau_2\, \xi^*_{dd}(\tau_1,\tau_2) - \int_{t_1}^{t_1+t_2+t_3} d\tau_1 \int_{t_1}^{\tau_1} d\tau_2\, \xi^*_{cc}(\tau_1,\tau_2) - \int_{t_1+t_2}^{t_1+t_2+t_3} d\tau_1 \int_{t_1+t_2}^{\tau_1} d\tau_2\, \xi_{bb}(\tau_1,\tau_2) - \int_0^{t_1} d\tau_1 \int_{t_1}^{t_1+t_2+t_3} d\tau_2\, \xi_{dc}(\tau_1,\tau_2) + \int_0^{t_1} d\tau_1 \int_{t_1+t_2}^{t_1+t_2+t_3} d\tau_2\, \xi_{db}(\tau_1,\tau_2) + \int_{t_1}^{t_1+t_2+t_3} d\tau_1 \int_{t_1+t_2}^{t_1+t_2+t_3} d\tau_2\, \xi_{cb}(\tau_1,\tau_2)\} \quad (4\text{-}43)$$

$$H_4(t_3,t_2,t_1) = \sum_{abcd} P_a(t_0)\mu_{ad}\mu_{dc}\mu_{cb}\mu_{ba} \exp\{-i\omega_{da}t_3 - i\omega_{ca}t_2 - i\omega_{ba}t_1\} \exp\{-\int_{t_1+t_2}^{t_1+t_2+t_3} d\tau_1 \int_{t_1+t_2}^{\tau_1} d\tau_2\, \xi_{dd}(\tau_1,\tau_2) - \int_{t_1}^{t_1+t_2} d\tau_1 \int_{t_1}^{\tau_1} d\tau_2\, \xi_{cc}(\tau_1,\tau_2) - \int_0^{t_1} d\tau_1 \int_0^{\tau_1} d\tau_2\, \xi_{bb}(\tau_1,\tau_2) - \int_{t_1+t_2}^{t_1+t_2+t_3} d\tau_1 \int_{t_1}^{t_1+t_2} d\tau_2\, \xi_{dc}(\tau_1,\tau_2) - \int_{t_1+t_2}^{t_1+t_2+t_3} d\tau_1 \int_0^{t_1} d\tau_2\, \xi_{db}(\tau_1,\tau_2) - \int_{t_1}^{t_1+t_2} d\tau_1 \int_0^{t_1} d\tau_2\, \xi_{cb}(\tau_1,\tau_2)\} \quad (4\text{-}44)$$

Here, $P_a(t_0)$ is the Bolzmann probability of finding the quantum state $|a\rangle$ at time t_0 at temperature T. The complex conjugate was denoted as *c.c.* The transition electric dipole matrix element μ_{ba} is defined as $\mu_{ba} = \langle b|\mu|a\rangle$. When the statistics of the fluctuating bath degrees of freedom that are coupled to the electronic transitions obeys a Gaussian distribution function, the linear and nonlinear response functions in eqs 4-35−4-44 are determined by the *complex* autocorrelation and cross-correlation functions of the fluctuating transition frequencies, defined as

$$\xi_{xy}(\tau_1,\tau_2) \equiv \langle \delta\omega_{xa}(\tau_1)\, \delta\omega_{ya}(\tau_2)\rangle \quad (4\text{-}45)$$

Here, it was assumed that the transition frequency that fluctuates in time due to the coupled bath degrees of freedom can be written as a sum of ensemble averaged transition frequency $\bar{\omega}_{xa}$ and fluctuating part, i.e.,

$$\omega_{xa}(t) = \bar{\omega}_{xa} + \delta\omega_{xa}(t) \quad (4\text{-}46)$$

The linear and nonlinear response functions were thus expressed in terms of the correlation functions of the bath degrees freedom that are coupled to the molecular vibrational or electronic transition. If each individual molecule has a different local environment, one should further consider the static inhomogeneity and perform a separate averaging of the response function over the inhomogeneous distribution.

4.5. Inhomogeneous Line Broadening and Discrete Inhomogeneity

Although it was assumed that the transition frequency fluctuation obeys Gaussian statistics in the previous subsection, there are cases for which such an assumption is not valid. As an example, let us consider the amide I vibration of *N*-methylacetamide in methanol.[13,79] The amide I mode frequency in this case depends on the local solvation structure, and it was found that the carbonyl oxygen can form either one or two hydrogen-bonding interactions with surrounding methanol molecules. Then, the amide I frequency distribution obtained from the molecular dynamics trajectories was found to be non-Gaussian.[13] This specific case can be described as a two-species model. When there are discretely different ensembles like this, the transition frequency of the *j*th vibrational chromophore should be written as

$$\omega^j_{xa}(t) = \bar{\omega}_{xa} + \delta\omega_{xa}(t) + \epsilon^j_{xa} \quad (4\text{-}47)$$

where $\bar{\omega}_{xa}$ is the ensemble averaged transition frequency over the homogeneous and inhomogeneous (two-species) distributions and ϵ^j_{xa} represents the inhomogeneous factor. Note that the fluctuating part $\delta\omega_{xa}(t)$ still describes the homogeneous dephasing process of all chromophores. The average over the inhomogeneous distribution, i.e., integration over ϵ, should be performed at the last stage of the entire calculation. In the above case of the two-species system, the distribution of discrete inhomogeneous local environments can be modeled as

$$\Delta(\epsilon) = p_1\delta(\epsilon - \epsilon_1) + p_2\delta(\epsilon - \epsilon_2) \quad (4\text{-}48)$$

where ϵ_1 and ϵ_2 are the frequency deviations of the two species from the ensemble averaged value $\bar{\omega}_{xa}$ and p_j is the relative population of the *j*th species. If there are *N* discrete species and associated ensembles and if the interconversion time scale among these different species is *sufficiently slower* than the experimental time scale, such as interpulse delay times, the normalized inhomogneous distribution function can be generally written as

$$\Delta(\epsilon) = \sum_{j=1}^{N} p_j\delta(\epsilon - \epsilon_j) \quad (4\text{-}49)$$

In the case when the static inhomogeneity of the chromophore's transition frequency is virtually continuous, e.g., optical impurities in polymers or amorphous solids, *N* becomes very large and the discreteness of the distribution function disappears.

Once the inhomogeneous distribution function is determined, the experimentally measured *n*th-order polarization $\mathbf{P}^{(n)}_s(t)$, which is now a function of ϵ, should be averaged ove the distribution, i.e.,

$$\mathbf{P}^{(n)}_s(t) = \int d\epsilon\, \Delta(\epsilon)\mathbf{P}^{(n)}_s(t,\epsilon) \quad (4\text{-}50)$$

In the case of the two-species model mentioned above, we have

$$\mathbf{P}^{(n)}_s(t) = p_1\mathbf{P}^{(n)}_s(t,\epsilon_1) + p_2\mathbf{P}^{(n)}_s(t,\epsilon_2) \quad (4\text{-}51)$$

This result suggests that the experimentally measured signal,

$\mathbf{E}_s = (2\pi i\omega_s L\Phi/n(\omega_s)c)\mathbf{P}_s^{(n)}$, is a consequence of interference between two electric fields from the two different ensembles even at the classical level—note that the electric field has been treated classically throughout this paper.

The more interesting case is the chemical exchange, where each different species undergoes chemical or physical transitions.[12,13,15,16,35,80−82] Then, the relative populations p_j become time-dependent and often they obey a conventional kinetic equation, i.e.,

$$\Delta(\epsilon,T) = \sum_{j=1}^{N} p_j(T)\,\delta(\epsilon - \epsilon_j) \tag{4-52}$$

$$\frac{\mathrm{d}}{\mathrm{d}T}\mathbf{p}(T) = -\mathbf{K}\mathbf{p}(T) \tag{4-53}$$

where $\mathbf{p}$ is the population vector with N elements and $\mathbf{K}$ is the N by N rate constant matrix. The off-diagonal matrix element K_{kj} is the transition rate constant from the jth to kth species, and the diagonal element K_{jj} is given as $K_{jj} = \sum_{l\neq j} K_{lj}$. In this case, the conditional probability $G_{kj}(T)$ of finding the kth species at time T, given that at $T = 0$ the species is the jth, obeys the same master equation,[10]

$$\frac{\mathrm{d}}{\mathrm{d}T}G_{kj}(T) = \sum_{l\neq k} K_{kl}G_{lj}(T) - \Big(\sum_{l\neq k} K_{lk}\Big)G_{kj}(T) \tag{4-54}$$

By solving this equation with the initial condition $G_{kj}(T{=}0) = \delta_{kj}$ by using the Laplace transformation technique, one can obtain the conditional probability as

$$G_{kj}(T) = \sum_{l} Q_{kl}Q_{lj}^{-1}\exp(-\lambda_l T) \tag{4-55}$$

where the matrix $\mathbf{Q}$ diagonalizes $\mathbf{K}$ and λ_l is the lth eigenvalue of the $\mathbf{K}$ matrix. In this case of chemical exchange, the nth-order polarization $\mathbf{P}_s^{(n)}(t)$ should be generalized as

$$\mathbf{P}_s^{(n)}(t,T) = \sum_k\sum_j G_{kj}(T)\,\mathbf{P}_s^{(n)}(t,T,\epsilon_k;T{=}0,\epsilon_j) \tag{4-56}$$

where $\mathbf{P}_s^{(n)}(t,T,\epsilon_k;T{=}0,\epsilon_j)$ is the nth-order polarization component representing the nonlinear transition pathway involving a transition from the jth species to the kth species during T. Equation 4-56 is an important result that can be used to obtain time-dependent 2D optical spectra of molecular systems involving either chemical exchanges between different species or excitation transfer processes within the one-exciton state manifold of coupled multichromophore systems.

As will be discussed in detail in sections 5.9−5.11 and 6.2−6.3, the kinetic network of all species, when each species has a distinctively different transition frequency and when the spectral bandwidths of pulses are broad enough to cover the entire transitions of all involved species, can be studied by examining the time-dependent changes of cross peaks in the T-dependent 2D spectrum. This shows a clear advantage of the 2D optical spectroscopic technique over the 1D techniques that only measure the time-averaged signal.

4.6. Molecular Dynamics Simulation and Spectral Density

In the previous subsections, theoretical procedures of calculating nonlinear response functions associated with various coherent 2D optical spectroscopies were outlined. It was shown that how to calculate the transition frequencies of chromophores in time as well as coupling constants is critical for numerical simulations of the spectroscopic signals and 2D spectra. The former constitutes the diagonal matrix elements of the one- and two-exciton Hamiltonians, whereas the latter does the off-diagonal Hamiltonian matrix elements.

For a variety of solute molecules that are *electronic* chromophores, the transition frequency fluctuations and the time−correlation function could be calculated by performing molecular dynamics simulations, where the solvation dynamics was assumed to be the dominant contribution to the transition frequency fluctuation. This requires both electronic structure calculation to obtain electronic transition charges (or charge density) and classical molecular dynamics simulation trajectories of the composite system. The Coulomb solvation energy trajectory was obtained by calculating the electrostatic interaction energy between the chromophore's electronic transition charges and the partial charges of the solvent molecules at each time step during the MD simulation.[83−86] This approach has proven to be quite useful and informative for understanding solvation dynamics and its contribution to linear and nonlinear optical line broadening and spectral diffusion processes of dye molecules in solution. However, the more popular but semiempirical method is to use the experimentally measured spectral density, which can be obtained with a time-dependent fluorescence Stokes shift (FSS) or a three-pulse photon echo peak shift (3PEPS) measurement.[5,87,88] Once the spectral density is obtained, using eqs 4-18 and 4-19 and subsequent theoretical results, one can directly calculate the nonlinear response function (see Figure 9).

This method was chosen to numerically simulate 2D PE spectra of a photosynthetic light-harvesting complex recently.[10] An essential advantage of the method can be understood by noting the fact that the nonlinear optical properties of a multichromophore system can be theoretically predicted by using those of a monomer in the same condensed phase and that the interchromophore interactions inducing delocalization of excited-state and exciton formation are treated separately by electronic couplings between monomers.

In the case of protein 2D IR spectroscopy, one can use a variety of molecular dynamics simulation packages available to simulate structures, conformational fluctuations, solvation dynamics, hydrogen-bonding dynamics, solvatochromic vibrational frequency shifts, etc.

The classical MD simulation method has been extensively used to sample allowed protein conformations and to examine the dynamics of biomolecules in solutions, which are necessary ingredients for numerical simulations of their 2D IR spectra. However, it does not provide direct information on the vibrational or electronic properties of the solute, unless an independent theoretical method is used for calculating the transition frequency of the chromophore for a given instantaneous solute−solvent configuration sampled from the MD trajectories. That is to say, it was necessary to obtain the transition frequency trajectories from the coordinate files of the MD trajectories. A few notable efforts have been reported and will be discussed later in section 5. Nevertheless, the classical MD simulation method with a certain set of force fields cannot accurately describe the vibrational properties of a solute molecule yet. The intramolecular potential energy surface obtained from MD force fields, for example,

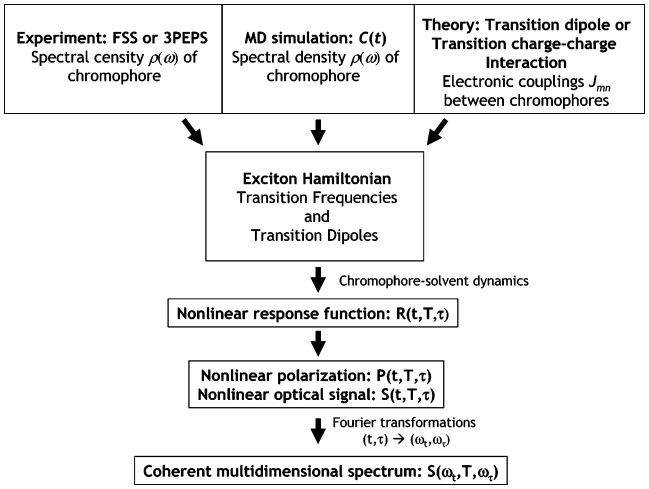

Figure 9. Flow chart describing how to numerically simulate the coherent 2D optical spectrum. Time-dependent fluorescence Stokes shift (FSS) or three-pulse photon echo peak shift (3PEPS) experimental results could be used to extract information on the spectral density reflecting the frequency distribution and coupling strength of bath modes. One can also use the molecular dynamics simulation method to directly obtain the spectral density by calculating the solvation correlation function, for example. Couplings between electronic or vibrational chromophores can be determined by using a simple transition dipole coupling theory, transition charge−charge interaction model, or *ab initio* calculation method. The Frenkel exciton Hamiltonian is then constructed, where the diagonal and off-diagonal Hamiltonian matrix elements are monomeric transition frequencies and coupling constants, respectively. Using the theoretical procedure outlined in the present section 4, the corresponding nonlinear response function can be calculated. Two-dimensional Fourier transformation of the nonlinear response function thus provides the 2D spectrum.

is not accurate enough to quantitatively reproduce the vibrational spectrum. Despite the fact that there exist a few interesting polarizable models, the solute−solvent interaction-induced fluctuations of atomic partial charges are still difficult to calculate unless one treats at least the solute molecule quantum mechanically.

To overcome these limitations of the purely classical MD simulation technique with fixed partial charges, it was shown that the quantum mechanical/molecular mechanical (QM/MM) MD simulation method can be a useful method for such purposes. In this case, a solute molecule was treated quantum mechanically by solving the associated Schrödinger equation, where the solute−solvent intermolecular interaction potential was incorporated in the quantum mechanical calculation. The solvent molecules were treated classically. As shown in ref 89, the atomic partial charges of a given solute, *N*-methylacetamide in that case, were calculated at each time step during the MD run. The partial charge trajectories $\{q_j(t)\}$ for all atoms were recorded. The time-dependent dipole moment trajectory $\mu(t)$ was directly obtained from the partial charge trajectories as

$$\mu(t) = \sum_{j=1}^{N} q_j(t)\, \mathbf{r}_j(t) \tag{4-57}$$

where $\mathbf{r}_j(t)$ is the position vector of the jth atom at time t. It should be emphasized that (1) the partial charge fluctuation, (2) the molecular structural fluctuation, and (3) the molecular rotation induced by the quantum solute−classical solvent interactions were properly taken into consideration here.

Then, the dipole−dipole time−correlation function $\langle \mu(t)\cdot\mu(0)\rangle$ was directly calculated—note that the dipole moment was considered as a classical quantity not a quantum mechanical operator, so that the ensemble averaging was performed with the semiclassical trajectory. The corresponding IR absorption spectrum can thus be calculated by directly carrying out Fourier transformation of $\langle \mu(t)\cdot\mu(0)\rangle$ and by multiplying an appropriate frequency-dependent semiclassical correction factor to the Fourier transformed spectrum. One of the most important advantages of the method is that in the QM/MM MD simulation the vibrational dynamics and its influences on the vibrational frequencies were treated quantum mechanically so that the potential energy surface determining the nuclear motions of all atoms is intrinsically anharmonic and can be realistic within the accuracy of the QM method and the solute−solvent interaction potential model chosen. Consequently, not only the fundamental transitions of normal modes but also other types of combination and overtone contributions to the IR spectrum can be correctly taken into account by the QM/MM MD method. Although up until now there are only a few works reporting the QM/MM MD approaches to the calculations of IR absorption spectra,[89−91] one can use the same idea of calculating the transition dipole trajectory for further simulating the high-order nonlinear vibrational spectroscopic response function in the future.

4.7. Quantum Chemistry Calculations of Protein Normal Modes and Vibrational Couplings

Over the past decade, a number of 2D IR spectroscopic investigations on amide I vibrations of peptides and proteins have been reported. The amide I vibration is mainly the C═O stretch of a given peptide bond. Since the line shape and frequency of the amide I IR band have been found to be highly sensitive to the polypeptide backbone structure, its vibrational properties have been paid quite a lot of attention. Although one can generalize the coupled oscillator model for other types of vibrational degrees of freedom of proteins, amide I vibrations will be mainly considered in this review.

To quantitatively simulate the linear and nonlinear vibrational spectra of amide I vibrations, it has been necessary to develop theoretical models and computational methods to predict the solvation-induced amide I frequency shifts and to estimate vibrational coupling between two different amide I local modes. Since the amide I mode was found to be fairly localized on a peptide bond, one can use the Frenkel exciton theory to describe the delocalized amide I vibrations that are critically dependent on the 3D backbone structure of a given polypeptide. In an aqueous solution, however, each amide I local mode frequency is shifted due to the solvatochromic effects induced by the intermolecular peptide−solvent and interpeptide interactions. The same interactions cause amide I local mode frequency fluctuations. In addition, due to structural fluctuations of polypeptide in solution, vibrational coupling constants between two different amide I local modes could also fluctuate in time. Therefore, numerical simulations of the 2D IR spectra of polypeptides have required extensive theoretical modeling and computation taking into account these effects.

One of the most powerful methods for obtaining normal mode frequencies and associated eigenvectors was to carry out quantum chemistry calculations directly for an isolated polypeptide. By choosing a high-level *ab initio* calculation method and a large basis set, normal mode frequencies and

associated transition dipoles of polypeptides could be accurately calculated. However, one cannot solely rely on *ab initio* calculations because for a realistic protein in solution it constantly interacts with solvent molecules and undergoes structural fluctuations even for those native structure proteins. In such a case, it is not possible to carry out full quantum chemistry calculations to obtain vibrational frequency and transition dipole trajectories. As an alternative approach, classical MD simulation methods have been widely used. However, due to the limited accuracy of currently available MD force fields for calculating intramolecular vibrational frequencies, it was necessary to combine both MD simulation and *ab initio* calculation methods to obtain a better result with chemical accuracy. One of the most popular ideas is to develop a theory that connects a vibrational frequency to a local solvation environment such as partial charge distributions of the solvent molecules at a time step in the MD simulation. A few different connection formulas were theoretically proposed and tested recently. Nevertheless, one still needs to know how frequencies of well-defined local modes and vibrational coupling constants depend on polypeptide structure. This goal was achieved by carrying out extensive *ab initio* calculations for small oligopeptides with varying secondary structures.

Ab initio geometry optimization and vibrational analysis of polypeptides provide information on eigenvectors, frequencies, and transition dipoles of normal modes. Using the so-called Hessian matrix reconstruction method developed recently, one can transform such information into the frequencies of well-defined local modes and intermode vibrational couplings to construct the corresponding Frenkel exciton Hamiltonian (see Figure 10). Then, by carrying out classical MD simulations and by using approximate theory to calculate local mode frequencies from the local solvation environment and the instantaneous peptide configuration, it is possible to obtain local mode frequency and vibrational coupling constant trajectories. Then, diagonalizing the instantaneous Hessian matrix results in normal mode frequencies and eigenvectors, which are used to calculate the 1D and 2D spectra of the polypeptide. In the case of the amide I vibration, a detailed analysis of vibrational couplings as a function of dihedral angles determining the peptide backbone structure was presented.

4.8. Coupling Constants between Optical Chromophores

The coherent 2D vibrational and electronic spectroscopies are known to be useful for determining vibrational and electronic coupling constants between nearby chromophores. In the case of vibrational excitation, even in the limiting case of weak anharmonic coupling, due to the electrostatic interaction between two vibrational chromophores, the coupling strength can be sizable enough to make the vibrationally excited-state delocalize over a number of coupled vibrational chromophores. Similarly, the excited states of a coupled two-level-chromophore system are delocalized over more than one chromophore due to nonzero electronic coupling.

The coupling strength is known to be sensitive to the distance and relative orientation of the two chromophores. One of the simple models for quantitatively predicting the coupling constant is the so-called transition dipole coupling theory. Let us consider two vibrational degrees of freedom,

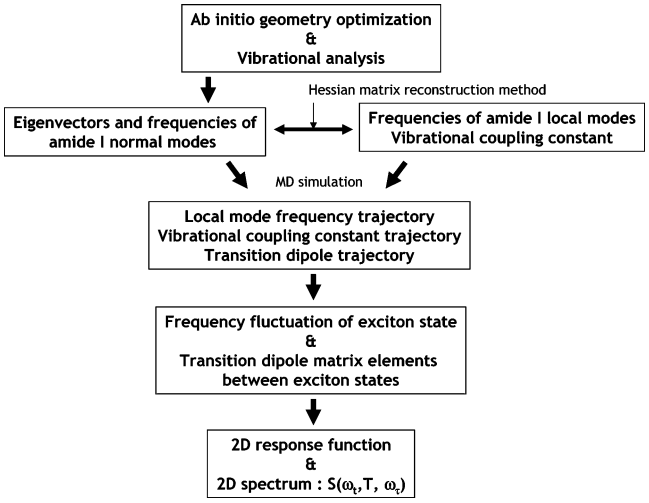

Figure 10. Flow chart describing how to calculate the amide I 2D vibrational spectrum of a polypeptide. *Ab initio* geometry optimization and vibrational analysis of a polypeptide provide information on eigenvectors and vibrational frequencies of the amide I normal modes. Using the Hessian matrix reconstruction method, one can obtain the amide I local mode frequencies and coupling constants. They constitute the diagonal and off-diagonal Hamiltonian matrix spanned in the amide I local mode space. Carrying out molecular dynamics simulation of the polypeptide in solution, it becomes possible to calculate the solvatochromic amide I mode frequency shifts and fluctuations. Then, in the delocalized exciton representation, the normal mode transition frequency fluctuations and transition dipole matrix elements are calculated by following the theoretical procedure discussed in this section. The final step is to calculate the 2D response function in the time domain and then to perform a 2D Fourier transformation of the 2D response function to get the corresponding 2D spectrum.

Q_1 and Q_2. Then, the vibrational coupling force constant between the two modes can be calculated as[67,92−94]

$$F_{12} = -\frac{1}{4\pi\epsilon_0}\left(\frac{\partial\mu_1}{\partial Q_1}\right)_0 \cdot T_{12} \cdot \left(\frac{\partial\mu_2}{\partial Q_2}\right)_0 \qquad (4\text{-}58)$$

where $(\partial\mu_j/\partial Q_j)_0$ is the transition dipole moment of the jth mode. T_{12} is the dipole−dipole interaction tensor, defined as

$$T_{12} = \frac{3\mathbf{r}_{12}\mathbf{r}_{12} - r_{12}{}^2 I}{r_{12}{}^5} \qquad (4\text{-}59)$$

where $\mathbf{r}_{12}$ is the vector pointing from chromophore 1 to 2, its magnitude is denoted as r_{12}, and I is the 3×3 indentity matrix. Although, in eq 4-58, the vibrational coupling force constants that constitute the off-diagonal Hessian matrix elements are given, one can easily transform them into the vibrational coupling constant in wavenumbers. Similarly, in the case of electronically coupled chromophore systems, the same transition dipole coupling model has been extensively used to quantitatively determine the extent of delocalization or the Förster energy transfer rate constant.

However, as the size of the unit vibrational or electronic chromophore increases, the point dipole approximation breaks down. In such cases, the Coulomb interaction between the two units can be computed by calculating the transition charge densities.[95−97] If the interaction between different chromophores is assumed to be electrostatic in nature, the

coupling constants constituting the off-diagonal Hamiltonian matrix elements are given by

$$J_{12} = \int_{\mathbf{r}_1}\int_{\mathbf{r}_2} d\mathbf{r}_1\, d\mathbf{r}_2\, \frac{\rho_1(\mathbf{r}_1)\,\rho_2(\mathbf{r}_2)}{4\pi\epsilon_0 r_{12}} \qquad (4\text{-}60)$$

where $\rho_j(\mathbf{r}_j)$ represents the transition electron density on the jth chromophore. One can further approximate the transition charge density by a distribution of partial (Mulliken) charges and charge fluxes.[98−102] In the case of two interacting *oscillators*, the site−site interaction potential can be approximated as

$$V_{12} = \frac{1}{2}Q_1Q_2\left[\frac{1}{4\pi\epsilon_0}\sum_{m,n}\frac{\partial^2}{\partial Q_1 \partial Q_2}\left(\frac{(q_{1m}^0 + \delta q_{1m}Q_1)(q_{2m}^0 + \delta q_{2m}Q_2)}{r_{1m,2n}}\right)_0\right] \qquad (4\text{-}61)$$

Here, q_{1m}^0 is the partial charge of the mth atom of chromophore 1 and δq_{1m} is the charge flux associated with the mth atom of chromophore 1 in the normal mode Q_1. The coupling force constant corresponds to the term in the square bracket in eq 4-61, and the charge fluxes associated with a given normal mode (or electronic transition) are readily calculable by using any *ab initio* calculation methods.

Although these approximate theories were found to be extremely useful and to some extent quantitatively reliable, such a simple Coulomb interaction model cannot fully take into account the effects from the electron correlation, anharmonic coupling, and polarizable nature when the two chromophores are strongly interacting with each other via covalent bonds, e.g., two neighboring peptides in a given polypeptide backbone. Therefore, one can use the vibrational coupling constant map obtained from the full *ab initio* calculations for a model coupled-dimer system, e.g., an alanine dipeptide analogue. In the following section, such theoretical attempts and a resultant coupling constant map for proteins will be provided and discussed.

5. Two-Dimensional Vibrational Spectroscopy

The 2D vibrational spectroscopic technique has certain advantages in comparison to conventional 1D vibrational spectroscopy such as IR absorption, Raman scattering, vibrational circular dichroism, etc. Due to a doubly vibrationally resonant condition, IR fields different in frequency can be simultaneously resonant with two different vibrational degrees of freedom and cross peaks in a two-dimensionally displayed spectrum arise from their couplings that are hard to be estimated from 1D spectra. Also, the two oscillators have to be anharmonic to avoid complete destructive interference among different nonlinear optical transition pathways—note that the nonlinear response function of completely harmonic oscillators vanishes due to perfect cancellation of signals originating from different transition pathways. This enables us to determine anharmonicities.

An early study of 2D vibrational spectroscopy focused on the fifth-order Raman spectroscopy that was theoretically suggested in 1993.[23] Initially, it was directed toward investigating the relative contributions of homogeneous and inhomogeneous line broadening in a vibrational spectrum. The majority of the experimental efforts have involved

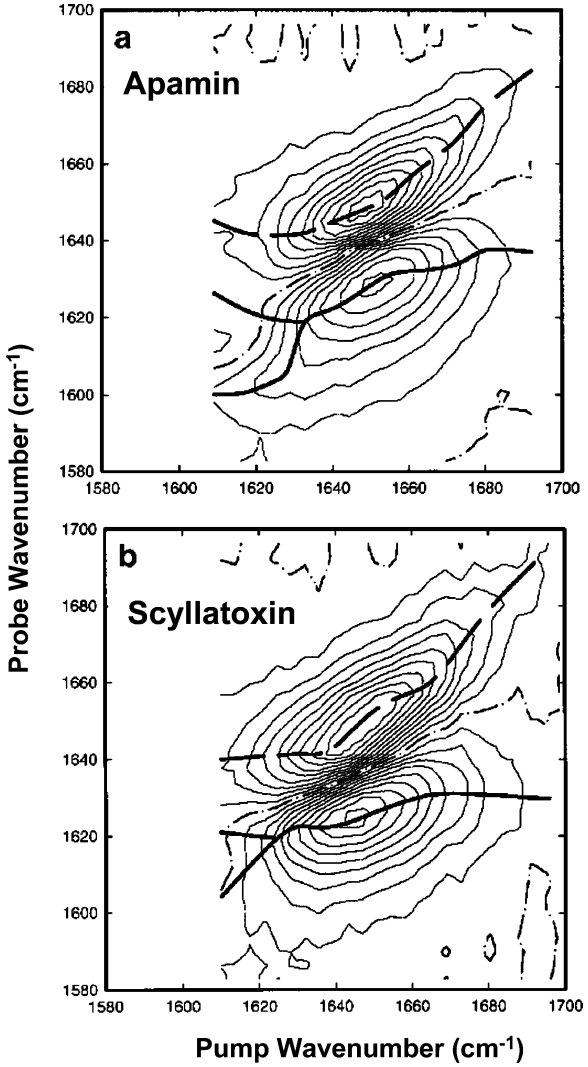

Figure 11. 2D-IR pump−probe spectra of apamin and scyllatoxin shown as contour plots.[8] The spectra were constructed by plotting the spectral response of the sample as a function of the peak position of the narrow band pump pulse. Note that the dynamic hole burning experiments were carried out. The spectral width of the pump pulses was 14 cm^{-1} in this experiment, and the delay time was set to zero. The isosbestic line is marked by a dashed-dotted line. The thick lines mark the position of the local maxima (thick solid lines) and minima (thick broken line) of the probe spectra as a function of the pump frequency.

probing the intermolecular modes of liquid CS_2,[103−115] which served as a standard system in nonresonant Raman spectroscopy due to its very large polarizability and the wealth of available experimental results. It was shown that the existence of coupling between Raman active modes is intrinsic to the generation of the fifth-order signal, which makes the experiment a highly sensitive probe of these microscopic interactions. Nevertheless, it turned out that cascading third-order processes, which are produced by two sequential or parallel third-order Raman scattering processes in the optical sample, were major unwanted signals and their amplitudes were found to be large and even dominant in some cases.[112−115] Later, two-dimensional IR spectroscopy based on 2D IR pump−probe and dynamic hole-burning techniques, as discussed in section 3−4, was applied to a few polypeptides, where the pump frequency scanning was required to fully construct the 2D spectrum with respect to the pump and probe frequencies. In Figure 11, the 2D IR pump−probe spectra of apamin and scyllatoxin are shown,[8]

where the *x*-and *y*-axes represent the pump and probe frequencies in wavenumbers.

Instead of the pump frequency scanning, one can scan the first delay time in an infrared photon echo experiment to obtain the 2D IR PE spectra of peptides. Over the past decade, a number of 2D IR experiments have been performed and most of them focused on the amide I vibrations of polypeptides, since the amide I band shape and center frequency have been known to be highly sensitive to protein secondary structures.[92,116] Now, a rapidly growing number of papers reporting novel applications of the 2D IR photon echo method to a variety of IR-active vibrational degrees of freedom including the amide I vibration have been published. In the present section, we will provide summaries on these experimental and theoretical works.

5.1. Fifth-Order Raman Scattering Spectroscopy

There has been significant interest in the extension of nonlinear optical spectroscopy to higher orders involving multiple time and/or frequency variables. For example, fifth-order Raman scattering spectroscopy was used to study low-frequency intermolecular vibrations in liquids.[23] Fifth-order, three-pulse electronic spectroscopy involving creations of two consecutive electronic coherences was theoretically proposed in 1994 to investigate the underlying dynamics and short-time inhomogeneity of a two-level chromophore in solution.[117] Recently, experimental attempts to carry out triply vibrationally enhanced IR[118−122] and fifth-order IR spectroscopy[123,124] were reported as potential candidates for even 3D vibrational spectroscopy. The two early developed multidimensional techniques, fifth-order Raman scattering[23] and fifth-order three-pulse scattering[117] spectroscopies, were initially motivated by the desire to probe microscopic details of a system that are often obscured by the ensemble averaging. A notable work of extending time domain coherent Raman scattering spectroscopy to higher dimensionality, which is the topic discussed in the present subsection, involved the use of multiple nonresonant Raman techniques.

In time domain nonresonant Raman spectroscopy of isotropic media, the lowest-order nonzero response is the third-order one, and it is governed by the third-order susceptibility, $\chi^{(3)}(\omega)$, or equivalently the third-order response function $R^{(3)}(t)$ in the time domain. Here, the effective field−matter interaction is given as $H_{\mathrm{int}} = -\alpha:\mathbf{E}^2(\mathbf{r},t)$. Experimental examples include impulsive stimulated scattering (ISS),[125−131] optical Kerr-effect spectroscopy (OKE), and optical heterodyne-detected Raman-induced Kerr-effect spectroscopy (OHD-RIKES).[132−159] Since two field−matter interactions initially overlapped in time drive a vibrational coherence by exerting a virtually impulsive force $(\partial\alpha/\partial Q_j)\delta(t)$ on the *j*th vibrational mode at time zero, its time evolution is probed by a final Raman interaction occurring at some adjustable time *t* later and the measured response carries the same information that is contained in an incoherent Raman scattering experiment in a frequency domain.[159] The fifth-order Raman experiment, however, involves two pairs of light pulses exerting time-separated forces $(\partial\alpha/\partial Q_j)\delta(t)$ and $(\partial\alpha/\partial Q_k)\delta(t - t_1)$, which produce two vibrational coherences. The fifth pulse at $t = t_1 + t_2$ arrives at the sample, it is Raman-scattered, and the scattered field intensity is measured. Consequently, the fifth-order Raman signal is a function of two delay times (i.e., it is a two-dimensional technique), and its signal is governed by the fifth-order Raman response function, $R^{(5)}(t_2,t_1)$.[23,25,160−167] Its 2D Fourier transform thus provides the 2D Raman spectrum, which was shown to be directly related to the extended Kramers−Heisenberg expression for the fifth-order Raman scattering cross section.[168] Here, brief outlines of the theory of the fifth-order Raman scattering process, cascading contributions to the fifth-order signal, and some experimental efforts detecting the pure fifth-order Raman signal will be provided.

The fifth-order Raman response function describing the system's response to two impulsive Raman stimulations was found to be[23,33]

$$R^{(5)}(t_2,t_1) = -\frac{1}{\hbar^2}\langle[[\alpha(t_2+t_1),\alpha(t_1)],\alpha(0)]\rho_{\mathrm{eq}}\rangle \qquad (5\text{-}1)$$

Due to the phase-matching condition, the wave vector of the fifth-order Raman scattering signal field is $\mathbf{k}_s = \mathbf{k}_1 - \mathbf{k}_2 - \mathbf{k}_3 + \mathbf{k}_4 + \mathbf{k}_5$ and its frequency is $\omega_s = \omega_1 - \omega_2 - \omega_3 + \omega_4 + \omega_5$. Then, within the impulsive limit, the amplitude of the direct fifth-order nonresonant scattering polarization can be written as

$$P^{(5)}_{\mathrm{dir}}(t) = NE^5R^{(5)}(t_2,t_1)\,\delta(t-t_2-t_1) \qquad (5\text{-}2)$$

and the electric field generated from the direct fifth-order polarization is expressed as

$$E^{(5)}_{\mathrm{dir}}(t) = iAF^{(5)}P^{(5)}_{\mathrm{dir}}(t) = iAF^{(5)}NE^5R^{(5)}(t_2,t_1)\delta(t-t_2-t_1) \qquad (5\text{-}3)$$

where $A = 2\pi\omega_sL/n_sc$ and $F^{(5)} = \{\sin[\Delta kL/2]/(\Delta kL/2)\}\exp(i\Delta kL/2)$. Here, *E* is the electric field amplitude of the incident pulse. For the sake of notational simplicity, we have dropped the tensor or vector indices in the nonlinear response function, nonlinear polarization, and emitted electric field.

The 2D Raman response can be expressed in terms of the vibrational coordinates by inserting a Taylor-expanded form of the polarizability operator:[23]

$$\alpha(t) = \alpha_0 + \sum_j \alpha^{(1)}_j Q_j(t) + \frac{1}{2}\sum_{j,k}\alpha^{(2)}_{j,k}Q_j(t)\,Q_k(t) + \ldots \qquad (5\text{-}4)$$

where $\alpha^{(n)}$ is the *n*th derivative of the polarizability with respect to the vibrational coordinates. It turned out that there are two types of couplings that can generate the fifth-order signal, i.e., anharmonicity in the vibrational potential energy surface, AN, and nonlinearity in the dependence of the polarizability operator on the vibrational coordinate, NP. The resulting response can be expressed as the sum of the two individual contributions[25,112,160,162−165,169]

$$R^{(5)}(t_2,t_1) = R^{(5)}_{\mathrm{AN}}(t_2,t_1) + R^{(5)}_{\mathrm{NP}}(t_2,t_1) \qquad (5\text{-}5)$$

The AN contribution was shown to be linearly proportional to the cubic anharmonicities in the multidimensional potential surfaces of polyatomic molecules or liquids, and the NP contribution is proportional to the second derivative of the polarizability with respect to the vibrational coordinates.

To numerically simulate the fifth-order Raman response functions of a few selected liquids, many different computational and theoretical investigations have been performed. For low-frequency intermolecular vibrations in liquids, they can be treated as classical degrees of freedom so that molecular dynamics simulations were carried out extensively. The first step was to rewrite the fifth-order Raman response

function, which involves two commutators and quantum mechanical polarizability operators, to the classical correlation function involving Poisson brackets.[170,171] For liquids CS_2 and water, extensive MD simulation results were reported in refs 170 and 172. Instead of carrying out a long equilibrium MD simulation, one can perform a number of independent nonequilibrium MD simulations by exerting impulsive forces onto the Raman-active modes in a given liquid.[173,174] Then, the fifth-order Raman response function calculated by averaging over a number of nonequilibrium MD trajectories was doubly Fourier-transformed to obtain the 2D Raman spectrum. Instead of molecular liquids, simple liquids were theoretically considered in detail and the fifth-order Raman response function was calculated by using a mode-coupling theory, and the results were directly compared with MD simulations.[175−178] Recently, a hybrid equilibrium/nonequilibrium MD simulation method for calculating the fifth-order Raman response function was theoretically proposed and used to calculate the 2D Raman spectra of liquid Xe, CS_2, and water for the sake of direct comparisons with previous theoretical and experimental results.[179] Despite the successes of these theoretical and computational efforts of simulating fifth-order Raman response functions of molecular and simple liquids, a complicating difficulty was rather found in experiments. The detected fifth-order Raman signals were found to be largely dictated by the cascading contributions, which are not sensitive to couplings between vibrational degrees of freedom.[113,180−182]

In the case of the direct fifth-order Raman response, the five field−matter interactions were strictly with the five external fields. However, the internal field created by the third-order Raman scattering processes can participate in the field−matter interaction to produce a high-order nonlinear optical signal. More specifically, the total electric field involved in the nonlinear optical transition processes should be written as $\mathbf{E}_{tot}(\mathbf{r},t) = \mathbf{E}(\mathbf{r},t) + \mathbf{E}^{(3)}(\mathbf{r},t) + ...$, where $\mathbf{E}(\mathbf{r},t)$ is the external Maxwell field and $\mathbf{E}^{(3)}(\mathbf{r},t)$ is the third-order electric field generated by the third-order polarizations of the optical sample itself. This has been known as the cascading contribution to the nonlinear optical signal in the literature. In the present case, there are two types of third-order cascading contributions leading to an overall fifth-order signal. Depending on the time-ordering of the two different third-order Raman scattering processes, they were called either sequential or parallel terms and they satisfy the same phase-matching condition with $\mathbf{k}_s = \mathbf{k}_1 - \mathbf{k}_2 - \mathbf{k}_3 + \mathbf{k}_4 + \mathbf{k}_5$. In total, there are four third-order intermediate polarizations, and two of them are sequential cascade intermediates with (i) $\mathbf{k}_{s1} = \mathbf{k}_1 - \mathbf{k}_2 - \mathbf{k}_3$, $\omega_{s1} = \omega_1 - \omega_2 - \omega_3$ and (ii) $\mathbf{k}_{s2} = \mathbf{k}_1 - \mathbf{k}_2 + \mathbf{k}_4$, $\omega_{s2} = \omega_1 - \omega_2 + \omega_4$, and the other two are parallel cascade intermediates with (i) $\mathbf{k}_{p1} = \mathbf{k}_1 - \mathbf{k}_2 + \mathbf{k}_5$, $\omega_{p1} = \omega_1 - \omega_2 + \omega_5$ and (ii) $\mathbf{k}_{p2} = -\mathbf{k}_3 + \mathbf{k}_4 + \mathbf{k}_5$, $\omega_{p2} = -\omega_3 + \omega_4 + \omega_5$. The corresponding third-order induced polarizations are expressed as, in the impulsive limit,

$$P^{(3)}_{s1}(t) = P^{(3)}_{s2}(t) = NE^3R^{(3)}(t)\,\delta(t-\tau_2)$$

$$P^{(3)}_{p1}(t) = NE^3R^{(3)}(t)\,\delta(t-\tau_2-\tau_4)$$

$$P^{(3)}_{p2}(t) = NE^3R^{(3)}(t-\tau_2)\,\delta(t-\tau_2-\tau_4) \qquad (5\text{-}6)$$

where the third-order Raman response function is

$$R^{(3)}(t) = \frac{i}{\hbar}\langle[\alpha(t),\alpha(0)]\rho_{eq}\rangle \qquad (5\text{-}7)$$

The spatial amplitude of the electric fields generated by these third-order induced polarizations can be obtained, and the four electric fields are then expressed as

$$E^{(3)}_{s1}(t) = iA_{s1}F^{(3)}_{s1}\,P^{(3)}_{s1}(t) = iA_{s1}F^{(3)}_{s1}NE^3R^{(3)}(t)\,\delta(t-\tau_2)$$

$$E^{(3)}_{s2}(t) = iA_{s2}F^{(3)}_{s2}\,P^{(3)}_{s2}(t) = iA_{s2}F^{(3)}_{s2}NE^3R^{(3)}(t)\,\delta(t-\tau_2)$$

$$E^{(3)}_{p1}(t) = iA_{p1}F^{(3)}_{p1}\,P^{(3)}_{p1}(t) = iA_{p1}F^{(3)}_{p1}NE^3R^{(3)}(t)\delta(t-\tau_2-\tau_4)$$

$$E^{(3)}_{p2}(t) = iA_{p2}F^{(3)}_{p2}\,P^{(3)}_{p2}(t) = iA_{p2}F^{(3)}_{p2}NE^3R^{(3)}(t-\tau_2)\delta(t-\tau_2-\tau_4) \qquad (5\text{-}8)$$

with $A_{sj} = 2\pi\omega_{sj}L/n_sc_j$ and $F^{(n)} = \{\sin[\Delta kL/2]/(\Delta kL/2)\}\exp(i\Delta kL/2)$. If one of the internal fields in eq 5-8 participates in yet another third-order Raman process, a cascading coherent field whose amplitude is proportional to the fifth power of the external Maxwell field amplitude will be generated. It was found that the cascading contribution to the total fifth-order polarization with the same phase-matching condition is

$$P^{(5)}_{cas}(t) = iAN^2E^5(F^{(3)}_{s1} + F^{(3)}_{s2})R^{(3)}(t-t_1)\,R^{(3)}(t_1)\,\delta(t-t_1-t_2) + iAN^2E^5(F^{(3)}_{p1} + F^{(3)}_{p2})\,R^{(3)}(t-t_1)\,R^{(3)}(t)\,\delta(t-t_1-t_2) \qquad (5\text{-}9)$$

where $A = A_{s1} = A_{s2} = A_{p1} = A_{p2}$. Therefore, the fifth-order signal with $\mathbf{k}_s = \mathbf{k}_1 - \mathbf{k}_2 - \mathbf{k}_3 + \mathbf{k}_4 + \mathbf{k}_5$ is given as the sum of direct and cascading terms, i.e.,[112]

$$\begin{aligned}E^{(5)}(t) &= E^{(5)}_{dir}(t) + E^{(5)}_{cas}(t)\\ &= iAF^{(5)}NE^5R^{(5)}(t_2,t_1)\,\delta(t-t_2-t_1) -\\ &A^2F^{(5)}N^2E^5(F^{(3)}_{s1} + F^{(3)}_{s2})\,R^{(3)}(t-t_1)\,R^{(3)}(t_1)\,\delta(t-t_1-t_2) -\\ &A^2F^{(5)}N^2E^5(F^{(3)}_{p1} + F^{(3)}_{p2})R^{(3)}(t-t_1)\,R^{(3)}(t)\,\delta(t-t_1-t_2)\end{aligned} \qquad (5\text{-}10)$$

Since the direct and cascading responses satisfy the same phase-matching condition, the total nonresonant fifth-order Raman signal must contain both contributions. The ratio between the absolute values of the direct and cascaded contributions is[112]

$$\frac{|P^{(5)}_{cas}(t)|}{|P^{(5)}_{dir}(t)|} = \left(\frac{2\pi\omega_0LN}{nc}\right)\frac{|\{(F^{(3)}_{s1} + F^{(3)}_{s2})R^{(3)}(t_1) + (F^{(3)}_{p1} + F^{(3)}_{p2})R^{(3)}(t_1+t_2)\}R^{(3)}(t_2)|}{|R^{(5)}(t_2,t_1)|} \qquad (5\text{-}11)$$

The ratio depends on (i) a few experimental parameters such as the effective path length determined by the beam crossing, number density, refractive index, and phase-matching factors and (ii) the intrinsic magnitudes of the third-order and fifth-order response functions that are critically dependent on the cubic anharmonicities and nonlinearity of the polarizability with respect to vibrational coordinates.

To selectively measure the direct fifth-order Raman signal, three different phase-matching geometries were experimentally examined because the phase-matching is not perfect

and the corresponding factors associated with the direct fifth-order and third-order Raman scattering processes are slightly different for those cases. It turned out that the fifth-order signal is quite strongly contaminated or in some cases dominated by the undesired cascading contributions to the homodyne-detected fifth-order Raman signal. As discussed in ref 112, heterodyne detection, in contrast to homodyne detection, is sensitive to the phase of the electric fields. If the phase-matching conditions for both the third- and fifth-order processes are assumed to be perfect, the cascading fifth-order scattering field, $E^{(5)}_{cas}$ (the sum of the second and third terms in eq 5-10), is $\pi/2$ out-of-phase in comparison to the direct fifth-order field, $E^{(5)}_{dir}$ (the first term in eq 5-10). Therefore, by using a phase-controlled local oscillator field employing a heterodyne-detection technique, the cascading and direct contributions could be separately measured. However, experimentally this was found to be extremely challenging. That is because (i) it is not possible to have perfect phase-matching in an experiment with finite laser pulse dimensions, (ii) the phase-matching factors become complex, not purely real, and (iii), therefore, one cannot separately measure the two contributions by simply controlling the phase of the local oscillator field only. Nevertheless, 2D Raman spectroscopy utilizing femtosecond visible pulses would be a useful technique for studying vibrational couplings between intramolecular Raman-active modes,[169] if the above experimental difficulty is resolved in the future.

5.2. 2D IR Pump–Probe and Photon Echo Spectroscopy

One of the early IR photon echo experiments was performed for $^{13}CH_3F$ and NH_2D by applying Stark pulses in 1971.[183] In 1993, a free electron laser for an IR pulse source was used to perform a picosecond IR photon echo experiment for a liquid and a glass for the first time.[6] However, as mentioned earlier in this review, a series of IR hole burning experiments were performed in 1998 and the measured spectra were reconstructed to obtain the first 2D IR pump probe spectra of polypeptides.[8] Later, the photon echo setup in combination with the spectral interferometric detection method became routinely used to record the 2D IR PE signal in the time domain. The signal was then Fourier-transformed with respect to τ (excitation time) and t (probing, emission, or detection time) to obtain the 2D IR spectrum. Detailed experimental setups and schemes were already discussed in section 3.

One of the interesting ideas was a polarization-control experiment.[184,185] In an early experiment, the polarization directions of the injected laser pulses and the detected signal field were controlled to be parallel to the z-axis in a space-fixed frame, when the propagation directions of the pulses are assumed to be along the x-axis. However, a proper choice of beam polarization directions enables us to selectively eliminate the diagonal peaks in a given 2D IR spectrum.[185] For example, the difference between the [$zzzz$]-signal and three times the [$yyzz$]-signal in a 2D pump−probe technique is mainly determined by the nonlinear optical transition pathways producing off-diagonal cross peaks. In the case of the 2D IR photon echo, the $S_{zzzz} - 3S_{zyyz}$ spectrum was recorded to measure the cross peaks.[185,186] Other interesting beam configurations for eliminating diagonal peaks are [0,π/3.- π/3,0] and [π/4.- π/4, π/2,0] schemes, where π/3, for example, is the angle of the second laser pulse polarization with respect to that of the first laser pulse.

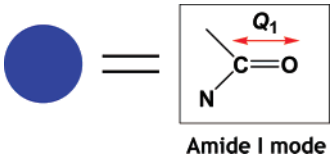

Figure 12. Amide I vibrational chromophore. A protein with N peptide bonds has N amide I local modes (vibrational chromophores). Due to the couplings among them, the amide I vibrational states are delocalized in nature.

In the following subsections, these 2D IR pump−probe and photon echo spectroscopic studies of single oscillator systems, coupled two-oscillator systems, coupled multioscillator systems, protein folding−unfolding dynamics, and chemical exchange dynamics will be discussed to show how useful the 2D vibrational spectroscopic technique indeed is in studying ultrafast solvent−solute dynamics, protein structure determination, structural changes of proteins, and hydrogen-bonding dynamics.

5.3. Single Oscillator Systems

Despite the fact that the 2D vibrational spectroscopic technique has been proven to be exceptionally useful in studying molecular complexes that can be modeled as coupled multichromophore systems, it was necessary to apply it to single oscillator systems to obtain vital information on the solvent−chromophore (oscillator) dynamics in condensed phases. In this subsection, two representative example, which are the amide I vibration of *N*-methylacetamide (NMA) and the O−D (or O−H) stretching mode of HOD in H_2O (HOD in D_2O), will be discussed. NMA has been considered to be an excellent model system for understanding the vibrational dynamics of peptides in solution. The HOD/D_2O and HOD/H_2O solutions were found to be quite important and useful for studying hydrogen-bonding dynamics in water in general. In these two cases, the vibrational chromophores are fairly uncoupled from other intramolecular vibrational degrees of freedom or from solvent modes.

5.3.1. N-Methylacetamide

NMA containing a single peptide bond is a prototype model for peptides. By treating it as a unit peptide, a polypeptide can be described as a collection of such unit peptides with certain configurations representing its backbone structure. For the NMA in solutions, 2D pump−probe and heterodyne-detected photon echo experiments were carried out to investigate the peptide−water interaction dynamics as well as to estimate the overtone anharmonicity of the amide I oscillator (Figure 12).

The hydrogen-bonding interactions between NMA and surrounding protic solvent molecules induce an amide I mode frequency red-shift. From the IR absorption spectra of a few different amide molecules in various polar and nonpolar solvents, the solvatochromic amide I frequency shift has been studied in detail. To quantitatively describe the hydrogen-bonding effect on the frequency of the amide I mode frequency, $\delta\tilde{\nu}_I$, it was suggested that $\delta\tilde{\nu}_I$ is linearly proportional to the hydrogen-bond distance r(O···H) in angstroms, i.e.,

$$\delta\tilde{\nu}_I = -\alpha_{Hyd}\{2.6 - r(O\cdots H)\} \qquad (5\text{-}12)$$

where the slope α_{Hyd} was typically assumed to be 30 $cm^{-1}/Å$.[8,187] Although this simple relationship between $\delta\tilde{\nu}_I$ and

r(O···H) was found to be of use,[188] its validity is guaranteed only for a short distance range around the optimum hydrogen-bond distance. This model therefore has limited validity because (i) the amide I mode frequency shift observed when the N−H group of a given peptide is hydrogen-bonded to a water molecule cannot be explained by the same empirical formula above, (ii) the fitting constant α_{Hyd} may depend on hydrogen-bond donor, and (iii) it does not properly take into account the dependency of $\delta\tilde{\nu}_I$ on the relative orientation of the hydrogen-bond partner molecule.

To elucidate the hydrogen-bonding effects on the amide I frequency, *ab initio* calculation studies on the amide I mode frequency shift ($\delta\tilde{\nu}_I$) for a number of NMA−$(D_2O)_n$ (n = 1−5) clusters were carried out to establish the relationship between $\delta\tilde{\nu}_I$ and electrostatic potentials at six different sites (O, C, N, H, CH_3(O), and CH_3(C)) of the NMA molecule, where the electrostatic potential is created by the distributed partial charges of the surrounding solvent water molecules, i.e.,[189−193]

$$\tilde{\nu}_I = \tilde{\nu}_I^{\,0} + \delta\tilde{\nu}_I = \tilde{\nu}_I^{\,0} + \sum_{a=1}^{6} l_a \phi_a \qquad (5\text{-}13)$$

where ϕ_a is the electrostatic potential at the ath site of the NMA. Expansion coefficients, l_a, were presented in refs 190. In ref 13, the same calculations were performed for various NMA−$(CH_3OD)_n$ clusters, and it was shown that the set of parameters obtained from the NMA−$(D_2O)_n$ clusters successfully reproduce the amide I mode frequency shift of the NMA−$(CH_3OD)_n$ cluster system too. The electrostatic potential, ϕ_a, in this case is

$$\phi_a = \frac{1}{4\pi\epsilon_0}\sum_m \sum_j \frac{C_{j(m)}^{\text{solvent}}}{r_{aj(m)}} \qquad (5\text{-}14)$$

where $C_{j(m)}^{\text{solvent}}$ denotes the partial charge of the jth site of the mth solvent molecule and $r_{aj(m)}$ is the distance between the NMA site a and the jth site of the mth solvent molecule.

In addition to the electrostatic potential model mentioned above, there exist other approaches to the amide I frequency calculations. For instance, instead of electrostatic potential calculations at each site, the vibrational Stark effect approach was used to simulate the amide I frequency shift and fluctuation of the same NMA−water solution.[194] The amide I frequency is in this case assumed to be linearly dependent on the electric field components as

$$\tilde{\nu}_I = \tilde{\nu}_I^{\,0} + \sum_{i\alpha} c_{i\alpha} E_{i\alpha} \qquad (5\text{-}15)$$

where $\alpha = \{x, y, z\}$, $E_{i\alpha}$ is the α-component of the electric field on atom i, i corresponds to either the C, O, N, or D atom on the deuterated NMA, and $c_{i\alpha}$ are the expansion coefficients. Here, the electric field vector at the ith solute atom could be calculated by

$$\mathbf{E}_i = \frac{1}{4\pi\epsilon_0}\sum_{j=1}^{3N} \frac{C_j}{r_{ij}^{\,2}}\hat{\mathbf{r}}_{ij} \qquad (5\text{-}16)$$

where j runs over the charged sites on the surrounding water molecules, $\hat{\mathbf{r}}_{ij}$ is a unit vector pointing from solvent atomic site j to solute atom i, N is the number of water molecules, and r_{ij} denotes the distance between the two sites. This method utilizing the electric field vector calculation was also found to be quantitatively acceptable in reproducing the amide I band of NMA and the OH stretch band of water.[194] Using the modified quantum mechanical/molecular mechanical method, the authors of ref 91 were able to successfully calculate the instantaneous vibrational frequency of azide ion in solution. In ref 195, a transferable electrostatic map for solvation effects on amide I frequency was provided. Also, an electrostatic map for the complete vibrational amide band of NMA, which was obtained by carrying out density functional theory calculations, was presented in ref 196.

For the NMA−water solution, by using the above relationship in eq 5-13 and by carrying out classical MD simulations of the NMA−water solution, it was possible to estimate the amide I mode frequency shift from that of an isolated NMA molecule. Note that the MD simulation trajectories were used to obtain the electrostatic potentials at each site as a function of time, which in turn were used to obtain the fluctuating amide I frequency trajectories $\tilde{\nu}_I(t)$. The theoretically predicted amide I mode frequency shift, defined as $\langle\delta\tilde{\nu}_I\rangle = \langle\tilde{\nu}_I(t)\rangle - \tilde{\nu}_I^{\,0}$, was found to be -78 cm^{-1},[191] which is in excellent agreement with the experimental value of -81 cm^{-1}. Amide I vibrational dephasing was investigated by calculating the frequency−frequency correlation function $\langle\delta\tilde{\nu}_I(t)\,\delta\tilde{\nu}_I(0)\rangle$. The spectral density $\rho(\omega)$ of the coupled bath modes was obtained by carrying out the cosine transformation, i.e.,

$$\rho(\omega) = 2\tanh(\hbar\omega/2k_BT)\int_0^\infty dt\,\cos(\omega t)\{\langle\delta\tilde{\nu}_I(t)\,\delta\tilde{\nu}_I(0)\rangle/\langle\delta\tilde{\nu}_I^{\,2}\rangle\} \qquad (5\text{-}17)$$

The resultant $\rho(\omega)$ showed that the librational motions of the water molecules directly hydrogen-bonded to the NMA play critical roles in modulating the amide I frequency in time. Once the amide I frequency−frequency correlation function is obtained, the corresponding I IR absorption spectrum can be calculated as[37]

$$I(\omega) \propto \int_{-\infty}^{\infty} dt\, e^{i\omega t}\exp(-i\bar{\omega}_{10}t - g(t)) \qquad (5\text{-}18)$$

where $\bar{\omega}_{10}$ is the average angular frequency of the NMA amide I mode and $g(t)$ is the line shape function defined as

$$g(t) = \int_0^t dt_1 \int_0^{t_1} dt_2\,\langle\delta\omega_{10}(t_2)\,\delta\omega_{10}(0)\rangle \qquad (5\text{-}19)$$

The simulated amide I IR spectrum was found to be in good agreement with the experimentally measured spectrum.[191]

The 2D IR experiment of the NMA−water (D_2O) solution was performed and reported in refs 197 and 198. The time-dependent 2D pump−probe spectra with respect to the waiting time T are shown in Figure 13 (see the upper-right panel in this figure).

The positive (blue) peak in the 2D IR pump−probe spectrum is produced by the ground-state bleaching and stimulated emission contributions, whereas the negative (red) peak is produced by the excited-state absorption. Due to the 16 cm^{-1} overtone anharmonicity, the two peaks do not cancel out completely. An interesting observation is that the 2D contour line is diagonally elongated at short time, but it rotates in time and becomes vertically aligned in about 4 ps. The short-time behavior of the nonlinear response function was theoretically examined, and it was shown that

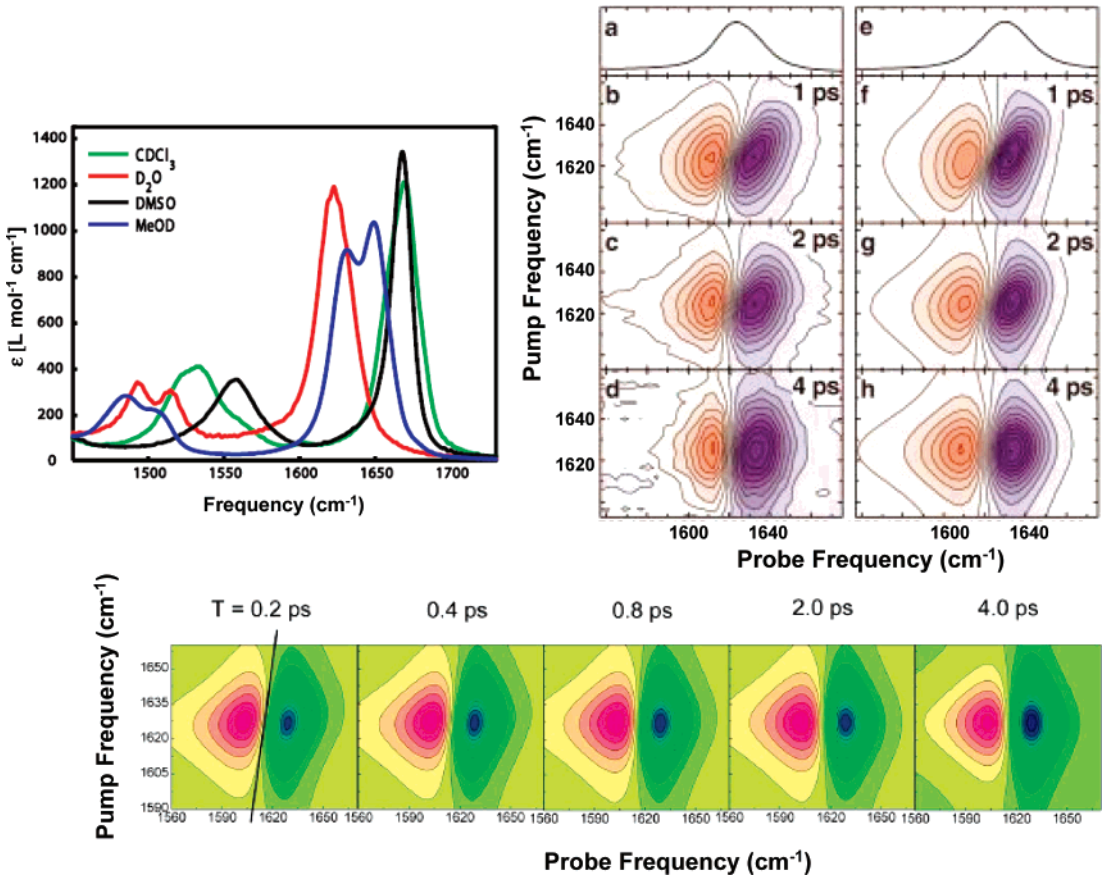

Figure 13. Amide I IR absorption spectra of NMA in $CDCl_3$ (green), D_2O (red), DMSO-d_6 (black), and MeOD (blue) are shown in the upper-left panel.[199] 2D IR pump−probe spectra[198] of NMA in D_2O at the waiting time $T = 1$, 2, and 4 ps are shown in the upper-right panel with their simulation results in the right column of this panel. The bottom figure depicts the numerically simulated 2D IR pump−probe spectra of NMA in D_2O, where the electrostatic potential model was used to calculate instantaneous amide I vibrational frequencies.

the slope of the nodal line, $\sigma_{PP}(T)$, is inversely proportional to the correlation function of the fluctuating amide I mode frequency, i.e., $1/\sigma_{PP}(T) = \langle \delta\omega(T)\ \delta\omega(0)\rangle/\langle \delta\omega^2\rangle$,[200] where $\sigma_{PP}(T)$ is the slope of the tangential line shown in the lower panel of Figure 13. The 2D IR PE spectrum of the NMA−water solution becomes horizontally aligned at long time—note that the x- and y-axis labels are ω_τ and ω_t in this case (see the top panel in Figure 14). The corresponding slope, $\sigma_{PE}(T)$, of the nodal line in the 2D IR PE spectrum is then directly and linearly related to the normalized frequency−frequency correlation function. In Figure 13 (lower panel), the simulated 2D IR pump−probe spectra at $T = 0.2$, 0.4, 0.8, 2, and 4 ps are shown for the sake of comparison with the experimental result, where the electrostatic potential method outlined above was used to obtain the amide I frequency trajectories and its correlation function. Overall, it is now clear that the 2D IR pump−probe (or photon echo) spectroscopy can provide direct information on the vibrational frequency fluctuation dynamics that reflects the peptide−water interaction as well as the dynamic inhomogeneity.

In addition, the 2D IR photon echo studies of NMA in $CDCl_3$ and DMSO-d_6 solvents were also performed and the time-dependent 2D spectra are shown in Figure 14. Although $\sigma_{PE}(T)$ of the NMA−water solution approaches zero in about 2 ps, that of NMA/DMSO-d_6 does so in about 6 ps. This reveals that the solvent response time scale is rather slower in DMSO than in water. When the NMA is dissolved in $CDCl_3$, the 2D IR PE spectrum at 6 ps still exhibits a certain degree of inhomogeneity—note that the slope of the nodal line is not zero yet. From the MD simulation study, this additional inhomogeneity was found to originate from the improper hydrogen-bonding interactions between NMA and D-atoms of $CDCl_3$ molecules. This is the first evidence showing the existence and time scale of the improper hydrogen-bonding interactions.

5.3.2. HOD/H_2O and HOD/D_2O

The dynamics of water is highly important, and it has crucial effects on diverse areas of science. It has been known that the water properties are largely dominated by the strong hydrogen bonds. Thus formed hydrogen bond networks are evolving in time, and its time and length scales are critically dependent on the hydrogen bond forming and breaking dynamics. Such hydrogen-bonding dynamics of liquids has been extensively studied by using femtosecond IR spectroscopic methods such as transient absorption experiments[201−210] and femtosecond IR photon echo studies.[6,211−213] Here, the recent 2D IR photon echo experimental and theoretical (MD simulation) works reported over the years are primarily discussed in this subsection. The vibrational chromophore is the O−D stretch for HOD in H_2O (Figure 15).

In Figure 16, the 2D IR correlation spectra of the OD stretch of HOD in H_2O as a function of waiting time T are shown. The upper positive peak originates from the contributions from the ground-state bleaching and stimulated emission processes, whereas the lower negative peak is associated with the vibrationally excited-state absorption. Initially, the 2D spectrum is diagonally elongated, indicating a presence of large inhomogeneity in such a short time scale. As the

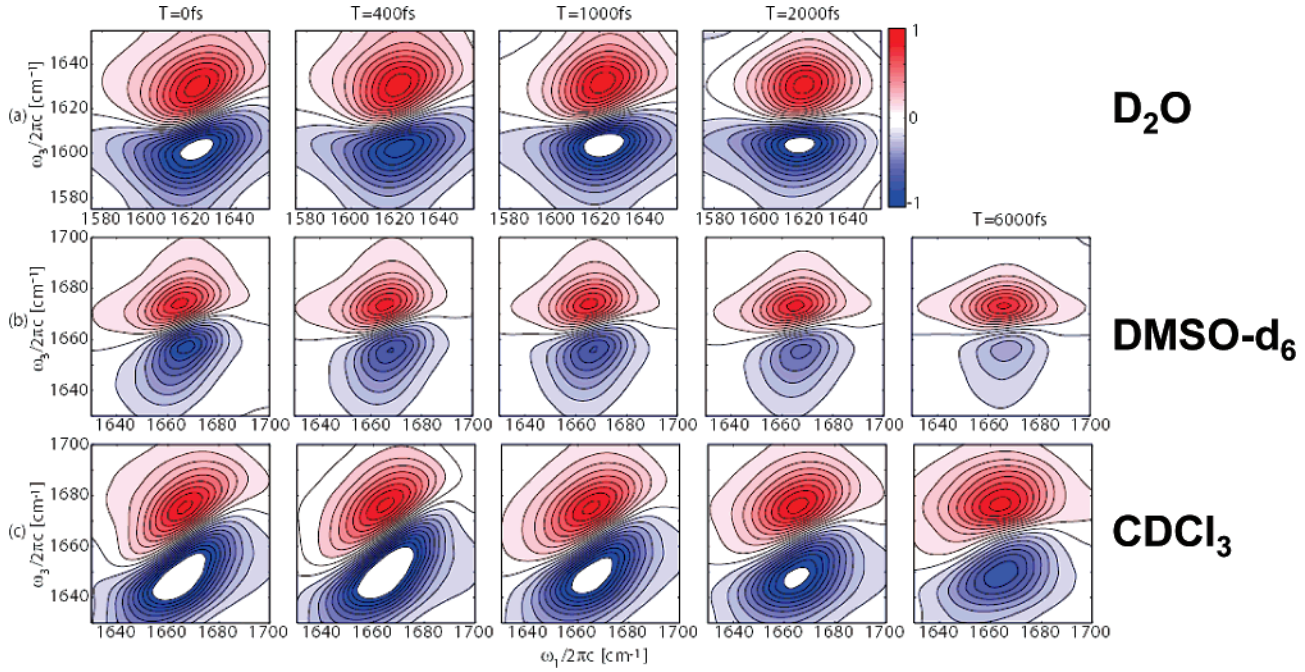

Figure 14. 2D IR line shapes of NMA in the three solvents (D_2O, DMSO-d_6, and $CDCl_3$) for varying waiting times.[199] Individual spectra were normalized to the peak of the fundamental transition and plotted in 10% contours.

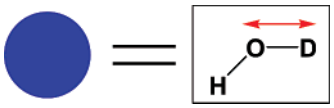

Figure 15. O−D stretching vibrational chromophore. The O−D stretch is a reporter mode for HOD in H_2O solution.

waiting time T increases from 0.1 to 1.6 ps, the widths of the peaks increase and the slope $\sigma_{PE}(T)$ decreases from about 1 to zero. Much like the case of NMA in water, inhomogeneity persists in the hydroxyl stretching frequency distribution for a couple of picoseconds, which evidently corresponds to the lifetime of the local hydrogen-bond network around the OD vibrational chromophore. In ref 18, the width of the upper peak along the x-axis (ω_τ-axis) was measured as a function of T and it was found that the width monotonically increases in time. This was attributed to the spectral diffusion of the hydroxyl stretching mode frequency that is induced by the hydrogen-bond forming and breaking processes.[18,214−219]

In order to quantitatively describe the time-dependent change of the 2D IR correlation spectrum, an extensive theoretical study with combining molecular dynamics simulations was presented and the resultant simulated spectra were directly compared with the experiment. The OD stretch frequency was assumed to be linearly proportional to the electric field component E, which is the projected electric field vector onto the OD bond,[215] as

$$\omega_{OD} = \omega_{OD}^0 + \alpha E \tag{5-20}$$

where ω_{OD}^0 is the OD frequency of an isolated HOD molecule and E is calculated as

$$E = \frac{1}{4\pi\epsilon_0}\bar{\mathbf{r}}_{OD}\cdot\sum_{j=1}^{3N}\frac{C_j}{r_{jD}^2}\bar{\mathbf{r}}_{jD} \tag{5-21}$$

Here, $\bar{\mathbf{r}}_{OD}$ is a unit vector pointing from O to D in the direction of the OD bond, the summation is over all charged sites of solvent water molecules, and $\bar{\mathbf{r}}_{jD}$ is the unit vector pointing from the solvent site j to the D atom of the HOD molecule. From the *ab initio* calculations of $HOD(H_2O)_n$ clusters sampled from the MD trajectories, the expansion coefficient α in eq 5-20 was estimated to be -10792 cm^{-1}/au with a correlation coefficient of 0.89.[194] Because surrounding solvent water molecules around the HOD solute continually change its relative distances and orientations, the site−site distances r_{jD} and the projection angles determining the factor of $\bar{\mathbf{r}}_{OD}\cdot\bar{\mathbf{r}}_{jD}$ are time-dependent. These modulate the electric field component E in eq 5-21, and consequently the OD stretch frequency fluctuates, which reflects intermolecular interaction dynamics. From the OD stretch frequency trajectory, the frequency−frequency correlation function could be directly calculated for the sake of comparisons with experiment and for the numerical simulations of linear and nonlinear vibrational spectra.

A critical observation was that the frequency−frequency correlation function obtained from the MD simulations by employing the above connection formula in eq 5-20 was found to be in excellent agreement with the experimentally retrieved time-correlation function whose decaying pattern is multimodal with a wide range of different time scales. Not only the 2D IR spectrum but also the linear absorption spectrum was quantitatively reproduced. However, the time-dependency of the width of the 2D peak was not successfully described by the simulation at that time. Although there exists a large-amplitude slow (∼400 fs) component in experimentally retrieved frequency−frequency correlation function, the time-correlation function predicted by using the SPC/E and TIP4P MD simulation trajectories was shown to decay too fast. Nevertheless, the fast component (∼32 fs) in the correlation function appears to be related to the fluctuations of the hydrogen-bond length coordinate. On the other hand, the slow (∼2 ps) component is likely due to hydrogen bond making and breaking dynamics, which is consistent with some MD simulations showing that the hydrogen bond lifetime is about 2 ps.

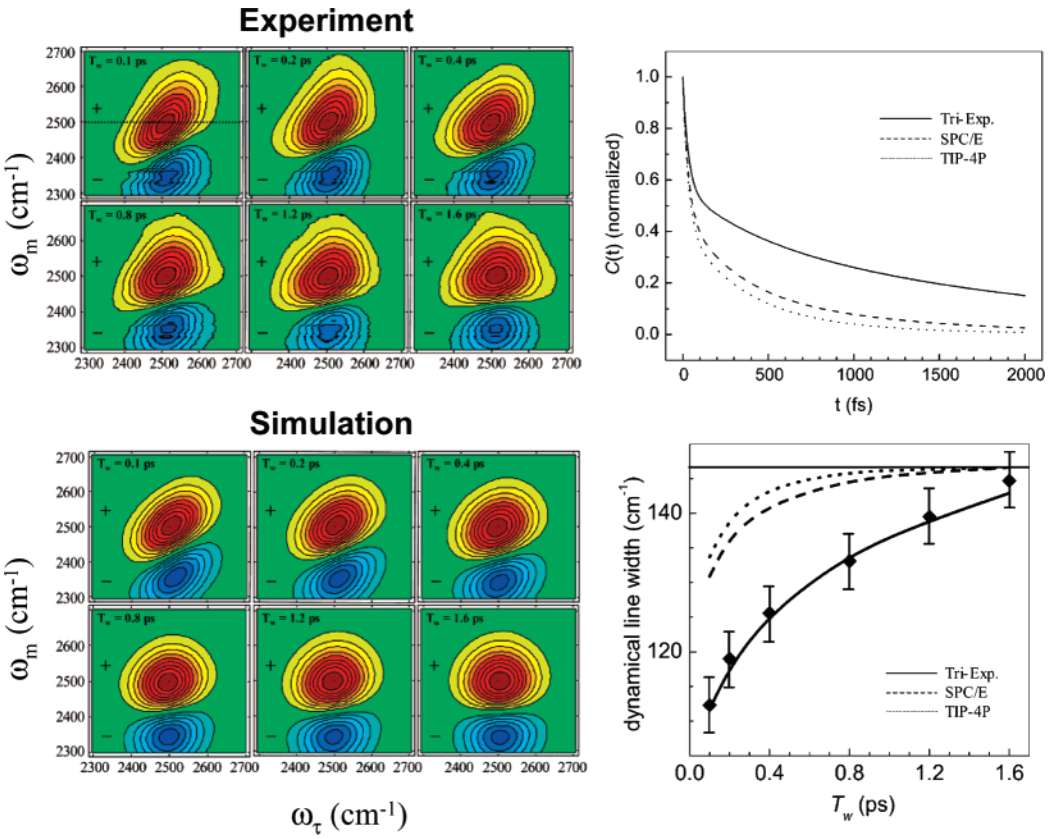

Figure 16. Experimental vibrational echo correlation spectra (upper-left) of the OD stretch of HOD in H_2O.[18] Each contour represents a 10% change. The positive-going peak arises from the 0 → 1 transition. The negative-going peak arises from the 1 → 2 transition. The 0 → 1 and 1 → 2 peaks are elongated along the diagonal, indicating that inhomogeneity persists in the hydroxyl stretching frequency distribution. Spectral diffusion broadens the widths of the peaks as the waiting time *T* increases from 0.1 to 1.6 ps. Simulated vibrational echo correlation spectra calculated from the time-correlation function that was derived from the SPC/E model of water are shown in the lower-left corner of this figure. Comparison of the phenomenological time-correlation function with the MD simulation-derived time-correlation functions is shown in the upper-right panel. They both share a fast component comprising about 50% of the amplitude, but the MD-derived time-correlation functions were found to be slightly different from the phenomenological time-correlation function in the amplitude and time scale of the slowest component. Comparison of the dynamical line widths of the phenomenological triexponential fit (solid line through the data) and experimental correlation spectra (diamonds with error bars) obtained from the 2D Gaussian fits is shown in the lower-right panel. In addition, the TIP4P (dots) and SPC/E (dashes) dynamical line widths are shown in this figure. The horizontal line at 147 cm^{-1} is the long-time asymptotic line width. It was found that the triexponential phenomenological TCF does a good job of reproducing the data.[18]

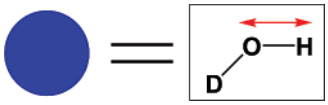

Figure 17. O−H stretching vibrational chromophore. The O−H stretch is a good reporter mode for HOD in D_2O solution.

In ref 220, a heterodyne-detected 2D IR photon echo experiment on HOD/D_2O solution was performed, where the OH stretch frequency fluctuation and ultrafast hydrogen-bond dynamics were investigated (Figure 17). One of the issues in understanding hydrogen bond networks in water was the roles of non-hydrogen-bonded configurations and dangling hydrogen bonds. The non-hydrogen-bonded configuration can be considered as a transition state in an event of thermally activated hydrogen bond breaking and subsequent new hydrogen bond forming with a different partner. From the ultrafast IR photon echo spectroscopic and MD simulation studies, it was shown that virtually all water molecules in the non-hydrogen-bonded configurations return to a hydrogen-bonding partner in 200 fs, strongly indicating that hydrogen bonds in water are broken only fleetingly.[220−222]

In Figure 18, the time-dependent snapshot 2D IR PE spectra of HOD in D_2O are shown in the upper panel, whereas their simulation results are shown in the lower panel. The slope of the nodal line calculated by fitting a straight line through the node of each surface decays in time, and its decaying pattern was found to be in agreement with the OH stretch mode frequency−frequency correlation function experimentally measured from the photon echo peak shift. The MD simulations suggested that the nonhydrogen-bonded configuration is nothing but a transitory state and that most likely librations on the 50 fs time scale are mainly responsible for making the non-hydrogen-bonded configurations proceed to a new hydrogen bond or return back to the original hydrogen bond. This picture is in contrast to that treating various hydrogen-bonded species such as non-hydrogen-bonded molecules, dangling waters, and hydrogen-bonded molecules with different coordination numbers as chemically distinct states. Later, in ref 223 they provided a new set of collective solvent coordinates for the same system, and the vibrational spectrum of HOD in D_2O was theoretically calculated by using an *ab initio* electrostatic map, which was shown to be quantitatively reliable in describing the OH frequency fluctuation and its statistical distribution.[224−226]

5.4. Coupled Two-Oscillator Systems

Although the NMA was shown to be an excellent model system for understanding peptide−solvent intermolecular

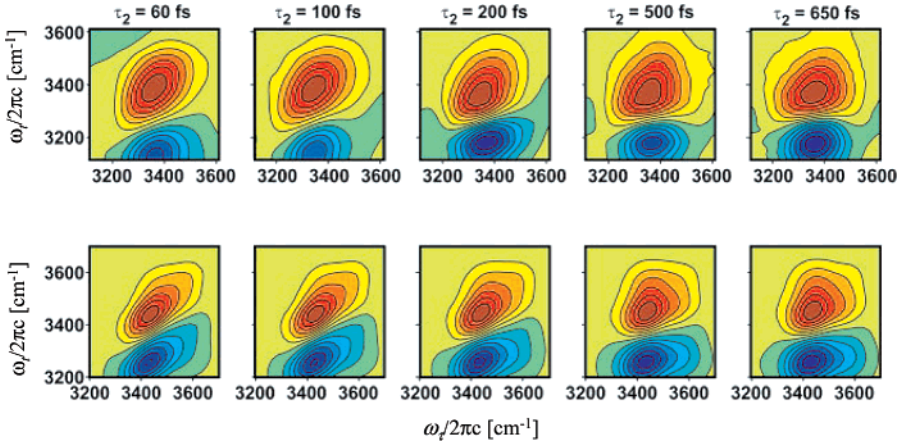

Figure 18. Experimental (upper) and simulated (lower) 2D IR spectra of HOD in D_2O.[220] 2D IR correlation spectra from experiments (upper) are compared with the 2D line shape calculated from MD simulation (lower) for a variety of waiting times *T*. Reprinted with permission from Eaves, J. D.; Loparo, J. J.; Fecko, C. J.; Roberts, S. T.; Tokmakoff, A.; Geissler, P. L. *Proc. Natl. Acad. Sci. U.S.A.* **2005**, *102*, 13019. Copyright 2005 National Academy of Sciences, U.S.A.

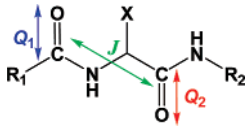

Figure 19. Molecular structure of a dipeptidyl compound. Amino acids are different from one another by the side group X. Two amide I local oscillators Q_1 and Q_2 are coupled to each other via *J*, which is a function of dihedral angles ϕ and ψ. The coupling constant map $J(\phi,\psi)$ for a model dipeptide was reported in refs 227−229. Amide I local mode frequencies were also found to be dependent on ϕ and ψ angles.[227,230,231]

interaction and hydrogen-bonding dynamics, it is not a suitable model for polypeptides because it contains only one amide I oscillator. In this regard, a few different peptides containing two peptide bonds have been extensively studied with the 2D IR spectroscopic methods. As shown in ref 67, the amide I band of a dipeptide can be described as an excitonic band where each individual amide I local mode is coupled to the other amide I local mode by electrostatic and mechanical interactions. The coupling strength *J* in Figure 19 is then dependent on the relative distance and angle between the two transition dipoles associated with the Q_1 and Q_2 oscillators.

To determine the amide I vibrational states, a coupled anharmonic oscillator model was used, where the system Hamiltonian is written as, with the local mode basis set of $\{|0,0\rangle, |1,0\rangle, |0,1\rangle, |2,0\rangle, |0,2\rangle, |1,1\rangle\}$,[232,233]

$$H_S = \begin{bmatrix} 0 & 0 & 0 & 0 & 0 & 0 \\ 0 & \omega_1 & J & 0 & 0 & 0 \\ 0 & J & \omega_2 & 0 & 0 & 0 \\ 0 & 0 & 0 & 2\omega_1 - \Delta & 0 & \sqrt{2}\,J \\ 0 & 0 & 0 & 0 & 2\omega_2 - \Delta & \sqrt{2}\,J \\ 0 & 0 & 0 & \sqrt{2}\,J & \sqrt{2}\,J & \omega_1 + \omega_2 + \Delta' \end{bmatrix} \quad (5\text{-}22)$$

Here, Δ and Δ' are the potential anharmonic frequency shifts of the overtone and combination states, and *J* is the vibrational coupling constant. The Hamiltonian matrix consists of three blocks with 1, 2, and 3 diagonal elements. The second 2 × 2 block matrix corresponds to the first excited state Hamiltonian. The third 3 × 3 block matrix describes the overtone and combination states. Carrying out DFT calculations, one can obtain the eigenvectors and frequencies of the two amide I *normal* modes of the dipeptide.[229,234−236] Then, by using the Hessian matrix reconstruction method, both the amide I local mode frequencies and the coupling constant were obtained. In eq 5-22, ω_j is the *j*th amide I *local* mode frequency. The symmetric and asymmetric amide I normal mode frequencies are denoted as ω_+ and ω_-, respectively. The overtone anharmonicity of the amide I local mode has been experimentally determined to be 16 cm^{-1}. The vibrational coupling constant *J* is critically dependent on the dipeptide conformation. In order to get the eigenvalues and eigenvectors of the one-quantum and two-quantum excited states, it is necessary to find the orthogonal transformation matrix *U*, defined as

$$U^{-1}H_S U = \Omega \quad (5\text{-}23)$$

where Ω_{22} and Ω_{33} are the energies of the two one-quantum excited states, $|+\rangle$ and $|-\rangle$, and Ω_{44}, Ω_{55}, and Ω_{66} are the three doubly (two-quantum) excited-state energies. The latter states will be denoted as $|2+\rangle$, $|2-\rangle$, and $|a\rangle$, respectively, where the $|2+\rangle$ ($|2-\rangle$) state is close to the overtone state of the $|+\rangle$ ($|-\rangle$) mode and $|a\rangle$ is approximately the combination state of the $|+\rangle$ and $|-\rangle$ modes in nature.

From the amide I local mode frequencies and coupling constant, one can obtain the excited states expressed as linear combinations of the local mode states,[237]

$$\begin{pmatrix} |+\rangle \\ |-\rangle \end{pmatrix} = \begin{pmatrix} c_1^+ & c_2^+ \\ c_1^- & c_2^- \end{pmatrix} \begin{pmatrix} a_1^+|0,0\rangle \\ a_2^+|0,0\rangle \end{pmatrix} \quad (5\text{-}24)$$

where a_j^+ (a_j) is the creation (annihilation) operator of the *j*th local mode excited state. The eigenvector elements are $c_1^+ = c_2^- = \cos\theta$ and $c_2^+ = -c_1^- = \sin\theta$ with $\theta = 0.5 \arctan\{2J/(\omega_1 - \omega_2)\}$. The transition dipole vectors are

$$\begin{pmatrix} \mu_{+,0} \\ \mu_{-,0} \end{pmatrix} = \begin{pmatrix} (\partial\mu/\partial Q_+) \\ (\partial\mu/\partial Q_-) \end{pmatrix} = \begin{pmatrix} c_1^+ & c_2^+ \\ c_1^- & c_2^- \end{pmatrix} \begin{pmatrix} \mu_1^{(1)} \\ \mu_2^{(1)} \end{pmatrix} \quad (5\text{-}25)$$

where $\mu_1^{(1)} \equiv (\partial\mu/\partial q_1)$ and $\mu_2^{(1)} \equiv (\partial\mu/\partial q_2)$ are the transition dipole vectors of the two amide I local modes. Q_+ and Q_- are the symmetric and asymmetric amide I normal coordinates, respectively, and q_j is the *j*th amide I local coordinate.

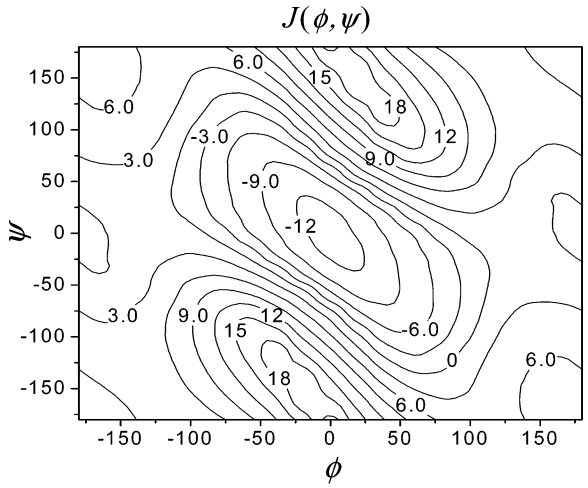

Figure 20. Coupling constant J between two amide I local modes of a glycine dipeptide analogue (Ac-Gly-NHMe) with respect to ϕ and ψ angles.[227] To obtain the map, the HF/6-311++G** method was used. Later, the B3LYP/6-31G(d) method was used to obtain the $J(\phi,\psi)$ map for an alanine dipeptide analogue (Ac-Ala-NHMe).[229] It was found that the maps thus obtained are quantitatively similar to each other.

The factor determining the mode-mixing, transition dipoles and frequencies of the two amide I normal modes, and vibrational spectra is the coupling constant J between the two amide I local modes. By using the isotope-labeling-induced-decoupling method,[228] the coupling constant between the two peptide amide I local modes in a model dipeptide was calculated with respect to the two dihedral angles ϕ and ψ, which determine the backbone conformation of a given dipeptide. Later, the so-called Hessian matrix reconstruction method was developed to extract both the coupling constant J (off-diagonal Hamiltonian matrix element) and the amide I local mode frequencies (diagonal Hamiltonian matrix elements in the amide I vibrational subspace).[230,231,238,239] In Figure 20, the thus determined coupling constant map, $J(\phi,\psi)$, obtained from Hartree−Fock calculations (with the 6-311++G** basis set) of the glycine dipeptide analogue (Ac-Gly-NHMe) is shown.[227]

In addition, it was found that the amide I local mode frequencies, i.e., site energies, also strongly depend on the peptide backbone conformation because the electrostatic and other types of interactions between peptide groups can induce frequency shifts.

5.4.1. Acetylproline

As a simple model dipeptide system, acetylated proline amide has been studied by using the 2D IR photon echo method.[186,240,241] Due to the five-membered pyrrolidine ring strain, the amide I local mode frequency of the acetyl-end peptide is about 30 cm^{-1} red-shifted from that of the amide-end peptide.[240] Therefore, the amide I IR band appears as a doublet. Nevertheless, depending on the peptide backbone conformation, the vibrational coupling strength can be sizable enough to make the two amide I normal modes delocalized over the two peptide groups. One of the issues extensively investigated over the years is the solvation effect on the peptide conformation. It has been known that the acetylproline-NH_2 in nonpolar aprotic solvent adopts a C_{7eq} conformation because the intramolecular hydrogen bonding interaction is a critical factor stabilizing the structure. This was found to be consistent with the quantum chemistry calculation result

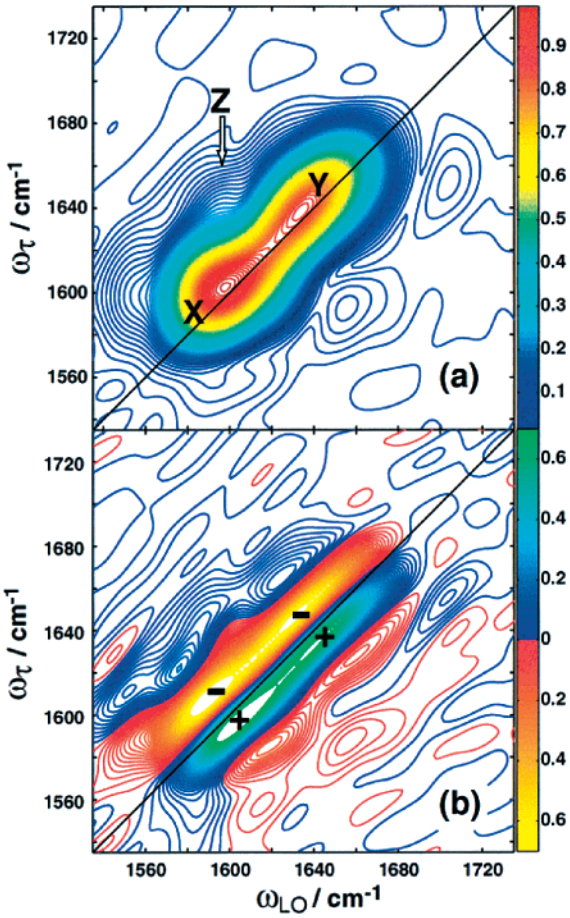

Figure 21. 2D IR spectrum for acetylproline-ND_2 in D_2O.[186] The magnitude and real parts of the S_{zzzz} spectrum are plotted in parts a and b, respectively. Diagonal peaks X and Y correspond to the two peaks in the amide I IR absorption spectrum. The cross peak Z reveals coupling. In the real spectrum, the signs of the diagonal peaks X and Y are labeled with "+" and "−" for clarification.

for an isolated acetylproline molecule.[242] On the other hand, when it is dissolved in water, the two peptide groups can form strong hydrogen bonds with surrounding water molecules so that its structure is different from that in a nonpolar solvent. As can be seen in Figure 20, depicting the vibrational coupling constant with respect to ϕ and ψ angles, the extent of mode mixing depends on the peptide conformation. Therefore, examination of cross peaks in the 2D IR spectrum of such a coupled oscillator system could provide information on the magnitude of the coupling constant and thus on the peptide conformation.

The 2D spectra shown in Figure 21 are the magnitude and real parts of the 2D IR PE spectrum, $S_{zzzz}(\omega_\tau,\omega_t,T)$, of the acetylproline-$ND_2$ in D_2O. The two diagonal peaks labeled as X and Y correspond to the two amide I modes relatively localized on the acetyl- and amide-end peptides, respectively. A cross peak labeled as Z in Figure 21 was observed even though its magnitude is relatively small. However, the [$zzzz$] component of the 2D spectrum itself is not enough to uniquely determine the peptide conformation, so that the cross polarization ([$zxxz$] tensor component) spectrum was also independently measured. The difference spectrum defined as $S_{zzzz}(\omega_\tau,\omega_t,T) - 3S_{zxxz}(\omega_\tau,\omega_t,T)$ is solely determined by the cross peaks, and its amplitude analysis was found to be of use in determining the angle β_{12} between the transition dipoles of the two amide I *normal* (not local) modes. It was shown that the ratio $|S_{zzzz}(\omega_\tau,\omega_t,T)|/3|S_{zxxz}(\omega_\tau,\omega_t,T)|$ of the

cross peak is a function of β_{12} as

$$\frac{|S_{zzzz}(\omega_\tau,\omega_t)|}{3|S_{zxxz}(\omega_\tau,\omega_t)|} = \left|\frac{4\cos^2\beta_{12}+2}{9\cos^2\beta_{12}-3}\right| \quad (5\text{-}26)$$

If the 2D IR pump−probe measurement was performed, the cross peak anisotropy could be used to estimate the angle β_{12}, where the cross peak anisotropy is defined as

$$\frac{S_{zzzz}^{\text{pump-probe}}(\omega_\tau,\omega_t) - S_{zzxx}^{\text{pump-probe}}(\omega_\tau,\omega_t)}{S_{zzzz}^{\text{pump-probe}}(\omega_\tau,\omega_t) + 2S_{zzxx}^{\text{pump-probe}}(\omega_\tau,\omega_t)} = \frac{1}{5}(3\cos^2\beta_{12}-1) \quad (5\text{-}27)$$

In addition, two more relationships between experimentally measured cross peak amplitudes and β_{12} were proposed in ref 242 and examined in detail for this molecular system. Although these four different relationships are interesting and simple, it was found that they are not quantitatively reliable in the cases when the cross peaks are not well-resolved in frequency and when the excited-state absorption contribution to the signal strongly interferes with the ground-state bleaching and stimulated emission contributions. Therefore, as discussed in refs 243 and 244, an independent spectroscopic or molecular dynamics simulation study would be of help to extract an additional piece of information on the peptide conformation. In relation to these 2D IR studies, vibrational circular dichroism spectroscopy with a constrained molecular dynamics simulation method was used to determine the solution structure of the acetylproline-ND_2 in D_2O.[243] It was concluded that its solution structure is close to the polyproline II (P_{II}) conformation, which is a 3-fold left-handed helical structure.

5.4.2. Alanine Dipeptide

There are two different alanine dipeptide systems that both contain two peptide bonds. The first is the trialanine (Ala-Ala-Ala) with free amine and carboxyl groups, and the second is Ac-Ala-NHMe, which is alanine capped by an acetyl group at the amino terminal and by an *N*-methyl amino group at the carboxyl terminal. Due to the two ionizable groups in the trialanine, the aqueous solution structure could be sensitive to pH, whereas the latter is not.

In order to determine the solution structure of trialanine, the 2D IR pump−probe experiments on the trialanine and its two isotopomers (Ala*-Ala-Ala and Ala-Ala*-Ala) in combination with classical MD simulation studies were carried out and reported in refs 198, 245, and 246. Here, the asterisk represents that the amino acid has a ^{13}C-isotope-labeled carbonyl group. From the measured anisotropy values of these three trialanines, they were able to estimate the angle β_{12} between the two amide I transition dipoles, which is about 106°. Also, from the least-squares fit, the coupling constant J between the two amide I local modes was obtained to be 6 cm^{-1}. Then, using the maps of the coupling constant as well as of the angle between the two transition dipoles with respect to the ϕ and ψ angles, they concluded that the secondary structure of trialanine does not change upon isotope substitution and that the average ϕ and ψ angles are about −60° and 140°. Later, carrying out molecular dynamics simulation studies with the GROMOS96 force field and SPC water, the relative populations of P_{II} and right-handed α-helical (α_R) conformations are about 80 and 20%, respectively.[198] Some related molecular dynamics simulation studies were also reported, and they suggested that the trialanine conformation distribution is relatively little dependent on force fields such as AMBER, CHARMM, GROMOS, and OPLS.[247,248] In ref 198, they found that the conformational dynamics (conformational fluctuations as well as transitions between two different conformers) can cause an additional spectral broadening and that the spectral inhomogeneity is critical in understanding the 2D vibrational spectrum and its time evolution. Recently, a few different theoretical models for quantitatively predicting the amide I IR absorption spectrum of trialanine were critically compared in detail in ref 249.

The alanine dipeptide analogue (Ac-Ala-NHMe) and its isotopomers were also investigated in detail by using the 2D IR photon echo method.[250,251] They found that the two amide I modes are highly localized due to weak coupling, which was estimated to be about 1.5 cm^{-1}. The polarization-controlled experiments showed that the allowed angle between the two transition dipoles is likely to be 52° or 128°. This indicates that the most probable conformation is polyproline II with Ramachandran angles ($\phi = -70°$ and $\psi = 120°$). Also, the population relaxation times were measured from the transient grating experiments and the two values for the amide I mode of the acetyl- and amide-end are 415 and 576 fs for the isotopomer of which the amide-end peptide is ^{13}C-labeled. This indicates that the lifetime broadening is a significant contribution to the total vibrational dephasing.[251]

In both cases of dipeptides, i.e., acetylproline-NH_2 and alanine dipeptide analogue, the overall peptide structure was found to be close to the P_{II} conformation. However, what causes this high P_{II} propensity in dipeptides was not clearly understood. One of the quantum chemistry calculation studies of the alanine dipeptide analogue with a few solvated water molecules showed that water bridges connecting two carbonyl groups in the dipeptide could play an important role in stabilizing the P_{II} conformation.[252] However, in the case of the acetylproline-NH_2, due to the presence of a five-membered pyrrolidine ring, it does not have an N−H group at the acetyl-end peptide, so that one possible water-assisted hydrogen-bond network cannot be formed intrinsically.[243] Nevertheless, the vibrational circular dichroism spectrum and constrained MD simulation showed that the acetylproline-NH_2 structure is also P_{II}.[243] This result was found to be consistent with the previous works,[253−255] where the major factor determining the dipeptide conformation in water is from the intramolecular steric repulsive interaction.[253]

Although there are a number of theoretical methods for simulating the 1D and 2D IR spectra of peptides, only recently were nonadiabatic effects on the linear and nonlinear vibrational spectral simulations of alanine dipeptide studied—note that the frequency trajectories of the two amide I normal modes undergo avoided crossings when the site energies cross.[256] Due to the coupling between the two local modes, the eigenenergies should not cross. The nonadiabatic effects were taken into consideration in their numerical simulation of the 2D IR spectrum of alanine dipeptide by numerical integration of the Schrödinger equation. Further studies along this line for polypeptides will be highly interesting and important.

5.4.3. Rigid Dipeptide

Although the coupled oscillator systems discussed above are peptides containing two peptide bonds, 2D vibrational

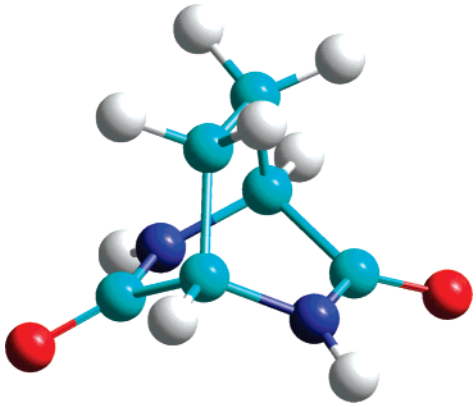

Figure 22. Molecular structure of 2,5-diazabicyclo[2,2,2]octane-3,6-dione (DABCODO).[258]

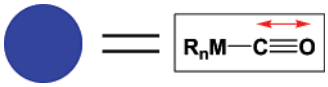

Figure 23. CO stretching vibrational chromophore in metal carbonyl compounds.

spectra of a rigid dipeptide, 2,5-diazabicyclo[2,2,2]octane-3,6-dione (DABCODO), shown in Figure 22, were theoretically calculated by performing density functional theory simulations.[257] The two peptide groups are rigidly held by a bridge, and thus, the conformational inhomogeneity could be ignored. Also, due to its relatively small size, they were able to use high-level quantum chemistry calculation methods to obtain vibrational frequencies, quartic anharmonicities, mode couplings, Fermi resonances, and transition dipoles. In addition to the amide I vibrations, amide II and amide A modes were also considered in their calculations. Therefore, two-color 2D IR spectroscopy, which involves pulses having two different center frequencies that are resonant with two different stretching vibrations, was shown to be a useful technique for examining mode couplings induced by multidimensional potential anharmonicities. One of the interesting observations is that there is a Fermi resonance coupling between the amide II overtone and the amide A (N−H stretch) mode, and it was shown that such a phenomenon could be monitored by a two-color 2D IR spectroscopic method.

5.4.4. Dicarbonyl Metal Complex

The dicarbonylacetylacetonato rhodium complex (RDC) has been found to be an excellent model for a coupled oscillator system, and it is a square-planar compound with two equivalent CO groups and a bidentate acac ($OC(CH_3)$-$CHC(CH_3)O$) ligand coordinated to the rhodium metal center.[30,259−262]

Due to the strong coupling between the two CO stretching vibrations (Figure 23), symmetric and asymmetric CO stretching normal modes are formed and the frequency splitting of about 70 cm^{-1} directly reflects the coupling strength. In addition to these two fundamental transition states, there are three doubly excited states. For RDC in hexane, the anharmonic frequency shifts of the overtone states were found to be 11 and 14 cm^{-1} for the symmetric and asymmetric CO stretch normal modes, respectively. The combination band is red-shifted by 26 cm^{-1} with respect to the sum of the fundamental frequencies due to the coupling between the carbonyls. Since the line widths in the IR spectrum were about 2.6 cm^{-1}, which is significantly smaller than the anharmonic frequency shifts, one can resolve all possible resonant transition peaks in the 2D IR spectrum. In Figure 24a and b, the 2D IR rephasing and non-rephasing spectra for the RDC in hexane are shown. The purely absorptive spectrum,[259] which results from the addition of equally weighted rephasing and non-rephasing spectra, is also shown in Figure 24c. The two diagonal peaks, denoted as 1′ and 1, in the $\tilde{S}_C$ spectrum correspond to the asymmetric and symmetric fundamental peaks, respectively. The negative peaks 3 and 3′ (5 and 5′) in the off-diagonal region are excited-state absorptions from the symmetric and asymmetric mode excited states to their overtone (combination) states. Due to the overtone frequency shifts, Δ_s and Δ_a, these two peaks appear in the off-diagonal region. The other two cross peaks, 2 and 2′, are produced by coupling. Again, due to the anharmonicity of the combination band, Δ_{as}, the conjugate cross peaks 4 and 4′ can be found in the $\tilde{S}_C$ spectrum.

Later, signatures of vibrational coherence transfer processes were investigated by using FT 2D IR spectroscopy.[263] From the measured absolute value 2D IR rephasing spectra as a function of waiting time T, a few interesting peak amplitude changes were observed. The coherence transfer between the two fundamental vibrations can affect the amplitude of all the peaks. Time evolution of the symmetric and asymmetric superposition state (off-diagonal density matrix) appears as modulated cross and diagonal peak amplitudes in the rephasing and non-rephasing spectra, respectively, where the modulation frequency corresponds to the frequency splitting between the two fundamental modes, ∼70 cm^{-1}. Population transfers between the two excited states lead to the growth of relaxation-induced cross peaks. Finally, the slow population relaxation to the ground state induces simultaneous decays of all resonance peaks, and the time scale was estimated to be about 60 ps. Most of the salient features of 2D vibrational spectroscopy of a coupled oscillator system have thus been discussed in these works for a simple model system, RDC.[30,263] Later, an *ab initio* simulation study on this system was reported.[264]

5.4.5. Acetic Acid Dimer

As a good model system for understanding the hydrogen-bonding interaction, acetic acid dimer has been studied.[265−270] Particularly, 2D IR photon echo experiments on acetic acid in CCl_4 solvent with a concentration of 0.2 M were performed, where the O−H stretching vibrations (Figure 25) were investigated because the OH group directly participates in the hydrogen bonds in a cyclic acetic acid dimer.

It was known that, at this high concentration, the cyclic dimer is the predominant molecular species.[271] The absorption spectrum is broad, and two peaks at 2920 and 2990 cm^{-1} are prominent in the spectrum. In Figure 26, the absorption spectrum (see the solid line in Figure 26a) and the heterodyne-detected 2D PE spectra at $T = 0$ (Figure 26b) and 400 fs (Figure 26c) are shown.[265] Not only the cross peaks between two fundamental OH modes but also other cross peaks in the low-frequency ranges are evident in the $T = 0$ spectrum. The excited-state absorption peaks, which appear negatively in the 2D spectrum at $T = 0$, disappear in about 200 fs, since the lifetime of the $v = 1$ state is about 200 fs. Therefore, the 2D spectrum at T =400 fs shows no negative cross peaks. Nevertheless, the ground-state bleaching contribution can persist even after depopulation of the first excited-state, so that the spectral features around 2950 cm^{-1} remain strong even at $T = 400$ fs. In addition to the cross peaks originating

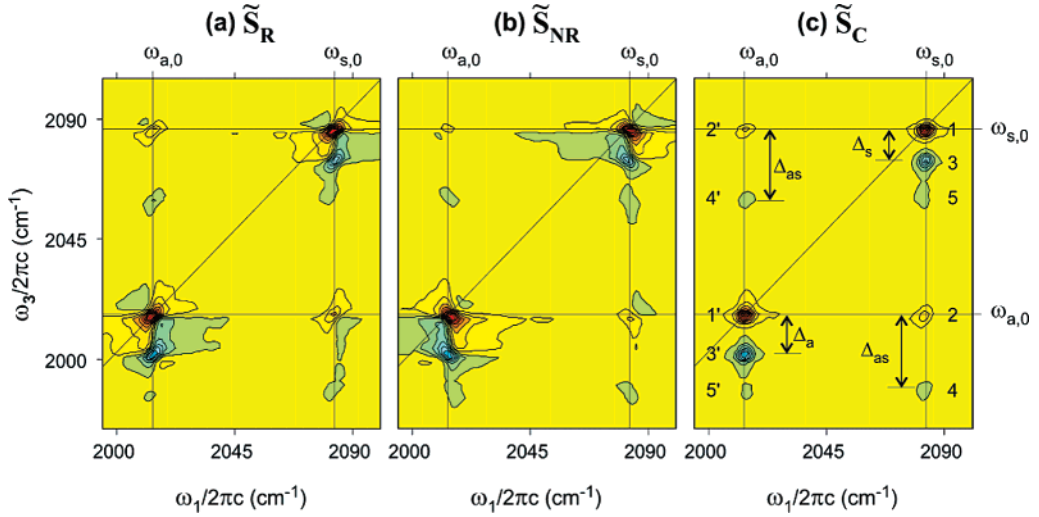

Figure 24. Two-dimensional IR rephasing (a), non-rephasing (b), and correlation (c) spectra for RDC (dicarbonylacetylacetonato rhodium complex) in hexane at the waiting time $T = 0.30$. These spectra were obtained in the all-parallel [zzzz] geometry. Fifteen equally spaced contour levels from the minimum to the maximum value were drawn for each 2D plot.

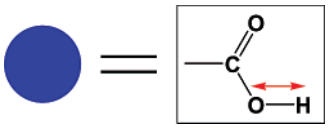

Figure 25. OH stretching vibrational chromophore of acetic acid. When two acetic acid molecules form a cyclic dimer, the two O−H stretching modes are coupled to each other to form two normal modes, symmetric and asymmetric O−H stretching vibrations.

from $v = 1$ to $v = 2$ transitions, there are a number of cross peaks arising from other mechanisms. In ref 265, a few different possibilities were suggested and discussed in detail. For instance, (i) Fermi resonances of the OH stretching oscillator with other combination modes and (ii) anharmonic couplings of the high-frequency OH stretching excitations with lower-frequency modes were discussed and the DFT calculation results including a one-quantum excited-state manifold were directly compared with experimental data—note that full quantum chemistry calculations considering all possible vibrational excitations are still prohibitively difficult. From their homodyne-detected photon echo experiment, the initial decay within 200 fs was observed and recurrences after that were also found. The latter phenomenon was interpreted as multilevel coherences in the anharmonically coupled low-frequency vibrations with relatively long dephasing times of 1−2 ps. It is interesting to note that the acetic acid dimer system exhibits quite a different nonlinear optical response in comparison to the more well-known and important hydrogen-bond network system, water. 2D IR experimental results on the latter will be discussed later in this section.

5.4.6. Dual Frequency 2D IR Spectroscopy of Coupled Oscillator Systems

The previously discussed examples in this subsection are the cases when the two vibrational oscillators are identical in nature. However, using dual frequency 2D IR spectroscopy,[272−277] where IR pulses with different center frequencies that are resonant with two completely different oscillators are used, one can directly measure vibrational coupling-induced cross peaks. This is analogous to heteronuclear 2D NMR spectroscopy. In ref 273, vibrational couplings between amide I and amide A (N−H stretch) modes in two model peptides, Ac-Ala-OMe and caprolactam

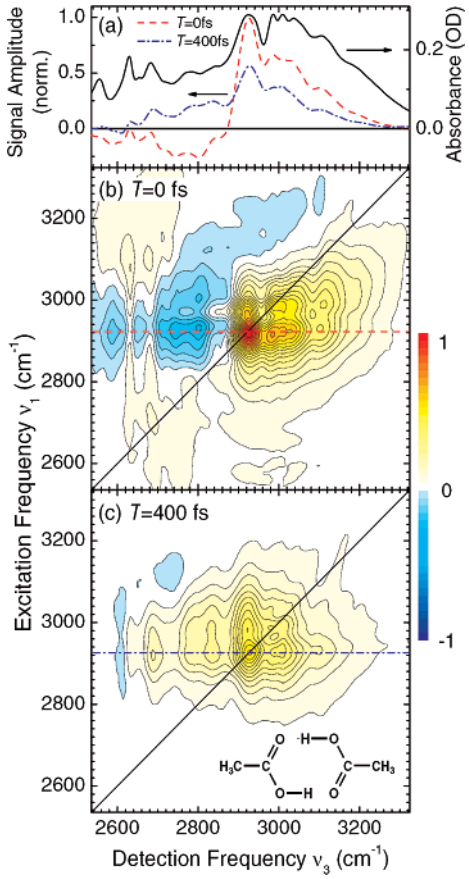

Figure 26. (a) Linear spectrum of the O−H stretching band of cyclic dimers of acetic acid in CCl_4 (solid line). Cross sections through the two-dimensional vibrational spectra at an excitation frequency of 2920 cm^{-1} for population times $T = 0$ (dashed line) and 400 fs (dash-dotted line). (b, c) Two-dimensional vibrational spectra of cyclic acetic acid dimers (inset of part c) measured for population times of $T = 0$ and 400 fs. The amplitude of the photon-echo signal was plotted as a function of the excitation frequency ν_1 (ω_t) and the detection frequency ν_3 (ω_t). Reprinted with permission from Huse, N.; Bruner, B. D.; Cowan, M. L.; Dreyer, J.; Nibbering, E. T. J.; Miller, R. J. D.; Elsaesser, T. *Phys. Rev. Lett.* **2005**, *95*, 147402. Copyright 2005 by the American Physical Society.

in $CHCl_3$ solvent, were studied, where two IR fields are at 3.3 μm and one is at 6 μm. Due to the anharmonic couplings

between the two modes, the corresponding cross peak revealing a positive correlation between the two frequencies in the same amide unit was observed. A few possible applications of this technique for peptide structure determination were mentioned.[272,273] More recently, for the model compound, 2-cyanocoumarin, a dual-frequency 2D IR experiment was carried out, where coupling between CN and C═O stretching modes was investigated. Here, it is interesting to note that the weak IR reporter, the CN stretch mode, is rather highly sensitive to the local electrostatic environment, so that the strongly IR-active modes such as the C═O stretch and amide I modes in peptides can induce frequency and cross peak amplitude changes of such a weak IR reporter mode. In addition, a dual-frequency 2D IR spectroscopic study on coupling between C−D and CN stretch modes in a CD_3CN molecule was carried out.[276]

5.5. Secondary Structure Peptides

Proteins in nature contain varying extents of secondary structure peptides. Therefore, small polypeptides that can adopt a specific secondary structure have been considered to be a valuable model system to study vital factors influencing protein stability and folding.[278,279] In order to establish the secondary structure−2D vibrational spectrum relationship, steady-state 2D IR spectroscopic studies of secondary structure proteins have been performed over the past few years. Also, an isotope-labeling technique was used to determine spatially the local peptide backbone conformation in a given polypeptide. In this subsection, 2D vibrational spectroscopic investigations of an α-helix, *β*-sheet, *β*-hairpin, and 3_{10}-helix will be outlined by making direct comparisons with recent computational studies.

5.5.1. Right-Handed α-Helix

The first 2D IR pump−probe spectroscopic study of the amide I band of the *Fs* helix in D_2O was carried out and reported in ref 101. The *Fs* helix is an alanine-based 21-residue right-handed α-helical peptide. Its amide I absorption spectrum appears to be a broad and featureless single band with its peak maximum at approximately 1637 cm^{-1} at 4 °C (see the linear absorption spectrum in the top panel of Figure 27). The parallel and cross polarization 2D pump−probe spectra are also shown in Figure 27.

Due to the amide I overtone anharmonicity of about 16 cm^{-1}, the positive and negative peaks are separated in frequency. However, the 2D contour line shape does not exhibit any distinctively notable features that can be considered to be characteristic for the right-handed α-helix. Nevertheless, it was possible to show that there is sizable inhomogeneity associated with conformational disorder. Furthermore, the time-resolved 2D measurements indicated that the conformational fluctuation time scale is about on the order of picoseconds. Later, by carrying out molecular dynamics simulations of an alanine-based helical polypeptide in water by employing the electrostatic potential model described in section 5.3, conformational fluctuations, frequency−frequency correlations, and the delocalized nature of amide I excitation states were studied.[239] The linear correlation between C═O bond length and the amide I local mode frequency was confirmed by analyzing the geometry optimized structure and vibrational frequencies and eigenvectors obtained by using a semiempirical (AM1) quantum chemistry calculation method. When the polypeptide forms a stable and structurally uniform α-helix, the average amide

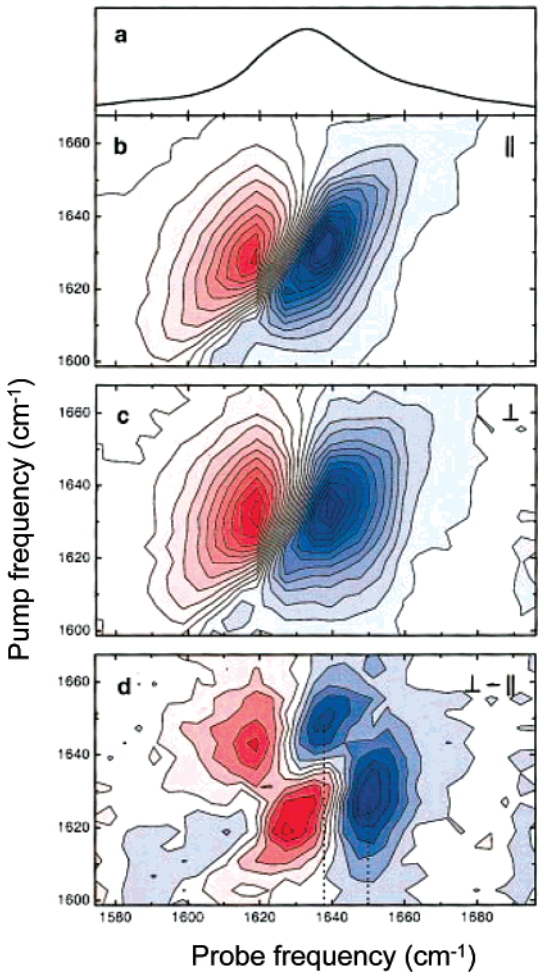

Figure 27. (a) Linear absorption spectrum of the F_S peptide in D_2O at 277 K.[101] (b) 2D spectrum at waiting time $T = 1$ ps, for parallel polarizations of the pump and probe pulses, showing the absorption change as a function of pump and probe frequency. Blue colors indicate negative absorption change; red colors indicate positive absorption change. Contour intervals are 0.048 mOD (optical density). (c) 2D spectrum for perpendicularly polarized pump and probe. Contour intervals are 0.020 mOD. (d) Difference between perpendicular and parallel signals (both scaled to the maximum value occurring in the respective 2D scans). Contour intervals are 0.023 mOD.

I local mode frequencies for all peptides are approximately constant, even though each individual amide I local mode frequency fluctuates in time due to hydrogen-bonding and electrostatic interactions with surrounding water molecules. Despite the fact that the coupling constants also fluctuate due to thermal conformational fluctuations, their fluctuation amplitudes, i.e., standard deviations, are comparatively small, which suggests that the off-diagonal Hamiltonian matrix element fluctuations and disorders could be ignored in this case. Furthermore, the cross correlations between any two amide I local mode frequencies were also found to be negligible, which is supporting evidence for the approximation in eq 4-14. Not only the dipole strengths of all one-exciton (amide I normal mode) transitions but also the density of two-exciton states were examined in detail. Finally, the numerically simulated 2D IR pump−probe spectra were directly compared with the experimental results in ref 101, and the agreement was found to be quantitative.

Since the 2D IR spectrum of the *Fs* helix is featureless, it was difficult to extract structural information from the measured 2D spectrum of the *Fs* helix. Therefore, it was

natural to apply the 2D spectroscopic technique to site-specifically isotope-labeled helical polypeptides. The isotope-labeling technique in combination with vibrational spectroscopy has been found to be extremely useful in elucidating peptide's local structure,[231,246,280−290] because the isotope-labeled amide I peak frequency and line shape are highly sensitive to the secondary structure around the labeled peptide groups. Typically, a ^{13}C-isotope-labeling induces a frequency red-shift by about 40 cm^{-1} so that the isotope peak can be frequency-resolved from the main amide I IR band. Furthermore, a ^{13}C═^{18}O labeled peptide has an amide I vibrational frequency shifted by about 65 cm^{-1} from that of an unlabeled peptide.[231,291,292]

In ref 292, 2D IR photon echo studies of isotopomers of an alanine rich α-helix, Ac-(A)$_4$K(A)$_4$K(A)$_4$K(A)$_4$K(A)$_4$Y-NH$_2$, were reported. Particularly, the 2D spectra of [0,11], [12,13], [11,13], and [11,14], where the notation for these compounds: [alanine residue with ^{13}C═^{16}O, alanine residue with ^{13}C═^{18}O], were measured. The two frequency-resolved isotope-labeled peaks could be easily identified in both 1D and 2D IR spectra, and the corresponding absorptive 2D IR spectra of isotope-labeled amide I modes are shown in Figure 28. The cross peak intensity shows the trend [12,13] > [11.14] > [11,13]. The off-diagonal anharmonicity values for [12,13], [11,14], and [11,13] were estimated to be 0.9, 3.2, and 4.5 cm^{-1}, respectively.[292] The cross peak intensity trend is also in agreement with the trend of coupling constants, i.e., $|J_{n,n+1}|$ (6.5 cm^{-1}) > $|J_{n,n+3}|$ (−4.4 cm^{-1}) > $|J_{n,n+2}|$ (−3.4 cm^{-1}).[280]

To shed light on site-specific conformational inhomogeneity, a series of singly ^{13}C═^{18}O-labeled 25-residue α-helical polypeptides were also studied by a 2D IR spectroscopic method. The labeling site is at residue numbers 11−14 on the middle of the helix. The elongation of the diagonal isotope-labeled peaks was clearly observed, indicating that there is a sizable inhomogeneous contribution. Furthermore, amide I frequencies at residues 11 and 14 have large inhomogeneous distributions in comparison to those at 12 and 13. This was found to be induced by the modifications of the intrahelical hydrogen-bond network by the nearby lysine residues, which are spatially close to residues 11 and 14. The nature of the structural inhomogeneity, their influences on linear and nonlinear spectra, and thermal unfolding signatures in the temperature-dependent IR spectrum of isotope-labeled helical polypeptide were elucidated by examining classical MD simulation trajectories with numerical simulations of vibrational spectra.[293,294]

5.5.2. Antiparallel and Parallel β-Sheet Polypeptides

In ref 295, theoretically calculated amide I local mode frequencies and vibrational coupling constants in various multiple-stranded antiparallel β-sheet polyalanines were presented and used to describe various spectroscopic properties of these peptides with respect to the size, i.e., numbers of strands as well as of peptide bonds in a single strand. Instead of more realistic β-sheet peptides, an ideal β-sheet peptide was also considered to find its 2D IR spectroscopic signatures.[296] In these two works, it was found that the coupling constants between two amide I local modes on hydrogen-bonded peptides are fairly large, whereas the vibrational coupling constant between two neighboring amide I local modes on a given strand is comparatively small. This shows that the delocalized nature of the amide I normal modes is largely determined by the interstrand vibrational

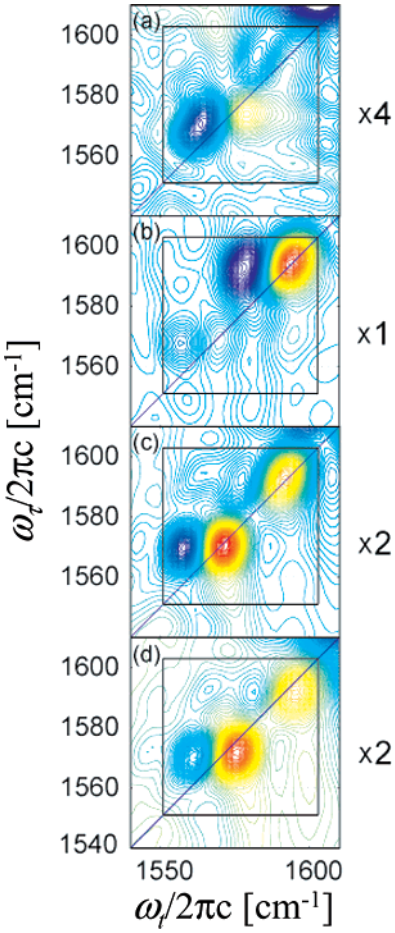

Figure 28. Sum of the real parts of the 2D IR rephasing (R) and nonrephasing (NR) spectra of [0,11], [12,13], [11,13], and [11,14] isotopomers (see the context for notations).[292] In particular, the isotope-labeled peaks are shown in these figures. The relative signal strengths were chosen for each spectrum to show the proper contrast between the negative (blue) and positive (red) features, and the contour lines were drawn in 1% intervals from the minimum to the maximum value of each region shown. The listed multiplication factors indicated the relative intensity ratios between each spectrum presented here in reference to their main helical band, which should have a similar signal amplitude in all four cases.

coupling constants between two hydrogen-bonded peptide groups. In addition, the amide I local mode frequency itself was found to be strongly dependent on the number of hydrogen bonds.

As can be seen in Figure 29, vibrational couplings among amide I local modes in the multiple-stranded β-sheets were shown to be fully characterized by eight different coupling constants (see ref 295 for values of these coupling constants denoted as F's in Figure 29). The inverse participation ratios, which are approximate measures of the numbers of participating amide I local modes in each amide I normal mode, were calculated. In an ideal antiparallel β-sheet, the amide I normal modes are significantly delocalized. The calculated phase-correlation factors[239] that were introduced to quantitatively estimate correlations between oscillation phases of two local oscillators for a given normal mode, were calculated to identify the two characteristic $\omega_\perp$- and $\omega_\parallel$-modes—note that the $\omega_\perp$($\omega_\parallel$)-mode has a transition dipole perpendicular (perpendicular) to the constituent strands.[295] It turned out that the $\omega_\parallel-\omega_\perp$ frequency splitting magnitude denoted as Δ in Figure 29 is strongly dependent on the number of strands but not on the length of each strand

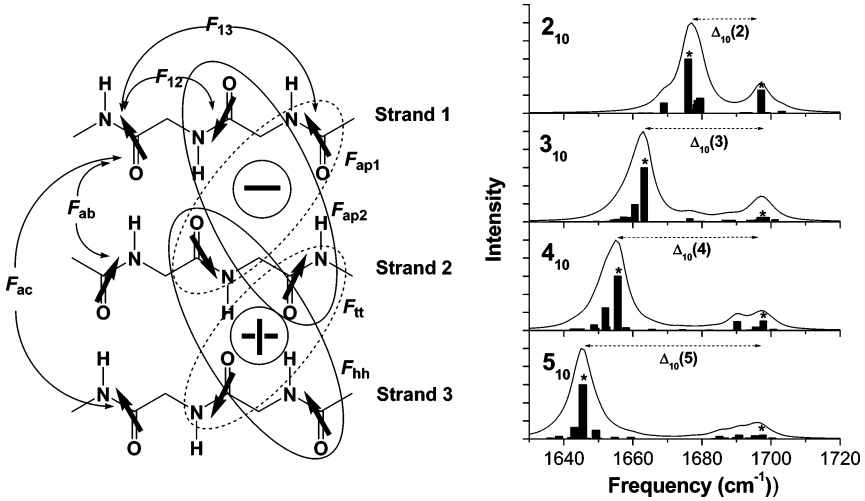

Figure 29. Eight different vibrational coupling constants and simulated amide I IR absorption spectra of antiparallel β-sheet polypeptides.[295] The transition dipoles of amide I local modes are shown as thick arrows (left). The frequency splitting amplitude Δ increases as the number of strands in a given antiparallel β-sheet polypeptide increases. M_{10} (for $M = 2-5$) means that the antiparallel β-sheet contains M strands and each strand includes 10 peptide bonds that are capable of making hydrogen-bonding interactions with peptides in a neighboring strand.

constituting the antiparallel β-sheet. Consequently, it was possible to describe such size-dependency of Δ by using an approximately one-dimensional Frenkel exciton model, where a linear chain of amide I local modes on the peptides wasconnected to each other by hydrogen-bonds.[295]

The figure on the right-hand side of Figure 29 depicts the simulated amide I IR spectra for antiparallel β-sheet polyalanines with 2 to 5 strands, where each strand has 10 peptide groups—note that the notation 5_{10}, for example, represents an antiparallel β-sheet polyalanine with 5 strands and 10 peptides in each strand. From the calculated frequency splitting magnitude $\Delta(M)$, it was possible to fit the data with a stretched-exponentially rising function as[295]

$$\Delta(M) = \Delta(\infty) - (\Delta(\infty) - \Delta(2)) \exp\{-k(M-2)^{\alpha}\} \quad (5\text{-}28)$$

The parameters in eq 5-28 were determined: $\Delta(\infty) = 57$ cm^{-1}, $\Delta(2) = 20$ cm^{-1}, $k = 0.47$, and $\alpha = 1.17$. Although a series of antiparallel β-sheet polyalanines were theoretically considered, the relationship between the frequency splitting magnitude and the number of strands in real antiparallel β-sheet polypeptides would be valid even for some real proteins with a number of β-sheet segments.

The first 2D IR experiment on a model peptide known to form a β-sheet structure was reported in ref 297. From a theoretical study on the 2D vibrational property of an ideal antiparallel β-sheet peptide,[296] they were able to identify two strongly IR-active modes, of which transition dipoles are perpendicular and parallel to the constituent strands. The two are low- and high-frequency modes denoted as $\alpha-$ ($\omega_{\perp}$) and $\alpha+$ ($\omega_{||}$), respectively.[297] Poly-L-lysine at high pH and temperature (>30 °C) was however to form an extended antiparallel β-sheet conformation.[298−300] Thus, this model system was chosen for the 2D IR spectroscopic investigation. In Figure 30, the amide I IR absorption and two different 2D IR spectra are shown.[297] The two peaks at 1611 and 1680 cm^{-1} are clearly observable in the IR spectrum. The large frequency splitting magnitude of 69 cm^{-1} indicates that the number of strands involved in the antiparallel β-sheet of poly-L-lysine is significantly large.

Figures 30b and c are the 2D IR correlation spectra for the parallel ([*zzzz*]) and cross ([*zzyy*]) polarization geometries. The cross peaks in the upper and lower diagonal regions are

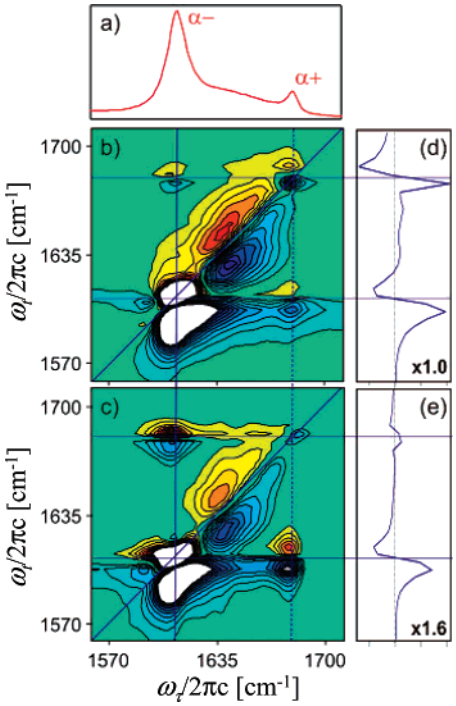

Figure 30. (a) FTIR spectrum of poly-L-lysine at high pD.[297] At this condition, poly-L-lysine is known to form a stable antiparallel β-sheet structure. 2D IR correlation spectra of poly-L-lysine for the (b) parallel (*zzzz*) and (c) crossed (*ZZYY*) polarization geometries. Nineteen equally spaced contours are plotted between −20% and 20% of the peak maximum. Slices at $\omega_{\tau} = 1680$ cm^{-1} (dashed line) are plotted for (d) *zzzz* and (e) *zzyy*. The projection angle between the two transition dipoles of the $\alpha+$ and $\alpha-$ modes is determined from the observed cross peak amplitude ratio in these slices.

clearly visible, which suggests strong coupling and delocalized natures of the two modes. The overall 2D line shape was found to be the "Z"-form, so that this Z-shape 2D spectrum has been considered to be a characteristic feature of the antiparallel β-sheet conformation. Their experimental and theoretical findings were used to further elucidate the 2D IR spectra of a few different globular proteins containing a significant amount of β-sheet segments (see section 5.6 below).

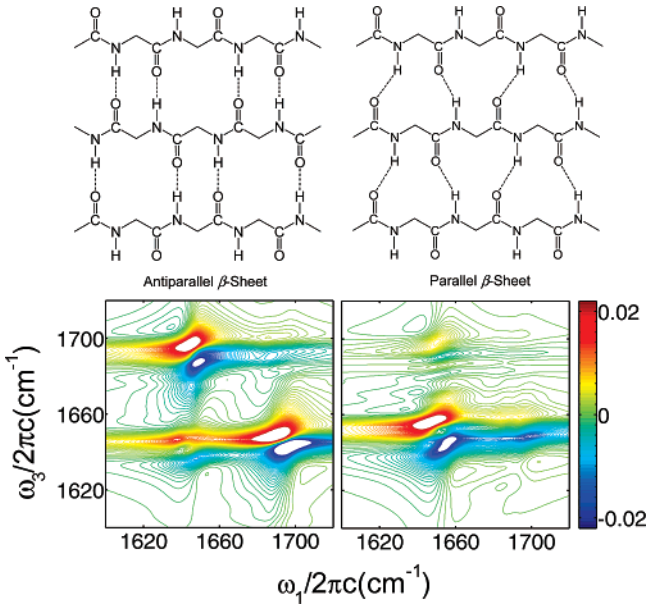

Figure 31. Molecular structure of model antiparallel and parallel β-sheet polypeptides. Despite the fact that the two structures appear to be different, spectroscopically it is quite difficult to distinguish one from the other. The difference 2D IR rephasing spectra, defined as $\Delta S(T) = S^{zzzz}(T) - 3S^{zxxz}(T)$ for antiparallel and parallel β-sheet polypeptides are shown here.[302] The cross peak amplitudes are notably large when the β-sheet adopts an antiparallel structure, whereas they are small for a parallel β-sheet structure.

One of the critical issues in spectroscopic investigations of β-sheet polypeptides is to find characteristic features separating antiparallel β-sheets from parallel β-sheets, when the precise protein structure containing a large amount of β-sheet peptides is not known.[301,302] Linear absorption spectroscopy cannot provide incisive information for distinguishing an antiparallel β-sheet from a parallel β-sheet. After carrying out quantum chemistry calculations and model simulations, we showed that the polarization-controlled 2D IR photon echo spectroscopy can be of critical use in distinguishing these two different β-sheets.[302] Particularly, the ratios of the diagonal peak amplitudes to the cross peak amplitudes were found to be strongly dependent on the quasi-2D array of the amide I local mode transition dipole vectors. Although the parallel or cross polarization 2D IR PE spectrum of the model antiparallel β-sheet peptide was found to be different from that of the parallel β-sheet peptide, the spectral difference is not distinctively large. However, it was shown that the relative amplitudes of the cross peaks in the 2D difference spectrum, which is defined as $\Delta S(T) = S^{zzzz}(T) - 3S^{zxxz}(T)$, of an *antiparallel* β-sheet are significantly larger than those of the diagonal peaks, whereas the cross peak amplitudes in the 2D difference spectrum of a *parallel* β-sheet are much weaker than the main diagonal peak amplitudes (see Figure 31).

Assuming that the excited-state absorption contributions to the 2D difference spectrum do not strongly overlap with the ground-state bleaching and stimulated emission contributions in the 2D difference spectrum, it was found that the cross peak amplitude at ($\omega_\tau = \bar{\omega}_j$, $\omega_t = \bar{\omega}_k$), when the jth and kth modes are coupled, is approximately determined by the product of the two dipole strengths and the angle factor, i.e.,[302]

$$\Delta S_{kj}(T) = S_{kj}^{zzzz}(T) - 3S_{kj}^{zxxz}(T) \propto \mu_k^2 \mu_j^2 \sin^2 \theta_{kj} \quad (5\text{-}29)$$

Here, the transition dipole matrix elements associated with the vibrational transitions of the jth and kth modes are denoted as μ_j and μ_k. The angle between the two transition dipole vectors is denoted as θ_{kj} ($= \vec{\mu}_k \cdot \vec{\mu}_j / |\vec{\mu}_k||\vec{\mu}_j|$). It was found that the low frequency $\omega_\perp$-mode has a transition dipole vector that is perpendicular to that of the high-frequency $\omega_\parallel$-mode, when the β-sheet forms an antiparallel structure. Thus, the cross peak amplitude in the 2D difference spectrum is very large (see Figure 31). In contrast, there is no such high-frequency mode for which the transition dipole vector is large in magnitude and perpendicular to that of the low-frequency $\omega_\perp$-mode, for the parallel β-sheet peptide, which results in weak cross peaks in the 2D difference spectrum. This clearly shows why the 2D spectroscopic method is a better tool to determine the global minimum structure of a polypeptide that cannot be easily determined by other linear vibrational spectroscopic means such as IR and Raman spectroscopies. In the present section, only the 2D vibrational spectroscopic investigations are discussed, but there exist a number of interesting experimental and theoretical works on the vibrational properties of β-sheet peptides,[284,303−309] which have not been discussed here because they are beyond the scope of this article.

5.5.3. β-Hairpin

The β-hairpin secondary structure motif is critical for 3D structure formation of a protein. Furthermore, its thermodynamic stability and conformational fluctuation dynamics are important in understanding and studying protein folding and unfolding dynamics and mechanisms.[238,286,310−328] Two characteristic features of a β-hairpin that distinguish its amide I IR spectrum from that of an antiparallel β-sheet peptide were discussed in ref 329. First, the low-frequency band of the 16-residue β-hairpin GEWTYDDATKTFTVTE is at 1620 cm^{-1}, whereas that of an antiparallel β-sheet is at 1632 cm^{-1}. Second, the high-frequency peak does not undergo any isotopic shift in D_2O solvent. However, a later study on another 16-residue β-hairpin (KKYTVSINGKKITVSI) showed no notable difference in the amide I IR spectrum, indicating that there is a significant contribution from the interstrand hydrogen-bonding interactions. In order to understand the line shape of the amide I IR spectrum and the effects from hydrogen-bonding interaction and couplings on the vibrationally excited states of β-hairpins (both the alanine-based β-hairpin and GEWTYDDATKTFTVTE), quantum chemistry calculation and equilibrium MD simulation studies were carried out.[238] It was shown that the 2D IR spectrum of the β-hairpin is largely determined by the amide I normal modes that are delocalized on the peptides in the two antiparallel strands.[238] For an isolated β-hairpin, the amide I local mode frequencies (site energies) in the β-turn region are much larger than those in the antiparallel strands, because of a repulsive dipolar interaction between the two amide I modes in the β-turn region. However, the peptides in the turn region are strongly solvated by surrounding water molecules via hydrogen-bonding interactions. Consequently, the ensemble-averaged amide I local mode frequencies in the turn region become quantitatively similar to those in the strands.[238] Despite the fact that the average local mode frequencies are uniform throughout the peptides, their fluctuation amplitudes are sizable so that the amide I normal modes are relatively localized on just a few peptide groups that are strongly interacting with each other via hydrogen bonds. The amide I local mode frequency fluctuation appears to be uncorrelated with those of neighboring peptide groups.[238]

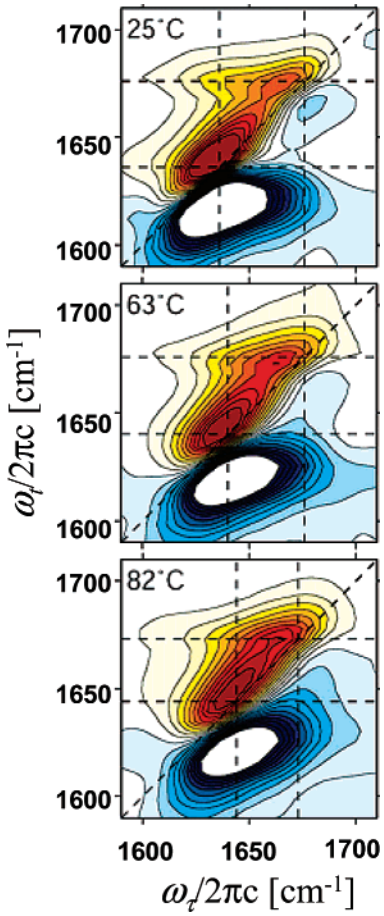

Figure 32. 2D IR spectra of Trpzip2 (tryptophan zipper 2: SWTWENGKWTWK) at three representative temperatures: 25, 63, and 82 °C.[319] 20 equally spaced contour levels are drawn to ±60% of peak intensity. The vertical line in the low-frequency region shows the position of the $\nu_{\perp}$-mode whose transition dipole vector is approximately perpendicular to the constituent strands, whereas that in the high-frequency region shows that of the $\nu_{||}$-mode with its transition dipole vector parallel to the strands. As the temperature is increased from 25 to 82 °C, the frequency difference between the $\nu_{\perp}$- and $\nu_{||}$-modes decreases. This indicates that the hydrogen-bonding interactions are weakened. Nevertheless, the "Z"-shape of the 2D IR spectrum even at the high temperature of 82 °C suggests that the native hairpin conformation remains.

The first 2D IR study concerned thermal denaturation of tryptophan zipper 2 (Trpzip2: SWTWENGKWTWK), which is a 12-residue peptide with a type I′ turn using the ENGK sequence. The FT IR experiment showed that the melting temperature is about 60 °C, which was deduced by examining the amide I band change with respect to temperature.[330] The amide I IR band of Trpzip2 is peaked at 1636 cm^{-1} and has a shoulder band at ~1676 cm^{-1}. The temperature-dependent IR spectrum did not indicate a sharp transition in the temperature range from 20 to 85 °C, even though it was clear that thermal denaturation causes weakening of interstrand couplings and interactions. Three representative 2D IR spectra at the temperatures 25, 63, and 82 °C are shown in Figure 32. The Z-shape pattern in the 2D IR spectrum is a characteristic signature of an antiparallel β-sheet structure. Note that the Z-shape form is created by a combination of four peaks, two diagonal and two off-diagonal peaks. The corresponding two modes have transition dipoles that are perpendicular and parallel to the two strands, and thus the notations $\nu_{\perp}$ and $\nu_{||}$ were used. As can be seen in Figure 32, even though the frequency splitting between the two modes decreases as temperature increases, cross peaks revealing couplings between the two are still observable, strongly indicating that the interstrand hydrogen-bonding interactions in Trpzip2 even at high temperature of 82 °C remain.

Although the persistence of interstrand hydrogen-bonding contacts in Trpzip2 even at high temperature was clearly observed by the 2D IR spectroscopic study of Trpzip2,[319] increased amide I frequency fluctuation amplitudes with respect to temperature, site-specific denaturation propensity, and residue-sensitive local solvation dynamics and structural changes could not be easily studied by examining spectrally congested 2D IR spectra of normal Trpzip2. In this regard, 2D IR spectroscopy of site-specific isotope-labeled Trpzip2 peptides could provide more detailed pictures.[238,321,331] The ^{13}C-isotope-labeled peptide was introduced in the terminal (Trp2) or turn (Gly7) region of the hairpin. These two isotopomers were denoted as L2 and L7, whereas the unlabeled Trpzip2 was denoted as UL.

In Figure 33, the FT IR spectra of UL, L2, and L7 and the difference spectra (L2-UL and L7-UL) are shown on the left-hand side. In addition, two sets of 2D IR correlation spectra of UL (a and d), L2 (b and e), and L7 (c and f) are shown in Figure 33, where the three (a−c) in the first column are those obtained with the IR laser center frequency at 1592 cm^{-1} and the three (d−f) in the second column are those with the IR laser center frequency at 1680 cm^{-1}. Although the isotope peak in the L2 IR spectrum appears as a shoulder at ~1600 cm^{-1}, that in the L7 IR spectrum at ~1590 cm^{-1} is frequency-resolved from the main band. Even from the analysis of the IR absorption spectra, one could deduce that the two peptides (Trp2 and Gly7) have different dephasing environments. The line shape of UL is quite similar to that of L7 in the frequency range from 1620 to 1700 cm^{-1}, whereas the peak maximum frequency of 1635 cm^{-1} for UL shifts to 1640 cm^{-1} upon ^{13}C-isotope labeling of Trp2. This is consistent with the fact that the IR spectrum is largely determined by the amide I normal modes that are delocalized on peptide groups in the two strands.[238] Upon isotope-labeling at Trp2, its amide I local mode frequency becomes separated from all other amide I local mode frequencies of other residues constituting the two strands. Therefore, the amide I normal modes are more strongly disrupted by an isotope-labeling at peptides in the strands than in the turn. The 2D IR spectra of L2 and L7 exhibit cross peaks between ^{13}C-labeled and unlabeled modes, indicating couplings between the amide I local mode of labeled peptide and those of nearby unlabeled ones. Furthermore, the slope of the nodal line separating the $v = 0 \rightarrow v = 1$ and $v = 1 \rightarrow v = 2$ transitions and the aspect ratio of the diagonal isotope peaks of L2 and L7 were estimated. If the slope (aspect ratio) is close to 1, the vibrational dephasing is dictated by inhomogeneous (homogeneous) broadening. It turned out that the amide I frequency of Trp2, a terminal residue, has larger inhomogeneity than that of Gly7, a turn-region residue. This is consistent with the picture that the terminal region of the β-hairpin is structurally flexible in comparison to the turn region.

5.5.4. 3_{10}-Helix

There has been great attention paid to the 3_{10}-helical structural motif, which has hydrogen bonds between the C═O oxygen of the jth amino acid and the N−H hydrogen atom of the $(j+3)$th amino acid. The 3_{10}-helix has been known to play important roles in proteins.[332−338] A transmembrane

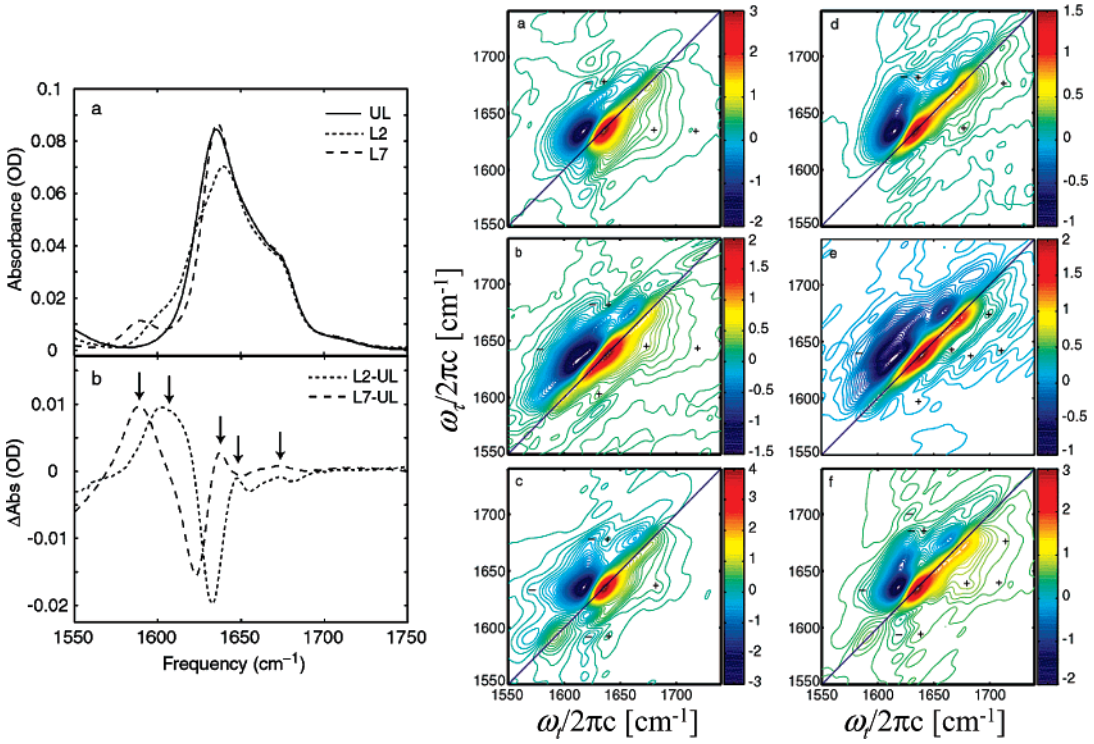

Figure 33. (Left panel) FTIR spectra of three Trpzip2 isotopomers in D_2O (upper-left).[321] The three peptides used are the unlabeled (UL), L2 ($^{13}C{=}^{16}O$ labeled on Trp2), and L7 ($^{13}C{=}^{16}O$ labeled on Gly7). (b) Difference spectra: L2 − UL and L7 − UL. Arrows indicate positive-going peaks. (Right panel) Real part of the 2D IR correlation spectra of Trpzip2 isotopomers: (a and d) UL, (b and e) L2, and (c and f) L7. The cross peaks are marked with "+" and "−" for positive and negative components. (a−c) were collected with the IR laser central frequency at 1592 cm^{-1}; (d−f) were collected with the IR laser central frequency at 1680 cm^{-1}.

channel-forming antibiotic[339] contains a large portion of the 3_{10}-helical conformation, and it was considered to be an intermediate structure in folding or melting of the α-helix.[293,338] Although there already exist a number of spectroscopic investigations to identify 3_{10}-helix formation of synthetic model oligopeptides in nonaqueous solutions,[340−343] a lack of sufficient time resolution of the previous techniques, such as electronic and vibrational CD and 2D NMR, prohibited discriminating α-helix and 3_{10}-helix at an early stage of the helix formation processes. In this regard, 2D IR spectroscopy could be a useful tool for extracting unambiguous information on transient 3_{10}-helix formation.[344,345] The first attempt was made recently for three model octapeptides, i.e., Z-[L-(αMe)Val]$_8$-O*t*Bu, Z-(Aib)$_8$-O*t*Bu, and Z-(Aib)$_5$-L-Leu-(Aib)$_2$-O*t*Bu (*Z* = benzyloxycarbonyl; (αMe)Val = C^{α}-methylvaline; Aib = α-aminoisobutyric acid; O*t*Bu = *tert*-butoxy), in organic solvents. It was known that the N^{α}-acetylated octapeptide adopts the 3_{10}-helical conformation when it is dissolved in $CDCl_3$, but its structure in other fluoro alcohols is an α-helix. Although the amide I IR spectra appear as a broad featureless singlet, the [$\pi/4$, $-\pi/4$, $\pi/2$, 0] 2D IR spectrum of the 3_{10}-helix (three octapeptides in $CDCl_3$) shows a doublet peak above and below the diagonal line. Particularly, the 2D IR amide I cross peak pattern was found to be highly sensitive to the difference between the 3_{10}- and α-helical structures because these two conformations have quite different vibrational coupling constants.[230,345] When the first octapeptide is dissolved in 1,1,1,3,3,3-hexafluoro-2-propanol, the 2D IR spectrum changes in a time scale of days. The cross peak pattern therefore changes in time and was found to sensitively reflect the 3_{10}-to-α-helix transition. These experiments demonstrate that the 2D IR spectroscopic technique can be used to study transient structural changes in the helix−coil or coil−helix transition.

Despite the fact that 2D IR spectroscopy has proven its usefulness in identifying various secondary structure peptides in condensed phases, there are a number of issues needed to be resolved in the future. When the structurally unknown peptide contains varying extents of secondary structure elements in it, the spectral congestion that obscures any further quantitative analysis of linear spectra still prohibits component analysis of the 2D spectra. In this regard, the site-specific isotope-labeling technique will be of critical use, but the sensitivity of 2D spectroscopy should be improved to detect just one or two relatively isolated oscillators from hundreds of amide I transitions. Also, a design of novel IR probes that have large IR intensity and are spectrally separated from other peptide vibrations will be highly desirable to selectively measure the local protein environment around the oscillator and its change during biochemical, folding or unfolding, and physiological processes in the immediate vicinity of the IR probe.

5.6. Globular Proteins

By considering the same amide I vibrations, 2D IR experiments for concanavalin A, ribonuclease A, lysozyme, and myoglobin were performed (see Figure 34 for the ribbon structures of these four globular proteins).[297] A notable difference among the four proteins is the relative amount of β-sheet peptides. The first three proteins contain 46, 32, and 6% antiparallel β-sheet and 0, 18, and 31% α-helical structure. Particularly, concanavalin A has two almost flat six-stranded antiparallel β-sheets so that its 2D IR correlation spectrum (Figure 34a) is qualitatively similar to that of poly-L-lysine. The two characteristic peaks for an antiparallel β-sheet are at 1635 and 1693 cm^{-1}. As the extent of β-sheets decreases from concanavalin A to lysozyme, the characteristic Z-form 2D line shape disappears with a concomitant

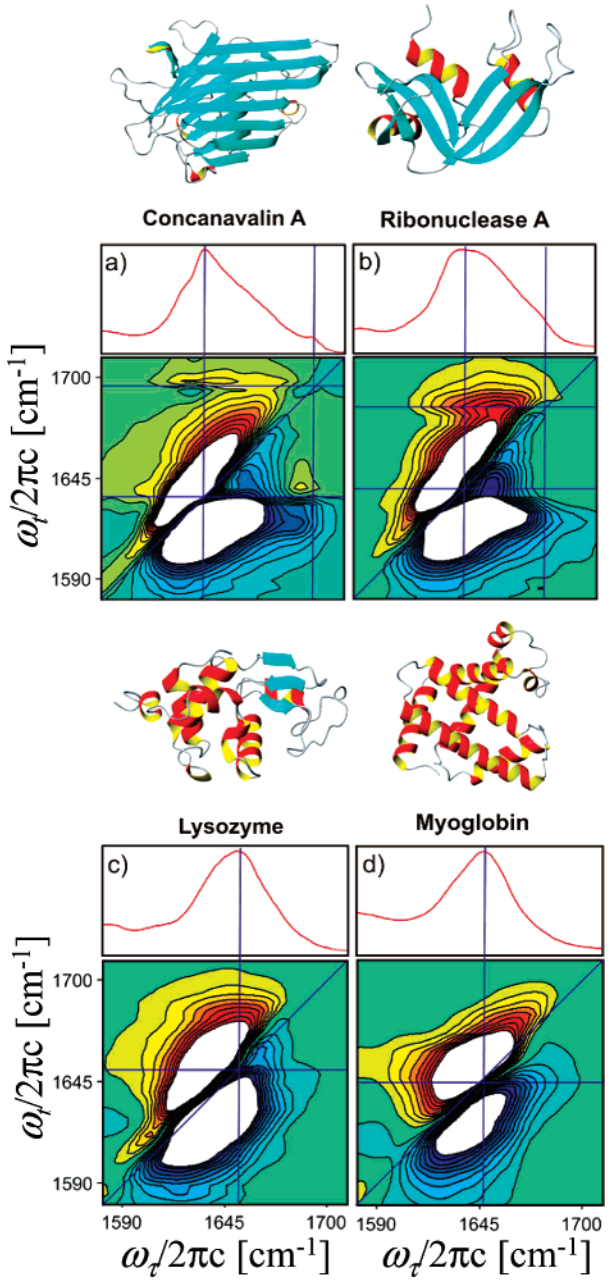

Figure 34. Ribbon diagrams of the four proteins: concanavalin A, ribonuclease A, lysozyme, and myoglobin. FTIR spectra and crossed-polarization 2D IR correlation spectra of the amide I transitions of (a) concanavalin A, (b) ribonuclease A, (c) lysozyme, and (d) myoglobin.[297]

frequency blue-shift of the main peak from 1635 to 1650 cm^{-1}. Furthermore, the 2D line shape becomes more symmetric in frequency domain as the β-sheet content decreases. As discussed in the previous subsection, the frequency splitting is related to the extent of delocalization of the two characteristic modes of the β-sheet. This was confirmed by comparing the 2D spectra of concanavalin A and ribonuclease A. These results clearly indicated that the 2D IR spectra of amide I bands offer a sensitive measure of the underlying β-sheet content and detailed structural variables.[297]

5.7. Membrane Bound Proteins and Lipid Bilayer

The first 2D IR study of a membrane bound peptide was reported in ref 287. The target peptide was the transmembrane domain of the T-cell receptor CD3ζ, which has been known to be essential for T-cell receptor expression.[346−349] Although the human CD3ζ chain has 163 residues, only its transmembrane segment (DPKLGYLLDGILFIYGVILTALFLRVK) from residue 31 to 51 was taken for 2D IR spectroscopic investigation.[287,350,351] The first three residues (DPK) are in the extracelluar region, and the last three (RVK) are exposed to the intracellular environment. Initially, the 49-Leu residue was labeled with $^{13}C{=}^{18}O$ so that its amide I band was separated from the main amide I IR band. Noting that the line width and frequency of such an isotope-labeled peak carries information on the homogeneous and inhomogeneous broadenings and local solvation environment, they were able to estimate a variety of fundamental vibrational properties. The pure dephasing line width, inhomogeneous line width, and population relaxation time were estimated to be 2, 32, and 9 cm^{-1}, respectively, where the transient grating experiment was independently performed to measure the population relaxation time constant.[287] Here, it should be noted that conventional linear spectroscopy cannot be used to separately measure the homogeneous and inhomogeneous line widths. From their 2D IR data, it was possible to show that the amide I vibrational dynamics are not uniform along the transmembrane peptide chain, as expected.

Later, they considered 11 isotopomers of CD3ζ, where each peptide was again labeled with $^{13}C{=}^{18}O$. The CD3ζ peptide is known to form a tetrameric bundle in the membrane, and the helices are kinked at residue 39-Leu (see Figure 35b).[346,347] Therefore, such site-specifically labeled CD3ζ isotopomers would be interesting systems for detailed understanding of site inhomogeneity and dynamics along the transmembrane peptide backbone. Using the 2D IR spectroscopic techniques with enhanced frequency resolution, it was possible to measure the isotope-labeled amide I band widths and frequencies of the 11 different residues. The average frequency is highest in the middle and lowest at the two ends, though the distribution of frequency is not symmetric. The experimental 2D IR diagonal line width for the amide I band of the inner residues is 25% narrower than that of the residue near the water−membrane interface. This is consistent with the expectation that the vibrational dynamics of residues in the middle is likely to be different from those near the membrane surface, due to the water solvation dynamics and structural inhomogeneity of peptides near the interface. Nevertheless, these two variables, line width and frequency, exhibit nonmonotonic behavior with respect to the distance of the residue from the surface. They carried out molecular dynamics simulations using the GROMACS package with GROMOS87 force field parameters. It was found that the water and lipid head-groups near the surface induced a partial denaturation of the helix, which results in amide I frequency shifts and additional broadenings for the residues near the surface. The peptide backbone structure in the middle was found to be relatively rigid so that the inhomogeneity of amide I frequencies of inner residues is comparatively small. The bundle asymmetry associated with the kink at 39-Leu was manifest in the amide I frequencies and line widths too. Note that an isotope-labeling does not induce any peptide structure change, unlike electron spin resonance labels or fluorophores. Thus, the vibrational dynamics of individual amide I modes were successfully probed with 2D IR spectroscopy combined with the isotope-labeling technique.

Another interesting application of 2D IR spectroscopy to membrane bound proteins was performed for a transmem-

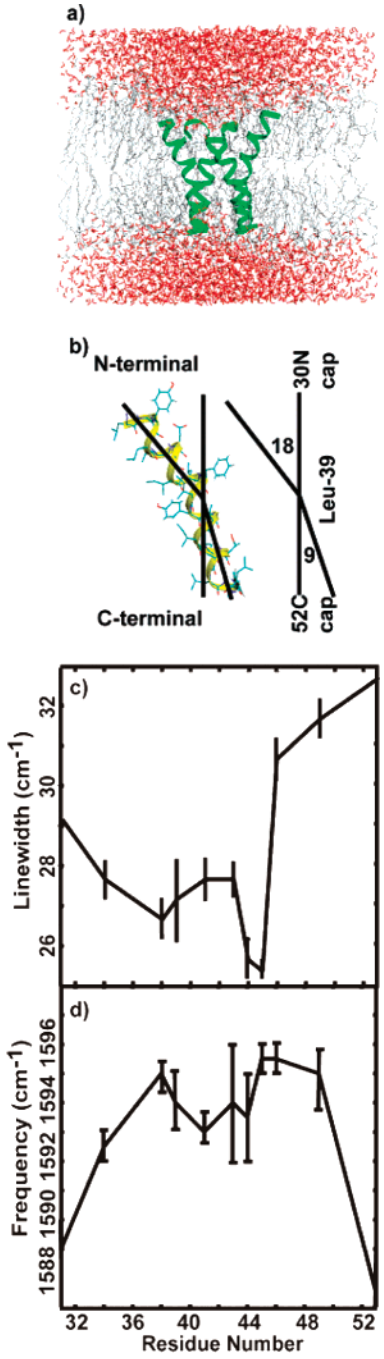

Figure 35. (a) Structure of the CD3ζ transmembrane peptide bundle inside the bilayer membrane. Water and the lipid molecules are shown in red and gray, respectively. The tetrameric helical bundle is shown in green. This tetramer forms a funnel-like structure with the *N*-terminal residues (the top residues) approaching the membrane surface more gradually than the *C*-terminal (bottom). (b) Structure of a single helix. There is a kink in the peptides at Leu-39. (c) Experimentally measured 2D IR line widths of the 11 different singly $^{13}C{=}^{18}O$ isotopically labeled residues reported previously. (d) Infrared absorption frequencies of the 11 different isotopically labeled residues measured from FTIR and 2D IR experiments.[350]

brane helix dimer, which is the 27-residue human erythrocyte protein Glycophorin A (KKITLIIFG$_{79}$VMAGVIGTILLISWG$_{94}$IKK), which was denoted as GpA.[352] Its structure[353] is shown in Figure 36.

Note that the two residues G$_{79}$ and G$_{94}$ were labeled with $^{13}C{=}^{16}O$ or $^{13}C{=}^{18}O$ to separate the isotope-labeled amide I bands from the main band associated with all other amide I normal mode transitions. By considering a variety of combinations of isotope-labeled GpA's, i.e., homodimers and heterodimers, they were able to determine its structure.

The isotope-labeled amide I band of the homodimer system with $^{13}C{=}^{18}O$-labeled at Gly$_{79}$ was found to be asymmetric and consists of two underlying bands with a frequency difference of 8.6 cm^{-1}. This is the most direct and clear evidence of coupling between the two amide I modes localized on the two Gly$_{79}$ peptides, which was successfully interpreted by using an exciton coupling model. A more detailed picture of the delocalized nature of the amide I modes in the dimer was obtained by examining various 2D IR spectra of homo- and heterodimer systems (Figure 36). First of all, cross peaks between the $^{13}C{=}^{18}O$-labeled G$_{79}$ in one of the two monomers and the $^{13}C{=}^{16}O$-labeled G$_{79}$ in the other were clearly observed. On the other hand, when one GpA has $^{13}C{=}^{16}O$-labeled G$_{94}$ and the other has $^{13}C{=}^{18}O$-labeled G$_{79}$, no cross peak appears. These observations indicate coupling between the two modes of neighboring G$_{79}$ peptide groups, and the coupling was estimated to be in the range from 4.3 to 6.3 cm^{-1}. Furthermore, from the polarization-controlled experiments, they were able to estimate the angle θ between the transition dipoles of the $^{13}C{=}^{18}O$-labeled G$_{79}$ in one of the two monomers and the $^{13}C{=}^{16}O$-labeled G$_{79}$ in the other (see section 5.4 for a detailed discussion of how to extract such angle information from polarization-controlled experiments). The angle θ was estimated to be 103° from IR absorption spectroscopy and 110° from 2D IR spectroscopy, and thus, the helix crossing angle was determined to be 45°. These results were found to be consistent with NMR results on the same helix dimers.

Instead of membrane bound peptides, there was a report on a lipid bilayer itself.[354] In a native membrane, a lipid bilayer can have structural segregation and microdomain formation, which could affect recognition, molecular transport, and signal transduction of a cell.[355] In order to probe the molecular dynamics of a sphingomyelin/phospholipid binary membrane, 2D IR pump−probe spectroscopy was used—here the phospholipid used in this experiment was 1-palmitoyl-2-linoleyl phosphatidylcholine. Note that the sphingomyelin has a single amide group and that the phospholipid has two ester groups. Therefore, the amide I band from sphingomyelin and the ester C=O stretch band from phospholipid appear in two different frequency regions at around 1645 and 1730 cm^{-1}, respectively. In the experimentally measured 2D IR pump−probe spectra, off-diagonal cross peaks were observed, though they are fairly weak. By comparing model calculations of coupling constants with their estimated *J* values from experiments and from the cross peak intensity analysis, they concluded that the lipid bilayer has segregation of two components into phospholipid and sphingomyelin domains.

5.8. Nucleic Acids

Linear vibrational spectroscopy is a powerful tool for investigating structural fluctuations and transitions, hydrogen bonding interactions,[356−361] and global structures of nucleic acid (NA) bases, base pairs (BP),[362−365] and various NA's.[366−369] A collection of IR spectra of nucleic acids in solution was presented in a review article in ref 370. The effects of hydrogen bond-induced base pairing,[371−373] base stacking,[374,375] coordination of metal ions,[376,377] and solvation on NA structure were studied by examining marker band frequency shifts. Recently, the natures of delocalized normal

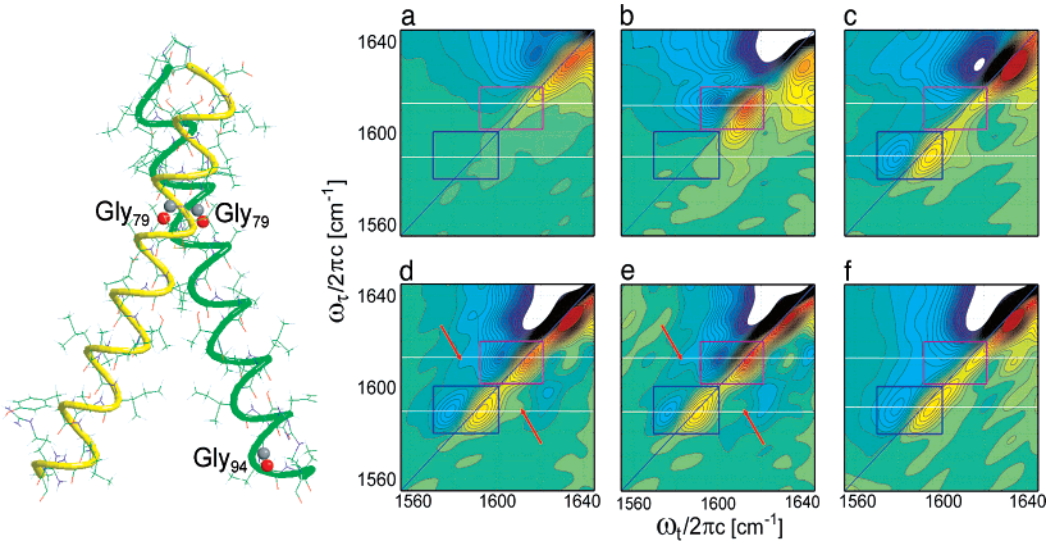

Figure 36. Structure of the Glycophorin A (GpA) transmembrane helix dimer.[352] The backbones of the two helical segments are yellow and green. The carbonyl atoms of the interfacial Gly_{79} positions and the control Gly_{94} position are represented as spheres. The 2D correlation spectra of GpA transmembrane homodimers G_{79} (a), $G_{79}(^{13}C{=}^{16}O)$ (b), and $G_{79}(^{13}C{=}^{18}O)$ (c); heterodimers $G_{79}(^{13}C{=}^{16}O) + G_{79}(^{13}C{=}^{18}O)$ (d) and $(G_{79}(^{13}C{=}^{16}O) + G_{79}(^{13}C{=}^{18}O)) - 0.25\ G_{79}(^{13}C{=}^{18}O)$ (e); and control sample $G_{94}(^{13}C{=}^{16}O) + G_{79}(^{13}C{=}^{18}O)$ (f) in 5% SDS. The $^{13}C{=}^{16}O$ and $^{13}C{=}^{18}O$ isotopomer diagonal regions are highlighted by rectangular boxes, and the arrows point to the cross peaks.[352] Reprinted with permission from Fang, C.; Senes, A.; Cristian, L.; DeGrado, W. F.; Hochstrasser, R. M. *Proc. Natl. Acad. Sci. U.S.A.* **2006**, *103*, 16740. Copyright 2006 National Academy of Sciences, U.S.A.

modes in base pairs and DNA oligomers have been theoretically described in terms of vibrational basis modes.[378−381] In comparison to many different spectroscopic methods, IR spectroscopy has a few notable advantages:[382] (1) the IR spectroscopic technique is a nondestructive method, (2) it has no limit on the size and molecular weight of DNA, and (3) various effects from ionic strength, pH, temperature, etc. on the DNA conformation can be easily monitored. However, yet another critical advantage of the IR spectroscopic method would be its capability of probing real time dynamics of fast processes involving DNA.

The four nucleic acid bases, i.e., guanine, cytosine, adenine, and thymine, have distinctively different vibrational modes and frequencies. As they form Watson−Crick base pairs, their IR spectra become quite different from the sum of corresponding base spectra. For example, it was observed that the guanine and cytosine carbonyl stretching mode frequencies in poly(dG):poly(dC) are shifted by 21 cm^{-1} and -2 cm^{-1}, respectively, when the poly(dG):poly(dC) spectrum is compared with those of poly(dG) and poly(dC) (see the references cited in ref 379). In the cases of the poly(dA), poly(dT), and poly(dA):poly(dT) spectra, the 1632 cm^{-1} thymine band in the poly(dT) spectrum is blue-shifted to 1641 cm^{-1} in the poly(dA):poly(dT) spectrum, while the 1626 cm^{-1} adenine band in the poly(dA) spectrum, on the contrary, is red-shifted down to 1622 cm^{-1} in the poly(dA):poly(dT) spectrum.[382,383] These notable changes of the IR absorption line shape when a DNA double helix is formed indicate that the vibrational degrees of freedom become mixed through the Watson−Crick hydrogen-bonding and stacking interactions. An explanation that these vibrational shifts are induced by the transition dipole coupling in the poly(A):poly(U) was provided in ref 384.

In addition to the linear vibrational spectroscopic investigations, the heterodyne-detected 2D IR photon echo technique was recently used to elucidate the strengths of vibrational couplings and the nature of delocalized normal modes in a DNA double helix in heavy water.[385,386] In Figure 37 the IR absorption and 2D IR spectra of a dG_5C_5 duplex are shown.[385] The three 2D IR spectra in Figure 37b, c, and d are different from one another by beam polarization geometry, and they correspond to [0°, 0°, 0°, 0°], [0°, 90°, 90°, 0°], and [45°, −45°, 90°, 0°], respectively. The FT IR spectrum exhibits four different bands in the frequency range 1580−1720 cm^{-1}, and the corresponding diagonal peaks labeled as A−D are visible in the [0°, 0°, 0°, 0°] 2D spectrum in Figure 37b. In addition, cross peaks labeled as E−J are also observed, which indicates couplings between basis modes. By using the Frenkel exciton model and carrying out numerical simulations of both 1D and 2D IR spectra, the vibrational coupling constants and anharmonicities of guanine and cytosine C═O stretching vibrations were determined. The two strongly IR-active C═O stretching vibrations are responsible for the two IR absorption bands C and D in Figure 37a. From the fits to the linear and 2D IR spectra, the interstrand coupling between the guanine and cytosine C═O stretching modes was estimated to be −7.4 cm^{-1}, the intrastrand couplings between cytosine C═O stretching modes and between guanine C═O stretching modes was estimated to be 2.3 and 9.7 cm^{-1}, and the interstrand coupling between the guanine C═O stretching mode at the jth base pair and the cytosine C═O stretching mode at the $(j+1)$th base pair was estimated to be −5.0 cm^{-1}. The anharmonicities of the guanine and cytosine C═O stretching modes were found to be 14 and 9 cm^{-1}, respectively.

To elucidate the delocalized nature of vibrationally delocalized modes in various DNA double helices, extensive quantum chemistry calculation (B3LYP/6-31G*) studies of nucleic acid bases, base pairs, and base pair stacks in H_2O and D_2O were performed and reported in refs 378 and 379. Among various vibrational degrees of freedom, only the vibrational modes of which frequency is in the range from 1400 to 1800 cm^{-1} were considered in detail because they have been known to be highly sensitive to the Watson−Crick base pair formation, DNA structure, and melting process.

The structures of the deuterated base molecules and Watson−Crick base pairs are shown in Figure 38. The reason why the deuterated bases were considered is because the IR

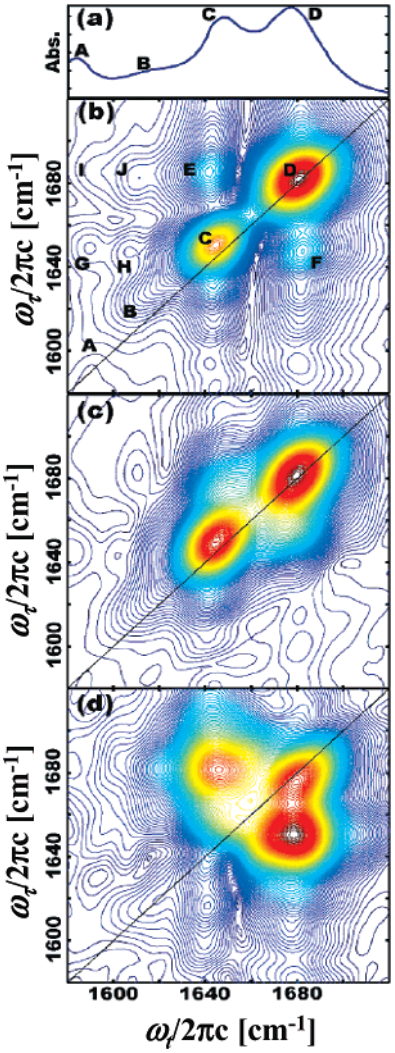

Figure 37. Normalized linear and heterodyned 2D-IR spectra of dG_5C_5:[385] (a) linear spectrum; (b) [0°,0°,0°,0°]; (c) [0°,90°,90°,0°]; and (d) [45°,−45°,90°,0°]. The spectra are normalized to their peak heights, and the contour lines are shown in 1% intervals. Peaks A−D are diagonal peaks, and peaks E−J are cross peaks. The diagonal peaks obscure most of the cross peaks below the diagonal. The relative intensities of the cross peaks in parts b and c depend on the angles between the transition dipoles. Only cross peaks appear in part d, because the polarization condition eliminates the diagonal peaks.

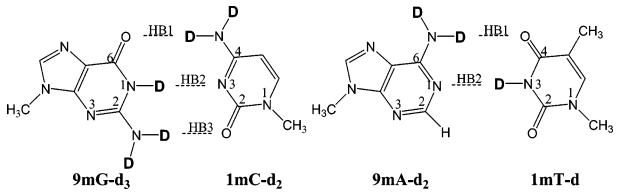

Figure 38. Molecular structures of Watson−Crick pairs of deuterated 9-methyl guanine (9mG-d_3), 1-methyl cytosine (1mC-d_2), 9-methyl adenine (9mA-d_2), and 1-methyl thymine (1mT-d).

spectra had to be recorded for the D_2O solution sample to avoid any spectral congestion by the water OH bend bands.

Here, the notation 9mG-d_3, for example, represents 9-methylguanine, which has three D atoms instead of amino H atoms.[379] To quantitatively describe vibrationally delocalized excited states, the LCBM-Exciton (linear combination of basis modes-exciton) theory discussed in section 4 was used. Basis modes and coupling constants were identified and calculated, respectively.

5.8.1. Guanine

In the case of 9mG-d_3, the G_s mode, which is mainly a combination of C═O stretch and N−D bending vibrations, and the G_r mode, which is the purine ring deformation vibration, are the two basis modes. Note that the dipole strengths of the G_s and G_r modes were found to be comparatively large.

5.8.2. Cytosine

The two basis modes for the deuterated cytosine, 1mC-d_2, are the C_s (C═O stretch + ND bending) and C_r (pyrimidine ring deformation) modes.

5.8.3. Adenine

The deuterated adenine, 9mA-d_2, has two purine ring deformation modes, denoted as A_{r1} and A_{r2}.

5.8.4. Thymine

In the case of the thymine, 1mT-d, the two C═O stretching modes, denoted as T_{2s} and T_{4s}, are the basis modes chosen. Although there is a pyrimidine ring deformation mode denoted as T_r, its dipole strength is relatively small.

The next step toward understanding the vibrationally delocalized excited states of DNA was to consider two Watson−Crick base pairs.

5.8.5. GC Base Pair

Due to the coupling between the two C═O stretching vibrations of deuterated G and C bases, there are two normal modes denoted as $G_sC_s(-)$ and $G_sC_s(+)$, which are asymmetric and symmetric C═O stretches. From the DFT calculation, it was found that the vibrational coupling constant between the basis G_s and C_s modes, denoted as $J(G_sC_s)$, is about -10.5 cm^{-1}. In refs 385 and 387, the $|J(G_sC_s)|$ and $J(G_sC_s)$ values were experimentally estimated to be 15 cm^{-1} and -7.4 cm^{-1} by using an isotope-labeling technique and by fitting to the measured 2D IR spectrum of the dG_5C_5 duplex, respectively. All the other vibrational coupling constants between the basis modes of G and C bases were presented in ref 379. It was found that the ring deformation normal modes are relatively localized on each base due to the frequency mismatch of the two basis modes, i.e., G_r and C_r, even though the corresponding coupling constants are sizable. In addition, the ring deformation basis modes are weakly coupled to the base C═O stretch basis modes.

5.8.6. AT Base Pair

The thymine base, 1mT-d, has two C═O stretch basis modes, whereas the adenine, 9mA-d_2, has two ring deformation basis modes. For the AT base pair, we found the two normal modes denoted as AT_{2s} and AT_{4s}, which are largely thymine C═O stretch modes, are relatively localized on the C═O group in the thymine base even for the AT base pair, despite the fact that the vibrational coupling constants of these C═O stretch basis modes, T_{2s} and T_{4s}, with adenine ring deformation modes are sizable, e.g., $J(A_{r1}T_{4s}) = -10.7$ cm^{-1} and $J(A_{r2}T_{4s}) = -6.9$ cm^{-1}.[379] Similarly, the two low frequency normal modes denoted as $A_{r1}T$ and $A_{r2}T$, respectively, are localized on the deuterated adenine base and the eigenvectors are close to those of A_{r1} and A_{r2}.

5.8.7. Hydration Effects

The basis mode frequencies and vibrational coupling constants of deuterated base pairs are essential ingredients

in the numerical simulations of the IR absorption and 2D IR PE spectra of DNA oligomers. However, in a real DNA solution, the DNA base pairs are solvated by surrounding water molecules so that it was necessary to carry out an additional set of quantum chemistry calculations of deuterated base pairs with five D_2O molecules.[379,388] It was found that the $G_sC_s(-)$ mode becomes further red-shifted by 26 cm^{-1} due to the hydrogen-bonding interactions with two D_2O molecules and the $G_sC_s(+)$ mode is red-shifted by 28 cm^{-1} by hydration. In addition, the IR intensities and absolute magnitude of transition dipoles significantly increase. In contrast to the C═O stretch normal modes, the ring deformation G_sC_r and G_rC_s mode frequencies decrease and increase, respectively, when the GC base pair is hydrated. It turned out that the origin of the frequency shifts and intensity changes induced by hydration is partly from the changes of basis mode transition dipole vectors. In the case of the AT base pair, the two thymine C═O stretching normal modes, AT_{2s} and AT_{4s}, become red-shifted, whereas the $A_{r1}T$ and $A_{r2}T$ modes are blue- and red-shifted when the deuterated AT base pair is hydrated. A notable change is that the dipole strength of the T_r mode significantly increases upon hydration of the AT base pair.

5.8.8. Interlayer Vibrational Couplings

Although the most important vibrational interactions between different basis modes are associated with the Watson−Crick base pairing, to quantitatively describe delocalized vibrationally excited states of multiple layer base pairs, one should properly take into consideration both the interlayer and interstrand base−base vibrational couplings too. The DFT calculation results were reported in ref 379.

5.8.9. Vibrational Anharmonicities

To calculate the overtone anharmonicities of basis modes, DFT calculations with the finite difference method were performed.[380] The overtone anharmonic frequency shifts of the guanine and cytosine C═O stretching modes of 9mG-d_3 and 1mC-d_2 were found to be about 17 and 16 cm^{-1}, respectively. This is in good agreement with the experimentally determined value of 14 cm^{-1} in ref 385. The other two C═O stretching modes, T_{2s} and T_{4s}, of 1mT-d have anharmonic frequency shifts of 13 and 18.4 cm^{-1}, respectively. Those of the ring deformation modes vary from 0.8 to 13 cm^{-1}. These anharmonic frequency shift values were needed in constructing the doubly excited state Hamiltonian matrix (see eq 4-2).

A few different sets of parameters for basis mode frequencies and coupling constants that constitute the Frenkel exciton Hamiltonian matrix were proposed and tested (see ref 380 for detailed discussions and computational methods). The diagonal Hamiltonian matrix elements (basis mode frequencies) and the coupling constants between basis modes in a given base pair were obtained from the hydrated Watson−Crick base pairs. All other inter- and intralayer coupling constants were extracted from the *ab initio* vibrational analyses of triple- or quadruple-layer GC and AT pairs. Once all these parameters are determined, it is then ready to numerically calculate the linear and nonlinear vibrational spectra of double helical DNA.

However, it should be noted that the DNA double-helix is polymorphic and its structure depends on a number of different parameters such as base composition, water content, pH, counterions, etc. The three main antiparallel double-

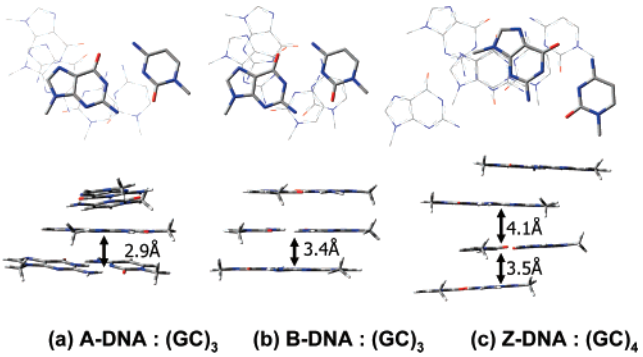

Figure 39. Structures of A-, B-, and Z-DNA's: $A(GC)_3$, $B(GC)_3$, and $Z(GC)_4$.

stranded helical geometries of DNA are the right-handed A- and B-forms and the left-handed Z-form.[389] In Figure 39, the three geometry optimized structures of DNA oligomers considered for the theoretical study in ref 381 are shown, where the interlayer distance, twist angle between two neighboring base pairs, and other geometric parameters were fixed to mimic the A-, B-, and Z-forms. Although the interlayer distances in the A- and B-form DNAs are constant throughout the DNA helices, the Z-form DNA has two different, alternating interlayer distances. Furthermore, the Z-form DNA is a left-handed double helix. The geometry-optimized structures were found to be consistent with previous quantum chemistry calculations results.[390−396]

With quantum chemistry calculation results for the three oligomers in Figure 39 and various parameters determined as outlined above, both 1D and 2D IR spectra of $X(GC)_n$ and $X(AT)_n$ (for X = A, B, or Z) were numerically simulated to find characteristic features of these three different DNA structures (see Figure 40).[381]

The IR spectrum of the $A(GC)_{10}$ was found to be similar to that of $B(GC)_{10}$, whereas the spectrum of $Z(GC)_{12}$ is different from the other two spectra. First of all, the peak frequency of the $G_sC_s(-)$ band, which corresponds to the highest frequency carbonyl stretch normal modes in the frequency range from 1400 to 1700 cm^{-1}, is strongly dependent on the DNA form. More specifically, the $G_sC_s(-)$ band frequency shows a trend: $A(GC)_{10} > B(GC)_{10} > Z(GC)_{12}$. This blue-shifting behavior of the $G_sC_s(-)$ mode frequency as the DNA conformation changes from Z to B to A appeared to be related to the intrastrand coupling constants between C═O stretching modes in the upper and lower guanines, which were estimated to be 17.41, 8.17, and 1.03 cm^{-1} for A-, B-, and Z-form DNAs. Another notable marker band was found to be the G_sC_r band, which appears at 1630, 1623, and 1622 cm^{-1} for $A(GC)_{10}$, $B(GC)_{10}$, and $Z(GC)_{12}$, respectively. Although its peak frequency does not exhibit a strong dependency on the DNA form, its band intensity is quite large when the $(GC)_n$ oligomer adopts the Z-form. This is mainly because the transition dipoles associated with the C_r basis modes in the $Z(GC)_{12}$ are properly oriented to make the transition dipole of the delocalized G_sC_r normal mode large.

The highest frequency band in the $X(AT)_n$ (for X = A, B, or Z) IR spectra in the frequency range from 1550 to 1750 cm^{-1} was assigned to the AT_{2s} mode, which is relatively localized on the T_{2s} basis mode. Its peak frequency at about 1700 cm^{-1} does not depend on the DNA form, which is because the intrastrand vibrational coupling constant between two different T_{2s} modes is fairly small for all A-, B-, and

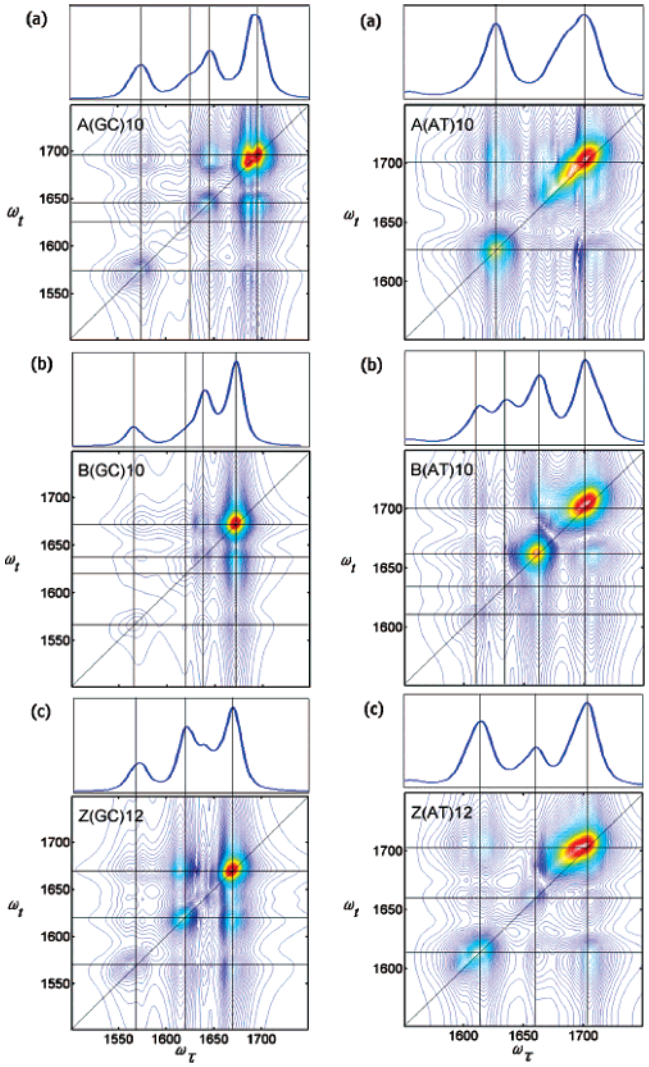

Figure 40. Simulated IR absorption spectra and 2D IR (magnitude) photon echo spectra (left column) of $A(GC)_{10}$, $B(GC)_{10}$, and $Z(GC)_{12}$. Simulated IR absorption spectra and 2D IR (magnitude) photon echo spectra (right column) of $A(AT)_{10}$, $B(AT)_{10}$, and $Z(AT)_{12}$.[381]

Z-DNAs. The overall spectrum however was found to be strongly dependent on the DNA structure because the other lower frequency band positions and intensities change much as the DNA structure changes.

In Figure 40, the numerically calculated 2D IR photon echo *magnitude* spectra of $X(GC)_{10}$ and $X(AT)_{10}$ are plotted. In addition to the diagonal peaks that are directly corresponding to the peaks in the IR spectrum, one can find distinctive cross peaks revealing vibrational couplings among the constituent basis modes. The 2D IR spectrum of $B(GC)_{10}$ is quite similar to that of $A(GC)_{10}$, which could be inferred from the comparison between the two IR absorption spectra also. In contrast, the 2D IR spectrum of $Z(GC)_{12}$ is distinctively different from those of $A(GC)_{10}$ and $B(GC)_{10}$, mainly because the intensity of the G_sC_r band of $Z(GC)_{12}$ is comparatively large. Consequently, it was suggested that any structural transition from B- to Z-form DNAs could be monitored by examining the 2D IR spectrum changes in the frequency range from 1600 to 1700 cm^{-1}, such as frequency shifts of the diagonal peaks and intensity changes of cross peaks. Next, the three 2D IR spectra of $A(AT)_{10}$, $B(AT)_{10}$, and $Z(AT)_{12}$ are shown in Figure 40 (see the three figures in the right column). Again there is a strong dependency of the 2D IR spectrum of the AT-rich DNA double helix on its conformation, as evident in the numerically simulated spectra.

5.9. Hydrogen-Bonding Dynamics and Chemical Exchange

Solvents play a critical role in chemistry and biology by actively participating in solvation and energy dissipation and by controlling thermodynamic and kinetic properties of reactions.[397] Among many different solute−solvent interactions, hydrogen-bonding is crucial and thus formed solute−solvent complexes can be constantly forming and breaking under thermal equilibrium conditions on very short time scales.[398] In such a case of an ultrafast dynamical equilibrium process between two or multiple chemical species, ultrafast laser spectroscopies have offered a means of probing rapid dynamics and chemical evolutions.[399] Particularly, chemical exchange processes in dynamical equilibrium have been studied by using 1D and 2D NMR methods for determining associated rate constants.[1] Only recently, a few applications of 2D IR spectroscopy to directly probe hydrogen-bonding and van der Waals complexation dynamics in condensed phases, where the formation and dissociation time scales are on the order of picoseconds, have been reported.

5.9.1. NMA–Methanol Solution (Chemical Exchange 1)

Time-resolved 2D IR pump−probe spectroscopy of the hydrogen-bond chemical exchange dynamics of an NMA in methanol solution was investigated and reported in ref 12. The 2D IR spectra of NMA in MeOD at waiting times of 750 fs and 4.5 ps are shown in Figure 41 (see the upper-right panel). Later, a heterodyne-detected 2D IR photon echo study on the same solution was performed (see Figure 41 (middle panel)). The amide I IR band of NMA in MeOD, which is also shown in Figure 13, appears as a doublet. This already indicates that there exist two NMA−MeOD complexes having distinctively different solvation environments.

One of the most important observations made in these 2D IR experiments is that the amplitudes of cross peaks increase as the waiting time increases. To elucidate the underlying physics and NMA−methanol hydrogen-bonding dynamics, molecular dynamics simulation studies were carried out, where the NMA amide I frequency fluctuation and shift were theoretically taken into account by using the electrostatic potential model outlined in section 5.3.[13,400] It turned out that the low-frequency amide I band is associated with the NMA with two hydrogen-bonded methanol molecules at the carbonyl group, whereas the high-frequency band is associated with that having just one hydrogen-bonded methanol molecule. The former species was denoted as NM_2 and the latter as NM_1. Note that a single hydrogen-bond with a C=O oxygen atom can induce a frequency red-shift of the amide I mode by about 20 cm^{-1}. The two species are in an equilibrium state due to constant forming and breaking of hydrogen-bonds between NMA and MeOD.

This is a good example of a dynamic inhomogeneous system discussed in section 4.5. Here, the average amide I mode frequencies of the two species are representative inhomogeneity parameters ϵ_j and time-dependent populations obey simple kinetics. Following the argument in section 4.5 and from detailed theoretical discussion in refs 13 and 400 it is clear that the time-dependent cross peak amplitude at ($\omega_\tau = \omega_1$, $\omega_t = \omega_2$) is linearly proportional to the conditional probability function $G_{21}(T)$. In Figure 42, the numerically

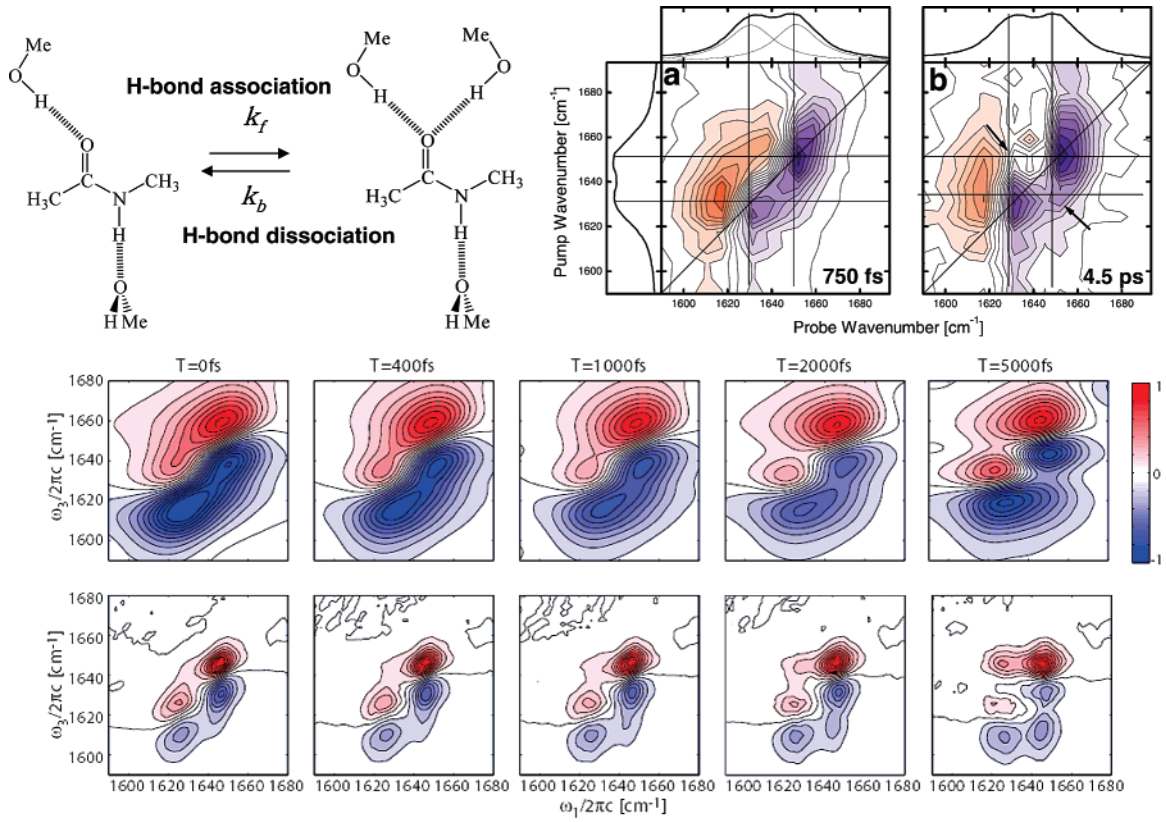

Figure 41. Two species different from each other by the number of hydrogen-bonded methanol molecules at the C═O oxygen atom. The hydrogen bond formation and dissociation rate constants are denoted as k_f and k_b, respectively. The 2D IR pump−probe spectra at waiting time T = 750 fs and 4.5 ps are shown in the upper-right panel.[12] The 2D IR photon echo spectra at T = 0, 400, 1000, 2000, and 5000 fs are shown in the middle, and the simulated spectra are at the bottom.[199] As the waiting time increases, the cross peak amplitude increases. This indicates the chemical exchange processes between the two species. Reprinted with permission from Woutersen, S.; Mu, Y.; Stock, G.; Hamm, P. Hydrogen-bond lifetime measured by time-resolved 2D-IR spectroscopy. N-methylacetamide in methanol. *Chem. Phys.* **2001**, *266*, 137. Copyright 2001 Elsevier.

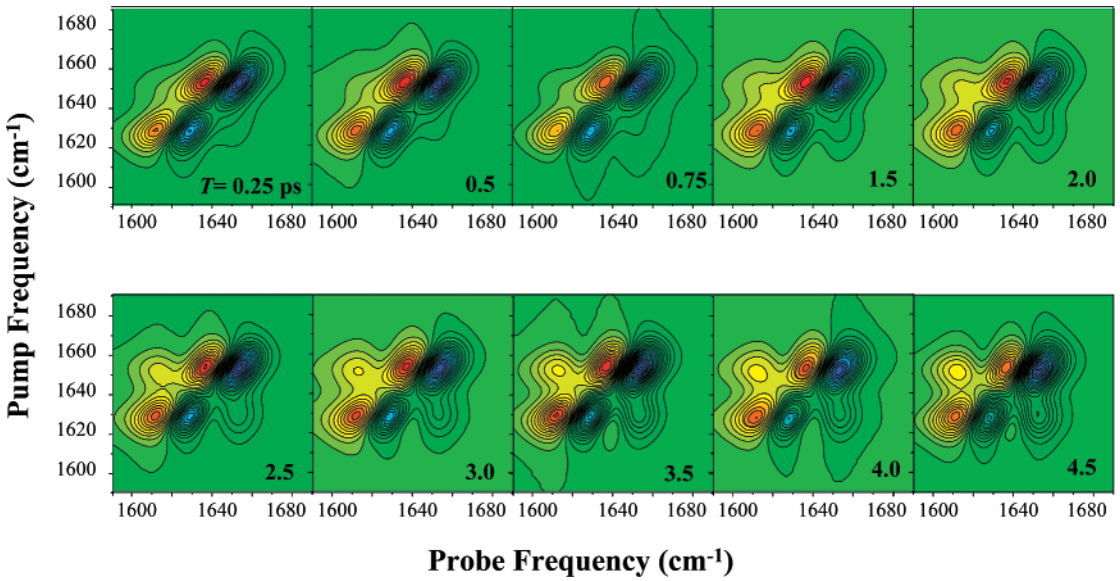

Figure 42. Simulated 2D IR pump−probe spectra of the amide I vibration in NMA/MeOD solution. The electrostatic potential model for calculating the instantaneous amide I frequency of the NMA in MeOD was used to obtain the fluctuating amide I frequency trajectories.[13,400]

simulated 2D IR pump−probe spectra of the NMA−MeOD solution as a function of waiting time T, where the two-spieces model was used, are shown.[13] The cross peak in the upper off-diagonal region is related to the hydrogen-bond making ($NM_1 \rightarrow NM_2$) process, whereas that in the lower off-diagonal region is associated with the hydrogen-bond breaking ($NM_2 \rightarrow NM_1$) process. This does not mean that the rising rate constants of the two cross peak amplitudes are the hydrogen-bond making and breaking rate constants (see ref 13 for detailed discussion).

Then, from the equilibrium constant and relaxation rate constant (sum of the two rate constants of the hydrogen-bond making and breaking processes), one can determine the two rate constants separately. As demonstrated in ref 400,

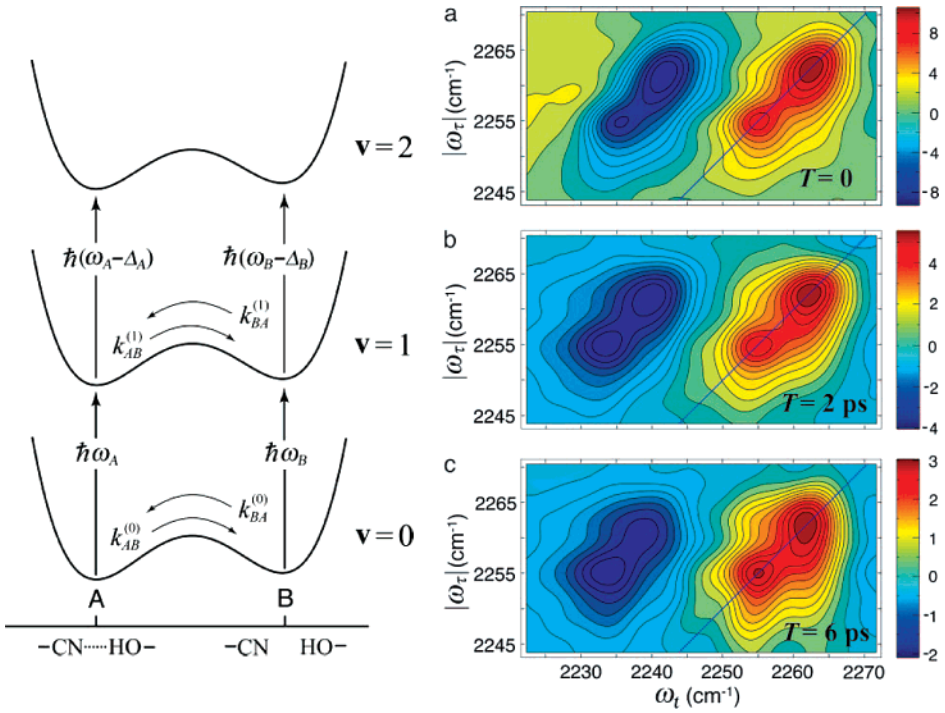

Figure 43. Schematic representation of the free energy along a low-frequency hydrogen-bond coordinate for the CN stretch mode in its $v = 0$, $v = 1$, and $v = 2$ states (left). The real part of the purely absorptive 2D IR spectrum of CH_3CN in MeOD at various waiting times, T, at −17 °C. (a) $T = 0$; (b) $T = 2$ ps; (c) $T = 6$ ps.[15] As the waiting time T increases, the cross peak amplitude increases. This is clear evidence for chemical exchange processes between two different solvation species. Reprinted with permission from Kim, Y. S.; Hochstrasser, R. M. *Proc. Natl. Acad. Sci. U.S.A.* **2005**, *102*, 11185. Copyright 2005 National Academy of Sciences, U.S.A

one can extract thermodynamic properties such as hydrogen-bond formation and dissociation reaction enthalpies and entropies by carrying out the chemical exchange 2D IR spectroscopic studies for varying temperature.

5.9.2. Acetonitrile–Methanol Solution (Chemical Exchange 2)

As shown in ref 15, the FT IR absorption spectrum of the CN stretch in a $CH_3CN-MeOH$ solution appears as a doublet at low temperature, −17 °C, where the frequency splitting is about 8 cm^{-1}. Similar to the case of a NMA−MeOD solution, the high- and low-frequency peaks were assigned to the CH_3CN molecules with one and zero hydrogen-bonded methanol, respectively. Note that the σ-bonding interaction between a CN nitrogen atom and a H−O−Me hydrogen atom induces a frequency blue-shift in this case. In Figure 43, the real parts of the purely absorptive 2D IR spectra at waiting time $T = 0$, 2, and 6 ps are shown. Due to a large anharmonicity of ∼19 cm^{-1}, the positive peaks associated with ground-state bleaching and stimulated emission between $v = 0$ and $v = 1$ are well separated from the negative peaks associated with excited-state absorption from $v = 1$ to $v = 2$. Again, the cross peak amplitude increases as T increases, which reflects the hydrogen-bond making and breaking processes. The T-dependent changes of cross peak amplitudes were successfully interpreted in terms of conditional probabilities.

An interesting point made in ref 15 is that, unlike NMR, the $v = 0 \rightarrow v = 1$ transitions are separately displayed from the $v = 1 \rightarrow v = 2$ transitions. Consequently, the hydrogen-bonding dynamics of the ground and first excited states of the CN group can be investigated separately. Note that the solute−solvent interaction strength can be dependent on the quantum states of a given oscillator, CN stretch (see the left panel in Figure 43). The chemical exchange rate constants for the ground-state molecular system were denoted as $k_{AB}^{(0)}$ and $k_{BA}^{(0)}$, where A and B are the two different species with one and zero hydrogen-bonded methanol, respectively. Those for the first excited-state are denoted as $k_{AB}^{(1)}$ and $k_{BA}^{(1)}$. The hydrogen-bond dissociation rate constants $k_{AB}^{(0)}$ and $k_{AB}^{(1)}$ at 22 °C were estimated to be 1.07×10^{10} s^{-1} and 1.27×10^{11} s^{-1}, respectively. The hydrogen-bond formation rate constants could be estimated by using these quantities and equilibrium rate constants.[15]

5.9.3. MeOD Oligomers in CCl_4

Hydrogen bonding in alcohol liquids and water is crucial in network formation so that a great deal of experimental and theoretical studies have been carried out to elucidate their important roles in chemical and biological systems.[18,201,202,207,210,401−432] In particular, 2D IR spectroscopy was applied to the study of 10% MeOD oligomers in CCl_4 to study hydrogen-bond breaking and making processes.[401]

From the FT IR spectrum of the OD stretch band, three components were identified and they were denoted as δ, γ, and β. δ represents OD that is both a hydrogen bond donor and acceptor. γ-OD is a hydrogen bond donor but not an acceptor. β-OD is a hydrogen bond acceptor. These three components (or species) have distinctively different center frequencies, and furthermore, they are in a dynamical equilibrium state due to constant forming and breaking of hydrogen bonds. Therefore, the time evolution of the hydroxyl stretch spectrum reflects the population dynamics of the hydrogen bonds in such a composite system. Consequently, the time-dependent change of the 2D IR spectrum as a function of waiting time T could reveal a detailed kinetic network of these constituent species, when proper fitting and numerical simulation methods are used.[401] In Figure 44 (see the right panel), four snapshot 2D IR correlation spectra at

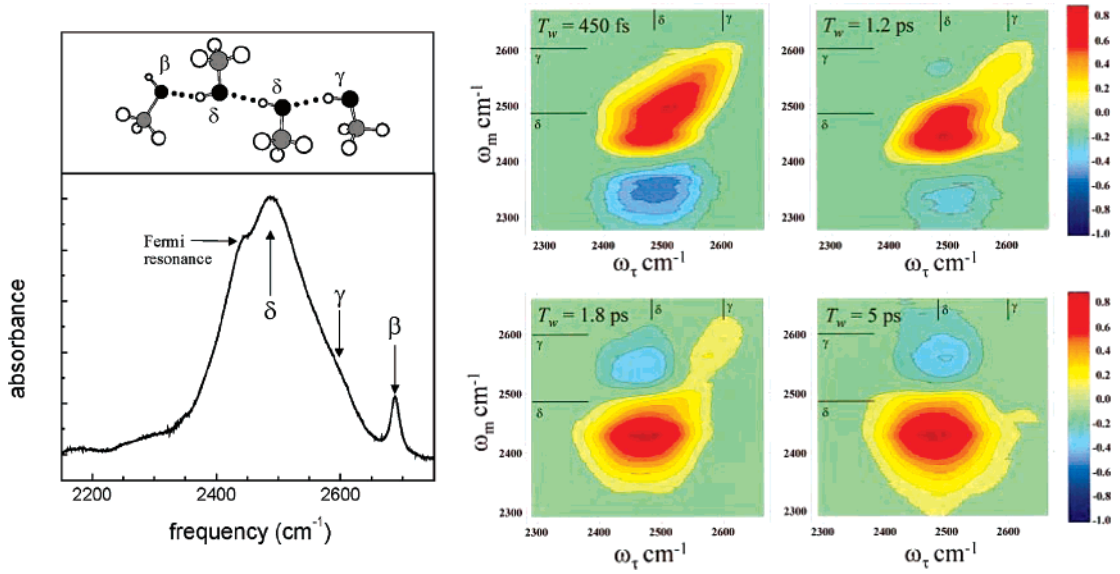

Figure 44. (Left) The linear absorption spectrum of a 10% solution of methanol-OD in CCl_4. β's are hydroxyls that are acceptors but not donors. γ's are donors but not acceptors. δ's are both donors and acceptors. These are illustrated schematically at the top of the figure. The shoulder on the red side of the IR absorption spectrum is a Fermi resonance with the overtone of the methyl rocking mode. This feature is absent in fully deuterated methanol. (Right) Contour plots of the correlation spectra for waiting time $T = 450$ fs, 1.2 ps, 1.8 ps, and 5 ps.[401] As T increases, the off-diagonal negative going 1−2 band (blue) decays, the main band on the diagonal changes shape by collapsing to the red and shifts somewhat off the diagonal, and a new off-diagonal negative going peak appears. Reprinted with permission from Asbury, J. B.; Steinel, T.; Stromberg, C.; Gaffney, K. J.; Piletic, I. R.; Fayer, M. D. *J. Chem. Phys.* **2003**, *119*, 12981. Copyright 2003 American Institute of Physics.

$T = 450$ fs, 1.2 ps, 1.8 ps, and 5 ps are shown. The 2D spectrum at $T = 450$ fs shows a diagonally elongated positive peak that is associated with the 0−1 transition of the δ and γ bands. The negative peak in that spectrum corresponds to the 1−2 transition of the δ band. From the comparisons of the two 2D spectra at $T = 450$ fs and 1.2 ps, it was found that the negative peak intensity decreases as T increases from 450 fs to 1.2 ps. This indicates the population relaxation of the excited state. Since the lifetimes of the δ and γ components are different, the diagonal γ peak on the blue side of the 2D IR spectrum at $T = 1.2$ ps is pronounced. The echo signal was observed for even long times compared to the vibrational lifetime (~500 fs), which indicates the breaking of hydrogen bonds. An interesting time-dependent feature of 2D IR spectra with respect to T can be seen by comparing two 2D IR spectra at $T = 1.2$ and 1.8 ps. The positive δ band at $T = 1.2$ ps shifts downward and appears in the lower diagonal region. This is clear evidence of hydrogen bond breaking (transitions of δ species to other species). Directly comparing model calculation results with the experimental 2D spectra, it was concluded that initially strongly hydrogen-bonded (red side of δ band) δ species selectively break hydrogen bonds following vibrational energy relaxation. This work showed the advantages of the 2D IR spectroscopic technique in elucidating the detailed mechanism of hydrogen bond breaking in MeOD oligomers in a nonpolar solvent.

5.9.4. Liquid Water

The three-dimensional network structure formed by hydrogen bonds in water is random and constantly fluctuating in time.[433−436] The IR spectrum of the OH stretching vibration is one of the most direct probes of the dynamics of the water molecular network.[215,222,406,415,437−442] As already mentioned in this paper (see section 5.3), 2D IR spectroscopic investigations of the OH stretch in D_2O and the OD stretch in H_2O to understand the local hydrogen-bonding dynamics around the energetically isolated oscillator OH or OD stretching vibration were reported. However, it was difficult to perform a 2D IR study of pure liquid water due to the high optical density of the OH stretching mode in pure water. Using a specially designed ultrathin (500 nm) sample cell, it became possible to record the time-dependent 2D IR spectra of liquid water.[17] From the spectrally resolved transient grating signal with respect to waiting time T, it was found that the $v = 1 \rightarrow v = 2$ transition frequency is blue-shifted and the $v = 0 \rightarrow v = 1$ transition frequency is red-shifted on a 50 fs time scale. Other reorientation and energy transfer processes occur in the subpicosecond to picosecond time domain. The ultrafast component was attributed to the ultrafast loss of memory induced by fast librational (hindered rotational) motions instead of structural dynamics related to O−H··· hydrogen bond.

Clear evidence of such an ultrafast memory loss in the hydrogen bond network of liquid water was found in the spectral evolution of absorptive 2D IR spectrum with respect to the waiting time (see Figure 45).[17] At $T = 0$ fs, the positive and negative peaks that are associated with the $v = 0 \rightarrow v = 1$ transitions and the $v = 1 \rightarrow v = 2$ transitions were observed. Also, the diagonal peak is elongated along the diagonal, indicating sizable inhomogeneous broadening. At $T = 50$ fs, this inhomogeneity almost completely vanished. This shows that the structural variations reflected in the OH stretch frequency distribution disappear by extremely fast processes on a 50 fs time scale.

5.10. Solute–Solvent Complexation and Microsolvation

One of the fundamentally important issues in chemistry is the nature of organic solutes in condensed phases. The homogeneous dielectric continuum concept for solvent is a simple but quite often unrealistic approach to the description of solvent roles in chemical reaction dynamics. In simple

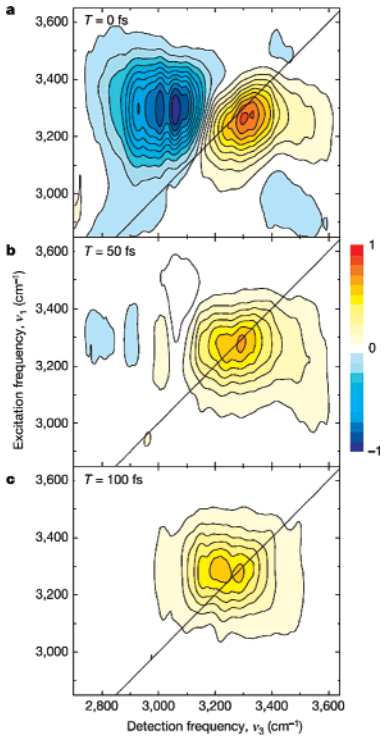

Figure 45. Absorptive components of the 2D-IR spectra of pure liquid H_2O for different waiting times.[17] (a) $T = 0$ fs; (b) $T = 50$ fs; (c) $T = 100$ fs. The inhomogeneity indicated by the stretching of the positive peak along the diagonal in the $T = 0$ spectrum has almost completely decayed by $T = 50$ fs, clearly showing the very rapid dephasing and loss of memory in the system. Reprinted by permission from Macmillan Publishers Ltd: [*Nature*] ref 17, copyright 2005.

liquids, due to the isotropic and spherically symmetric properties of intermolecular interactions, the radial distribution function can provide detailed information on the local solvation structure, thermodynamic properties, and diffusive dynamics around a solute molecule.[443,444] Unlike simple liquids, intermolecular interactions between typical organic solutes and solvents are anisotropic and their strengths can be comparable or even larger than their thermal energy. Consequently, solute−solvent complexes can exist for finite times and their dynamical behaviors are important in understanding chemical reactions involving such molecules.

Recent experimental and theoretical 2D vibrational spectroscopic studies on a phenol−benzene−CCl_4 solution showed how such phenomena can be investigated and what quantitative information can be extracted from experimental data.[14,16,36,82,445] Phenol molecule has been known to form a complex with a benzene molecule. Therefore, by using a mixed solvent, benzene + CCl_4, it was possible to generate a 50−50 mixture of phenol complex and free form, where free phenol represents the case when phenol does not form a van der Waals complex configuration with benzene. The IR spectrum of the OD stretch of phenol-D in the mixed solvent is shown in Figure 46a, which clearly exhibits two peaks that can be assigned to complex and free phenol species. The phenol complex has a lower frequency OD stretch mode. By carrying out quite extensive quantum chemistry calculations for a phenol−benzene heterodimer, it was found that the most stable complex is the T-form structure.[16] Furthermore, the electron correlation effects on the intermolecular interaction are very important so that Hartree−Fock or density functional theory cannot provide a quantitatively reliable potential energy surface in this case.

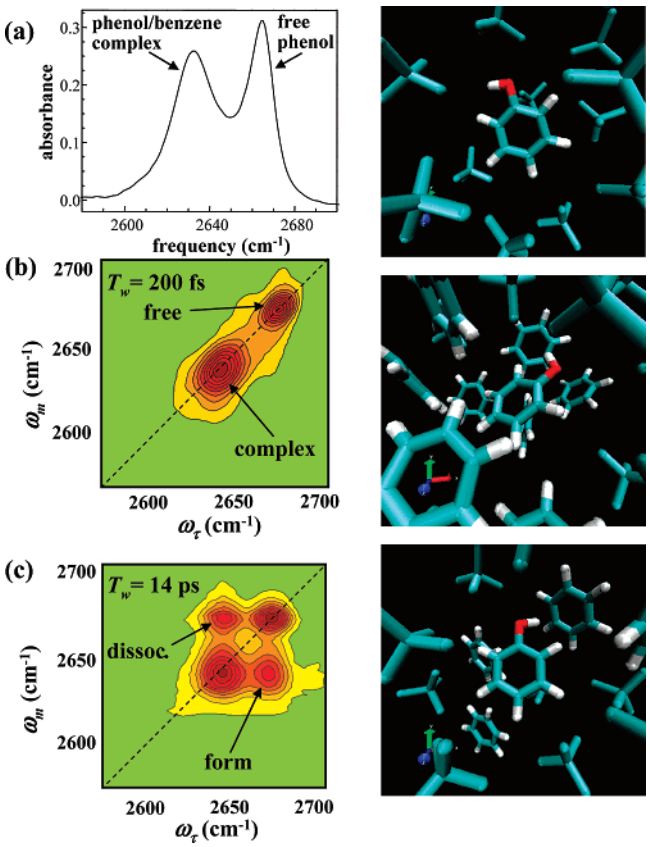

Figure 46. (a) FTIR spectra of the OD hydroxyl stretch of phenol for the phenol−benzene complex and free phenol in the benzene/CCl_4 mixed solvent. (b) 2D vibrational echo spectrum at a time (200 fs) short compared to complex formation and dissociation showing two peaks on the diagonal. (c) 2D vibrational echo spectrum at a time (14 ps) long compared to complex formation and dissociation showing two peaks on the diagonal and two additional off-diagonal cross peaks. The off-diagonal peaks grow in as complex formation and dissociation proceed. Representative configurations extracted from the simulations are shown in the right column. Top panel: free phenol surrounded by CCl_4 molecules. Middle panel: phenol−benzene complex surrounded mainly by benzene molecules. Bottom panel: phenol−benzene complex surrounded by a mix of benzene and CCl_4 molecules. See ref 16.

Now, similar to the cases mentioned in the previous subsection, these two species are in an equilibrium state so that the time-dependent 2D IR spectra would reveal the underlying chemical exchange processes through the cross peak intensity changes (compare the two 2D IR spectra at T =200 fs and at T =14 ps in Figure 46). The integrated volumes of the two diagonal peaks and the two cross peaks were calculated with respect to the waiting time, which were successfully used to determine the complex formation and dissociation rate constants. More specifically, the experimentally estimated complex dissociation time was found to be 8 ps. To numerically simulate the 1D and 2D IR spectra, the vibrational Stark effect theory, which was discussed in section 5.3, was used to obtain the OD frequency trajectory from MD simulation results.[16] In addition, the transition dipole of the OD stretch was also found to be strongly dependent on the electric field along the OD bond, indicating that the non-Condon effect should not be ignored. The comparisons between theory and experiment were found to be excellent. However, the more important conclusion drawn from the comparative investigation was that the 2D IR spectroscopy of such a complex system can provide detailed information on the local solvation environment and micro-

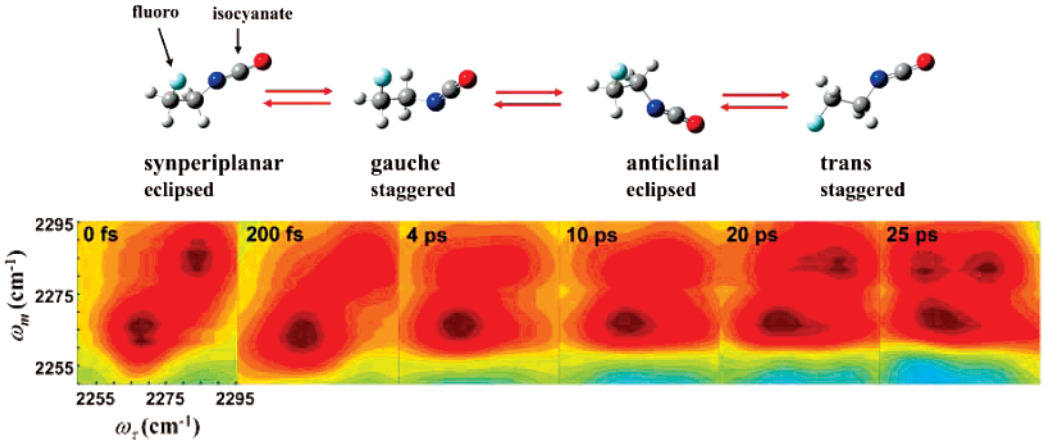

Figure 47. Calculated structures for two eclipsed conformations (anticlinal and synperiplanar) and two staggered conformations (gauche and trans (or anti)) of 1-fluoro-2-isocyanatoethane. 2D IR spectra of 1-fluoro-2-isocyanatoethane in a CCl_4 solution at room temperature.[81] The data have been normalized to the largest peak at each waiting time. Each contour is a 10% change. The red contours are positive-trending, and the blue contours are negative-trending. At short times, only two diagonal red peaks appear, representing the gauche (lower frequency) and trans (higher frequency) conformers. At long times, isomerization causes two additional red peaks on the off-diagonal to grow in. The peak at the upper left is larger than the peak at the lower right, because the lower right peak overlaps with a negative-trending peak. From Zheng, J. R.; Kwak, K.; Xie, J.; Fayer, M. D. *Science* **2006**, *313*, 1951. Reprinted with permission from AAAS.

solvation domain formation. Direct evidence of the heterogeneity of the solvation environment around a phenol was obtained by examining configurations from the MD trajectories (see the three figures on the right-hand side of Figure 46). The top configuration is the case when the phenol is completely surrounded by CCl_4 molecules, whereas in the second one it is surrounded by benzene molecules only. The third one shows a phenol−benzene complex dimer with CCl_4 and benzene molecules around it. Consequently, a plausible picture of the dynamical process revealed by this 2D spectroscopy is that the phenol solute undergoes random jumps from one microsolvation domain to the other, which are reflected by OD stretch frequency changes.[16,80] By counting the numbers of benzene and CCl_4 molecules in the vicinity of the phenol, the local number fraction of benzene molecules was found to be quite different from the mole fraction of the bulk benzene−CCl_4 mixed solvent. More specifically, there are significant probabilities of finding a phenol surrounded either completely by benzene or completely by CCl_4. This suggests that the mixed solvent forms microscopic domains at the molecular level.[16] Furthermore, it was shown that the OD stretch frequency−frequency correlation function is directly related to the correlation function of the fluctuating number of benzene molecules in the immediate vicinity of the solute phenol.

5.11. Internal Rotation

Rotational isomerization around a chemical bond is an important process in the chemical reaction dynamics and reactivity and biological activity of proteins and biomolecules. One of the simplest model systems is ethane, which is a textbook example molecule on isomerization through internal rotation. However, due to the rotational symmetry, ethane could not be used for 2D vibrational spectroscopic investigation. Instead, a 1,2-disubstituted ethane derivative, 1-fluoro-2-isocyanatoethane (FICE), was chosen for the first 2D IR spectroscopic study of its rotational isomerization reaction in solution.[35,81]

Since the FICE contains two different substituents, there are four isomers, as can be seen in Figure 47. The FT IR spectrum of the isocyanate (−NCO) group in a FICE−CCl_4 solution shows two peaks at 2265 and 2280 cm^{-1} that correspond to the NCO stretching vibrations of the gauche and trans conformers. Since these two conformers are in an equilibrium state due to internal rotations, time-resolved 2D IR spectra were directly used to estimate the internal rotation time constants. The integrated volumes of diagonal and cross peaks were used to extract kinetic constants, and the isomerization time constant was found to be 43 ps.[81] Then, by carrying out density function theory calculations of the barrier heights of FICE, *n*-butane, and ethane, it was even possible to estimate the isomerization time constants of *n*-butane and ethane under the same conditions, which are about 40 and 12 ps, respectively.

5.12. Protein Folding and Unfolding: Transient 2D IR Spectroscopy

Protein folding, a conformational change of proteins as they fold from an ensemble of disordered denatured structures to a compact native structure, has been an important experimental and theoretical research subject. Protein folding or unfolding experiments using a variety of spectroscopic means aimed at measuring kinetics such as rate constants of increasing or decreasing spectroscopic signatures directly reflecting protein's structure. From the beginning of the new development of the 2D vibrational spectroscopic technique, the study of protein folding with this novel method has been considered to be one of the most important applications. However, it has been fairly difficult to perform such an experiment due to (1) sensitivity problems and (2) lack of proper model systems, (3) difficulty of selecting representative marker bands, etc. Nevertheless, a couple of attempts have been made recently.

5.12.1. Ubiquitin Unfolding Dynamics

By using the temperature-jump method utilizing a nanosecond pulse with a wavelength of 2 μm to excite the OD stretch overtone of the D_2O buffer solution, time-dependent dispersive vibrational echo spectra of the ubiquitin protein on nanosecond to millisecond time scales were recorded to elucidate the associated unfolding mechanism.[446] Here, dispersive vibrational echo spectroscopy, which is technically a simpler nonlinear IR experiment than 2D IR photon echo

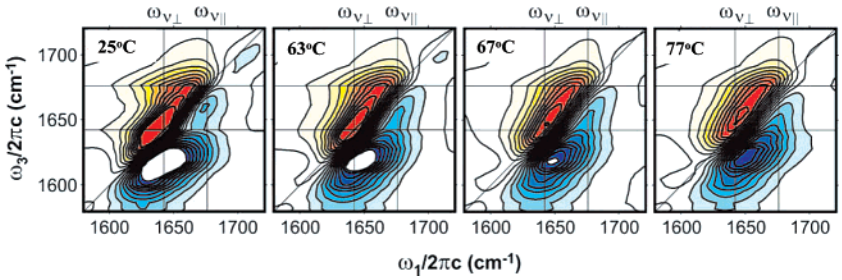

Figure 48. 2D IR spectra of ubiquitin from 25 to 77 °C.[446] Twenty-one equally spaced contours are drawn from −60% to 60% of the maximum amplitude of the 25 °C spectrum. Reprinted with permission from Chung, H. S.; Khalil, M.; Smith, A. W.; Ganim, Z.; Tokmakoff, A. *Proc. Natl. Acad. Sci. U.S.A.* **2005**, *102*, 612. Copyright 2005 National Academy of Sciences, U.S.A.

spectroscopy, is a technique to record the projected 2D IR spectrum onto one frequency axis.[447,448]

From the temperature-dependent dispersive vibrational echo spectra, the thermal melting temperature of ubiquitin in D_2O was estimated to be about 61 °C. The melting curve based on the singular value decomposition analysis of the temperature-dependent dispersive vibrational echo spectra was nicely fitted with a sigmoidal curve, suggesting simple two-state unfolding kinetics. In Figure 48, the temperature-dependent 2D IR spectra are shown for temperature varying from 25 to 77 °C. As the temperature was raised, a concerted blue-shift of the strongly IR-active amide I mode whose transition dipole is perpendicular to the β-sheet strands was observed. In addition, the cross peak ridges were shrunken, indicating unfolding of the β-sheet structure in ubiquitin. To follow the temperature-jump-induced unfolding process, they selected an initial temperature of 58 °C and the temperature increment induced by the nanosecond 2 μm pulse was about 12 °C. The dispersive vibrational echo spectra after the temperature-jump were recorded from 20 ns up to 9 ms and the relative intensity changes at 1621, 1658, and 1677 cm^{-1} were measured to extract information on the unfolding mechanism. Note that the different frequency regions of the dispersive vibrational echo spectrum represent different types of amide I vibrations that are critically dependent on the protein structure. They found that there are two stages of the course of unfolding, which are separated by the time scale. The short-time (tens of microseconds) nonexponential component was attributed to increased configurational flexibility and partial disruptions of antiparallel β-sheet and β-hairpin structures. Nevertheless, it was conjectured that for such a short time the global structure of ubiquitin is still rather close to the native-like one. The long-time (millisecond) component was then interpreted as a concerted unfolding, exhibiting two-state kinetics.

5.12.2. Transient 2D IR Spectroscopy of a β-Turn Peptide

In order to probe structural changes of proteins, it is necessary to introduce external perturbation to place the system into a new nonequilibrium state virtually instantaneously in comparison to the time scale of the folding or unfolding events. One of the most popular techniques is the temperature-jump method.[449] Yet, another popular triggering method is to use a photochemical reaction. In this regard, the disulfide bond is known as a good UV−vis photocleavable site with a dissociation energy of about 65 kcal/mol.

By introducing a disulfide bond into a short model peptide, a cyclic disulfide-bridged peptide containing three peptide bonds and two ester groups was synthesized (see Figure 49 for the molecular structure).[450] An intense UV−vis pulse can

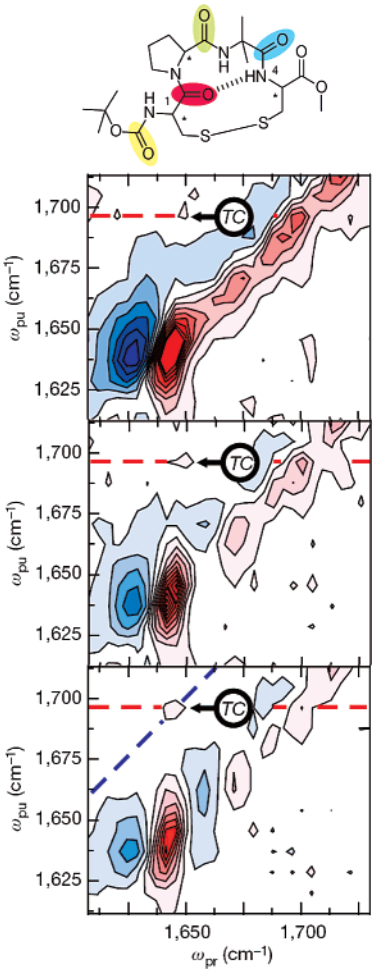

Figure 49. Chemical structure of the cyclic disulfide-bridged tetrapeptide cyclo(Boc-CPUC-OMe) (top). The dashed line in the top figure indicates the intramolecular hydrogen bond. Transient 2D IR spectra at ultraviolet pump to 2D-IR probe delay times of 3, 25, and 100 ps with parallel polarization of all pulses are shown.[450] In the transient two-dimensional spectra, negative signals are depicted in blue and positive signals in red. The arrow labeled "TC" highlights the transient cross peak. Reprinted by permission from Macmillan Publishers Ltd: [*Nature*] ref 450, copyright 2006.

break the disulfide bond to generate a linear peptide in a nonequilibrium state. Its subsequent structural change in a CD_3CN solution was monitored by using a 2D IR spectroscopic technique.[450] The model cyclic peptide used in that experiment has a single intramolecular hydrogen bond, since the tetrapeptide structure mimics a β-turn motif.

Due to this hydrogen-bonding interaction, the amide I local modes of the hydrogen bond donor and acceptor peptide groups are coupled, which produces corresponding cross

peaks in an equilibrium 2D IR spectrum. After the ultrafast photocleavage of the disulfide bond, the peptide unfolds and the hydrogen bond breaks. To obtain the transient 2D IR difference spectrum, two sets of 2D IR spectra had to be recorded simultaneously: one with the ultraviolet pulse switched on and one with the ultraviolet pulse switched off. The three transient 2D IR difference spectra at $T = 3$, 25, and 100 ps are shown in Figure 49. Among various peaks reflecting the structural changes of the peptide, they focused on the intensity change of the transient cross peak, emphasized as "TC" in Figure 49, which is the characteristic cross peak reporting the hydrogen-bond breaking. Carrying out a molecular dynamics simulation, they were able to show that the hydrogen-bond breaking induces a concomitant opening of the β-turn on a time scale of 160 ps. This experiment is a good example demonstrating the ability of transient 2D IR spectroscopy to directly probe changes of local contacts between small groups in biomolecules.

6. Two-Dimensional Electronic Spectroscopy

As a molecular system becomes increasingly complicated, such as photosynthetic complexes, molecular aggregates of quantum dots or nanoparticles, etc., conventional optical spectroscopic methods such as time- or frequency-resolved absorption spectroscopy or spontaneous emission spectroscopy are of limited use to extract direct information on the molecular properties such as electronic couplings between chromophores, structures, and excitation and coherence transfers among chromophores. In this regard, the 2D *electronic* spectroscopy based on the heterodyne-detected photon echo spectroscopic technique can provide far more detailed information. Despite the fact that there exist quite a number of 2D IR spectroscopic investigations of peptides and proteins over the past 10 years as outlined in the previous section, a relatively small number of experimental and theoretical studies with 2D electronic spectroscopy have been reported.[7,9−11,29,57,451−456] Nevertheless, except for the fact that an electronic chromophore can be approximately modeled as a two-level system in contrast to an effectively three-level anharmonic oscillator, one can use the same theoretical method developed for amide I vibrations of proteins to numerically calculate the 2D electronic spectra of coupled multichromophore systems.

Electronic photon echo spectroscopy based on a four-wave-mixing geometry has long been used to study ultrafast solvation dynamics and the inhomogeneity of the electronic transition frequency of a chromophore in condensed phases.[5,61] Furthermore, fifth-order electronic spectroscopy was theoretically proposed to address the question "can we separate homogeneous and inhomogeneous contributions to optical spectra?" and was shown to be of use in elucidating the underlying dynamic inhomogeneity of the solute transition frequency in detail.[117] By using a macroscopic phase-matching condition, the noncollinear PE signal could be selectively measured. Detecting phase modulation of the signal electric field in a noncollinear three pulse photon echo experiment was shown to be possible by employing the spectral interferometry.[29,56,57] As an example, a 2D FT electronic correlation spectrum of a 0.4 nM solution of IR144 in methanol at $T = 0$ was reported in ref 57. Later, the real and imaginary parts of IR144 2D electronic spectra with respect to waiting time from 0 to 100 fs were obtained (see Figure 50).[455]

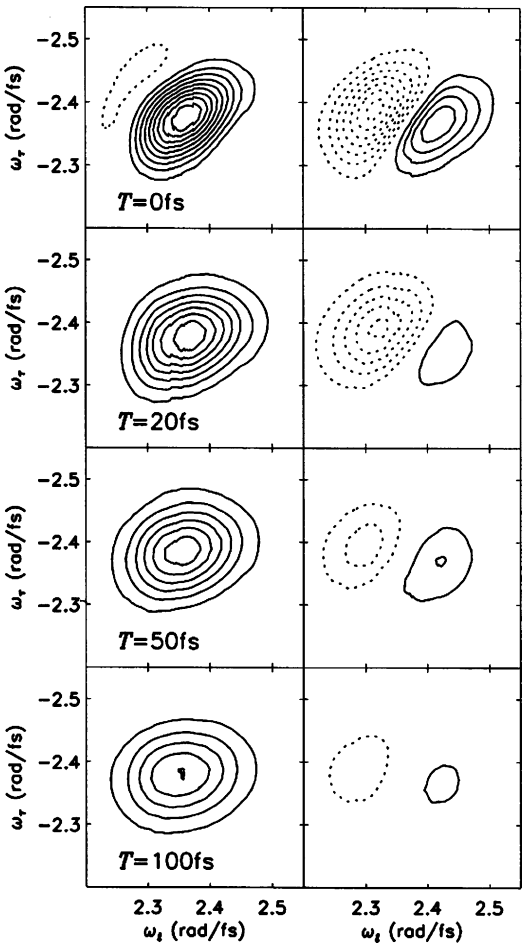

Figure 50. Experimental real (left) and imaginary (right) 2D spectra of IR144 in methanol for four values of T (top to bottom).[455] Contours are drawn at 10% of the $T = 0$ real maximum in both real and imaginary spectra. Positive contours (solid) represent decreased absorption or increased refractive index; negative contours are dashed. The top to bottom sequence of 2D spectra shows the rapid loss of correlation between excitation frequency ω_τ and signal frequency ω_t as the waiting time T is increased.

The waiting time-dependency of the 2D electronic spectrum of a two-level chromophore can be of critical use in studying the inhomogeneity of the transition frequency by examining the extent of diagonal elongation, the aspect ratio, and the diagonal and antidiagonal widths of the diagonal peak. Some important characteristics of the 2D spectrum $S^{(3)}(\omega_\tau,T,\omega_t)$ can be appreciated by noting that the experiment compares the frequency of electronic excitations (for a fixed value of T) in the two time periods of τ and t. For an effective two-level system with considerable inhomogeneous broadening, the transition frequency is widely distributed, though each individual two-level system has the same frequency in both time periods. Thus, this inhomogeneity can lead to elongation of the 2D signal along the diagonal ($\omega_\tau = \omega_t$). However, if there are dynamical processes, such as excitation transfer, solvent relaxation, structural fluctuation, etc., they can scramble the optical frequencies of the individual molecules. Which can in turn make the correlation magnitude between the frequencies in the coherence state evolution periods decrease in time T, and the 2D spectrum at sufficiently large T should become symmetric. Transient behavior of the 2D line shape can therefore provide information on the time scale of the system−bath interaction-induced decoherence process. In fact, the slope of the diagonally elongated peak decreases from 1 at $T = 0$ to 0 at $T = \infty$ if

there is no static inhomogeneity and was found to be linearly proportional to the transition frequency−frequency correlation function, i.e.,[200]

$$\sigma_{\text{2D-PE}}(T) \simeq \langle \delta\omega(T)\, \delta\omega(0)\rangle / \langle \delta\omega^2 \rangle \tag{6-1}$$

where $\sigma_{\text{2D-PE}}(T)$ is the slope of the diagonally elongated 2D photon echo contour.

Due to the similarity between the electronic Hamiltonian and the vibrational Hamiltonian, the same procedures used to describe the 2D vibrational spectroscopy of a single oscillator, which were outlined in the previous section, can also be applied to the interpretation of the 2D electronic spectroscopy of such a two-level electronic chromophore, i.e., IR144 in solution. The more interesting molecular systems would be coupled multichromophore complexes, such as photosynthetic protein, semiconductors, DNA, etc., since they undergo exciton migration, coherence transfer, population relaxation, electron transfer, and so on. These chemical and physical changes of photoexcited states would affect cross peak amplitudes and frequencies in time, which reveal detailed spatial correlation and wave function overlaps between excitonic states. A few critical examples will be discussed in this section.

6.1. Coupled Dimer System

As a model system, a coupled electronic chromophore system was considered, where each monomer is assumed to be a two-level system. From the Frenkel exciton Hamiltonian model discussed in section 4.3, the zero-order Hamiltonian for this coupled dimer system can therefore be written as

$$H_0 = \epsilon_1 a_1^+ a_1 + \epsilon_2 a_2^+ a_2 + J\{a_1^+ a_2 + a_2^+ a_1\} + H_{\text{ph}} \tag{6-2}$$

where the mth site energy, the electronic coupling constant between the mth and nth chromophores, and the phonon bath Hamiltonian are denoted as ϵ_m, J, and H_{ph}, respectively. The chromophore−phonon bath interaction and the interchromophore distance and orientation fluctuations will induce fluctuations of both site energies and coupling constant. Thus, the electron−phonon interaction Hamiltonian is often written as

$$H^{\text{e-p}} = q_1(\mathbf{Q}) a_1^+ a_1 + q_2(\mathbf{Q}) a_2^+ a_2 + q_c(\mathbf{Q})\{a_1^+ a_2 + a_2^+ a_1\} \tag{6-3}$$

where $q(\mathbf{Q})$'s are operators of bath coordinates, $\mathbf{Q}$, $q_1(\mathbf{Q})$, and $q_2(\mathbf{Q})$ describe the site energy fluctuations, and $q_c(\mathbf{Q})$ describes the coupling constant fluctuation. Note that the monomer-to-monomer distance and the relative orientation fluctuate in time and they modulate coupling. If the intermolecular distance oscillates due to a specific vibrational degree of freedom, the fluctuation dynamics of electronic coupling can be modeled as a damped oscillator. A direct evidence of the coupling constant fluctuation is that the cross peak is antidiagonally elongated.

Now, the basis set in the site representation is $\{|0,0\rangle, |1,0\rangle = a_1^+|0,0\rangle, |0,1\rangle = a_2^+|0,0\rangle, |1,1\rangle = a_1^+ a_2^+|0,0\rangle\}$. The doubly excited two-exciton state ($|f\rangle$) energy, $\langle 1,1|H_0|1,1\rangle$, is $\hbar\omega_1 + \hbar\omega_2 + \hbar\Delta_{\text{ee}}$, where Δ_{ee} denotes the biexciton binding energy and ω_j is the transition frequency of the monomer j (= 1 or 2). Then, the two one-exciton states are obtained by diagonalizing the corresponding Hamiltonian matrix, and they can be expressed in terms of the mixing angle θ as

$$\begin{pmatrix} |e_1\rangle \\ |e_2\rangle \end{pmatrix} = U^{-1} \begin{pmatrix} a_1^+|0,0\rangle \\ a_2^+|0,0\rangle \end{pmatrix} = \begin{pmatrix} \cos\theta & \sin\theta \\ -\sin\theta & \cos\theta \end{pmatrix} \begin{pmatrix} a_1^+|0,0\rangle \\ a_2^+|0,0\rangle \end{pmatrix} \tag{6-4}$$

where $|0,0\rangle$ is the ground state and $\theta = 0.5 \arctan\{2J/(\omega_1 - \omega_2)\}$. The two one-exciton state energies, denoted as $\hbar\Omega_1^0$ and $\hbar\Omega_2^0$, are given by, from eq 4-8,

$$\hbar\Omega_1^0 = \epsilon_1 \cos^2\theta + \epsilon_2 \sin^2\theta + 2J\cos\theta\sin\theta$$

$$\hbar\Omega_2^0 = \epsilon_1 \sin^2\theta + \epsilon_2 \cos^2\theta - 2J\cos\theta\sin\theta \tag{6-5}$$

Due to the solvent reorganizations, the ensemble-averaged one- and two-exciton state energies are

$$\hbar\Omega_1 = \hbar\Omega_1^0 + \lambda_1 \cos^2\theta + \lambda_2 \sin^2\theta + 2\lambda_c \cos\theta\sin\theta$$

$$\hbar\Omega_2 = \hbar\Omega_2^0 + \lambda_1 \sin^2\theta + \lambda_2 \cos^2\theta - 2\lambda_c \cos\theta\sin\theta$$

$$\hbar\Omega_f = \hbar\Omega_f^0 + \lambda_1 + \lambda_2 \tag{6-6}$$

where λ_j, for $j = 1$, 2, or c, are the corresponding solvent reorganization energies. The transition dipole vectors are, from eq 4-12,

$$\begin{pmatrix} \mu_{+0} \\ \mu_{-0} \end{pmatrix} = U^{-1} \begin{pmatrix} \mathbf{d}_1 \\ \mathbf{d}_2 \end{pmatrix} = \begin{pmatrix} \cos\theta & \sin\theta \\ -\sin\theta & \cos\theta \end{pmatrix} \begin{pmatrix} \mathbf{d}_1 \\ \mathbf{d}_2 \end{pmatrix} \tag{6-7}$$

where $\mathbf{d}_1 = \langle 1,0|\mu_1|0,0\rangle$ and $\mathbf{d}_2 = \langle 0,1|\mu_2|0,0\rangle$. The electric dipole operator acting on the jth chromophore wave function was denoted as μ_j. The transition dipoles from $|e_1\rangle$ to $|f\rangle$ and from $|e_2\rangle$ to $|f\rangle$ are given as

$$\begin{pmatrix} \mu_{e_1 f} \\ \mu_{e_2 f} \end{pmatrix} = \begin{pmatrix} \sin\theta & \cos\theta \\ \cos\theta & -\sin\theta \end{pmatrix} \begin{pmatrix} \mathbf{d}_1 \\ \mathbf{d}_2 \end{pmatrix} \tag{6-8}$$

In the exciton representation, the transformed chromophore−bath interaction Hamiltonians for the one-exciton and two-exciton states are

$$\tilde{\Xi}_1^{e-p}(\mathbf{Q}) = U^{-1} H_1^{e-p}(\mathbf{Q}) U$$

$$= \begin{pmatrix} q_1\cos^2\theta + q_2\sin^2\theta + 2q_c\cos\theta\sin\theta & -(q_1 - q_2)\cos\theta\sin\theta + q_c\cos 2\theta \\ -(q_1 - q_2)\cos\theta\sin\theta + q_c\cos 2\theta & q_1\sin^2\theta + q_2\cos^2\theta - 2q_c\cos\theta\sin\theta \end{pmatrix}$$

$$\tilde{\Xi}_2^{e-p}(\mathbf{Q}) = q_1(\mathbf{Q}) + q_2(\mathbf{Q}) \tag{6-9}$$

The diagonal matrix elements $[\tilde{\Xi}_1^{e-p}(\mathbf{Q})]_{jj}$ describe the fluctuations of the jth one-exciton state energy, whereas the off-diagonal matrix elements $[\tilde{\Xi}_1^{e-p}(\mathbf{Q})]_{jk}$ induce exciton population transfer between two different one-exciton states.

Although the general expressions for the nonlinear response functions were given in section 4, in ref 68, a short-time expansion of the line shape function was considered in detail to obtain approximate expressions for the three-pulse photon echo response functions. One- and two-color photon

echo peak shifts and their physical interpretations and relationships with 2D spectroscopic features were given in that paper. If the population transfer processes are relatively slow in comparison to the solvation dynamics and correlation times of the frequency−frequency correlation functions, the one-color photon echo peak shift was found to be linearly proportional to the frequency−frequency autocorrelation function of a specific resonant state. In the same limiting case, the two-color photon echo peak shift was shown to be useful in measuring the frequency−frequency cross-correlation function.[68] Additional discussions on the two-color photon echo peak shift can be found in refs 457−461.

When the population transfer between two one-exciton states is relatively slow and furthermore when the two local transition dipoles $\mathbf{d}_1$ and $\mathbf{d}_2$ have the same magnitudes, i.e., $d = d_1 = d_2$, one can estimate the maximum (or minimum) amplitudes of the diagonal and cross peaks, denoted as S^0_{jk}, by[68]

(1) Diagonal peak at $(\omega_\tau = \Omega_1, \omega_t = \Omega_1)$

$$S^0_{11} = \frac{2\pi}{\langle \delta\Omega_1^{\,2}\rangle}\{2\langle \mu_{e_1}^{\,2}\mu_{e_1}^{\,2}\rangle\} = \frac{2\pi|d|^4}{\langle \delta\Omega_1^{\,2}\rangle}\{12(1+2\kappa\cos\phi)^2\} \tag{6-10}$$

(2) Diagonal peak at $(\omega_\tau = \Omega_2, \omega_t = \Omega_2)$

$$S^0_{22} = \frac{2\pi}{\langle \delta\Omega_2^{\,2}\rangle}\{2\langle \mu_{e_2}^{\,2}\mu_{e_2}^{\,2}\rangle\} = \frac{2\pi|d|^4}{\langle \delta\Omega_2^{\,2}\rangle}\{12(1-2\kappa\cos\phi)^2\} \tag{6-11}$$

(3) Off-diagonal peak at $(\omega_\tau = \Omega_1, \omega_t = \Omega_2)$

$$S^0_{12} = \frac{2\pi}{\sqrt{\langle \delta\Omega_1^{\,2}\rangle\langle \delta\Omega_2^{\,2}\rangle}}\{\langle \mu_{ge_1}^{\,2}\mu_{ge_2}^{\,2}\rangle - \langle \mu_{ge_1}\mu_{e_1f}\mu_{fe_1}\mu_{e_1g}\rangle\} = -\frac{2\pi|d|^4}{\sqrt{\langle \delta\Omega_1^{\,2}\rangle\langle \delta\Omega_2^{\,2}\rangle}}\{8(2\kappa^2+3\kappa\cos\phi+4\kappa^2\cos^2\phi)\} \tag{6-12}$$

(4) Off-diagonal peak at $(\omega_\tau = \Omega_2, \omega_t = \Omega_1)$

$$S^0_{21} = \frac{2\pi}{\sqrt{\langle \delta\Omega_1^{\,2}\rangle\langle \delta\Omega_2^{\,2}\rangle}}\{\langle \mu_{ge_2}^{\,2}\mu_{ge_1}^{\,2}\rangle - \langle \mu_{ge_2}\mu_{e_2f}\mu_{fe_2}\mu_{e_2g}\rangle\} = -\frac{2\pi|d|^4}{\sqrt{\langle \delta\Omega_1^{\,2}\rangle\langle \delta\Omega_2^{\,2}\rangle}}\{8(2\kappa^2-3\kappa\cos\phi+4\kappa^2\cos^2\phi)\} \tag{6-13}$$

Here, ϕ is the angle between the two monomeric transition dipole vectors and κ is a measure of the delocalization of the excited states and is defined as

$$\kappa \equiv \cos\theta\sin\theta \tag{6-14}$$

Here, it should be emphasized that the cross peak amplitude S^0_{12} is given by the difference between $\langle \mu_{ge_1}^{\,2}\mu_{ge_2}^{\,2}\rangle$ and $\langle \mu_{ge_1}\mu_{e_1f}\mu_{fe_1}\mu_{e_1g}\rangle$. That is to say, the two different transition pathways destructively interfere to produce the cross peak. However, these two terms exactly cancel out only when the two monomers do not electronically couple. Therefore, the existence of cross peaks is definite evidence of nonzero electronic coupling. It is also interesting to note that the cross peak amplitude can provide critical information on the relative orientation of the two monomers because it is a function of ϕ. In the case of a homodimer, the diagonal and cross peak amplitudes are a relatively simple function of ϕ so that by taking ratios of cross peak amplitude to diagonal peak amplitude one will be able to determine the angle ϕ, which contains structural information of this dimeric system. The same principles deduced from the work in ref 68 can be directly applied to even large multichromophoric systems, if the cross and diagonal peaks are well-resolved in the frequency domain.

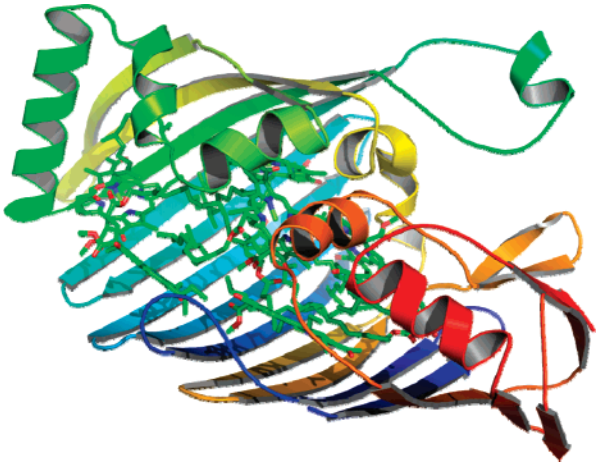

Figure 51. Ribbon diagram of an FMO complex from the PDB database (PDB code: 1M50). Seven BChl's are buried inside.

6.2. Application to a Fenna–Matthews–Olson Light-Harvesting Complex

Photosynthetic light-harvesting complexes containing a few to hundreds of chromophores, such as chlorophylls or bacteriochlorophylls and carotenoids, are important systems and have been investigated recently with 2D electronic spectroscopy.[9−11,462,463] Interchromophore electronic interactions and chromophore−solvent dynamics affect absorption of solar radiation, directional excitation transfer, and trapping of solar energy.[464] Unfortunately, linear spectroscopy cannot provide sufficient information to determine the corresponding electronic Hamiltonian, where the diagonal Hamiltonian matrix elements represent site energies of constituent chromophores and the off-diagonal elements are measures of electronic couplings. An appropriate model system can be developed and tested by comparing theoretical calculation results with multiple linear spectra such as absorption, linear dichroism, circular dichroism, etc. However, it was shown that incisive information on the spatial relationship of the excitonic states could only be extracted from 2D electronic spectroscopy of such a coupled multichromophore system.

The first 2D electronic spectroscopy experiment and theory was reported in ref 9, where the FMO (Fenna−Matthews−Olson) pigment protein complex[464−471] from the green sulfur bacterium *Chlorobium tepidum* was taken for the experimental study. The FMO complex was found to play a role as an energy transfer bridge connecting a large peripheral light-harvesting antenna, the chromosome, to the reaction center.[465,471,472] The crystal structure of the FMO complex taken from the Protein Data Bank (PDB code: 1M50) is shown in Figure 51. The seven bacteriochlorophylls are chromophores in this case (Figure 52).

In refs 9 and 10, by considering incoherent excitation transfers within the one-exciton state manifold, it was shown

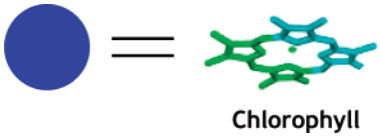

Figure 52. Chlorophyll electronic chromophore.

that the 2D PE spectrum was given by a sum of five distinctively different contributions:

$$S(\omega_\tau,T,\omega_t) = \mathrm{GB} + \mathrm{SE}(j\rightarrow j) + \mathrm{SE}(j\rightarrow k) - \mathrm{EA}(j\rightarrow j) - \mathrm{EA}(j\rightarrow k) \quad (6\text{-}15)$$

where GB, SE, and EA represent the ground-state bleaching, stimulated emission, and excited-state absorption, respectively. In the above expression, "$(j\rightarrow k)$" means that the initially created population on the jth one-exciton state transfers to the kth state during T, and summations over j and k should be performed. Note that the excited-state absorption contributes to the signal negatively and that the coherence transfer at short time was not taken into consideration in eq 6-15.

By using a short-time approximation to all frequency−frequency correlation functions in eqs 4-41−4-44, the 2D electronic spectrum with respect to T was obtained as[10]

$$\begin{aligned} S(\omega_\tau,T,\omega_t) = {} & \sum_{j=1}^{N} \langle \mu_{e_jg}\mu_{e_jg}\mu_{e_jg}\mu_{e_jg}\rangle \tilde{s}_{jj}^{(1)}(\omega_\tau=\Omega_j,T,\omega_t=\Omega_j) + \\ & \sum_{i=1}^{N}\sum_{j\neq i} \langle \mu_{e_ig}\mu_{e_ig}\mu_{e_jg}\mu_{e_jg}\rangle \tilde{s}_{ij}^{(1)}(\omega_\tau=\Omega_i,T,\omega_t=\Omega_j) - \sum_{j=1}^{N} \\ & \sum_{k=1}^{N(N-1)/2} G_{jj}(T)\langle \mu_{e_jg}\mu_{e_jf_k}\mu_{e_jf_k}\mu_{e_jg}\rangle \tilde{s}_{jk}^{(2)}(\omega_\tau=\Omega_j,T,\omega_t=W_k-\Omega_j) + \\ & \sum_{i=1}^{N}\sum_{j\neq i} G_{ji}(T)\langle \mu_{e_ig}\mu_{e_ig}\mu_{e_jg}\mu_{e_jg}\rangle \tilde{s}_{i\rightarrow j}^{(1)}(\omega_\tau=\Omega_i,T,\omega_t=\Omega_j) - \\ & \sum_{i=1}^{N}\sum_{j\neq i}^{N}\sum_{k=1}^{N(N-1)/2} G_{ji}(T)\langle \mu_{e_ig}\mu_{e_jf_k}\mu_{e_jf_k}\mu_{e_ig}\rangle \tilde{s}_{i\rightarrow j,k}^{(2)}(\omega_\tau=\Omega_i,T,\omega_t= \\ & W_k-\Omega_j) \quad (6\text{-}16) \end{aligned}$$

The auxiliary functions determining the 2D line shape of each term in eq 6-16 are given as

$$\tilde{s}_{jj}(\omega_\tau=\Omega_j,T,\omega_t=\Omega_j) = \frac{2\pi}{\sqrt{\langle\delta\Omega_j^2\rangle^2(1-a^2(T)/C_0^2)}} \exp\{-X_j^2(\Omega_j)\}[\exp\{-Y_{jj}^2(\Omega_j,\Omega_j)\} + G_{jj}(T) \exp\{-Y_{jj}^2(\Omega_j - 2\langle\delta\Omega_j^2\rangle\sigma(T)/C_0,\Omega_j)\}]$$

$$\tilde{s}_{ij}^{(1)}(\omega_\tau=\Omega_i,T,\omega_t=\Omega_j) = \frac{2\pi}{\sqrt{\langle\delta\Omega_i^2\rangle\langle\delta\Omega_j^2\rangle - \langle\delta\Omega_i\delta\Omega_j\rangle^2 a^2(T)/C_0^2}} \exp\{-X_i^2(\Omega_i)\}\exp\{-Z_{ij}^2(\Omega_i,\Omega_j)\}$$

$$\tilde{s}_{jk}^{(2)}(\omega_\tau=\Omega_j,T,\omega_t=W_k-\Omega_j) = \frac{2\pi}{\sqrt{\delta_j^2\Delta_{jk}^2 - H_{jk}^2(T)}} \exp\{-X_j^2(\Omega_j)\}\exp\{-\Lambda_{jk}^2(W_k-\Omega_j-Q_{jk}(T),\Omega_j)\}$$

$$\tilde{s}_{i\rightarrow j}^{(1)}(\omega_\tau=\Omega_i,T,\omega_t=\Omega_j) = \frac{2\pi}{\sqrt{\langle\delta\Omega_i^2\rangle\langle\delta\Omega_j^2\rangle - \langle\delta\Omega_i\delta\Omega_j\rangle^2 a^2(T)/C_0^2}} \exp\{-X_i^2(\Omega_j)\}\exp\left\{-Z_{ij}^2\left(\Omega_i - \frac{\langle\delta\Omega_i^2\rangle + \langle\delta\Omega_j^2\rangle}{C_0}\sigma(T),\Omega_j\right)\right\}$$

$$\tilde{s}_{i\rightarrow j,k}^{(2)}(\omega_\tau=\Omega_i,T,\omega_t=W_k-\Omega_j) = \frac{2\pi}{\sqrt{\delta_i^2\{\Delta_{ik}^2 + \Delta_{jk}^2 - H_{ik}^2(T) - H_{jk}^2(T)\}/2}} \exp\{-X_i^2(\Omega_i)\}\exp\{-\Lambda_{jk}^2(W_k-\Omega_j-[Q_{ik}(T)-Q_{jk}(T)]/2,\Omega_j)\} \quad (6\text{-}17)$$

Also, the remaining auxiliary functions used in eq 6-17 are defined as

$$X_j(\bar{\omega}) = \frac{\omega_\tau - \bar{\omega}}{\sqrt{2\langle\delta\Omega_j^2\rangle}}$$

$$Y_{jj}(\bar{\omega}_1,\bar{\omega}_2) = \frac{\omega_t - \bar{\omega}_1 - a(T)(\omega_\tau - \bar{\omega}_2)/C_0}{\sqrt{2\langle\delta\Omega_j^2\rangle[1 - a^2(T)/C_0^2]}}$$

$$Z_{ij}(\bar{\omega}_1,\bar{\omega}_2) = \frac{\omega_t - \bar{\omega}_1 - \langle\delta\Omega_i\delta\Omega_j\rangle a(T)(\omega_\tau - \bar{\omega}_2)/\{\langle\delta\Omega_i^2\rangle C_0\}}{\sqrt{2\left[\langle\delta\Omega_j^2\rangle - \frac{\langle\delta\Omega_i\delta\Omega_j\rangle^2 a^2(T)}{\langle\delta\Omega_i^2\rangle C_0^2}\right]}}$$

$$\Lambda_{jk}^2(W_k-\Omega_j-Q_{jk}(T),\Omega_j) = \frac{\omega_t - W_k + \Omega_j + Q_{jk}(T) - H_{jk}(T)(\omega_\tau - \Omega_j)/\delta_j^2}{\sqrt{2[\Delta_{jk}^2(T) - H_{jk}^2(T)/\delta_j^2]}}$$

$$C_0 = C(T=0) = \int_0^\infty d\omega\, \omega^2\rho(\omega)\coth\left[\frac{\hbar\omega}{2k_BT}\right]$$

$$\sigma(T) = \int_0^\infty d\omega\, \rho(\omega)\omega\{\cos\omega T - 1\}$$

$$\delta_j^2 = \langle\delta\Omega_j^2\rangle$$

$$\Delta_{jk}^2 = \langle\delta W_k^2\rangle - 2\langle\delta\Omega_j\delta W_k\rangle + \langle\delta\Omega_j^2\rangle$$

$$H_{jk}(T) = \{\langle\delta\Omega_j\delta W_k\rangle - \langle\delta\Omega_j^2\rangle\}a(T)/C_0$$

$$Q_{jk}(T) = 2\{\langle\delta\Omega_j\delta W_k\rangle - \langle\delta\Omega_j^2\rangle\}\sigma(T)/C_0 \quad (6\text{-}18)$$

The fluctuation amplitudes, $\langle\delta\Omega_j^2\rangle$, $\langle\delta\Omega_j\delta\Omega_k\rangle$, $\langle\delta\Omega_j\delta W_k\rangle$, and $\langle\delta W_k^2\rangle$, and the correlation functions were already discussed in section 4. Note that $\sigma(T) - \sigma(\infty)$ is the function describing the spectral diffusion,[5] which is related to the time-dependent fluorescence Stokes shift, the change of the diagonally elongated peak shape in the 2D PE spectrum,[473] and the frequency−frequency correlation function.

The conditional probability of finding the kth exciton state at time T when the system was initially (at $T = 0$) on the jth exciton level was as usual denoted as $G_{kj}(T)$, and their time-

dependencies are determined by the corresponding Master equation as

$$\frac{\mathrm{d}}{\mathrm{d}t}G_{kj}(t) = \sum_{j \neq k} K_{kj} G_{jj}(t) - \left(\sum_{j \neq k} K_{jk}\right) G_{kj}(t) \qquad (6\text{-}19)$$

The excitation transition ($j \rightarrow k$) rate constant from j to k is denoted as K_{kj}, and the Redfield or modified Redfield theory was used to calculate these values.[10,72,474] As shown earlier and as will be discussed in section 6.5, the population transfer rate constant between two one-exciton states is linearly proportional to the spatial overlap between $|\psi_j|^2$ and $|\psi_k|^2$, i.e.,

$$K_{kj} \propto \langle \delta\Omega_j \delta\Omega_k \rangle \qquad (6\text{-}20)$$

It should be noted that $\langle \delta\Omega_j \delta\Omega_k \rangle$ is the correlation magnitude between the two fluctuating transition frequencies and, in principle, is a measurable quantity by using the two-color photon echo peak shift measurement method.[68]

Now let us consider the off-diagonal (cross) peaks and their physical meanings. These peaks arise only when the electronic states of the individual molecules comprising the complex interact (mix). Their amplitudes and frequencies provide extra information on the molecular structure and coupling strength of the coupled multichromophore system. It turned out that the amplitude of the cross peak $S_{kj}(T)$ at ($\omega_\tau = \Omega_j$, $\omega_t = \Omega_k$), where Ω_j and Ω_k are the transition frequencies of the jth and kth excitonic states, is approximately proportional to the product of the associated conditional probability function and the transition dipole factors, i.e.,

$$S_{kj}(T) \propto G_{kj}(t)[\langle \mu_{gk}{}^2 \mu_{gj}{}^2 \rangle - \langle \mu_{gj} \mu_{kf}{}^2 \mu_{gj} \rangle] \qquad (6\text{-}21)$$

where μ_{gk} is the transition dipole from the ground state to the kth one-exciton state, μ_{kf} is that from the kth one-exciton state to the fth two-exciton state, and $\omega_{kf} \simeq \omega_{gk}$. Equation 6-21 shows that the appearance and disappearance of cross peaks are directly related to the excitation transfer within the one-exciton state manifold. This shows that 2D spectroscopy is a powerful method to delineate the complicated kinetic network among different quantum states, which in turn provides information on excitation migration among the coupled chromophores.

6.2.1. Population Relaxation

An early experimental and theoretical calculation study concerned population relaxation within the manifold of one-exciton states on a time scale on the order of a picosecond. In Figure 53, the T-dependent 2D spectra at 100, 200, 300, 600, and 1000 fs are shown with simulation results in the right column. Temporal evolutions of the diagonal and cross peak amplitudes and frequency shifts are clearly visible. A notable feature is that the cross peak amplitudes increase in time, indicating state-to-state population relaxation processes.

As emphasized in ref 10, the 2D spectrum is a product of complicated interferences between different nonlinear optical transition pathways, but to facilitate analysis of these experimental results, a computational description presented in ref 10 was found to be useful and provided the basis for an intuitive understanding of the 2D spectra. Since the electronic couplings are strongly dependent on the relative distance and orientation of a given pair of chromophores, a detailed understanding of transport mechanisms can be

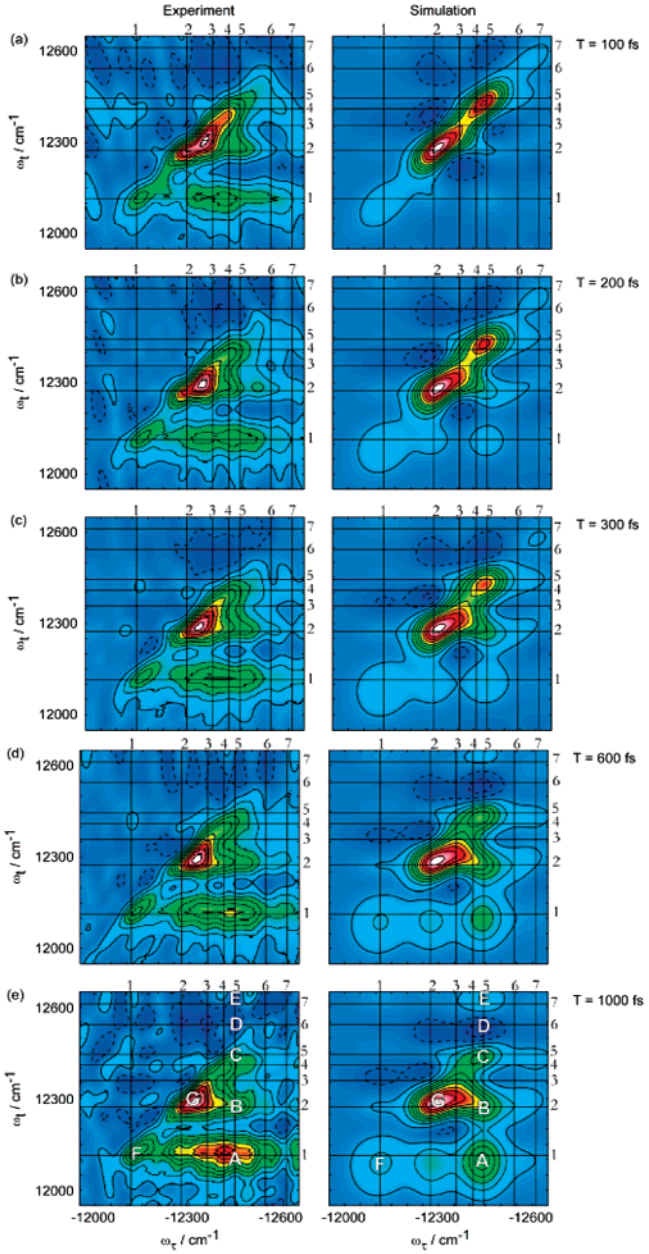

Figure 53. Experimentally measured (left) and numerically simulated (right) 2D spectra of FMO.[10] The absorptive (real) part is shown for different population times at (a) $T = 0$ fs, (b) $T = 200$ fs, (c) $T = 300$ fs, (d) $T = 600$ fs, and (e) $T = 1000$ fs. Positive signals ("increased light") are indicated by solid contour lines, and negative signals ("decreased light") are indicated by dashed lines. All traces have been normalized, and the absolute signal decays with T.

deduced by experimentally measuring the couplings. It was demonstrated that the high information content of the 2D electronic spectrum, in comparison to the more conventional linear spectroscopic techniques, could provide the means to determine the molecular Hamiltonian matrix elements. In parallel, it is highly desirable to develop an electronic structure calculation method to ultimately obtain accurate coupling constants and site energies of optical chromophores surrounded by protein and solvent in the future.

6.2.2. Signature of Coherence Transfer (Quantum Beats in 2D Spectra)

Later, for the same FMO protein complex, a refined 2D electronic spectroscopy experiment was carried out to shed

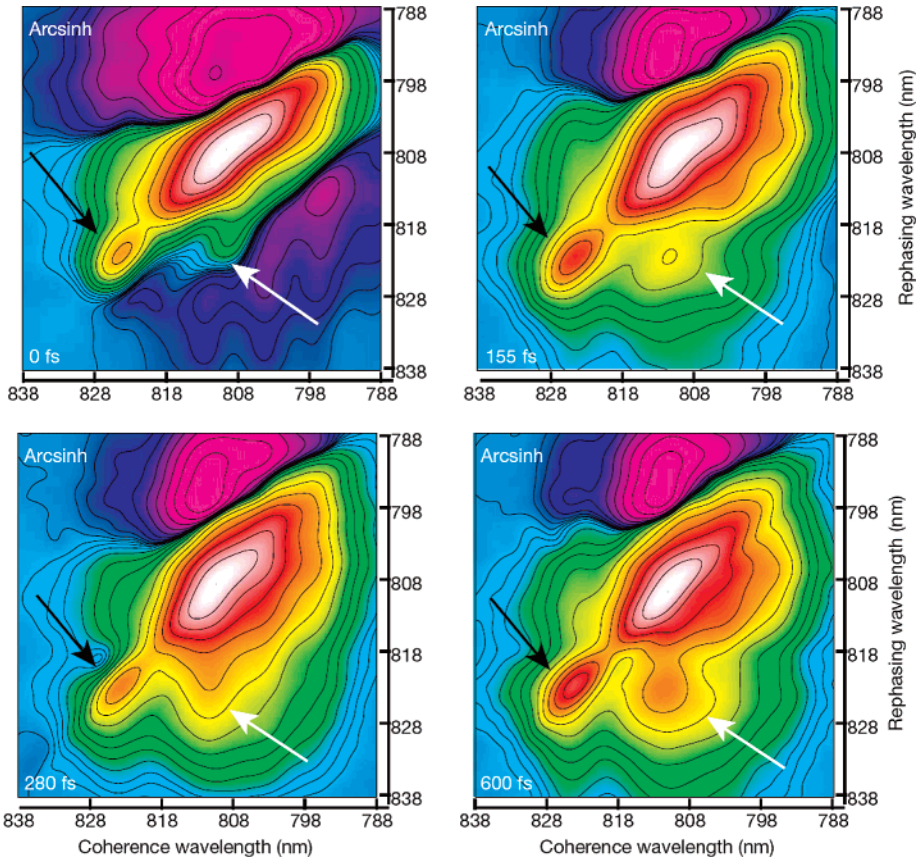

Figure 54. Two-dimensional electronic spectra of FMO.[11] Selected two-dimensional electronic spectra of FMO are shown at population times from $T = 0$ to 600 fs demonstrating the emergence of the exciton 1−3 cross peak (white arrows), amplitude oscillation of the exciton 1 diagonal peak (black arrows), the change in lowest energy exciton peak shape, and the oscillation of the 1−3 cross peak amplitude. The data are shown with an arcsinh coloration to highlight smaller features: amplitude increases from blue to white. Reprinted by permission from Macmillan Publishers Ltd: [*Nature*] ref 11, copyright 2007.

light on coherence transfer processes and mechanisms within the photosynthetic light-harvesting complex. Since the spectral bandwidth of the femtosecond laser pulse is broad enough to cover the entire one-exciton states of the FMO complex, the first field−matter interaction can generate an ensemble of multiple electronic coherence states, which are superposition states of the electronic ground state and one-exciton states. Then, the second field−matter interaction generates (1) ground-state bleaching (hole), (2) population on the one-exciton states (diagonal density matrix elements), and (3) electronic coherence states (off-diagonal density matrix elements in the one-exciton block). These three types of density matrix elements evolve differently during the waiting time T. The time-dependencies of the ground-state bleaching state and the population state were examined previously in ref 9, but the coherence state evolution and its transition to another coherence state were only recently investigated by measuring the short-time 2D spectra of the FMO complex and by examining the quantum beats of the diagonal and off-diagonal peaks in the 2D spectra.[11]

In Figure 54, the 2D electronic spectra of FMO at $T = 0$, 155, 280, and 600 fs are shown. The data are shown with an arcsinh coloration to highlight smaller diagonal and cross peaks. In the series of selected 2D spectra in Figure 54, the amplitudes of the lowest-energy diagonal peak (denoted by a black arrow) and the corresponding cross peak (denoted by a white arrow) oscillate in time, i.e., quantum beating. In addition, the ratio of the diagonal to antidiagonal widths of the lowest-energy diagonal peak oscillates with the same frequency of its peak amplitude, but they are anticorrelated. This was found to be strong evidence of excitonic quantum coherence.[475]

The power spectrum of the oscillating lowest-energy diagonal peak shows six different frequency components, which correspond to the energy differences between exciton 2−7 states and exciton 1. Note that the off-diagonal density matrix element, which describes the time-evolution of the electronic coherence state between the jth and kth excitons, is approximately given as $\rho_{jk}^{(2)}(T) \sim \exp\{i(E_j - E_k)T/\hbar\}$, without a dephasing term—note that the superscript "(2)" in $\rho_{jk}^{(2)}(T)$ means that it is a second-order density matrix with respect to the field−matter interaction Hamiltonian. Therefore, the experimental measurement of the diagonal peak quantum beat clearly provides information on the excitonic state energies. Second, the quantum beats of the diagonal and cross peaks persist even longer than the population relaxation times, which is in stark contrast with the notion that the coherences are destroyed quite rapidly in comparison to population relaxation times. It was therefore suggested that chromophore−bath interactions are correlated for different chromophores. Third, direct evidence on coherence transfer was observed by examining the oscillating behavior of the cross peak between excitons 1 and 3, which is one of the most clearly frequency-resolved cross peaks. Although, from the corresponding power spectrum, all frequency components coupled to either exciton 1 or 3 were identified, the cross peak amplitude and beating did not appear at time

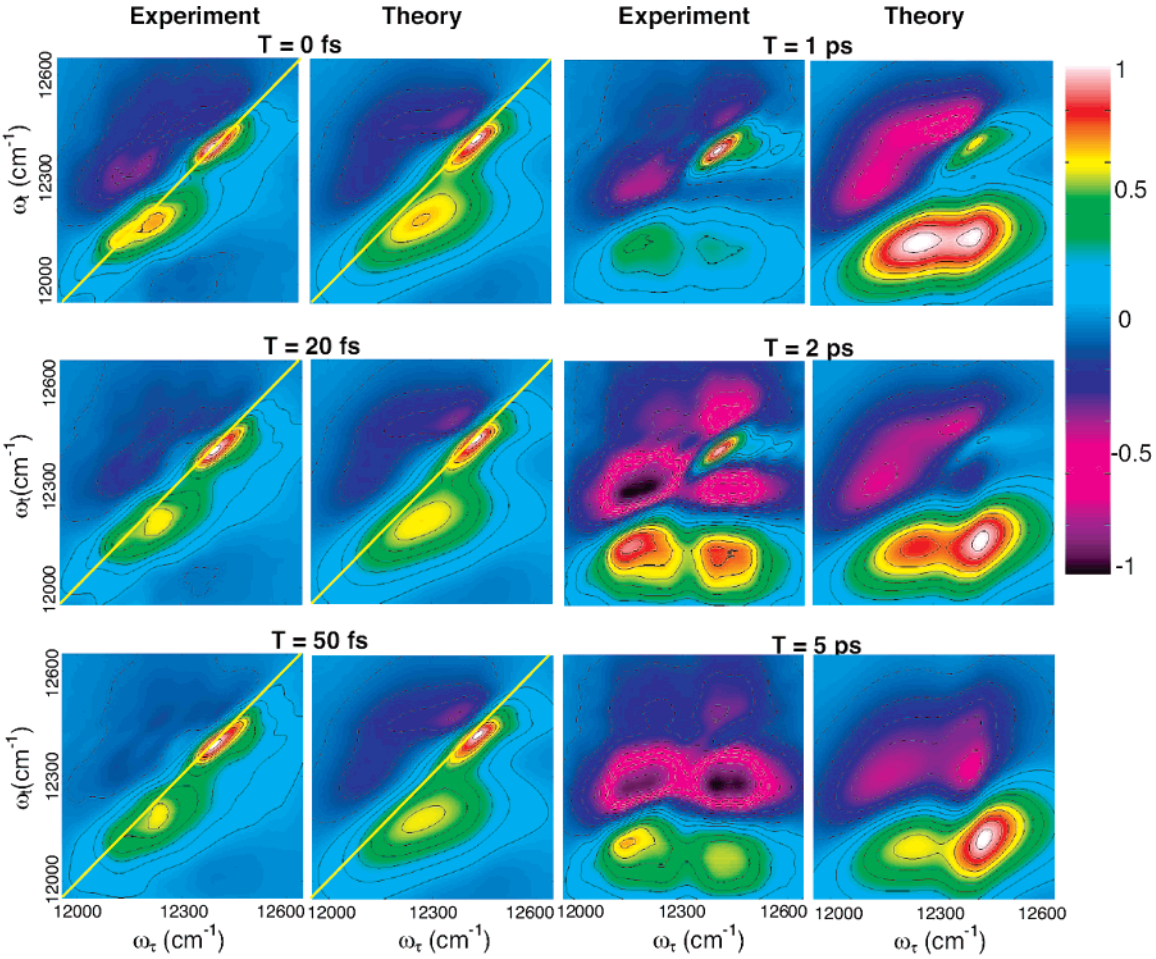

Figure 55. Experimental and theoretical 2D spectra of the LH3 (light-harvesting complex III from purple bacteria *Rhodopseudomonas acidophila* strain 7050) complex,[463] corresponding to the real part of the electric field at 77 K at population times $T = 0$, 20, and 50 fs (left) and $T = 1$, 2, and 5 ps (right). Each spectrum is normalized to its absolute maximum; positive features correspond to ''more light'' and negative to ''less light.'' Contours are drawn at ±5%, ±15%, ..., ±95% of the absolute peak amplitude, with solid lines corresponding to positive contributions and dashed lines corresponding to negative contributions. Reprinted with permission from Zigmantas, D.; Read, E. L.; Mancal, T.; Brixner, T.; Gardiner, A. T.; Cogdell, R. J.; Fleming, G. R. *Proc. Natl. Acad. Sci. U.S.A.* **2006**, *103*, 12672. Copyright 2006 National Academy of Sciences, U.S.A.

zero. This indicates that the 1−3 coherence state was generated at a finite time later, i.e., coherence transfer from another coherence state to the 1−3 coherence state.

An interesting picture of the implication of quantum coherence involved in energy transfer was that the generated superposition states are efficient in directing the energy transfer in such a light-harvesting complex, which is analogous to a single quantum computation. This is in contrast with an incoherent hopping mechanism. A further study is required of whether a real light-harvesting complex absorbing incoherent sunlight instead of femtosecond coherent laser photons is affected by such effects. In addition, a more refined chromophore−bath interaction model should be developed to address the issue on bath-mediated correlation effects on line broadening and exciton population and coherence transfers.

6.3. Application to the B800−B820 Light-Harvesting Complex

An application of the 2D electronic spectroscopic technique to the light-harvesting complex III (LH3)[476] from the purple bacteria *Rhodopseudomonas acidophila* strain 7050, which contains 27 chromophores, was reported.[463] It was denoted as the B800-B820 complex because it consists of two concentric BChl rings labeled B800 (with 9 weakly interacting BChls) and B820 (with 18 strongly coupled BChls). The absorption spectrum at 77 K therefore shows two bands at around 800 and 820 nm. Therefore, this system is ideal for studying energy transfer between the two complexes by employing the 2D spectroscopic method.

In Figure 55, six representative 2D spectra of the B800-B820 complex are shown, where the numerical simulation results are also plotted for comparisons.[463] The first three spectra on the left side of Figure 55 were presented to provide information on ultrafast (≤50 fs) coherence dynamics. The line shapes, frequencies, extents of diagonal elongation, and relative intensity changes of the two diagonal peaks were examined and led to a conclusion that B8200 chromophores are strongly coupled and coherences are quickly relaxed on such an ultrafast time scale. The three on the right in Figure 55 clearly show excitation transfer from B800 to the B820 complex, as evidenced by the increasing cross peak amplitude. The population relaxation associated with B800 → B820 occurs with a time constant of about a picosecond. Although the line shape of the B800 diagonal peak does not change much as T increases from 1 to 2 ps, the B820

diagonal peak becomes round as T increases. This indicates that the memory loss rate of B820 exciton states is faster than that of B800, which is likely to originate from strong coupling-induced relaxation of B820 excitonic states as well as from strong chromophore−bath interactions, i.e., large reorganization energies. From a modeling study of the 2D spectra of the LH3, in particular from the line shape analysis of the B800 diagonal peak, direct evidence that the B800 ring should be described by an exciton picture was found,[477] even though the coupling constants are known to be relatively small, ∼30 cm^{-1}. Whether the excited states of the B800 ring should be treated as delocalized excitons or just a collection of monomeric excited states was one of the issues debated over the years.[463,478] It was found that, only when the B800 excited states are treated as delocalized excitons, was the B800 diagonal peak shape successfully reproduced. In addition, the B800 → B820 energy transfer rate extracted from the 2D spectroscopic experiment was found to be inconsistent with the conventional Förster theory in that system, but the so-called generalized Förster theory[479−482] was found to be acceptable.

6.4. Application to Semiconductors

2D electronic spectroscopy has been applied to semiconductors for studying exciton dynamics, interexciton coupling, and exciton−continuum state coupling.[483−486] Optical excitation of a direct gap semiconductor produces electron−hole pairs, which are called excitons because electron and hole pairs can result in a bound state due to the Coulomb attraction between the two particles.[487] In the case of a GaAs (gallium arsenide) semiconductor heterostructure, an excitonic resonance appears at low temperature because the exciton binding energy is just about 10 meV. In order to study the exciton dynamics whose time scale varies from femtosecond to picosecond, a variety of ultrafast spectroscopic means have been used.[51,487−500]

The first 2D optical spectroscopy experiment on a semiconductor was performed for GaAs semiconductor quantum wells consisting of 10 periods of a 10 nm GaAs well and a 10 nm Al−GaAs barrier at 8 K. The heavy-hole and light-hole valence bands were formed, and the two are energetically separated from each other by about 6 meV.

In Figure 56, the absorption spectrum exhibiting a heavy-hole exciton band, a light-hole exciton band, and a continuum band is shown. The spectrum of the excitation pulse is also shown in the same figure (see the red line). The normalized magnitude of the 2D Fourier-transform spectrum shows four well-resolved peaks. First of all, the cross peaks in this spectrum originate from coherent coupling between the heavy-hole exciton and the light-hole exciton. Interestingly, the upper-left cross peak intensity is even stronger than the two diagonal peaks. The two cross peak intensities are different from each other. It turned out that the excitation induced dephasing,[492] which is related to incoherent many-body effects, and excitation induced shift[494] play important roles in couplings. Here, the excitation induced dephasing means that the effective dephasing rate of the off-diagonal density matrix element for a two-level system contains a term that is linearly proportional to the number density of oscillators. Similarly, the excitation induced shift means that the resonance frequency shifts linearly with respect to the number density.

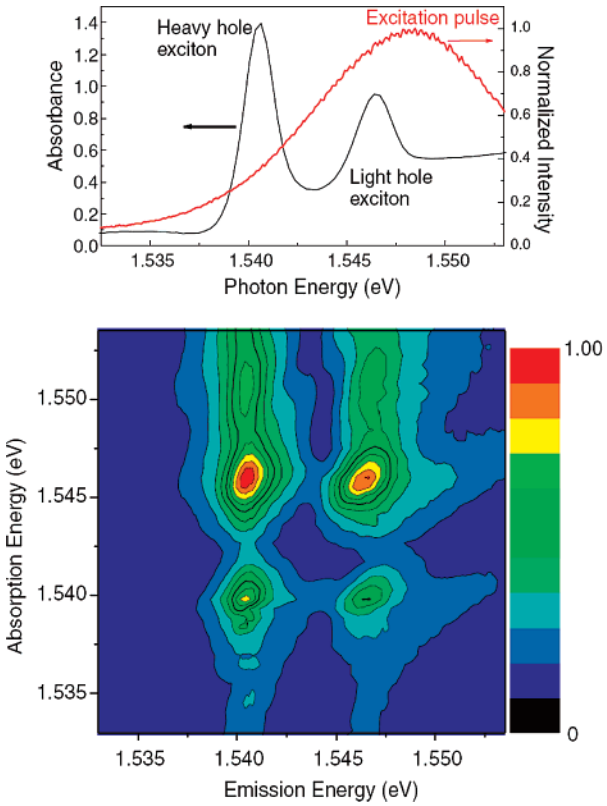

Figure 56. Linear absorption spectrum of GaAs semiconductor quantum wells consisting of 10 periods of a 10 nm GaAs well and a 10 nm Al−GaAs barrier at 8 K (upper). The spectrum of the excitation pulses is also shown in red. The normalized magnitude of the two-dimensional Fourier-transform spectrum is shown in the bottom panel.[483] Reprinted with permission from Optical two-dimensional Fourier transform spectroscopy of semiconductors. Borca, C. N.; Zhang, T. H.; Li, X. Q.; Cundiff, S. T. *Chem. Phys. Lett.* **2005**, *416*, 311. Copyright 2005 Elsevier.

Another notable feature in the 2D spectrum (Figure 56) is the two vertical ridges. If the continuum states are modeled as a collection of inhomogeneously distributed two level systems, the peaks would appear diagonally elongated. From the model simulations with and without excitation induced dephasing, the excitation induced dephasing was found to play a critical role. From this experiment, it is clear that the 2D spectroscopic method can give insight into the microscopic nature of the many-body interactions in semiconductors. Later in ref 484, the real and imaginary parts of the 2D spectrum were separately measured and reported. Since their measurement is phase-sensitive, it was possible to distinguish two different mechanisms, i.e., excitation induced dephasing and an excitation induced shift. The former affects the off-diagonal density matrix amplitude, whereas the latter changes its oscillation frequency. They found that the excitation induced dephasing of the heavy-hole exciton is different from that of the light-hole exciton. In order to further elucidate the origin of cross peaks between the heavy-hole and light-hole excitons, theoretical results was reported.[485]

6.5. Exciton Population and Coherence Transfer Rates

In section 6.2, it was demonstrated that the population and coherence transfers are critical in understanding the time-dependent changes of the 2D spectra of coupled multichro-

mophore systems, e.g., a photosynthetic light-harvesting complex. In the present subsection, a brief discussion of the theory of exciton population and coherence transfer rates is presented because parts of the results are related to 2D spectroscopic features, where the projection operator technique is used. Suppose that the molecular Hamiltonian can be divided into two parts as

$$H = H^0 + H' \tag{6-22}$$

where H^0 and H' represent the reference and perturbation Hamiltonian, respectively. For example, if the site representation Hamiltonian in eqs 4-1 or 4-2 is used, the second term in that equation can be considered as the perturbation Hamiltonian. On the other hand, in the delocalized exciton representation, two terms in eq 4-7 are the perturbation Hamiltonian matrices for the one- and two-exciton states. The time evolution of the molecular density matrix is then described by the following quantum Liouville equation:

$$\frac{\partial \rho(t)}{\partial t} = -iL\rho(t) = -i(L_0 + L')\rho(t) \tag{6-23}$$

Now, let us introduce the projection operator:

$$\mathbf{P} = \mathbf{P}_0 + \sum_\mu \mathbf{P}_\mu \tag{6-24}$$

where the operational definition of an individual term is

$$\mathbf{P}_\mu \rho \equiv |\mu\rangle \rho^{\mathrm{eq}}_{\mu\mu} \langle \mu | Tr_{\mathrm{B}}[\rho_{\mu\mu}]$$

$$\rho^{\mathrm{eq}}_{\mu\mu} = \frac{\exp[-\beta H_\mu{}^\circ]}{Z} \tag{6-25}$$

Then, the complementary operator $\mathbf{Q}$, which projects the density matrix onto the manifold of off-diagonal (coherence) density matrix components, is defined as

$$\mathbf{Q} = 1 - \mathbf{P} \tag{6-26}$$

Using the projection operator method,[501,502] one can obtain the equations describing time evolutions of the diagonal and off-diagonal density operators, which describe population and coherence state evolutions, respectively, as[503,504]

$$\frac{\partial \mathbf{P}\rho(t)}{\partial t} = -i\mathbf{P}L\mathbf{P}\rho(t) - \int_0^t \mathrm{d}\tau\ \mathbf{P}L\mathbf{Q}\mathrm{e}^{-i(t-\tau)\mathbf{Q}L}\mathbf{Q}L\mathbf{P}\rho(\tau) - i\mathbf{P}L\mathrm{e}^{-it\mathbf{Q}L}\mathbf{Q}\rho(0) \tag{6-27}$$

$$\frac{\partial \mathbf{Q}\rho(t)}{\partial t} = -i\mathbf{Q}L\mathbf{Q}\rho(t) - \mathbf{Q}L\int_0^t \mathrm{d}\tau\ \mathrm{e}^{-i(t-\tau)\mathbf{P}L}\mathbf{P}L\mathbf{Q}\rho(\tau) - i\mathbf{Q}L\mathrm{e}^{-it\mathbf{P}L}\mathbf{P}\rho(0) \tag{6-28}$$

Equation 6-27 describes a population transfer process between eigenstates, since it determines the time evolutions of diagonal density matrix elements, whereas eq 6-28 determines coherence transfer processes between two different coherence states.

6.5.1. Population Transfer

At time zero, if the system is purely on population states, $\mathbf{Q}\rho(0) = 0$ and the last term in eq 6-27 vanishes. Then, up to the second-order terms with respect to H', one can find that eq 6-27 is approximately written as

$$\frac{\partial \mathbf{P}\rho(t)}{\partial t} = -\int_0^t \mathrm{d}\tau\ \mathbf{P}L'\mathrm{e}^{-i(t-\tau)L_0}L'\mathbf{P}\rho(\tau) \tag{6-29}$$

Here, the formulas $\mathbf{P}^2 = \mathbf{P}$, $L_0\mathbf{P} = \mathbf{P}L_0 = 0$, and $\mathbf{P}L'\mathbf{P} = 0$ were used. This is the starting point for further derivation of the Markovian relaxation equation (quantum master equation) for the projected density matrix (population states):

$$\frac{\partial \rho_{\alpha\alpha}(t)}{\partial t} = -\sum_{\beta\neq\alpha} K_{\beta\beta,\alpha\alpha}\rho_{\alpha\alpha}(t) + \sum_{\beta\neq\alpha} K_{\alpha\alpha,\beta\beta}\rho_{\beta\beta}(t) \tag{6-30}$$

The rate constant $K_{\beta\beta,\alpha\alpha}$ in the Markovian limit, which describes population transfer from the α to β state, is given as

$$K_{\beta\beta,\alpha\alpha} = 2\mathrm{Re}\int_0^\infty \mathrm{d}\tau\ \mathrm{Tr}_{\mathrm{B}}[\mathrm{e}^{iH^0_\alpha\tau}H'_{\alpha\beta}\mathrm{e}^{-iH^0_\beta\tau}H'_{\beta\alpha}\rho^{\mathrm{eq}}_{\alpha\alpha}] \tag{6-31}$$

Depending on the choice of H° and H', one can obtain the Forster energy transfer rate, Redfield rate,[505,506] or generalized Redfield rate. As discussed in ref 503, within the site representation with H' chosen to be the second term in eq 4-1, the resultant rate constant corresponds to the Forster theory. On the other hand, if the reference eigenstates are delocalized excitonic states ignoring the diagonal Hamiltonian matrix elements in eq 4-7, the rate constant thus obtained with eq 6-31 corresponds to the Redfield rate constants for the population transfer processes. However, if the diagonal Hamiltonian matrix elements in eq 4-7 are included in the zero-order Hamiltonian H°, one can obtain the modified Redfield theory expressions for the population transfer rate constants. The latter theory was chosen for numerical calculations of exciton population transfer rate constants in refs 9 and 10.

More specifically, in the Forster regime, the rate constant $K_{\beta\beta,\alpha\alpha}$, where $|\alpha\rangle$ and $|\beta\rangle$ are the excited states of the αth and βth chromophores, is given as

$$K_{\beta\beta,\alpha\alpha} = \frac{|J_{\beta\alpha}|^2}{2\pi}\int_{-\infty}^{\infty}\mathrm{d}\omega\ A_\beta(\omega)\,F_\alpha(\omega) \tag{6-32}$$

where $A_\beta(\omega)$ and $F_\alpha(\omega)$ are the line shape functions of the absorption and fluorescence of the αth and βth chromophore, respectively. Note that the rate constant in eq 6-32 is linearly proportional to both the square of coupling constant and the frequency overlap between $A_\beta(\omega)$ and $F_\alpha(\omega)$.

In the case of Redfield regime, the population transfer rate constant from the jth exciton state to the kth exciton state is

$$K_{kk,jj} = 2\mathrm{Re}\int_0^\infty \mathrm{d}t\ \langle [U^{-1}H^{(1)}_{\mathrm{SB}}(\mathbf{Q}(t))U]_{jk}[U^{-1}H^{(1)}_{\mathrm{SB}}(\mathbf{Q}(0))U]_{kj}\rangle \exp\{-i\Delta\Omega_{kj}t\} \tag{6-33}$$

where the frequency difference between the kth and jth

one-exciton states was denoted as $\Delta\Omega_{kj}$. Then, eq 6-33 can be rewritten as, from eq 4-1,

$$K_{kk,jj} = 2\mathrm{Re}\int_0^\infty \mathrm{d}t \sum_{m,n}\sum_{m',n'} U_{jm}{}^{-1}U_{nk}U_{km'}{}^{-1}U_{n'j} \langle q_{mn}(\mathbf{Q}(t))q_{m'n'}(\mathbf{Q}(0))\rangle \exp\{-i\Delta\Omega_{kj}t\}$$

$$\cong 2\mathrm{Re}\int_0^\infty \mathrm{d}t \sum_{m}\sum_{m'} U_{jm}{}^{-1}U_{mk}U_{km'}{}^{-1}U_{m'j} \langle q_{mm}(\mathbf{Q}(t))q_{m'm'}(\mathbf{Q}(0))\rangle \exp\{-i\Delta\Omega_{kj}t\}$$

$$\cong 2\mathrm{Re}\int_0^\infty \mathrm{d}t \sum_{m} U_{mk}{}^2U_{mj}{}^2\langle q_{mm}(\mathbf{Q}(t))q_{mm}(\mathbf{Q}(0))\rangle \exp\{-i\Delta\Omega_{kj}t\}$$

$$\cong (\sum_m U_{mk}{}^2U_{mj}{}^2)2\mathrm{Re}\int_0^\infty \mathrm{d}t\, C(t)\exp\{-i\Delta\Omega_{kj}t\}$$

$$= (\sum_m U_{mk}{}^2U_{mj}{}^2)\pi|\Delta\Omega_{kj}|^2\left\{\coth\left(\frac{\beta\hbar|\Delta\Omega_{kj}|}{2}\right)\pm 1\right\}\rho(|\Delta\Omega_{kj}|) \quad (6\text{-}34)$$

Here, a series of approximations, eqs 4-9, 4-14, and 4-16, were invoked. Furthermore, we used the expression for $C(t)$ in terms of spectral density (see eqs 4-17−4-19). In eq 6-34, the upper (lower) sign is the case of a downhill (uphill) transition. This sign factor ensures the detailed balance condition. Note that the factor $\sum_m U_{mk}^2U_{mj}^2$, which appeared in eq 4-27, is the spatial overlap of the two probability density distributions of the kth and jth one-exciton states.[9,10,68,507,508] This quantity is spectroscopically measurable, as discussed in section 4.3. If a given pair of exciton wave functions is spatially overlapped with each other, the excitation transfer rate can be large, as long as the spectral density at the frequency of $\Delta\Omega_{kj}$ is sizable.[10,68]

The population transfer rate expression based on the generalized Redfield theory was found to be quite complicated, so that its physical meaning is less clear than the above two cases. Furthermore, since a detailed theoretical derivation can be found in refs 72 and 503, it will not be discussed in this paper.

6.5.1. Coherence Transfer

Coherence transfer is described by eq 6-28, since a given coherence state corresponds to the **Q**-projected density matrix element. Suppose that the system is initially on a coherence state at time zero. Then, we have $\mathbf{P}\rho(0) = 0$. The second-order equation with respect to L' was found to be[504]

$$\frac{\partial \mathbf{Q}\rho(t)}{\partial t} = -\int_0^t \mathrm{d}\tau\, \mathbf{Q}L'\mathbf{P}L'\mathbf{Q}\rho(\tau) \quad (6\text{-}35)$$

Unlike eq 6-29, the rate kernel function does not depend on time τ. From this equation, the equation for the conditional probability (Green function) was obtained:

$$\frac{\partial G_{\lambda\lambda'}(t)}{\partial t} = \sum_\alpha \int_0^t \mathrm{d}\tau\, \{K_{\lambda\alpha}G_{\alpha\lambda'}(\tau) - K_{\alpha\lambda}G_{\lambda\lambda'}(\tau)\} \quad (6\text{-}36)$$

where α, λ, and λ' are the coherence (not population) states, e.g., $\alpha = |j\rangle\langle k|$ with $j \neq k$. The rate kernel function

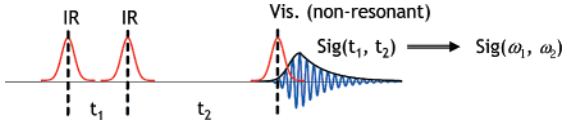

Figure 57. Schematic of the experimental beam configuration for IR−IR−vis FWM spectroscopy. The first two IR pulses separated by a delay time t_1 are used to create a 2D transient grating in the sample. The third electronically nonresonant pulse, which is delayed from the second IR pulse by t_2, is scattered by the 2D grating. The measured signal with respect to t_1 and t_2 is Fourier transformed to obtain the 2D IR−IR−vis FWM spectrum.[509] The phase-matching conditions for IR−IR−vis SFG and DFG are $\mathbf{k}_s = \mathbf{k}_1 + \mathbf{k}_2 + \mathbf{k}_3$ and $\mathbf{k}_s = \mathbf{k}_1 - \mathbf{k}_2 + \mathbf{k}_3$.

for the exciton coherence transfer from λ' to λ was found to be

$$K_{\lambda\lambda'} = -\mathrm{Tr}[\lambda^\dagger \mathbf{Q}_\lambda L'\mathbf{P}L'\rho_{\lambda'}] \quad (6\text{-}37)$$

A detailed expression for the above rate kernel, when the bilinear system−bath coupling model was used, is given in ref 504. An interesting finding here is that the coherence transfer kernel is independent of time—note that the Markovian approximation was not used. Unlike the case of the **P**-projected density operator given in eq 6-29, eq 6-35 does not contain a Liouville space time-evolution operator in between the L' and PL' operators, whereas eq 6-29 does. Although one could obtain the quantum Master equation in eq 6-30 from the equation for the **P**-projected density operator in eq 6-29, the **Q**-projected density operator does not provide the corresponding Master equation for coherence states. Equation 6-36 should be viewed as a coupled integrodifferential equation, not a conventional Master equation. Often, the population state was interpreted classically because it describes the probability of finding the system to be in a given state. However, the coherence state has no classical analogue, so that it may not be possible to make a direct connection of eq 6-36 to a classical kinetic equation.

In the present section, it was demonstrated that the 2D electronic spectroscopy of coupled multichromophore system enables us to quantitatively determine couplings, population and coherence transfer pathways and rates, and spatial relationships between exciton states. Also, by tracking the cross peak amplitudes in time, one can directly follow the energy flow and quantum coherence dynamics on a molecular length scale with femtosecond time resolution. Thus, two-dimensional electronic spectroscopy should provide insights into all systems with electronic band structures.

7. Two-Dimensional IR–vis Four-Wave-Mixing Spectroscopy

Most of the recent 2D experiments were based on the IR or vis four-wave-mixing techniques such as photon echo and pump−probe. However, there is another type of 2D four-wave-mixing method such as doubly vibrationally resonant infrared−vis four-wave-mixing spectroscopy, which was theoretically proposed and experimentally demonstrated. In the time domain, the first two IR pulses separated in time by t_1 create a transient 2D vibrational grating in the optical sample, where the two IR fields are resonant with particular vibrational modes that could be different from each other. Then, the third visible pulse, whose frequency is electronically nonresonant, is injected and the scattered IR−IR−vis sum or difference frequency field is measured as a function of the additional delay time t_2 (see Figure 57).

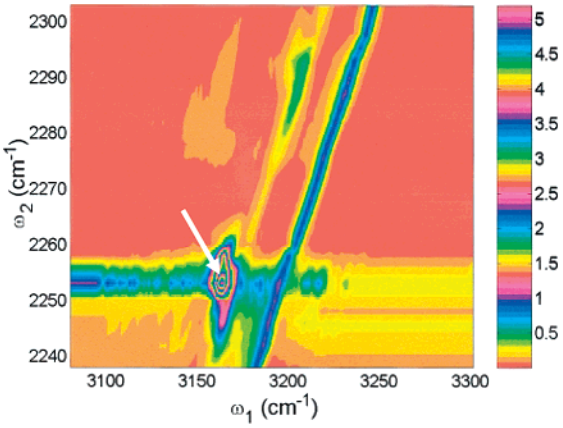

Figure 58. Two-dimensional doubly vibrationally enhanced IR−IR−vis FWM spectrum of CH_3CN with 8 mol % C_6D_6.[511] The color scale repeats 4 times to see the weakest features. Reprinted (figure) with permission from ref 511 as follows: Zhao, W.; Wright, J. C. *Phys. Rev. Lett.* **1999**, *83*, 1950. Copyright 1999 by the American Physical Society.

The measured signal is then double Fourier-transformed to obtain the 2D IR−IR−vis FWM spectrum. This type of 2D vibrational spectroscopy based on time-resolved IR−IR−vis FWM was theoretically proposed in 1998 for the first time.[25,28,509,510] In the frequency domain, one can tune the two IR field frequencies to drive the same 2D vibrational coherences, and the Raman scattered field intensity is measured as a function of the two IR frequencies, which directly corresponds to the 2D IR−IR−vis four-wave-mixing spectrum.[31,511−513]

Experimentally, IR−IR−vis difference-frequency-generation spectroscopy, which was called doubly vibrationally enhanced (DOVE) IR-FWM and DOVE Raman-FWM,[31] was performed for liquid acetonitrile, and a cross peak revealing anharmonic and nonlinear polarizability-driven couplings between the CC and CN stretch modes in MeCN was observed (see Figure 58).

In addition, it was demonstrated that the double vibrational resonance technique can clearly resolve the cross peak in the 2D IR−IR−vis FWM spectrum of the acetonitrile/water mixed solution, even though the corresponding combination band in the IR spectrum was buried beneath the water's stronger fundamental transition, i.e., the O−H stretch band. This showed that 2D IR spectroscopy can be a useful analytical tool for separately measuring a weak combination band even in the presence of complicating spectral congestion.

The experimental feasibility of IR−IR−vis sum-frequency-generation was investigated by applying it to CO molecules adsorbed on a Ru metal surface. The first two IR frequencies (ω_{IR}) are resonant with the delocalized CO vibrational phonons, and the final electronically nonresonant visible field with frequency of ω_{vis} is used to generate the sum-frequency-field with frequency of $2\omega_{IR} + \omega_{vis}$. The doubly resonant IR−IR−vis SFG field intensity and its dependency on the CO coverage on the metal surface were theoretically described by considering lateral dipole−dipole interactions, local field corrections, and delocalized CO phonon modes.

7.1. Nonlinear Response Function Theory of IR–IR–vis Four-Wave-Mixing Spectroscopy

In order to theoretically describe the IR−IR−vis FWM spectroscopy in Figure 57 in terms of the associated nonlinear response function, one should consider the following effective field−matter interaction Hamiltonian,

$$H_{int} = -\boldsymbol{\mu}\cdot\mathbf{E}(\mathbf{r},t) - \frac{1}{2}\boldsymbol{\alpha}:\mathbf{E}^2(\mathbf{r},t) \tag{7-1}$$

Then, it was found that the third-order polarization associated with the IR−IR−vis FWM polarization is given as

$$\mathbf{P}^{(3)}(\mathbf{r},t) = N\int_0^\infty dt_2 \int_0^\infty dt_1\, R^{(3)}(t_2,t_1) \otimes \mathbf{E}(\mathbf{r},t)\, \mathbf{E}(\mathbf{r},t-t_2)\, \mathbf{E}(\mathbf{r},t-t_2-t_1) \tag{7-2}$$

where the nonlinear response function is defined as[509]

$$R^{(3)}(t_2,t_1) = -\frac{1}{\hbar^2}\theta(t_2)\,\theta(t_1)\langle[[\alpha(t_2+t_1),\mu(t_1)],\mu(0)]\rho_0\rangle \tag{7-3}$$

This is a typical two-time impulsive response function that is a fourth-rank tensor. The corresponding cumulant expansion expression for the nonlinear response function associated with the case when all three field−matter interactions were between the molecular electric dipole and external electric field was already presented in section 4.4. Using the same theoretical results, it was found that

$$R^{(3)}(t_2,t_1) = \left(\frac{i}{\hbar}\right)^2 \theta(t_2)\,\theta(t_1)\sum_{abc} P_a(t_0)[\boldsymbol{\alpha}_{ab}\boldsymbol{\mu}_{bc}\boldsymbol{\mu}_{ca} \exp(-i\omega_{ba}t_2 - i\omega_{ca}t_1)G_{bc}^{(1)}(t_2,t_1) - \boldsymbol{\mu}_{ab}\boldsymbol{\alpha}_{bc}\boldsymbol{\mu}_{ca} \exp(-i\omega_{cb}t_2 - i\omega_{ca}t_1)G_{bc}^{(2)}(t_2,t_1)] + c.c. \tag{7-4}$$

where the line shape functions $G_{bc}^{(1)}(t_2,t_1)$ and $G_{bc}^{(2)}(t_2,t_1)$ were given in eqs 4-39 and 4-40.

The result in eq 7-4 was obtained by using the vibrational eigenstate representation—note that the states *a*, *b*, and *c* represent the vibrational quantum states. However, sometimes it is rather convenient and useful to express the nonlinear response function in the vibrational coordinate representation. This can be achieved by expanding the dipole and polarizability operators as power series of the system vibrational coordinates. The potential anharmonicity of the vibrational chromophores and the dipole and polarizability operators are assumed to be written as

$$V_{anh}(\mathbf{Q}) = \sum_{jkl}\left(\frac{V}{\partial Q_j Q_k Q_l}\right)_0 Q_j Q_k Q_l + ... \tag{7-5}$$

$$\boldsymbol{\mu} = \boldsymbol{\mu}(\mathbf{Q}=0) + \sum_i\left(\frac{\partial\boldsymbol{\mu}}{\partial Q_i}\right)_0 Q_i + \frac{1}{2}\sum_j\sum_i\left(\frac{\partial^2\boldsymbol{\mu}}{\partial Q_i\,\partial Q_j}\right)_0 Q_i Q_j + ... \tag{7-6}$$

$$\boldsymbol{\alpha} = \boldsymbol{\alpha}(\mathbf{Q}=0) + \sum_i\left(\frac{\partial\boldsymbol{\alpha}}{\partial Q_i}\right)_0 Q_i + \frac{1}{2}\sum_j\sum_i\left(\frac{\partial^2\boldsymbol{\alpha}}{\partial Q_i\,\partial Q_j}\right)_0 Q_i Q_j + ... \tag{7-7}$$

Inserting eqs 7-6 and 7-7 into eq 7-3 and considering the

cubic anharmonicities in eq 7-5, one can obtain the nonlinear response function:[509]

$$R^{(2)}(t_2,t_1) = R_{AN}(t_2,t_1) + R_{NL}(t_2,t_1) \qquad (7\text{-}8)$$

where

$$R_{AN}(t_2,t_1) = \frac{i}{\hbar^3}\sum_{i,j,k} V^{(3)}_{ijk}\alpha^{(1)}_i \mu^{(1)}_j \mu^{(1)}_k \int_0^\infty dt\, G_i(t_1+t_2-t)\, G_j(t-t_1)\, G_k(t)$$

$$R_{NL}(t_2,t_1) = -\frac{1}{\hbar^2}\sum_{j,k} \alpha^{(2)}_{jk}\mu^{(1)}_j \mu^{(1)}_k G_j(t_2)\, G_k(t_1+t_2) - \frac{1}{\hbar^2}\sum_{j,k} \alpha^{(1)}_j \mu^{(2)}_{jk} \mu^{(1)}_k G_j(t_2)\, G_k(t_1) \qquad (7\text{-}9)$$

Here, $V^{(3)}_{ijk} \equiv (\partial^3 V/\partial Q_i \partial Q_j \partial Q_k)_0$, $\mu^{(1)}_i \equiv (\partial \boldsymbol{\mu}/\partial Q_i)_0$, $\mu^{(2)}_{ij} \equiv (\partial^2 \boldsymbol{\mu}/\partial Q_i \partial Q_j)_0$, $\alpha^{(1)}_i \equiv (\partial \boldsymbol{\alpha}/\partial Q_i)_0$, and $\alpha^{(2)}_{ij} \equiv (\partial^2 \boldsymbol{\alpha}/\partial Q_i \partial Q_j)_0$. The retarded Green function of the jth system oscillator is denoted as $G_j(t)$, which is defined as

$$G_j(t) = (i/\hbar)\theta(t)\langle [Q_j(t), Q_j(0)]\rangle \qquad (7\text{-}10)$$

It should be noted that the three components in eq 7-9 are expressed in terms of products of retarded Green functions, where the Wick's theorem was used. If the system oscillator is assumed to obey the Langevin equation, i.e., a damped harmonic oscillator, the response function $G_j(t)$ is simply given as

$$G^{BO}_j(t) = \theta(t)\frac{\hbar}{iM_j\omega'_j}\exp(-\gamma_j t/2)\sin(\omega'_j t) \qquad (7\text{-}11)$$

where the renormalized frequency ω'_j is defined as $\omega'_j = [\omega_j^2 - (\gamma_j/2)^2]^{1/2}$ and γ_j is the vibrational dephasing constant. In this case when the response function is approximated to be eq 7-11, the 2D Fourier transform spectrum $\tilde{R}^{(2)}(\omega_2,\omega_1)$ can be obtained in an analytical form.[160,162,165]

From eqs 7-8 and 7-9, a set of vibrational selection rules for a nonzero IR−IR−vis FWM signal can be deduced. In order for $R_A(t_2,t_1)$ to be nonzero, the vibrational degrees of freedom should be IR- and Raman-active and the corresponding cubic anharmonicity coefficients should not be vanishingly small. Even the harmonic oscillator limit, $R^{(2)}(t_2,t_1)$, can be measurably large if the second derivatives of polarizability or the dipole moment with respect to the vibrational coordinates are finite and if the associated vibrational degrees of freedom are IR- and Raman-active.

To demonstrate the experimental possibility of IR−IR−vis FWM spectroscopy, an extensive quantum chemistry calculation study on an isolated chloroform was performed and reported in ref 510. The $CHCl_3$ molecule has 9 vibrational degrees of freedom: 2-fold degenerate asymmetric CCl bending, symmetric CCl bending, a symmetric CCl stretch, a 2-fold degenerate asymmetric CCl stretch, 2-fold degenerate CH bending, and a CH stretch. For these nine normal modes, frequencies, reduced masses, cubic potential anharmonic coefficients, transition dipole moments, transition polarizabilities, and second derivatives of dipole moments and polarizabilities with respect to the nine vibrational coordinates were all calculated by using the HF/6-311++G(2df,2pd) method. In ref 510, the symmetrized

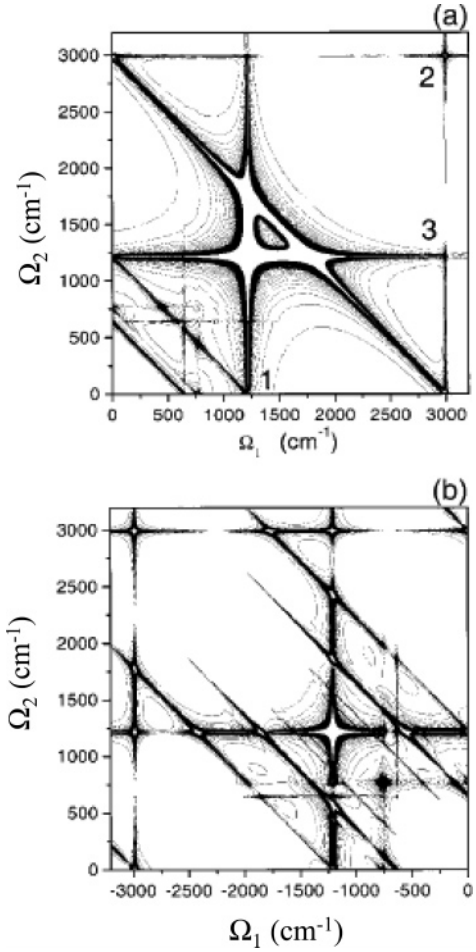

Figure 59. First (a) and second (b) quadrants of the symmetrized IR−IR−vis FWM spectrum $S_S(\omega_2,\omega_1)$ of $CHCl_3$ (see eq 7-12 for the definition of symmetrized 2D spectrum).[510]

IR−IR−vis FWM spectrum was introduced, which is defined as

$$S_S(\omega_2,\omega_1) \equiv |\tilde{R}^{(2)}(\omega_2+\omega_1,\omega_1) + \tilde{R}^{(2)}(\omega_2+\omega_1,\omega_2)| \qquad (7\text{-}12)$$

The first and second quadrants of the spectrum, where the first quadrant corresponds to the frequency region of ($\omega_1 \geq 0$, $\omega_2 \geq 0$) and the second quadrant corresponds to the frequency region of ($\omega_1 < 0$, $\omega_2 \geq 0$), were presented in ref 510 and are shown in Figure 59.

The first (second) quadrant in Figure 59a (Figure 59b) depicts the IR−IR−vis sum-frequency-generation (difference-frequency-generation) spectrum. From the quantum chemistry calculation studies, it was found that the major coupling sources are the cubic potential anharmonicities. As can be seen in Figure 59a, cross peak 3 shows the coupling between the CH bending and CH stretching vibrations, and this is a clear manifestation of the 2:1 Fermi resonance effect. From the entire 2D IR−IR−vis FWM spectrum, one can deduce the intramolecular mechanical anharmonicity coupling map that will be of use in understanding intramolecular mode-to-mode energy relaxation processes, i.e., IVR (intramolecular vibrational relaxation). Recently, the dual-frequency 2D IR photon echo spectroscopic technique also showed that coherent 2D vibrational spectroscopy can be used to elucidate the intramolecular vibrational coupling map of a complicated polyatomic molecule in condensed phases.[276,277]

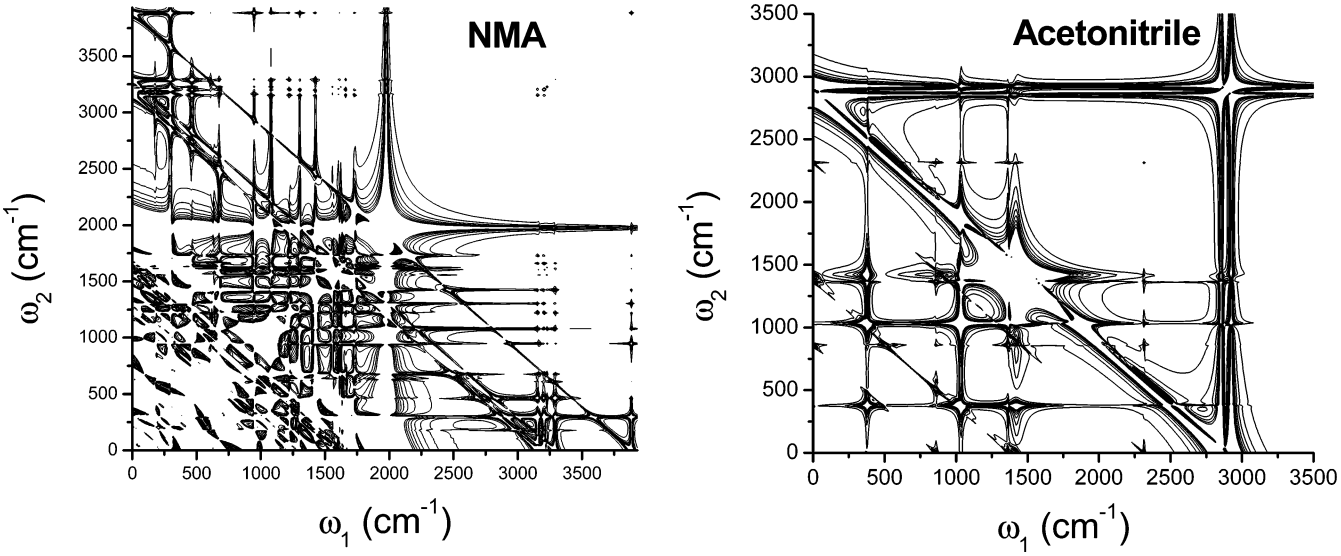

Figure 60. Symmetrized IR−IR−vis SFG spectra of *N*-methylacetamide (NMA) and acetonitrile. The same *ab initio* calculation method used to obtain the results in Figure 59 was used to obtain the parameters required in the numerical calculation. These are unpublished results.

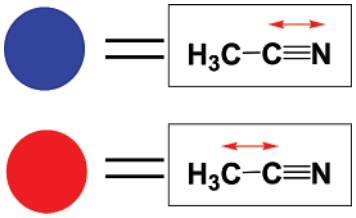

Figure 61. Two vibrational chromophores in acetonitrile. The CN and CC stretch frequencies are 2253 and 918 cm^{-1}.

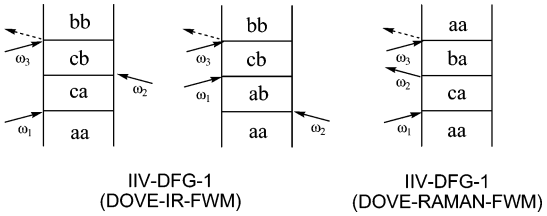

Figure 62. Double-sided Feynman diagrams associated with doubly vibrationally enhanced IR-FWM and Raman-FWM. Due to the differences in the nonlinear optical transition pathways and in the anharmonicities of the combination state, the corresponding peak frequencies are slightly different for the two cases. See ref 513 for a more detailed discussion.

By using the same computational methods, the 2D IR−IR−vis SFG spectra of N-methylacetamide and acetonitrile were calculated, and they are shown in Figure 60. In the following two subsections, two representative examples studied experimentally will be discussed to show the usefulness of the IR−IR−vis FWM spectroscopic technique.

7.2. Doubly Resonant Enhancement Effect on the IR–IR–vis FWM Signal

In the introduction to IR−IR−vis FWM spectroscopy above, an experimental result on CH_3CN was briefly mentioned, where frequency-domain 2D IR−IR−vis spectroscopy was used to directly observe the cross peak between the CC and CN stretch modes in this molecule (see the peak at (3164 cm^{-1}, 2253 cm^{-1})). Note that the CC and CN stretch mode frequencies, denoted as ω_{CC} and ω_{CN}, are 918 and 2253 cm^{-1}, respectively (Figure 61).

In this experiment, the first IR field frequency ω_1 was tuned to be in resonance with the combination band of the CC and CN stretch modes ($\omega_1 \simeq \omega_{CC} + \omega_{CN}$). Due to the combination band anharmonicity, the peak position along the ω_1 axis is not exactly identical to 3171 (=918 + 2253) cm^{-1}. The second IR field frequency was tuned around the CN stretch mode frequency. The final electronically nonresonant visible field with frequency ω_3 is Raman-scattered by the CC stretch mode, and its scattering field intensity was measured. Therefore, this experiment can be viewed as an IR−IR−vis difference frequency generation process, since the scattered field frequency is given as $\omega_s = (\omega_1 - \omega_2) + \omega_3$. The existence of this cross peak is direct evidence showing the nonzero coupling between the two modes.

Although the fitting analysis to reproduce the line shape of the cross peak in Figure 58 was successfully performed,[511] the origin of the vibrational coupling between the two stretch modes was further elucidated later by carrying out extensive quantum chemistry calculations of an isolated acetonitrile. From the nonlinear response function theory given in the previous subsection, both AN and NL couplings can contribute to the nonzero susceptibility associated with the cross peak.

From the *ab initio* geometry optimization and vibrational analysis, the frequencies, reduced masses, vibrational transition dipoles and polarizabilities, second-order derivatives of dipoles and polarizabilities, and cubic anharmonic coefficients of all twelve normal modes were determined.[513] As shown in Figure 62, two different types of nonlinear optical transition pathways contribute to the measured IR−IR−vis DFG signal, and they were called DOVE (doubly vibrational enhanced)-IR and DOVE-Raman FWM, respectively. In addition, the coherent anti-Stokes Raman scattering (CARS) and singly vibrational enhanced (SIVE) third-order nonlinear optical process can contribute to the susceptibility in the frequency-domain measurement, i.e.,

$$\chi^{(3)}(\omega_1,\omega_2) = \chi^{(3)}_{\mathrm{DOVE-IR}}(\omega_1,\omega_2) + \chi^{(3)}_{\mathrm{DOVE-RAMAN}}(\omega_1,\omega_2) + \chi^{(3)}_{\mathrm{CARS}}(\omega_1-\omega_2) + \chi^{(3)}_{\mathrm{SIVE}}(\omega_2) \quad (7\text{-}13)$$

The measured IR−IR−vis DFG spectrum is then given as

$$S(\omega_1,\omega_2) \propto |\chi^{(3)}(\omega_1,\omega_2)|^2 \tag{7-14}$$

Only the first two terms in eq 7-13 are doubly vibrational resonant contributions and can produce the cross peak in Figure 58. Before these two contributions are discussed, it is necessary to present detailed descriptions on the CARS and SIVE terms. The four vibrational quantum states are particularly important, and they are denoted as $|a\rangle = |0_{CC},0_{CN}\rangle$, $|b\rangle = |0_{CC},1_{CN}\rangle$, $|b'\rangle = |1_{CC},0_{CN}\rangle$, and $|c\rangle = |1_{CC},1_{CN}\rangle$. For example, the $|c\rangle$ state corresponds to the CC and CN stretch combination mode excited state. In the experimental frequency range, the CARS of the CC stretching mode is relevant and the CARS susceptibility[39] is given as

$$\chi^{(3)}_{CARS}(\omega_1-\omega_2) = -\frac{NF^{(3)}}{24}\left(\frac{1}{2\hbar M_{CC}\omega_{CC}}\right)\overline{\left(\frac{\partial\alpha}{\partial Q_{CC}}\right)\left(\frac{\partial\alpha}{\partial Q_{CC}}\right)_0}\left(\frac{\partial\alpha}{\partial Q_{CC}}\right)_0\frac{1}{(\omega_1-\omega_2-\omega_{b'a}+i\Gamma_{b'a})} \tag{7-15}$$

Here, N is the number density of acetonitrile and $F^{(3)}$ is the local field correction factor. Since the CARS contribution appears along the diagonal at $\omega_2 = \omega_1 - \omega_{b'a}$, it is distinctively different from the doubly resonant CC + CN cross peak.

The SIVE FWM is associated with the third-order nonlinear optical process with one vibrational resonance with ω_2-field, and it appears as a horizontally elongated peak in the 2D spectrum in Figure 58. It was found that $\chi^{(3)}_{SIVE}(\omega_2)$ is written as

$$\chi^{(3)}_{SIVE}(\omega_2) = \frac{NF^{(3)}}{48}\left(\frac{1}{2\hbar M_{CN}\omega_{CN}}\right)\overline{\left(\frac{\partial\beta}{\partial Q_{CN}}\right)\left(\frac{\partial\mu}{\partial Q_{CN}}\right)}\frac{1}{(-\omega_2-\omega_{ab}+i\Gamma_{ab})} \tag{7-16}$$

Here, β is the hyperpolarizability. The horizontal feature at $\omega_2 = \omega_{CN}$ in Figure 58 corresponds to the SIVE FWM signal, and it is again clearly distinguished from the cross peak at ($\omega_1 = \omega_{CC} + \omega_{CN}$, $\omega_2 = \omega_{CN}$).

The cross peak was shown to be produced by a sum of contributions from three different nonlinear optical transition pathways shown in Figure 62. The IR−IR−vis DFG-1 and DFG-2 that were called the DOVE-IR- and DOVE-Raman-FWM were found to be

$$\chi^{(3)}_{DOVE\text{-}IR} = -\frac{NF^{(3)}}{48}\left(\frac{1}{\hbar}\right)^2\frac{\langle b|\alpha|c\rangle\langle c|\mu|a\rangle\langle a|\mu|b\rangle}{(\omega_1-\omega_2-\omega_{cb}+i\Gamma_{cb})(\omega_1-\omega_{ca}+i\Gamma_{ca})} - \frac{NF^{(3)}}{48}\left(\frac{1}{\hbar}\right)^2\frac{\langle b|\alpha|c\rangle\langle c|\mu|a\rangle\langle a|\mu|b\rangle}{(\omega_1-\omega_2-\omega_{cb}+i\Gamma_{cb})(-\omega_2-\omega_{ab}+i\Gamma_{ab})} \tag{7-17}$$

$$\chi^{(3)}_{DOVE\text{-}Raman} = \frac{NF^{(3)}}{48}\left(\frac{1}{\hbar}\right)^2\frac{\langle a|\alpha|b\rangle\langle b|\mu|c\rangle\langle c|\mu|a\rangle}{(\omega_1-\omega_2-\omega_{ba}+i\Gamma_{ea})(\omega_1-\omega_{ca}+i\Gamma_{ca})} \tag{7-18}$$

Now, inserting the Taylor-expanded dipole and polarizability operators into eq 7-17 and taking into account the lowest-order nonzero contributions, one can obtain $\chi^{(3)}_{DOVE\text{-}IR}$ as the sum of the two contributions,

$$\chi^{(3)}_{DOVE\text{-}IR} \cong \chi^{AN}_{DOVE\text{-}IR} + \chi^{NL}_{DOVE\text{-}IR} \tag{7-19}$$

Here, the term resulting from the mechanical anharmonicity couplings is given

$$\chi^{AN}_{DOVE\text{-}IR} = \sum_{j=1}^{12}[\chi^{AN}_{DOVE\text{-}IR}]_j \tag{7-20}$$

where

$$[\chi^{AN}_{DOVE\text{-}IR}]_j = -\frac{NF^{(3)}}{48}\left(\frac{1}{\hbar}\right)^2\overline{\left[\left(\frac{\partial\alpha}{\partial Q_{CC}}\right)\left(\frac{\partial\mu}{\partial Q_j}\right)\left(\frac{\partial\mu}{\partial Q_{CN}}\right)\right]}\langle 0_{CC},1_{CN}|Q_{CC}|1_{CC},1_{CN}\rangle\langle 1_{CC},1_{CN}|Q_j|0_{CC},0^{ZZZZ}_{CN}\rangle\langle 0_{CC},0_{CN}|Q_{CN}|0_{CC},1_{CN}\rangle\left\{\frac{1}{(\omega_1-\omega_{ca}+i\Gamma_{ca})(\omega_1-\omega_2-\omega_{cb}+i\Gamma_{cb})}+\frac{1}{(-\omega_2-\omega_{ab}+i\Gamma_{ab})(\omega_1-\omega_2-\omega_{cb}+i\Gamma_{cb})}\right\} \tag{7-21}$$

In order to determine which term in the summation in eq 7-20 is dominant, one should evaluate the two-quantum transition matrix elements, $\langle 1_{CC},1_{CN}|Q_j|0_{CC},0_{CN}\rangle$, which do not vanish when the cubic anharmonic coefficients $(\partial^3V/\partial Q_{CC}\partial Q_j\partial Q_{CN})_0$ are finite and large. Treating these cubic anharmonic potential terms as a perturbation Hamiltonian, one can obtain the combination state wave function in terms of the product wave functions of perfect harmonic oscillators. It turned out that, except for the totally symmetric CH stretching and bending modes playing as promoting modes for the anharmonic coupling between the CC and CN stretches, the two coefficients, $(\partial^3V/\partial Q_{CC}{}^2\partial Q_{CN})_0$ and $(\partial^3V/\partial Q_{CN}{}^2\partial Q_{CC})_0$, are dominant in the summation of eq 7-20.

The electric anharmonicity coupling (NL) contribution, which is the second term in eq 7-19, to the DOVE-IR-FWM was found to be

$$\chi^{NL}_{DOVE\text{-}IR} = -\frac{NF^{(3)}}{48}\left(\frac{1}{\hbar}\right)^2\overline{\left(\frac{\partial\alpha}{\partial Q_{CC}}\right)\left(\frac{\partial^2\mu}{\partial Q_{CC}\,\partial Q_{CN}}\right)\left(\frac{\partial\mu}{\partial Q_{CN}}\right)}\langle 1_{CC},0_{CN}|Q_{CC}|1_{CC},1_{CN}\rangle\langle 1_{CC},1_{CN}|Q_{CC}Q_{CN}|0_{CC},0_{CN}\rangle\langle 0_{CC},0_{CN}|Q_{CN}|1_{CC},0_{CN}\rangle\left\{\frac{1}{(\omega_1-\omega_{ca}+i\Gamma_{ca})(\omega_1-\omega_2-\omega_{cb}+i\Gamma_{cb})}+\frac{1}{(-\omega_2-\omega_{ab}+i\Gamma_{ab})(\omega_1-\omega_2-\omega_{cb}+i\Gamma_{cb})}\right\} \tag{7-22}$$

The most important factor inducing the coupling between the two modes is $(\partial^2\mu/\partial Q_{CC}\partial Q_{CN})$. From the *ab initio* calculations, it was found that the absolute magnitudes of the mechanical and electrical anharmonicity contributions to the DOVE-IR-FWM are similar.

In addition to the IR−IR−vis DFG-1, one can obtain similar expressions for the IR−IR−vis DFG-2 (DOVE-

Raman-FWM), and they were calculated by following the same procedure. It should be noted that the peak positions of these two different contributions, IR−IR−vis DFG-1 and DFG-2, are slightly different due to the anharmonicity of the combination band. Second, it is interesting to note that the sign of the DOVE-Raman contribution to the IR−IR−vis DFG susceptibility is exactly the opposite of the DOVE-IR. Third, it was found that the magnitude of the DOVE-Raman-FWM is comparable with that of the DOVE-IR-FWM. Consequently, the experimentally measured cross peak in Figure 58 resulted from complicated interferences between the four terms in eq 7-13. Nevertheless, it was clearly shown that the cross peak in the IR−IR−vis FWM spectrum originates from intramolecular vibrational couplings. It will be interesting to use the same calculation method for the prediction of 2D vibrational spectra of polypeptides and to apply the IR−IR−vis FWM spectroscopic technique for structure determination of complex molecules in the future.

7.3. Application to Adsorbed Molecules on Metal Surfaces

The IR−IR−vis SFG spectroscopy experiment was performed for CO molecules adsorbed on a Ru metal surface, and the main theoretical and experimental results were presented in ref 514. This experiment was born out as an extension of the lower-order nonlinear optical spectroscopy such as IR−vis SFG, which will be discussed in detail in section 9−3. Despite the success of the IR−vis SFG method, it is one of the 1D vibrational spectroscopic techniques, whereas the IR−IR−vis SFG can be a 2D spectroscopy if the two IR field frequencies are independently tuned to measure the susceptibility in the frequency domain or if the time-domain response function is directly measured with ultrafast IR and visible pulses.

The experimental observation of IR−IR−vis SFG from the CO stretch vibration of CO molecules adsorbed on the Ru(001) surface demonstrated that the IR−IR−vis SFG method can provide useful information on the intermolecular coupling strength and intermolecular distances between neighboring CO molecules by comparing signals at different CO fractional coverage.[514−516] In the experiment, a ∼150 fs infrared pulse (10 μJ energy, full width at half-maximum ∼100 cm^{-1}) centered at ∼2000 cm^{-1} (5 μm), resonant with the C−O stretch vibration, and a narrow-band 800 nm pulse (5 cm^{-1}, ∼4 ps pulse duration) were overlapped spatially and temporally onto a single-crystal Ru(001) surface in ultrahigh vacuum onto which typically 0.33 monolayers of CO are adsorbed. As shown in Figure 63, a large IR−vis SFG signal was observed at 690 nm (=800 nm + 5 μm), and under the appropriate phase-matching conditions, achieved by rotating the crystal in the vertical plane, the IR−IR−vis SFG signal at 605 nm (=800 nm + 5 μm + 5 μm) was observed as well. In addition to the IR−vis SFG and IR−IR−vis SFG spectra, the nonresonant contributions from the bare Ru(001) surface are also shown in the measured spectrum. The SFG peak in the bottom panel of Figure 63 was interpreted as follows. Initially, the molecular system is in the ground vibrational state $|g\rangle$. Then, the first interaction of the adsorbed molecule with the infrared field at ω_1 induces a transition from $|g\rangle$ to $|a\rangle$, where $|a\rangle$ is one of the vibrationally excited states that are either monomeric excited-state or delocalized CO phonon modes depending on the CO coverage. The second interaction with the ω_2 infrared field induces the second vibrational transition from $|a\rangle$ to $|b\rangle$. Then, finally the third effective visible field−matter interaction (ω_3) creates a sum-frequency field whose frequency equals the sum of the three injected fields, $\omega_1 + \omega_2 + \omega_3$. Conservation of momentum parallel to the surface dictates that the associated parallel component of the wave vector $\mathbf{k}^{//}$ of the IR−IR−vis SFG field is given by $\mathbf{k}^{//}_1 + \mathbf{k}^{//}_2 + \mathbf{k}^{//}_3$.

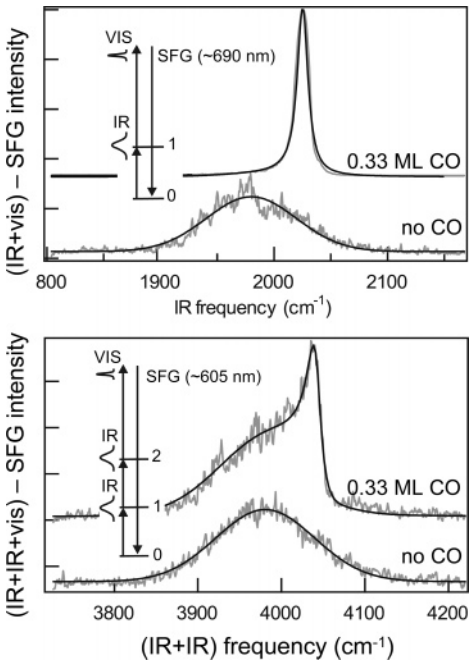

Figure 63. Upper panel: IR−vis SFG spectrum of the C−O stretching vibration of 0.33 ML (monolayer) of CO on Ru ($\sqrt{3} \times \sqrt{3}$)-CO/Ru(001) (12.0 cm^{-1} fwhm (full-width-at-half-maximum)) at 95 K and the nonresonant SFG signal from the bare surface. Lower panel: IR−IR−vis SFG spectrum from the ($\sqrt{3} \times \sqrt{3}$)-CO/Ru(001) surface, as well as from the bare surface. Scaling factors indicate the relative intensities of the signals. Lines through the data are fits.[515]

The center of the IR−vis SFG peak is at 2020 cm^{-1}, which is the fundamental transition frequency of the CO stretching mode at the fractional coverage of 0.33 ML (monolayer). The IR−IR−vis SFG signal peaks at 4040 cm^{-1}, which is exactly twice the fundamental transition frequency. As a second piece of information, it was found that the integrated IR−IR−vis SFG peak intensity of the resonant contribution does not change as the CO coverage increases from 0.33 to 0.68 ML. This is in strong contrast with the IR reflection absorption signal intensity as well as with the IR−vis SFG signal. On the basis of these experimental observations, it was suggested that (1) the intermolecular coupling effects should be incorporated, (2) the singly vibrationally resonant IR−IR−vis SFG contribution to the signal is negligible, (3) the cascading contribution can also be ignored, and (4) the resonant signal is from the doubly vibrationally resonant IR−IR−vis SFG of coupled admolecules on the metal surface at this high fractional coverage.

To theoretically describe this doubly resonant IR−IR−vis SFG spectroscopy of CO on a metal surface, it was necessary to obtain relationships of the molecular polarizability and hyperpolarizabilities with the macroscopic linear and nonlinear susceptibilities.[514] It begins with expanding the local field $E_l(\mathbf{r},t)$, Maxwell field $E(\boldsymbol{r},t)$, and polarization $P(\boldsymbol{r},t)$ in a discrete Fourier series, i.e., $E_l(\mathbf{r},t) = \sum_j [E_l(\mathbf{k}_j,\omega_j) \exp(i\mathbf{k}_j\cdot\mathbf{r} - i\omega_j t) + c.c.]$, etc. Here, the index j labels those

modes relevant for the experiment. The electric field and polarization are all vectors, but only the components normal to the surface are relevant and considered here. Since the magnitudes of the optical and IR wavevectors are usually small compared to the length scale of microscopic fluctuations, the system can be assumed to be homogeneous.

The polarization can be written as a power series with respect to local fields, i.e.,

$$P(\mathbf{r},t) = \rho_0 \sum_j \alpha(\omega_j)\, E_l(\mathbf{k}_j,\omega_j) \exp(i\mathbf{k}_j\cdot\mathbf{r} - i\omega_j t) + \rho_0 \sum_{j\geq n} \beta(\omega_j,\omega_n)\, E_l(\mathbf{k}_j,\omega_j)\, E_l(\mathbf{k}_n,\omega_n) \exp[(i\mathbf{k}_j+\mathbf{k}_n)\cdot\mathbf{r} - i(\omega_j+\omega_k)t] + \rho_0 \sum_{j\geq n\geq m} \gamma(\omega_j,\omega_n,\omega_m)\, E_l(\mathbf{k}_j,\omega_j)\, E_l(\mathbf{k}_n,\omega_n)\, E_l(\mathbf{k}_m,\omega_m) \exp[i(\mathbf{k}_j+\mathbf{k}_n+\mathbf{k}_m)\cdot\mathbf{r} - i(\omega_j+\omega_n+\omega_m)t] + \ldots \quad (7\text{-}23)$$

The three terms in eq 7-23 denote the linear and second- and third-order nonlinear optical contributions to the polarization. These are proportional to the linear polarizability, first hyperpolarizability, and second hyperpolarizability of a single molecule, respectively, denoted as α, β, and γ. The number density is denoted as ρ_0. Introducing the susceptibilities, one can expand the polarization in a power series of $E(\mathbf{r},t)$ as

$$P(\mathbf{r},t) = P^{(1)}(\mathbf{r},t) + P^{(2)}(\mathbf{r},t) + P^{(3)}(\mathbf{r},t) + \ldots \quad (7\text{-}24)$$

where

$$P^{(1)}(\mathbf{r},t) = \sum_j \chi^{(1)}(-\mathbf{k}_j,-\omega_j;\mathbf{k}_j,\omega_j)\, E(\mathbf{k}_j,\omega) \exp(i\mathbf{k}_j\cdot\mathbf{r} - i\omega_j t)$$

$$P^{(2)}(\mathbf{r},t) = \sum_{j\geq n} \chi^{(2)}(-\mathbf{k}_j-\mathbf{k}_n,-\omega_j-\omega_n;\mathbf{k}_j,\omega_j,\mathbf{k}_n,\omega_n)\, E(\mathbf{k}_j,\omega_j)\, E(\mathbf{k}_n,\omega_n) \exp[i(\mathbf{k}_j+\mathbf{k}_n)\cdot\mathbf{r} - i(\omega_j+\omega_n)t]$$

$$P^{(3)}(\mathbf{r},t) = \sum_{j\geq n\geq m} \chi^{(3)}(-\mathbf{k}_j-\mathbf{k}_n-\mathbf{k}_m,-\omega_j-\omega_n-\omega_m;\mathbf{k}_j,\omega_j,\mathbf{k}_n,\omega_n,\mathbf{k}_m,\omega_m)\, E(\mathbf{k}_j,\omega_j)\, E(\mathbf{k}_n,\omega_n)\, E(\mathbf{k}_m,\omega_m) \exp[i(\mathbf{k}_j+\mathbf{k}_n+\mathbf{k}_m)\cdot\mathbf{r} - i(\omega_j+\omega_n+\omega_m)t] \quad (7\text{-}25)$$

Here, the local field is related to the Maxwell field as

$$E_l(\mathbf{k},t) = E(\mathbf{k},t) - \rho_0^{-1} U(\mathbf{k})\, P(\mathbf{k},t) \quad (7\text{-}26)$$

where the second term represents the electrostatic field created by all other particles and represents the dipole−dipole and dipole−imaginary-dipole interactions etc.[517,518]

The first-order polarization is then $E_l^{(1)}(\mathbf{k},t) = E(\mathbf{k},t) - \rho_0^{-1} U(\mathbf{k})\, P^{(1)}(\mathbf{k},t)$. Inserting this equation into eq 7-23 and from the definition of the linear susceptibility, one can find that the linear susceptibility can be written as

$$\chi^{(1)}(-\mathbf{k},-\omega;\mathbf{k},\omega) = \frac{\rho_0 \alpha(\omega)}{1 + \alpha(\omega)\, U(\mathbf{k})} \quad (7\text{-}27)$$

Defining the local field correction factor as

$$S(\mathbf{k},\omega) \equiv \frac{1}{1 + \alpha(\omega)\, U(\mathbf{k})} \quad (7\text{-}28)$$

The local and Maxwell fields are related to each other as

$$E_l^{(1)}(\mathbf{k},\omega) = S(\mathbf{k},\omega)\, E(\mathbf{k},\omega) \quad (7\text{-}29)$$

Now, following the same procedure above, it was shown that the third-order susceptibility is given by the sum of direct and cascading contributions,

$$\chi^{(3)}(-\mathbf{k},-\omega;\mathbf{k}_1,\omega_1,\mathbf{k}_2,\omega_2,\mathbf{k}_3,\omega_3) = \chi^{(3)}_{\mathrm{dir}} + \chi^{(3)}_{\mathrm{cas}} \quad (7\text{-}30)$$

where

$$\chi^{(3)}_{\mathrm{dir}}(-\mathbf{k},-\omega;\mathbf{k}_1,\omega_1,\mathbf{k}_2,\omega_2,\mathbf{k}_3,\omega_3) = \rho_0 \gamma(\omega_1,\omega_2,\omega_3)\, S(\boldsymbol{k}_1,\omega_1)\, S(\boldsymbol{k}_2,\omega_2)\, S(\boldsymbol{k}_3,\omega_3)\, S(\boldsymbol{k},\omega) \quad (7\text{-}31)$$

and

$$\chi^{(3)}_{\mathrm{cas}}(-\mathbf{k},-\omega;\mathbf{k}_1,\omega_1,\mathbf{k}_2,\omega_2,\mathbf{k}_3,\omega_3) = \rho_0[\beta(\omega_1,\omega_2)\, \beta(\omega_1+\omega_2,\omega_3)\, T(\mathbf{k}_1+\mathbf{k}_2,\omega_1+\omega_2) + \beta(\omega_1,\omega_3)\, \beta(\omega_1+\omega_3,\omega_2)\, T(\mathbf{k}_1+\mathbf{k}_3,\omega_1+\omega_3) + \beta(\omega_2,\omega_3)\, \beta(\omega_2+\omega_3,\omega_1)\, T(\mathbf{k}_2+\mathbf{k}_3,\omega_2+\omega_3)]\, S(\mathbf{k}_1,\omega_1)\, S(\mathbf{k}_2,\omega_2)\, S(\mathbf{k}_3,\omega_3)\, S(\mathbf{k},\omega) \quad (7\text{-}32)$$

Here, the auxiliary function, $T(\mathbf{k},\omega)$, is defined as

$$T(\mathbf{k},\omega) \equiv -U(\mathbf{k})\, S(\mathbf{k},\omega) \quad (7\text{-}33)$$

The direct third-order nonlinear optical process is determined by the molecular second hyperpolarizability, $\gamma(\omega_1,\omega_2,\omega_3)$, whereas the cascading contributions are related to the first hyperpolarizability $\beta(\omega_1,\omega_2)$. For the IR−IR−vis SFG experiment, the two IR field frequencies are assumed to be independently controllable and the following notations will be used,

$$\omega_1 = \omega_{\mathrm{ir},1}, \quad \omega_2 = \omega_{\mathrm{ir},2}, \quad \text{and} \quad \omega_3 = \omega_{\mathrm{vis}} \quad (7\text{-}34)$$

The wavevector and frequency of the IR−IR−vis SFG field are, respectively,

$$\mathbf{k} = \mathbf{k}_1 + \mathbf{k}_2 + \mathbf{k}_3 \quad \text{and} \quad \omega_{\mathrm{IIV-SFG}} = \omega_1 + \omega_2 + \omega_3 \quad (7\text{-}35)$$

Since the visible field frequency is far from resonance with electronic as well as vibrational transitions, the following approximations can be made, i.e.,

$$\alpha(\omega_3) \cong \alpha_e, \quad \alpha(\omega_1+\omega_3) = \alpha(\omega_2+\omega_3) \cong \alpha_e, \quad \text{and} \quad \alpha(\omega_{\mathrm{IIV-SFG}}) \cong \alpha_e \quad (7\text{-}36)$$

where α_e is the electronic polarizability (see eq 7-40 below). Then, the IR−IR−vis SFG susceptibility can be written in terms of the molecular first and second hyperpolarizabilities as

$$\chi^{(3)}_{\mathrm{IIV-SFG}} = \chi^{\mathrm{direct}}_{\mathrm{IIV-SFG}} + \chi^{\mathrm{cascading}}_{\mathrm{IIV-SFG}} \quad (7\text{-}37)$$

where

$$\chi^{\mathrm{direct}}_{\mathrm{IIV-SFG}} \propto \frac{c\gamma(\omega_1,\omega_2,\omega_3)}{[1 + c\alpha(\omega_1)U_0][1 + c\alpha(\omega_2)U_0][1 + c\alpha_e U_0]^2} \quad (7\text{-}38)$$

$$\chi_{\mathrm{IIV-SFG}}^{\mathrm{cascading}} \propto -\Bigg[c^2\beta(\omega_1,\omega_2)\,\beta(\omega_1+\omega_2,\omega_3)\left\{\frac{U_0}{1+c\alpha(\omega_1+\omega_2)U_0}\right\} + c^2\beta(\omega_1,\omega_3)\,\beta(\omega_1+\omega_3,\omega_2)\left\{\frac{U_0}{1+c\alpha(\omega_1+\omega_3)U_0}\right\} + c^2\beta(\omega_2,\omega_3)\,\beta(\omega_2+\omega_3,\omega_1)\left\{\frac{U_0}{1+c\alpha_e U_0}\right\}\Bigg]\frac{1}{[1+c\alpha(\omega_1)U_0][1+c\alpha(\omega_2)U_0][1+c\alpha_e U_0]^2} \quad (7\text{-}39)$$

Here, the molecular polarizability can be written as the sum of the electronic and vibrational contributions, i.e.,

$$\alpha(\omega) = \alpha_e + \frac{\alpha_\nu}{1-(\omega/\omega_0{}^2)(\omega+2i\Gamma)} \quad (7\text{-}40)$$

where the vibrational frequency of the CO stretching mode for an isolated (from other CO molecules) CO molecule on a metal surface is denoted as ω_0, and the vibrational dephasing constant is denoted as Γ, which was estimated to be $\Gamma = 6.1\ \mathrm{cm}^{-1}$ for the IR−IR−vis SFG of the 0.33 ML sample, in this case. The electronic and vibrational polarizabilities are denoted as α_ν in eq 7-40, and they were estimated to be $\alpha_e = 3.2\ \text{Å}^3$ and $\alpha_\nu = 0.52\ \text{Å}^3$, respectively. From the experimentally measured center frequencies of the IR−vis SFG spectra for $0 < \theta$ (fractional coverage) < 0.5 ML, it was found that $\omega_0 = 1982.1\ \mathrm{cm}^{-1}$. Since the magnitudes of the IR and visible wavevectors are negligibly small in comparison to the length scale of the system, $|\mathbf{k}_{\mathrm{ir}}| = |\mathbf{k}_{\mathrm{vis}}| \cong 0$, $U_0 \equiv U(\mathbf{k}=0)$ is the only relevant quantity. Note that the dipole sum U_0 takes into account the lateral interactions between adsorbed CO molecules on the metal surface. By using the IR−vis SFG experimental results and fitting analysis, the dipole sum U_0 was estimated to be $U_0 = 0.082\ \text{Å}^{-3}$. The theoretical results in eqs 7-38 and 7-39 are valid for an incomplete monolayer, and the coverage of the adsorbed molecules, denoted as c in these equations, varies from 0 to 1, as the fractional coverage increases from 0 to 0.33 ML. Note that, at $\theta = 0.33$, the adsorbed CO molecules form a well-ordered $(\sqrt{3}\times\sqrt{3})$ structure.

Since the total signal is proportional to the absolute square of the susceptibility, the interference between the two distinctive contributions, $\chi_{\mathrm{IIV-SFG}}^{\mathrm{direct}}$ and $\chi_{\mathrm{IIV-SFG}}^{\mathrm{cascading}}$, may also play a role. However, as discussed in ref 515, the cascading contribution can be safely ruled out in comparison to the direct IR−IR−vis SFG contribution for the CO/Ru(001) system. The direct contribution to the IR−IR−vis SFG susceptibility is mainly determined by the molecular second hyperpolarizability $\gamma(\omega_1,\omega_2,\omega_3)$, which represents the IR−IR−vis SFG by an isolated (from the other adsorbed molecules) CO molecule adsorbed on a surface. A detailed theory on $\gamma(\omega_1,\omega_2,\omega_3)$ for the IR−IR−vis SFG was presented in ref 519, and it can be written as

$$\gamma(\omega_{\mathrm{ir}},\omega_{\mathrm{ir}},\omega_{\mathrm{vis}}) = \gamma_{\mathrm{non}} + \frac{\gamma_{\mathrm{res}}}{(1-\omega_{\mathrm{ir}}/\omega_0 - i\Gamma/\omega_0)(2-\Delta/\omega_0 - 2\omega_{\mathrm{ir}}/\omega_0 - 2i\Gamma/\omega_0)} \quad (7\text{-}40)$$

where the vibrationally nonresonant and resonant parts are weighted by γ_{non} and γ_{res}, respectively. If the molecular eigenstates of a CO stretch are denoted as $|0\rangle$, $|1\rangle$, and $|2\rangle$, the IR−IR−vis SFG process of a single molecule involves a sequence of vibrational transitions, i.e., $|0\rangle \rightarrow |1\rangle \rightarrow |2\rangle \rightarrow |0\rangle$. Note that the last transition from $|2\rangle$ to $|0\rangle$ is usually forbidden unless there are mechanical or electronic anharmonicities (see the discussion in section 7-1). Although the first transition frequency is ω_0, the second transition frequency from $|1\rangle$ to $|2\rangle$ is $\omega_0 - \Delta$, where Δ is related to the molecular anharmonicity. This quantity, Δ, was already estimated to be $54.4\ \mathrm{cm}^{-1}$, so that $\omega_0 = 1982.1$ and $2\omega_0 - \Delta = 3909.8\ \mathrm{cm}^{-1}$.[520,521] By using this theory, it was possible to quantitatively describe all experimental results for IR−IR−vis SFG with respect to the fractional coverage.

The examples discussed in this subsection are the only IR−IR−vis SFG experimental results on the vibrational interactions of adsorbed molecules on a metal surface. However, this is not a truly 2D experiment because neither frequency scanning nor time resolution of the two IR pulses was achieved for this experiment. Consequently, the measured spectrum was plotted with respect to (IR + IR) frequency. However, it should be emphasized that, since, in principle, the two infrared field frequencies are independently tunable, the measured susceptibility or the IR−IR−vis SFG signal intensity can be displayed in the two-dimensional frequency space. Thus, not only the diagonal peaks but also the off-diagonal peaks can be measured by scanning the two IR frequencies. Due to the screening factors in eq 7-38, not only the precise locations of the diagonal and cross peaks but also the integrated intensity will be notably different for different fractional coverage. Therefore, the IR−IR−vis SFG experiment can be of use in studying vibrational couplings between different molecules, including biomolecules adsorbed on surfaces.

8. Two-Dimensional Three-Wave-Mixing Spectroscopy: Second-Order Optical Acitivity Measurement Technique

The coherent 2D spectroscopic methods discussed in the previous sections are either four- or six-wave-mixing techniques. In general, an odd-number-wave-mixing technique has not been used as a potentially useful coherent multidimensional spectroscopic technique for an optical sample in an isotropic medium. As an example, due to the centrosymmetry of the solution sample, the three-wave-mixing (TWM) signal vanishes because the rotational average of the third-rank tensorial response function or the susceptibility over the random distribution of molecular orientations becomes zero within the electric dipole approximation.[522,523] Recently, however, it was theoretically shown that the TWM signal is detectably large when the dissolved solute has chiral properties, so that the antisymmetric Raman tensor elements do not vanish, or when the two-quantum transition dipole matrix elements are nonzero due to couplings between two chromophores in a chiral coupled multichromophore system.[41−44,524−529] An experimental demonstration for the former case was performed by employing IR−vis sum-frequency-generation spectroscopy, where the signal is plotted as a function of the IR frequency and typically the visible light is nonresonant with respect to the electronic transitions of the chromophore (limonene in this case).[527] This method is a 1D nonlinear optical spectroscopic technique probing vibrational optical activity. In addition, one can use circularly polarized lights to generate IR−vis SFG fields, as theoretically shown in refs 41 and 43. This will be discussed in section 9-3.

As a 2D *surface* vibrational spectroscopy, IR−IR sum (or difference)-frequency-generation was shown to be a useful technique revealing vibrational couplings between vibrational chromophores and shedding light on the local structure and dynamics of molecules adsorbed on a surface or at an interface.[530] However, there is no experimental report on such doubly resonant 2D IR−IR SFG (or DFG) experiments on adsorbed molecular systems, such as proteins, yet. Furthermore, doubly resonant TWM was proven to be useful in studying chiral coupled multichromophore systems dissolved in bulk solutions, and it could serve as an alternative coherent 2D electronic or vibrational spectroscopic technique. Typically one-quantum forbidden electronic or vibrational transition becomes allowed if the interaction-induced effect and second-order nonlinearities of the dipole moment are taken into consideration. In this section, we will summarize the nonlinear response theory for TWM spectroscopy of chiral molecules and discuss recent numerical simulation studies of peptides to demonstrate its experimental feasibility.

8.1. Nonlinear Response Function Theory

From eq 3-10 in section 3.1, the third-rank tensorial nonlinear response function associated with TWM spectroscopy is given as

$$R(t_2,t_1) = -\hbar^{-2}\langle[[\boldsymbol{\mu}(t_1+t_2),\boldsymbol{\mu}(t_1)],\boldsymbol{\mu}(0)]\rangle \qquad (8\text{-}1)$$

By expanding the two commutators in eq 8-1, the response function defined above can be written as

$$R = -\hbar^{-2}\langle e^{iH(t_1+t_2)/\hbar}\boldsymbol{\mu}e^{-iHt_2/\hbar}\boldsymbol{\mu}e^{-iHt_1/\hbar}\boldsymbol{\mu} - e^{iHt_1/\hbar}\boldsymbol{\mu}e^{iHt_2/\hbar}\boldsymbol{\mu}e^{-iH(t_1+t_2)/\hbar}\boldsymbol{\mu}\rangle + c.c. \qquad (8\text{-}2)$$

where *c.c.* denotes a complex conjugate. From eq 4-36, the [*ijk*]-element of the third-rank tensorial nonlinear response function is found to be[74,75,531]

$$R_{ijk}(t_2,t_1) = -\hbar^{-2}\sum_{abc}P_a\{\overline{[\boldsymbol{\mu}_{ab}\boldsymbol{\mu}_{bc}\boldsymbol{\mu}_{ca}]}_{ijk}\exp(-i\omega_{ba}t_2 - i\omega_{ca}t_1)G^{+}_{bc}(t_2,t_1) - \overline{[\boldsymbol{\mu}_{ab}\boldsymbol{\mu}_{bc}\boldsymbol{\mu}_{ca}]}_{ijk}\exp(-i\omega_{cb}t_2 - i\omega_{ca}t_1)G^{-}_{bc}(t_2,t_1)\} + \text{c.c.} \qquad (8\text{-}3)$$

where the two line shape functions $G^{+}_{bc}(t_2,t_1)$ and $G^{-}_{bc}(t_2,t_1)$ in eq 8-3 were already given in eqs 4-39 and 4-40.

Here, the important factor determining the signal field amplitude is $\overline{[\boldsymbol{\mu}_{ab}\boldsymbol{\mu}_{bc}\boldsymbol{\mu}_{ca}]}_{ijk}$, where the bar in this expression represents the rotational average of the third-rank tensor $\boldsymbol{\mu}_{ab}\boldsymbol{\mu}_{bc}\boldsymbol{\mu}_{ca}$. Carrying out the rotational averaging over the random distribution,[523] one can find that

$$\overline{[\boldsymbol{\mu}_{ac}\boldsymbol{\mu}_{cb}\boldsymbol{\mu}_{ba}]}_{ijk} = \frac{1}{6}\epsilon_{ijk}\sum_{\lambda,\mu,\nu}\epsilon_{\lambda\mu\nu}[\boldsymbol{\mu}_{ac}]_\lambda[\boldsymbol{\mu}_{cb}]_\mu[\boldsymbol{\mu}_{ba}]_\nu \qquad (8\text{-}4)$$

where ϵ_{ijk} is the Levi−Civita epsilon. One can rewrite the right-hand side of eq 8-4 as

$$\overline{[\boldsymbol{\mu}_{ac}\boldsymbol{\mu}_{cb}\boldsymbol{\mu}_{ba}]}_{ijk} = \frac{1}{6}\epsilon_{ijk}\boldsymbol{\mu}_{ac}\cdot(\boldsymbol{\mu}_{cb}\times\boldsymbol{\mu}_{ba}) \qquad (8\text{-}5)$$

To make $\overline{[\boldsymbol{\mu}_{ab}\boldsymbol{\mu}_{bc}\boldsymbol{\mu}_{ca}]}_{ijk}$ nonzero, the three indices "*ijk*" should be different from one another due to the Levi−Civita epsilon factor. That is to say, the two incident IR beam polarizations and the coherently emitting IR−IR SFG or DFG field polarization should be mutually perpendicular to one another. Without any loss of generality, the *ZYX* tensor element of $\overline{[\boldsymbol{\mu}_{ac}\boldsymbol{\mu}_{cb}\boldsymbol{\mu}_{ba}]}$, which is the experimentally measured component, is considered and then $\overline{[\boldsymbol{\mu}_{ac}\boldsymbol{\mu}_{cb}\boldsymbol{\mu}_{ba}]}_{ZYX}$ is found to be

$$\overline{[\boldsymbol{\mu}_{ac}\boldsymbol{\mu}_{cb}\boldsymbol{\mu}_{ba}]}_{ZYX} = \frac{1}{6}\boldsymbol{\mu}_{ac}\cdot(\boldsymbol{\mu}_{cb}\times\boldsymbol{\mu}_{ba}) \qquad (8\text{-}6)$$

Here, it should be noted that the three transition dipole vectors on the right-hand side of eq 8-6 are those in a *molecule-fixed* frame. From eq 8-6, one can immediately find that the three transition dipole vectors should not be on a single plane to make the above dot−cross product $\boldsymbol{\mu}_{ac}\cdot(\boldsymbol{\mu}_{cb}\times\boldsymbol{\mu}_{ba})$ nonzero. Consequently, when the three transition dipole vectors $\boldsymbol{\mu}_{ac}$, $\boldsymbol{\mu}_{cb}$, and $\boldsymbol{\mu}_{ba}$, in a molecule-fixed frame, do not lie on a common plane and when the angle between $\boldsymbol{\mu}_{cb}$ and $\boldsymbol{\mu}_{ba}$ is neither 0 nor π, the quantity $\boldsymbol{\mu}_{ac}\cdot(\boldsymbol{\mu}_{cb}\times\boldsymbol{\mu}_{ba})$ does not vanish.

In the cases of the IR−IR SFG and DFG, the corresponding signal fields have frequencies of $\omega_1+\omega_2$ and $\omega_1-\omega_2$ and the wave vectors $\mathbf{k}_1+\mathbf{k}_2$ and $\mathbf{k}_1-\mathbf{k}_2$, respectively. The *z* components of the second-order polarization vectors are found to be

$$P_Z^{\mathrm{SFG}}(\mathbf{k}_s,t) = \int_0^\infty dt_2\int_0^\infty dt_1\, R_{ZYX}(t_2,t_1)\,E_2(t-t_2)\,E_1(t-t_2-t_1)\exp[i(\omega_2+\omega_1)t_2 + i\omega_1 t_1]$$

$$P_Z^{\mathrm{DFG}}(\mathbf{k}_s,t) = \int_0^\infty dt_2\int_0^\infty dt_1\, R_{ZYX}(t_2,t_1)\,E_2(t-t_2)\,E_1(t-t_2-t_1)\exp[i(\omega_1-\omega_2)t_2 + i\omega_1 t_1] \qquad (8\text{-}7)$$

where the first and second IR beam polarization directions are assumed to be parallel to the *Y* and *X* axes in a space-fixed frame, respectively. The sum or difference frequency field amplitude is linearly proportional to the above second-order polarization, and its intensity is proportional to $|P_Z(\mathbf{k}_s,t)|^2$. In the case when a heterodyne-detection scheme is used, one can separately measure the real and imaginary parts of the second-order polarization.

If the SFG and DFG measurements are performed in the frequency domain by using temporally broad beams, the corresponding doubly resonant SFG susceptibilities are given as

$$\chi_Z^{\mathrm{SFG}}(-\omega_s;\omega_2,\omega_1) = \int_0^\infty dt_2\int_0^\infty dt_1\, R_{ZYX}(t_2,t_1)\{\exp[i(\omega_2+\omega_1)t_2 + i\omega_1 t_1] + \exp[i(\omega_2+\omega_1)t_2 + i\omega_2 t_1]\} \qquad (8\text{-}8)$$

$$\chi_Z^{\mathrm{DFG}}(-\omega_s;\omega_2,\omega_1) = \int_0^\infty dt_2\int_0^\infty dt_1\, R_{ZYX}(t_2,t_1)\{\exp[i(\omega_1-\omega_2)t_2 + i\omega_1 t_1] + \exp[i(\omega_2-\omega_1)t_2 + i\omega_2 t_1]\} \qquad (8\text{-}9)$$

Since there is no time ordering in the interactions of the molecular system with the two external fields, the susceptibility, $\chi_Z(-\omega_s;\omega_2,\omega_1)$, is a symmetric function with respect to ω_1 and ω_2.

8.2. Two-Electronic-Level Dimer System

As a model system, a coupled electronic chromophore system was considered, where each monomer was assumed to be a two-level system as usual. The basic model

Hamiltonian for such a coupled two-electronic-level dimer system was already discussed in section 6.1. The electronic structure of the dimer can be considered as a four-level system, i.e., the ground state, two one-exciton states, and one two-exciton state. Considering the case when two ultrafast laser pulses are used to create consecutive electronic coherence states and when the SFG or DFG signal is heterodyne-detected, one can obtain the two-dimensional spectra as

$$\tilde{R}^{\mathrm{SFG}}_{ZYX}(\omega_2,\omega_1) = \int_0^\infty \mathrm{d}t_2 \int_0^\infty \mathrm{d}t_1\, R^{\mathrm{SFG}}_{ZYX}(t_2,t_1)\exp[i(\omega_2+\omega_1)t_2 + i\omega_1 t_1]$$

$$\tilde{R}^{\mathrm{DFG}}_{ZYX}(\omega_2,\omega_1) = \int_0^\infty \mathrm{d}t_2 \int_0^\infty \mathrm{d}t_1\, R^{\mathrm{DFG}}_{ZYX}(t_2,t_1)\exp[i(\omega_1-\omega_2)t_2 + i\omega_1 t_1] \quad (8\text{-}10)$$

where the corresponding response functions are already given in eq 8-3.

By invoking the optical Bloch approximation, which means that the frequency−frequency correlation functions in eq 4-45 are assumed to be Dirac delta functions, i.e., the Markovian approximation, the 2D SFG and DFG spectra are simply given by[531]

$$\tilde{R}^{\mathrm{SFG}}_{ZYX}(\omega_2,\omega_1) = \hbar^{-2}\left\{\frac{[\overline{\boldsymbol{\mu}_{0a}\boldsymbol{\mu}_{a+}\boldsymbol{\mu}_{+0}}]_{ZYX}}{(\omega_1+\omega_2-\omega_a+i\gamma_a)(\omega_1-\omega_++i\gamma_+)} + \frac{[\overline{\boldsymbol{\mu}_{0a}\boldsymbol{\mu}_{a-}\boldsymbol{\mu}_{-0}}]_{ZYX}}{(\omega_1+\omega_2-\omega_a+i\gamma_a)(\omega_1-\omega_-+i\gamma_-)}\right\}$$

$$\tilde{R}^{\mathrm{DFG}}_{ZYX}(\omega_2,\omega_1) = \hbar^{-2}\left\{\frac{[\overline{\boldsymbol{\mu}_{0+}\boldsymbol{\mu}_{+a}\boldsymbol{\mu}_{a0}}]_{ZYX}}{(\omega_1-\omega_2-\omega_++i\gamma_+)(\omega_1-\omega_a+i\gamma_a)} + \frac{[\overline{\boldsymbol{\mu}_{0-}\boldsymbol{\mu}_{-a}\boldsymbol{\mu}_{a0}}]_{ZYX}}{(\omega_1-\omega_2-\omega_-+i\gamma_-)(\omega_1-\omega_a+i\gamma_a)}\right\} \quad (8\text{-}11)$$

where γ_j (for $j = +, -$, and a) is the dephasing constant. Here, it is noted that $\boldsymbol{\mu}_{+,0} = \boldsymbol{\mu}_{a,-}$ and $\boldsymbol{\mu}_{-,0} = \boldsymbol{\mu}_{a,+}$. However, to obtain the two-quantum transition dipole matrix element, $\boldsymbol{\mu}_{a0} = \langle 1,1|\bar{\mu}|0,0\rangle$, one needs to use the expanded dipole operator, i.e.,

$$\hat{\boldsymbol{\mu}} = \hat{\boldsymbol{\mu}}_1 + \hat{\boldsymbol{\mu}}_2 + \hat{\boldsymbol{\mu}}_1\tilde{\mathbf{T}}_{12}\hat{\boldsymbol{\alpha}}_2 + \hat{\boldsymbol{\mu}}_2\tilde{\mathbf{T}}_{21}\hat{\boldsymbol{\alpha}}_1 + \ldots \quad (8\text{-}12)$$

where $\boldsymbol{\alpha}_j$ is the molecular polarizability operator of the jth chromophore and $\tilde{\mathbf{T}}_{12}$ is the second-rank dipole−dipole interaction tensor (see eq 4-59). Due to the interaction-induced dipole, the two-quantum transition dipole matrix element $\boldsymbol{\mu}_{a,0}$ can be approximated as

$$\boldsymbol{\mu}_{a,0} \cong \mathbf{d}_1\tilde{\mathbf{T}}_{12}\boldsymbol{\alpha}_2 + \mathbf{d}_2\mathbf{T}_{21}\boldsymbol{\alpha}_1 \quad (8\text{-}13)$$

where $\boldsymbol{\alpha}_1 = \langle 1,0|\hat{\alpha}_1|0,0\rangle$ and $\boldsymbol{\alpha}_2 = \langle 0,1|\hat{\alpha}_2|0,0\rangle$. Finally, it was found that the 2D doubly resonant SFG and DFG spectra are theoretically given as

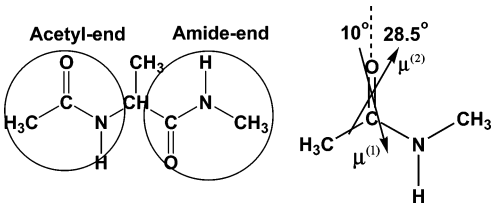

Figure 64. Chemical structure of the alanine dipeptide analogue (Ac-Ala-NHMe). It contains two peptide bonds denoted as acetyl-end and amide-end peptides. The first and second derivatives of the dipole moment with respect to the amide I coordinate of *N*-methylacetamide are shown. The two vectors are on the molecular plane, but their directions are different, as can be seen in this figure.

$$R^{\mathrm{SFG}}_{\mathrm{ZYX}}(\omega_2,\omega_1) = \frac{1}{6\hbar^2}(\mathbf{d}_1\tilde{\mathbf{T}}_{12}\boldsymbol{\alpha}_2 + \mathbf{d}_2\tilde{\mathbf{T}}_{21}\boldsymbol{\alpha}_1)\cdot(\mathbf{d}_2\times\mathbf{d}_1)\left\{\frac{1}{(\omega_1+\omega_2-\omega_a+i\gamma_a)(\omega_1-\omega_++i\gamma_+)} - \frac{1}{(\omega_1+\omega_2-\omega_a+i\gamma_a)(\omega_1-\omega_-+i\gamma_-)}\right\}$$

$$R^{\mathrm{DFG}}_{\mathrm{ZYX}}(\omega_2,\omega_1) = -\frac{1}{6\hbar^2}(\mathbf{d}_1\tilde{\mathbf{T}}_{12}\boldsymbol{\alpha}_2 + \mathbf{d}_2\tilde{\mathbf{T}}_{21}\boldsymbol{\alpha}_1)\cdot(\mathbf{d}_2\times\mathbf{d}_1)\left\{\frac{1}{(\omega_1-\omega_2-\omega_++i\gamma_+)(\omega_1-\omega_a+i\gamma_a)} - \frac{1}{(\omega_1-\omega_2-\omega_-+i\gamma_-)(\omega_1-\omega_a+i\gamma_a)}\right\} \quad (8\text{-}14)$$

Note that the SFG or DFG signal does not vanish when the three vectors, (1) $\mathbf{d}_1\tilde{\mathbf{T}}_{12}\boldsymbol{\alpha}_2 + \mathbf{d}_2\tilde{\mathbf{T}}_{21}\boldsymbol{\alpha}_1$, (2) $\mathbf{d}_2$, and (3) $\mathbf{d}_1$, are not on a common plane in a molecule-fixed frame.

Chiral molecule dimer or molecular complexes such as light-harvesting protein complexes are good examples for this type of experiment. In addition, it should be emphasized that the amplitude of the cross peak is directly proportional to the dipole−dipole interaction tensor that varies as $1/R^3$ with respect to the interchromophore distance R. Consequently, the heterodyne- or homodyne-detected signal intensity becomes a function of R as $1/R^3$ or $1/R^6$, respectively. These two important observations suggest that the doubly resonant 2D TWM measurement technique can be a new nonlinear optical activity spectroscopy probing molecular chirality and can serve as a new molecular ruler.[531]

8.3. Coupled Anharmonic Oscillator Systems

In comparison to the coupled two-level dimer system, the amide I vibrations of dipeptide (Figure 64) can be modeled as a coupled anharmonic oscillator system, where each amide I local oscillator has three vibrational quantum states, i.e., the ground, first excited, and overtone states. Recently, a model dipeptide, Ac-Ala-NHMe, was considered in detail. Particularly, eight different dipeptide conformations that are four helical structures and four extended structures, i.e., RHH (right-handed α-helix), LHH (left-handed α-helix), πH (π-helix), 3_{10}H (3_{10}-helix), APB (antiparallel β-sheet), PB (parallel β-sheet), PII (polyproline II), and FEB (fully extended β-sheet), were chosen for *ab initio* geometry optimization and vibrational analysis.

In Figure 65, the numerically simulated amide I IR bands of the eight different conformers are shown, where the line shape is assumed to be a Lorentzian with 5 cm^{-1} dephasing constants for both symmetric and asymmetric amide I normal modes.[531] Depending on the coupling constant and frequency difference between the two amide I local modes, one can find that the amide I vibrational line shape does depend on the dipeptide conformation. Nevertheless, it is not easy to directly obtain the one- and two-exciton state energies due to the spectral congestion.

Because of the three two-exciton states in the coupled anharmonic oscillator system, the expressions for the 2D IR−IR SFG or DFG spectra are slightly different from those for the coupled two-level dimer and they are found to be[531]

$$R^{\mathrm{SFG}}_{ZYX}(\omega_2,\omega_1) = \hbar^{-2} \left\{ \frac{[\overline{\boldsymbol{\mu}_{0,a}\boldsymbol{\mu}_{a,+}\boldsymbol{\mu}_{+,0}}]_{ZYX}}{(\omega_1+\omega_2-\omega_a+i\gamma_a)(\omega_1-\omega_++i\gamma_+)} + \frac{[\overline{\boldsymbol{\mu}_{0,a}\boldsymbol{\mu}_{a,-}\boldsymbol{\mu}_{-,0}}]_{ZYX}}{(\omega_1+\omega_2-\omega_a+i\gamma_a)(\omega_1-\omega_-+i\gamma_-)} + \frac{[\overline{\boldsymbol{\mu}_{0,2+}\boldsymbol{\mu}_{2+,+}\boldsymbol{\mu}_{+,0}}]_{ZYX}}{(\omega_1+\omega_2-\omega_{2+}+i\gamma_{2+})(\omega_1-\omega_++i\gamma_+)} + \frac{[\overline{\boldsymbol{\mu}_{0,2+}\boldsymbol{\mu}_{2+,-}\boldsymbol{\mu}_{-,0}}]_{ZYX}}{(\omega_1+\omega_2-\omega_{2+}+i\gamma_{2+})(\omega_1-\omega_-+i\gamma_-)} + \frac{[\overline{\boldsymbol{\mu}_{0,2-}\boldsymbol{\mu}_{2-,+}\boldsymbol{\mu}_{+,0}}]_{ZYX}}{(\omega_1+\omega_2-\omega_{2-}+i\gamma_{2-})(\omega_1-\omega_++i\gamma_+)} + \frac{[\overline{\boldsymbol{\mu}_{0,2-}\boldsymbol{\mu}_{2-,-}\boldsymbol{\mu}_{-,0}}]_{ZYX}}{(\omega_1+\omega_2-\omega_{2-}+i\gamma_{2-})(\omega_1-\omega_-+i\gamma_-)} \right\} \quad (8\text{-}15)$$

$$R^{\mathrm{DFG}}_{ZYX}(\omega_2,\omega_1) = \hbar^{-2} \left\{ \frac{[\overline{\boldsymbol{\mu}_{0,+}\boldsymbol{\mu}_{+,a}\boldsymbol{\mu}_{a,0}}]_{ZYX}}{(\omega_1-\omega_2-\omega_++i\gamma_+)(\omega_1-\omega_a+i\gamma_a)} + \frac{[\overline{\boldsymbol{\mu}_{0,-}\boldsymbol{\mu}_{-,a}\boldsymbol{\mu}_{a,0}}]_{ZYX}}{(\omega_1-\omega_2-\omega_-+i\gamma_-)(\omega_1-\omega_a+i\gamma_a)} + \frac{[\overline{\boldsymbol{\mu}_{0,+}\boldsymbol{\mu}_{+,2+}\boldsymbol{\mu}_{2+,0}}]_{ZYX}}{(\omega_1-\omega_2-\omega_++i\gamma_+)(\omega_1-\omega_{2+}+i\gamma_{2+})} + \frac{[\overline{\boldsymbol{\mu}_{0,-}\boldsymbol{\mu}_{-,2+}\boldsymbol{\mu}_{2+,0}}]_{ZYX}}{(\omega_1-\omega_2-\omega_-+i\gamma_-)(\omega_1-\omega_{2+}+i\gamma_{2+})} + \frac{[\overline{\boldsymbol{\mu}_{0,+}\boldsymbol{\mu}_{+,2-}\boldsymbol{\mu}_{2-,0}}]_{ZYX}}{(\omega_1-\omega_2-\omega_++i\gamma_+)(\omega_1-\omega_{2-}+i\gamma_{2-})} + \frac{[\overline{\boldsymbol{\mu}_{0,-}\boldsymbol{\mu}_{-,2-}\boldsymbol{\mu}_{2-,0}}]_{ZYX}}{(\omega_1-\omega_2-\omega_-+i\gamma_-)(\omega_1-\omega_{2-}+i\gamma_{2-})} \right\} \quad (8\text{-}16)$$

where $|+\rangle$ and $|-\rangle$ are the first excited ket-states of the symmetric and asymmetric amide I normal modes, respectively. $|2+\rangle$, $|2-\rangle$, and $|a\rangle$ are those of the three doubly excited states.

Once the vibrational quantum states of the amide I excited and doubly excited states of the dipeptide are determined, the remaining task is to calculate the transition dipole matrix elements in eqs 8-15 and 8-16. The two transition dipole matrix elements between the ground and $|+\rangle$ states and between the ground and $|-\rangle$ states are simply given as linear combinations of those of the two amide I local modes at the acetyl- and amide-end peptide bonds, denoted as $\boldsymbol{\mu}^{(1)}_{\mathrm{Ac}}$ and $\boldsymbol{\mu}^{(1)}_{\mathrm{Am}}$, respectively. The transition dipole matrix elements between the excited and doubly excited states are also given as linear combinations of $\boldsymbol{\mu}^{(1)}_{\mathrm{Ac}}$ and $\boldsymbol{\mu}^{(1)}_{\mathrm{Am}}$. However, the two-quantum transition dipole matrix elements such as $\mu_{2+,0}$ etc. require the second derivatives of the dipole moment with respect to the amide I local coordinates q_{Ac} and q_{Am}, such as $\boldsymbol{\mu}^{(2)}_{\mathrm{Ac}} \equiv (\partial^2\boldsymbol{\mu}/\partial q^2_{\mathrm{Ac}})$, $\boldsymbol{\mu}^{(2)}_{\mathrm{Am}} \equiv (\partial^2\boldsymbol{\mu}/\partial q^2_{\mathrm{Am}})$, and $\boldsymbol{\mu}^{(2)}_{\mathrm{Ac,Am}} \equiv (\partial^2\boldsymbol{\mu}/\partial q_{\mathrm{Ac}}\partial q_{\mathrm{Am}})$. The first two quantities $\boldsymbol{\mu}^{(2)}_{\mathrm{Ac}}$ and $\boldsymbol{\mu}^{(2)}_{\mathrm{Am}}$ were obtained by carrying out finite difference calculations for NMA by using a density functional theory. In Figure 64, the direction of $\boldsymbol{\mu}^{(2)}$ obtained for NMA is shown. Now, unlike $\boldsymbol{\mu}^{(2)}_{\mathrm{Ac}}$ and $\boldsymbol{\mu}^{(2)}_{\mathrm{Am}}$, $\boldsymbol{\mu}^{(2)}_{\mathrm{Ac,Am}}$ is strongly dependent on the two dihedral angles ϕ and ψ, which determine the dipeptide backbone conformation. It was shown that the $\boldsymbol{\mu}^{(2)}_{\mathrm{Ac,Am}}$ vector can be approximately estimated by using the following equation,[531,532]

$$\left(\frac{\partial^2\boldsymbol{\mu}}{\partial q_{\mathrm{Ac}}\partial q_{\mathrm{Am}}}\right) \approx \left(\frac{\partial\boldsymbol{\mu}}{\partial q_{\mathrm{Ac}}}\right)\tilde{T}\left(\frac{\partial\boldsymbol{\alpha}}{\partial q_{\mathrm{Am}}}\right) + \left(\frac{\partial\boldsymbol{\alpha}}{\partial q_{\mathrm{Ac}}}\right)\tilde{T}\left(\frac{\partial\boldsymbol{\mu}}{\partial q_{\mathrm{Am}}}\right) \quad (8\text{-}17)$$

where $\tilde{T}$ is the dipole−dipole interaction tensor. It was found that the magnitudes of $\boldsymbol{\mu}^{(2)}_{\mathrm{Ac}}$ and $\boldsymbol{\mu}^{(2)}_{\mathrm{Am}}$ are an order of magnitude larger than $\boldsymbol{\mu}^{(2)}_{\mathrm{Ac,Am}}$ for most dipeptide conformers.

In order for the IR−IR TWM signals of proteins and polypeptides to be nonzero, the following four conditions should be satisfied:[531] (i) conformational chirality, (ii) nonzero potential anharmonicities, (iii) nonzero dipole second derivatives, and (iv) nonzero vibrational couplings. For the eight representative dipeptide conformations, the amide I mode frequencies, transition dipoles and polarizabilities, and second derivatives of dipoles with respect to the amide I local coordinates were all calculated by using an *ab initio* calculation method. By assuming that the vibrational dephasing constants of the symmetric and asymmetric amide I normal modes are 5 cm^{-1} and those of the two-exciton states are 10 cm^{-1}, the 2D IR−IR SFG spectra were numerically simulated and are shown in Figure 66. The 2D spectra exhibit a strong dependency on the 3D structure of the dipeptide. Not only the peak positions but also the signs of the peaks are distinctively different from one another. The key determining factors are the relative angles of the transition dipole vectors of the two amide I local modes. In addition,

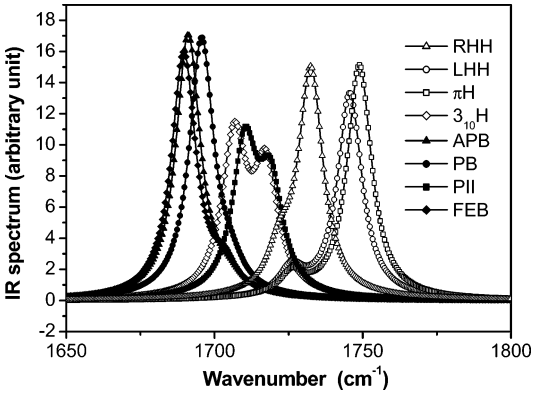

Figure 65. Simulated amide I IR absorption spectra for the eight representative secondary structure dipeptides (see ref 531 for a detailed description of the numerical simulation method).

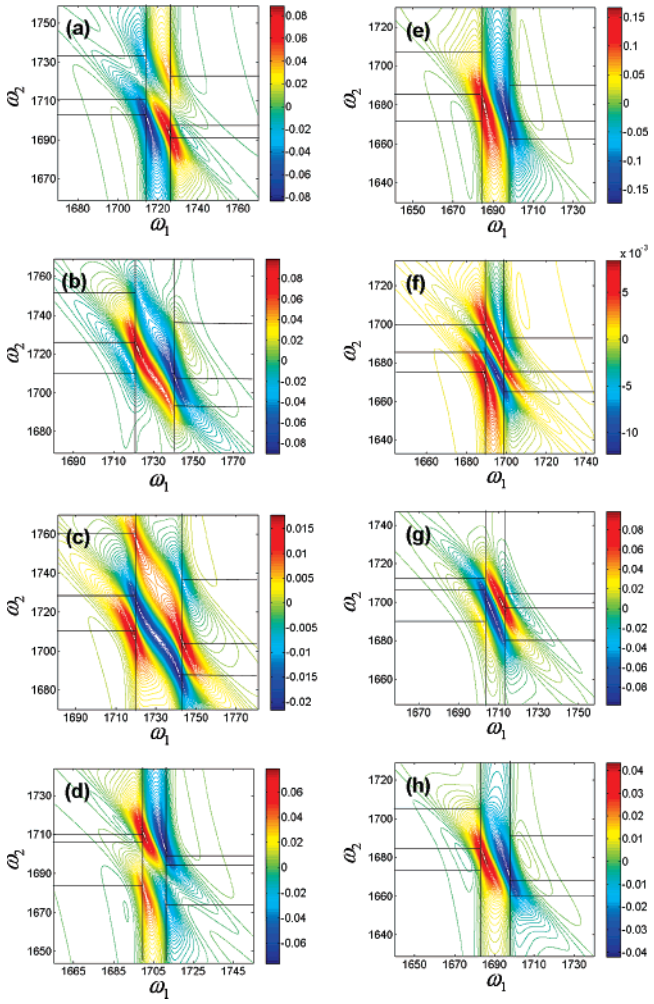

Figure 66. 2D IR−IR-SFG spectra, $\mathrm{Re}[\tilde{R}^{\mathrm{SFG}}_{zyx}(\omega_2,\omega_1)]$:[531] (a) right-handed α-helix; (b) left-handed α-helix; (c) π-helix; (d) 3_{10} helix; (e) antiparallel β-sheet; (f) parallel β-sheet; (g) polyproline II; and (h) fully extended β-sheet conformer. Frequency is in cm^{-1}.

depending on the vibrational coupling constant, the energy levels of the one-quantum excited and doubly excited states change very much.

In Figure 66, two vertical lines and six horizontal lines connected to each vertical line were shown. The positions of the two vertical lines correspond to the transition frequencies of the two amide I excited states, whereas those of the six horizontal lines are $|\omega_a - \omega_+|$, $|\omega_{2+} - \omega_+|$, $|\omega_{2-} - \omega_+|$, $|\omega_a - \omega_-|$, $|\omega_{2+} - \omega_-|$, and $|\omega_{2-} - \omega_-|$, which are the frequency differences between singly excited and doubly excited states. Consequently, the spectral line shape along the ω_1 axis can provide information on the one-quantum resonant (fundamental transition) frequencies between the ground state and the one-quantum excited state, and that along the ω_2 axis would show the doubly excited-state energies. An interesting feature of the 2D IR−IR SFG spectra is that they are highly frequency-resolved in comparison to the corresponding IR absorption or vibrational circular dichroism spectra. In addition, since the IR−IR SFG explores the doubly excited states, it can provide information on couplings and potential anharmonicities of the coupled multichromophore systems.

Most of the current 2D vibrational spectroscopy experiments were performed by using the 2D IR photon echo technique based on a four-wave-mixing scheme (see section 5). Since it is a four-wave-mixing, the number of nonlinear optical transition pathways contributing to the echo is intrinsically larger than that of the IR−IR SFG. Nevertheless, the 2D IR−IR SFG process requires nonzero two-quantum transition amplitudes, whereas the 2D IR photon echo process involves four one-quantum transitions. Therefore, it is expected that the magnitude of the IR−IR SFG polarization $|P^{(2)}|$ can also be small, even though it is the lowest-order nonlinear optical process compared to the third-order IR photon echo polarization $|P^{(3)}|$. An order of magnitude analysis comparing the relative magnitudes of the IR photon echo and IR−IR SFG polarizations was provided before. At the resonance conditions, $|P^{(2)}| \sim |\mu_{20}\mu_{10}^2E^2/\hbar^2\gamma^2|$ and $|P^{(3)}| \sim |\mu_{10}^4E^3/\hbar^3\gamma^3|$, where γ is the vibrational dephasing constant and E is the IR electric field amplitude. The transition dipole between the ground and the one-quantum excited states and that between the ground and the doubly excited states are denoted as μ_{10} and μ_{20}. The ratio $|P^{(3)}/P^{(2)}|$ is then approximately given as $|\mu_{10}/\mu_{20}||\mu_{10}E/\hbar\gamma|$. For an amide I oscillator, μ_{10} and μ_{20} were estimated to be about 0.4 and 0.02 Debyes. If the pulse power, pulse duration time, and radius of a focused laser beam are about 10 nJ, 100 fs, and 100 μm, respectively, the electric field is about 5×10^7 V/m. Then, for γ of 10 cm^{-1}, the ratio $|P^{(3)}/P^{(2)}|$ is ∼10. This means that the heterodyne-detected IR−IR SFG signal is about an order of magnitude smaller than the IR-photon echo in this particular case of the amide I oscillators.

Another interesting difference between the 2D IR photon echo and the IR−IR SFG can be found by comparing the line shapes. The 2D IR PE spectrum is given as a sum of three distinctively different contributions, i.e., $S_{\mathrm{PE}} = (S_{\mathrm{SE}} + S_{\mathrm{GB}}) - S_{\mathrm{EA}}$, where the three are stimulated emission, ground-state bleaching, and excited-state absorption, respectively. For perfect harmonic oscillators, the destructive interference among different pathways is complete to make the photon echo signal vanish. However, due to the potential anharmonicities, such as overtone and combination frequency shifts, the cancellation between $(S_{\mathrm{SE}} + S_{\mathrm{GB}})$ and S_{EA} is usually not complete. In contrast, the present IR−IR SFG (or DFG) spectrum, because it is a low-order nonlinear spectroscopy, is produced by a simple sum of contributions, even though there still exist different types of interferences among pathways. In addition, unlike the IR photon echo, the IR−IR SFG is an optical activity measurement technique, so that it is sensitive to molecular chirality. Therefore, the IR−IR SFG can be a 2D lowest-order nonlinear optical activity measurement spectroscopy, which distinguishes itself from the other 2D spectroscopic techniques.

9. Two-Dimensional Nonlinear Optical Activity Spectroscopy

The optical activity is, by definition, related to the differential interaction of a chiral molecule with left and right circularly polarized radiation during quantum excitation.[533−536] There are different types of optical activity measurement methods. In particular, circular dichroism (CD) measures the differential absorption of chiral molecules with left- and right-circularly polarize lights.[535] Generally, the CD intensity is linearly proportional to the so-called rotational strength, which is defined as, using the Rosenfeld equation,[537]

$$R_{\mathrm{eg}} = \mathrm{Im}[\langle g|\boldsymbol{\mu}|e\rangle\cdot\langle e|\mathbf{m}|g\rangle] \qquad (9\text{-}1)$$

where $\boldsymbol{\mu}$ and $\mathbf{m}$ are the electric and magnetic dipole operators, respectively, and $|g\rangle$ and $|e\rangle$ are the ket states of the ground

and excited states. Depending on the nature of the excited state, the rotational strength determines the electronic or vibrational circular dichroism intensity. Noting that the magnetic dipole operator is proportional to the $\mathbf{r} \times \mathbf{p}$ operator, the rotational strength in eq 9-1 becomes nonzero when the molecule has chirality in general. This is precisely why CD is a useful technique for studying molecular chirality and for determining its absolute configuration. In relation to the vibrational CD utilizing circularly polarized IR lights,[229,242,311,533,538−550] the Raman optical activity technique,[535,551−556] which is a Raman version of vibrational CD, has also been used to study chiral properties of polyatomic molecules and proteins in solution. Recently, IR−vis SFG spectroscopy was shown to be yet another vibrational optical activity measurement method, as mentioned in the previous section. Nevertheless, these spectroscopic techniques are one-dimensional in the sense that the corresponding spectra are measured as a function of a single experimentally controllable frequency.

Recently, there has been growing interest in extending such optical activity spectroscopy toward multidimensional nonlinear optical activity measurement techniques.[42,44,45,529,557,558] A few theoretical works have been reported and have demonstrated their potential uses in studying biomolecular structures and dynamics.

9.1. Electronic Circular Dichroism of Polypeptides

Electronic CD has been found to be particularly useful in determining the secondary structure contents of a given protein. For small systems, the electronic and magnetic dipole moments can be directly computed by using *ab initio* calculation methods. For large systems such as proteins, however, a full *ab initio* calculation is still computationally prohibitive. Therefore, a number of ingenious methods for numerically calculating the rotational strength of the protein were proposed and tested, and here an approximate theory called the matrix method will be briefly discussed. One begins by considering the protein as a set of M-independent chromophoric groups, each of which may have one or more electronic transitions. A Hamiltonian matrix is, as usual, constructed:

$$H = \sum_{i=1}^{M} H_i + \sum_{i=1}^{M-1} \sum_{j=i+1}^{M} V_{ij} \qquad (9\text{-}2)$$

where H_i is the Hamiltonian operator of the isolated model chromophore i. V_{ij} is the interaction between the groups i and j. In this case, each basis function, Φ_{ia}, is $\Phi_{ia} = \varphi_{10}...\varphi_{ia}...\varphi_{j0}...\varphi_{M0}$, where φ_{ia} represents the excited-state wave function of the ith chromophore and all the other chromophores are on the electronic ground state. Using these electronic basis functions, one can express the excited-state wave functions of the whole molecule, Ψ_k, as a linear superposition of these basis functions, i.e.,

$$\Psi_k = \sum_{i}^{M} \sum_{a}^{n_i} c_{ia} \Phi_{ia} \qquad (9\text{-}3)$$

The diagonal elements of the Hamiltonian matrix in eq 9-2 are the transition energies of each different electronic transition in a given chromophore, whereas the off-diagonal elements, V_{ij}, are the electronic coupling constants between two different chromophoric groups. As discussed in ref 559, one can approximately calculate these coupling constants as

$$V_{i0a;j0b} = \int_{r_i}\int_{r_j} \frac{\rho_{i0a}(r_i)\,\rho_{j0b}(r_j)}{4\pi\epsilon_0 r_{i,j}}\,\mathrm{d}\tau_i\,\mathrm{d}\tau_j \cong \sum_{s=1}^{N_s}\sum_{t=1}^{N_t} \frac{q_s q_t}{4\pi\epsilon_0 r_{st}} \qquad (9\text{-}4)$$

where ρ_{i0a} and ρ_{j0b} are the transition charge densities associated with the transition $0 \rightarrow a$ on the group i and the transition $0 \rightarrow b$ on the group j, respectively. The permanent and transition charge densities are represented by a set of point charges, q_s and q_t.

This approach requires parameters that describe the charge distributions associated with different electronic states of each chromophoric group. This parametrization is crucial for the success of this matrix method. A variety of parameters describing the N-methylacetamide and acetamide chromophores were reported, where the semiempirical complete neglect of differential overlap (CNDO/S) method[560] and gas-phase multireference configuration interaction (MRCI)[561] *ab initio* calculation were used. Yet another method was a different kind of semiempirical approach, where the electric transition dipole moment vector is taken from experimental results and the rest of the parameters are calculated from the intermediate neglect of differential overlap/spectroscopic (INDO/S) wave functions. Recently, the complete active space self-consistent-field method implemented within a self-consistent reaction field (CASSCF/SCRF) combined with multiconfigurational second-order perturbation theory (CASPT2-RF) was used to calculate the ground and electronic excited states of the NMA. That was found to be quite successful for 29 reference proteins.[559] Once the rotational strengths associated with electronic transitions are obtained, one can approximately calculate the CD spectrum by assuming that each individual line shape is a Gaussian,

$$[\theta](\lambda) = \sum_{K} [\theta^\circ]_K \exp[(-(\lambda - \lambda_K)^2/\Delta_K{}^2] \qquad (9\text{-}5)$$

where

$$[\theta^\circ]_K = 7515 R_K(DBM)\lambda_K/\Delta_K \qquad (9\text{-}6)$$

Here, λ_K and R_K are the wavelength and the rotational strength associated with the transition from the ground state to the Kth excited state. $[\theta^\circ]_K$ is the amplitude of the Kth CD band, and DBM means a Debye−Bohr magneton unit. The bandwidth was denoted as Δ_K for the transition $0 \rightarrow K$. As will be discussed later in section 9.4, novel nonlinear optical activity spectroscopy has been theoretically proposed and the spectral simulation requires quantitative determination of electronic transition magnetic dipole moments. Thus, the matrix theory outlined above will be of use in the future studies with this technique.

9.2. Vibrational Circular Dichroism of Polypeptides

In parallel with the development of the electronic CD, the vibrational CD technique has grown to be a successful tool for determining secondary structures of polypeptides in solution. Vibrational circular dichroism (VCD) is used to measure the rotational strength, defined as

$$R_j = \mathrm{Im}[(\partial\boldsymbol{\mu}/\partial Q_j)_0 \cdot (\partial\mathbf{m}/\partial Q_j)_0]\langle j|Q_j|0\rangle^2 \qquad (9\text{-}7)$$

where R_j is the rotational strength of the jth normal mode

whose coordinate is denoted as Q_j. The corresponding vibrational transition electric and magnetic dipoles are $(\partial\boldsymbol{\mu}/\partial Q_j)_0$ and $(\partial\mathbf{m}/\partial Q_j)_0$. Depending on the angle between $(\partial\boldsymbol{\mu}/\partial Q_j)_0$ and $(\partial\mathbf{m}/\partial Q_j)_0$, the rotational strength can be either positive or negative. Not only the VCD intensity but also the positive−negative spectral pattern of a given secondary structure polypeptide could be quantitatively described by examining the angle between transition electric and magnetic dipole vectors.[229,280,562] This additional feature makes the VCD method superior to conventional IR absorption or Raman scattering spectroscopy in determining the secondary structure of an unknown polypeptide.

For a given molecule, the rotational strength calculated by using the gauge-invariant magnetic field perturbation (MFP) theory[563] implemented in commercially available quantum chemistry calculation programs is invariant to the choice of the origin. However, to apply the fragmentation approximation and coupled oscillator theory to the calculation of transition magnetic dipoles in terms of local mode transition magnetic dipoles, one should perform transformations of the atomic axial tensor elements of each fragment to those in the global coordinate frame used to specify the polypeptide structure. For a polypeptide with N peptide bonds, there are N different local coordinate frames associated with each fragment. Therefore, the following procedure for calculating the transition electric and magnetic dipoles of a polypeptide was recently developed:[562]

(1) **Global Coordinate System**. The global coordinate system can be arbitrarily chosen, but for the sake of convenience, the origin was assumed to be at the carbonyl carbon atom of the first peptide. The z-axis in the global coordinate system is assumed to be along the C═O bond, and the three atoms O═C−N are on the $x-z$ plane in the global coordinate system.

(2) **Local Coordinate System**. A unit peptide such as NMA is properly aligned to be superimposed to the jth peptide in a given polypeptide chain. The local coordinate system of the jth unit peptide is assumed to be very similar to the case of the global coordinate system. The origin of the $\{x_j, y_j, z_j\}$ coordinate system is located at the carbonyl carbon of the jth unit peptide, the z_j-axis is on the C═O bond, and the O═C−N group is on the x_j-z_j plane.

(3) **Origin Transformation**. Since the origins of $N-1$ local coordinate systems, except for the first one, are displaced from that of the global coordinate system, the transition magnetic dipole of the jth unit peptide should be properly transferred to that in the global coordinate system. Suppose that the atomic axial tensor (AAT) elements of the jth unit peptide are denoted as $M^{(j)}_{\alpha b}$, where α and β are x_j, y_j, or z_j. Then, let us consider the translation of the origin of the jth local coordinate system to that of the global coordinate system. In this case, from the distributed origin gauge theory,[563] the AAT elements in the displaced origin can be calculated by using the following relationship,

$$\bar{M}^{(j)}_{\alpha\beta} = M^{(j)}_{\alpha\beta} + \frac{i}{4\hbar c}\sum_{\gamma\delta}\epsilon_{\beta\gamma\delta}Y^{(j)}_{\gamma}P^{(j)}_{\alpha\beta} \tag{9-8}$$

where $Y^{(j)}$ is the displacement vector from the origin of the global coordinate system to that of the jth local coordinate system, $P_{\alpha\beta}$ is the atomic polar tensor (APT) element, and $\epsilon_{\beta\gamma\delta}$ is the antisymmetric Levi−Civita tensor.

(4) **Transition Electric and Magnetic Dipoles before Coordinate Frame Rotation**. Now, the βth vector elements of the transition electric and magnetic dipoles of the jth fragment can be calculated as

$$(\partial\boldsymbol{\mu}_j/\partial q_j)_\beta = \sum_\alpha P^{(j)}_{\alpha\beta}S_{\alpha j} \tag{9-9}$$

$$(\partial\mathbf{m}_j/\partial q_j)_\beta = \sum_\alpha \bar{M}^{(j)}_{\alpha\beta}S_{\alpha j} \tag{9-10}$$

where $S_{\alpha j}$ is the eigenvector element of the amide I normal mode of the jth fragment.

(5) **Transition Electric and Magnetic Dipoles after Coordinate Frame Rotation**. Although the transition magnetic dipole in eq 9-10 was obtained by properly taking into account the origin-dependence of the magnetic dipole moment, still the $N-1$ coordinate systems differ from the global coordinate system because they were not properly rotated. These coordinate frame rotations can be achieved by using the 3×3 unitary transformation matrix, which can be determined by considering the relationship between the local coordinate frame and the global coordinate frame as

$$R^{(j)}(\phi_j,\theta_j,\chi_j) = \begin{bmatrix} \cos\phi_j\cos\theta_j\cos\chi_j - \sin\phi_j\sin\chi_j & \sin\phi_j\cos\theta_j\cos\chi_j + \cos\phi_j\sin\chi_j & -\sin\theta_j\cos\chi_j \\ -\cos\phi_j\cos\theta_j\sin\chi_j - \sin\phi_j\cos\chi_j & -\sin\phi_j\cos\theta_j\sin\chi_j + \cos\phi_j\cos\chi_j & \sin\theta_j\sin\chi_j \\ \cos\phi_j\sin\theta_j & \sin\phi_j\sin\theta_j & \cos\theta_j \end{bmatrix} \tag{9-11}$$

Then, finally, the αth vector element of the transition electric and magnetic dipoles of the jth peptide fragment in the global coordinate system can be calculated as

$$(\partial\boldsymbol{\mu}_j/\partial q_j)^{\mathrm{glb}}_\alpha = \sum_\beta R^{(j)}_{\alpha\beta}(\partial\boldsymbol{\mu}_j/\partial q_j)_\beta \tag{9-12}$$

$$(\partial\mathbf{m}_j/\partial q_j)^{\mathrm{glb}}_\alpha = \sum_\beta R^{(j)}_{\alpha\beta}(\partial\mathbf{m}_j/\partial q_j)_\beta \tag{9-13}$$

where the superscript "glb" emphasizes that the corresponding transition dipoles were transformed and given in the global coordinate system.

Hereafter let us focus on the amide I vibrations in detail. Once the transition dipoles of the amide I local modes in the global molecular coordinate system are obtained, the transition dipole associated with the jth amide I normal mode can be written as

$$(\partial\boldsymbol{\mu}/\partial Q_j) = \sum_k U_{jk}(\partial\boldsymbol{\mu}_k/\partial q_k)^{\mathrm{glb}} \tag{9-14}$$

where U is the eigenvector matrix obtained from the Hessian matrix constructed in the amide I local mode subspace.[231] From eq 9-14, the dipole strength of the jth normal mode can be divided into two parts as

$$D_j = |(\partial\boldsymbol{\mu}/\partial Q_j)|^2 = D_j^{\mathrm{diag}} + D_j^{\mathrm{cross}} \tag{9-15}$$

where the diagonal and cross terms, D_j^{diag} and D_j^{cross}, are defined as

$$D_j^{\text{diag}} = \sum_k U_{jk}^2 |(\partial \boldsymbol{\mu}_k/\partial q_k)^{\text{glb}}|^2 \cong D_0$$

$$D_j^{\text{cross}} = 2\sum_k \sum_{l>k} U_{jk} U_{jl} (\partial \boldsymbol{\mu}_k/\partial q_k)^{\text{glb}} \cdot (\partial \boldsymbol{\mu}_l/\partial q_l)^{\text{glb}} \cong 2D_0 \sum_k \sum_{l>k} U_{jk} U_{jl} \cos\theta_{kl} \quad (9\text{-}16)$$

Here, the diagonal term, D_j^{diag}, is simply identical to the dipole strength D_0 of the unit peptide. Note that D_j^{diag} is almost independent of the 3D conformation of the polypeptide. On the other hand, the cross term, D_j^{cross}, is sensitive to the 3D conformation of the polypeptide because the inner product, such as $(\partial \boldsymbol{\mu}_k/\partial q_k)^{\text{glb}} \cdot (\partial \boldsymbol{\mu}_l/\partial q_l)^{\text{glb}}$ (for $k \neq l$), and the angle θ_{kl} between the two vectors $(\partial \boldsymbol{\mu}_k/\partial q_k)^{\text{glb}}$ and $(\partial \boldsymbol{\mu}_l/\partial q_l)^{\text{glb}}$ are functions of the relative orientations of the corresponding two peptide bonds in a given polypeptide chain. Nevertheless, on the basis of quantum chemistry calculation studies, the dipole strength is largely determined by the diagonal contribution, D_j^{diag}, for a few representative secondary-structure polypeptides. This explains why the amide I IR absorption spectrum is less sensitive to the polypeptide 3D structure than the amide I VCD spectrum is.

The transition magnetic dipole of the jth amide I normal mode is also written as the linear combination of those of amide I local modes in the global molecular coordinate frame, i.e.,

$$(\partial \mathbf{m}/\partial Q_j) = \sum_k U_{jk} (\partial \mathbf{m}_k/\partial q_k)^{\text{glb}} \quad (9\text{-}17)$$

Similarly, the rotational strength of the jth normal mode, within the fragmentation approximation, is

$$R_j = \text{Im}[(\partial \boldsymbol{\mu}/\partial Q_j) \cdot (\partial \mathbf{m}/\partial Q_j)] = R_j^{\text{diag}} + R_j^{\text{cross}} \quad (9\text{-}18)$$

where the diagonal and cross terms, R_j^{diag} and R_j^{cross}, are found to be

$$R_j^{\text{diag}} = \sum_k U_{jk}^2 \text{Im}[(\partial \boldsymbol{\mu}_k/\partial q_k)^{\text{glb}} \cdot (\partial \mathbf{m}_k/\partial q_k)^{\text{glb}}]$$

$$R_j^{\text{cross}} = 2\sum_k \sum_{l>k} U_{jk} U_{jl} \text{Im}[(\partial \boldsymbol{\mu}_k/\partial q_k)^{\text{glb}} \cdot (\partial \mathbf{m}_l/\partial q_l)^{\text{glb}}] \quad (9\text{-}19)$$

On the basis of quantum chemistry calculations, similar to the dipole strength, the diagonal term, R_j^{diag}, contributing to the total rotational strength is quite insensitive to the secondary structure of the polypeptide, and more importantly, it is relatively small. In strong contrast to the dipole strength, the rotational strengths of amide I normal modes were found to be dictated by the cross term, R_j^{cross}, which is the linear combination of $\text{Im}[(\partial \boldsymbol{\mu}_k/\partial q_k)^{\text{glb}} \cdot (\partial \mathbf{m}_l/\partial q_l)^{\text{glb}}]$ for $k \neq l$.[564] This is the key for understating why the VCD spectrum is in general more featured and sensitive to the protein's secondary structure in comparison to the amide I IR spectrum.

In the present subsection, a theoretical description on how to calculate the transition electric and magnetic dipole matrix elements of delocalized amide I vibrations of proteins was presented. As will be discussed later in section 9.4, this computational method has been used to quantitatively simulate 2D nonlinear optical activity spectroscopic signals.

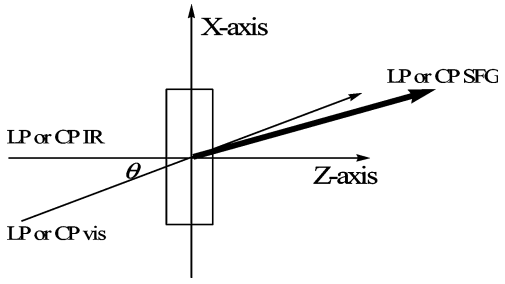

Figure 67. Schematic of the experimental beam configuration. The beam crossing angle is θ.

9.3. IR–vis Sum-Frequency-Generation of a Chiral Molecule Solution

In addition to the linear vibrational optical activity spectroscopy such as VCD and Raman optical activity, yet another vibrational optical activity spectroscopy based on a three-wave-mixing technique was experimentally and theoretically explored recently (see ref 525 for a recent review on nonlinear optical spectroscopy of chiral molecules).[525−528,565−567] In this case, the incident IR field is vibrationally resonant with a certain molecular vibrational degree of freedom and the visible field is electronically nonresonant. Consequently, the IR + vis SFG field is generated from the optical sample in an isotropic medium, where the chromophore should have nonzero antisymmetric Raman tensor elements as a selection rule. The latter condition is satisfied when the vibrational chromophore is chiral. Although this IR−vis SFG spectroscopy[568−570] is not a 2D vibrational spectroscopy because the signal is measured as a function of the IR field frequency, it is related to the four-wave-mixing-type nonlinear optical activity spectroscopy that will be discussed in subsection 9.4 below.

The first experiment demonstrated that the IR−vis SFG signal is measurably large for chiral molecules in liquid, where the three beams, i.e., IR, visible, and IV-SFG fields, are mutually perpendicular to one another.[526,527] Later, it was shown that there is a more general experimental scheme,[41,43] the so-called perpendicular detection method, which is shown in Figure 67.

The crossing angle between the incident IR and visible beam propagation directions is denoted as θ. The Y-component of the IR−vis SFG signal intensity is detected by placing a polarizer in between the optical sample and the detector. Here, the two incident beams propagate on the $X-Z$ plane. Since the polarization direction of the measured IR−vis SFG field is perpendicular to the plane of the two incident beams, this detection method was called the perpendicular detection scheme.

Depending on the polarization states of the three beams, four different types of IR−vis SFG were considered in detail (see the corresponding energy level diagrams in Figure 68).[43] The first case is when the IR and vis beams are linearly polarized (LP) and the polarization directions are on the (X,Z) plane. The IR beam that is resonant with the vibrational transition from the ground state to the $|r\rangle$ state is used to create a vibrational coherence state. The LP-vis beam puts

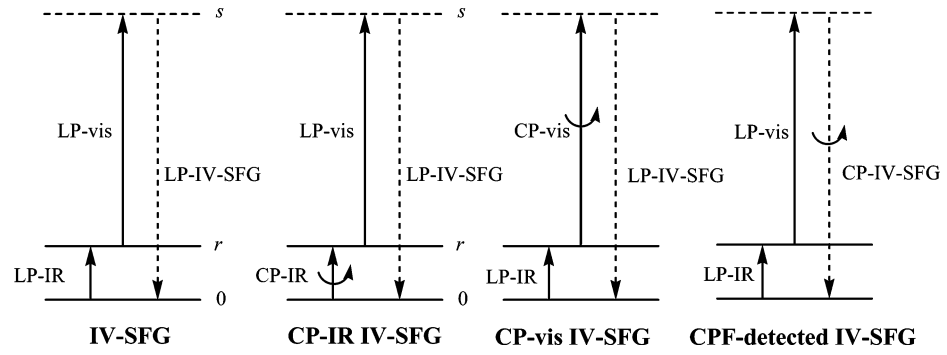

Figure 68. Energy level diagrams for IR−vis SFG spectroscopy.[43] The first diagram represents the IR−vis (IV) SFG with linearly polarized IR and visible beams. The second involves a circularly polarized IR beam. The third corresponds to the IR−vis SFG with a circularly polarized visible beam. The last one involves detection of a circularly polarized component of the IR−vis SFG field.

the molecule into an electronic coherence state and $|s\rangle$ is a virtual state in Figure 68. In contrast, the CP-IR IR−vis SFG in Figure 68 corresponds to the case when the incident IR beam is controlled to be left- and right-circularly polarized. Then, the difference of the two CP-IR IR−vis SFG signals with left- and right-CP IR beams is measured. The third experimental scheme in Figure 68 is different from the second by the point that the incident visible beam is now CP. The fourth case is identical to the normal IR−vis SFG, but the left- and right-CP components of the IR−vis SFG signal field are detected.

Although it is a straightforward exercise to develop a time-domain nonlinear response function theory for the IR−vis SFG, we found the multipolar quantum electrodynamics descriptions of these four different IR−vis SFG processes useful. It begins with an introduction of the field−matter interaction Hamiltonian,

$$H_{\text{int}} = -\epsilon_0^{-1}\int \mu_i \delta(\mathbf{r}-\mathbf{R}) d_i^{\perp}(\mathbf{r})\, \mathrm{d}V - \epsilon_0^{-1}\int Q_{ij}\delta(\mathbf{r}-\mathbf{R})\nabla_j d_i^{\perp}(\mathbf{r})\, \mathrm{d}V - \int m_i \delta(\mathbf{r}-\mathbf{R}) b_i(\mathbf{r})\, \mathrm{d}V \quad (9\text{-}20)$$

Here, the Einstein summation convention is used. ϵ_0 is the vacuum permittivity. The position vector of the molecular center is $\mathbf{R}$. V denotes the quantization volume. The mode-expanded transverse electric and magnetic fields are[523]

$$\mathbf{d}^{\perp}(\mathbf{r}) = i\sum_{k,\lambda}\left(\frac{\hbar c k \epsilon_0}{2V}\right)^{1/2}\{\mathbf{e}^{(\lambda)}(\mathbf{k})\, a^{(\lambda)}(\mathbf{k})\, \mathrm{e}^{i\mathbf{k}\cdot\mathbf{r}} - \bar{\mathbf{e}}^{(\lambda)}(\mathbf{k})\, a^{+(\lambda)}(\mathbf{k})\mathrm{e}^{-i\mathbf{k}\cdot\mathbf{r}}\}$$

$$\mathbf{b}(\mathbf{r}) = i\sum_{k,\lambda}\left(\frac{\hbar k}{2\epsilon_0 c V}\right)^{1/2}\{\mathbf{b}^{(\lambda)}(\mathbf{k})\, a^{(\lambda)}(\mathbf{k})\, \mathrm{e}^{i\mathbf{k}\cdot\mathbf{r}} - \bar{\mathbf{b}}^{(\lambda)}(\mathbf{k})\, a^{+(\lambda)}(\mathbf{k})\, \mathrm{e}^{-i\mathbf{k}\cdot\mathbf{r}}\} \quad (9\text{-}21)$$

where the wavevector of the electromagnetic field was denoted as $\mathbf{k}$ and c is the speed of light. The unit vectors of the electric and magnetic field vectors of the $(\mathbf{k},\lambda)$-mode are $\mathbf{e}^{(\lambda)}(\mathbf{k})$ and $\mathbf{b}^{(\lambda)}(\mathbf{k})$, respectively, and they are related to each other as $\mathbf{b}^{(\lambda)}(\mathbf{k}) = \hat{\mathbf{k}} \times \mathbf{e}^{(\lambda)}(\mathbf{k})$, where $\hat{\mathbf{k}} = \mathbf{k}/|\mathbf{k}|$. The creation and annihilation operators of the $(\mathbf{k},\lambda)$-mode are $a^{+(\lambda)}(\mathbf{k})$ and $a^{(\lambda)}(\mathbf{k})$, respectively. The bar in $\bar{\mathbf{e}}^{(\lambda)}(\mathbf{k})$ or $\bar{\mathbf{b}}^{(\lambda)}(\mathbf{k})$ represents the complex conjugate.

The IR−vis SFG involves two incident beams with the wavevectors of $\mathbf{k}_1$ and $\mathbf{k}_2$, respectively. Then, due to the phase-matching condition, the wavevector of the IR−vis SFG field, $\mathbf{k}_3$, is $\mathbf{k}_3 = \mathbf{k}_1 + \mathbf{k}_2$. The initial and final quantum states are

$$|i\rangle = |E_0;\, n_1(\mathbf{k}_1,\lambda_1),\, n_2(\mathbf{k}_2,\lambda_2)\rangle$$

$$|f\rangle = |E_0;\, (n_1-1)(\mathbf{k}_1,\lambda_1),\, (n_2-1)(\mathbf{k}_2,\lambda_2),\, 1(\mathbf{k}_3,\lambda_3)\rangle \quad (9\text{-}22)$$

where n_1 and n_2 denote the occupation numbers of the incident IR and visible fields, respectively, and $1(\mathbf{k}_3,\lambda_3)$ means that a single photon of an IR−vis SFG field is created. Since the magnetic dipole−magnetic field and electric quadrupole−electric field interactions are much smaller than the electric dipole−electric field term,[571] up to the first-order with respect to these two small interaction terms, it was found that the transition amplitude associated with the vibrationally resonant IR−vis SFG is given as a sum of seven distinctively different terms as[43]

$$\langle M^{(3)}\rangle = -i\left(\frac{\hbar}{2\epsilon_0 V}\right)^{3/2}(c n_1 n_2 k_1 k_2 k_3)^{1/2}[c\bar{e}_i^{(\lambda_3)}(\mathbf{k}_3) e_j^{(\lambda_2)}(\mathbf{k}_2) e_k^{(\lambda_1)}(\mathbf{k}_1)\langle\beta_{ijk}^{\alpha\mu}\rangle + \bar{e}_i^{(\lambda_3)}(\mathbf{k}_3)\, e_j^{(\lambda_2)}(\mathbf{k}_2)\, b_k^{(\lambda_1)}(\mathbf{k}_1)\langle\beta_{ijk}^{\alpha m}\rangle + \bar{e}_i^{(\lambda_3)}(\mathbf{k}_3)\, b_j^{(\lambda_2)}(\mathbf{k}_2)\, e_k^{(\lambda_1)}(\mathbf{k}_1)\langle\beta_{ijk}^{G\mu}\rangle + \bar{b}_i^{(\lambda_3)}(\mathbf{k}_3)\, e_j^{(\lambda_2)}(\mathbf{k}_2) e_k^{(\lambda_1)}(\mathbf{k}_1)\langle\beta_{ijk}^{\bar{G}\mu}\rangle + ci\bar{e}_i^{(\lambda_3)}(\mathbf{k}_3)\, e_j^{(\lambda_2)}(\mathbf{k}_2)\, e_k^{(\lambda_1)}(\mathbf{k}_1) k_l\langle\beta_{ijkl}^{\alpha Q}\rangle + ci\bar{e}_i^{(\lambda_3)}(\mathbf{k}_3)\, e_j^{(\lambda_2)}(\mathbf{k}_2)\, e_k^{(\lambda_1)}(\mathbf{k}_1) k'_m\langle\beta_{ijmk}^{A\mu}\rangle - ci\bar{e}_i^{(\lambda_3)}(\mathbf{k}_3)\, e_j^{(\lambda_2)}(\mathbf{k}_2)\, e_k^{(\lambda_1)}(\mathbf{k}_1) k''_n\langle\beta_{ijnk}^{\bar{A}\mu}\rangle] \quad (9\text{-}23)$$

The Feynman diagrams associated with these seven terms in eq 9-23 are shown in Figure 69. In eq 9-23, $\langle ... \rangle$ means the rotational average of either the third- or fourth-rank tensorial hyperpolarizabilities. Note that the corresponding susceptibility is linearly proportional to the molecular hyperpolarizability, as $\chi = NL(\omega_3,\omega_2,\omega_1)\langle\beta\rangle/\epsilon_0$, where $L(\omega_3,\omega_2,\omega_1) = l(\omega_3)l(\omega_2)l(\omega_1)$, $l(\omega)$ is the Lorentz local field correction factor, and N is the molecular number density.

The seven different molecular hyperpolarizability tensors in eq 9-23, which are directly related to the Feynman diagrams in Figure 69, are defined as

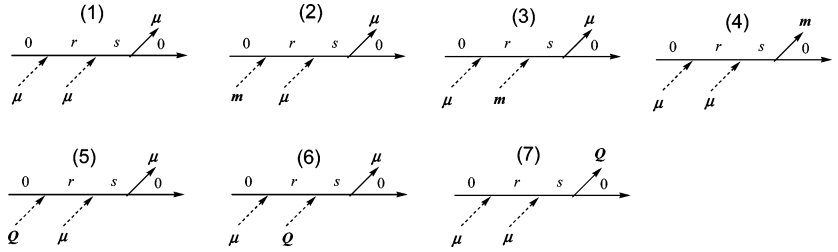

Figure 69. Feynman diagrams representing nonlinear optical transition pathways for IR−vis SFG spectroscopy.[43] Initially, the system is on the ground state $|0\rangle$. Vibrational transition from $|0\rangle$ to $|r\rangle$ occurs due to electric dipole−electric field, magnetic dipole−magnetic field, or electric quadrupole−electric field interaction. The second field−matter interaction creates a coherence state, which is a superposition state of $|0\rangle$ and a virtual state $|s\rangle$. The last field−matter interaction with vacuum field puts the system back into the ground state.

$$\beta_{ijk}^{\alpha\mu} = \sum_r \frac{\alpha_{ij}^{0r}\mu_k^{r0}}{E_{r0} - \hbar\omega_1 + i\Gamma_r}, \quad \beta_{ijk}^{\alpha m} = \sum_r \frac{\alpha_{ij}^{0r} m_k^{r0}}{E_{r0} - \hbar\omega_1 + i\Gamma_r},$$

$$\beta_{ijk}^{G\mu} = \sum_r \frac{G_{ij}^{0r}\mu_k^{r0}}{E_{r0} - \hbar\omega_1 + i\Gamma_r}, \quad \beta_{ijk}^{\bar{G}\mu} = \sum_r \frac{\bar{G}_{ij}^{0r}\mu_k^{r0}}{E_{r0} - \hbar\omega_1 + i\Gamma_r},$$

$$\beta_{ijkl}^{\alpha Q} = \sum_r \frac{\alpha_{ij}^{0r} Q_{kl}^{r0}}{E_{r0} - \hbar\omega_1 + i\Gamma_r}, \quad \beta_{ijmk}^{A\mu} = \sum_r \frac{A_{ijm}^{0r}\mu_k^{r0}}{E_{r0} - \hbar\omega_1 + i\Gamma_r},$$

$$\text{and} \quad \beta_{ijnk}^{\bar{A}\mu} = \sum_r \frac{\bar{A}_{ijn}^{0r}\mu_k^{r0}}{E_{r0} - \hbar\omega_1 + i\Gamma_r} \tag{9-24}$$

where the vibrational dephasing constant associated with the $0 \rightarrow r$ transition was denoted as Γ_r. The initial molecular quantum state and the first vibrationally excited state were denoted as $|0\rangle$ and $|r\rangle$, respectively. The polarizability, magnetic dipole−electric dipole ROA tensors, $G_{ij}^{\phi\psi}(\omega)$ and $\bar{G}_{ij}^{\phi\psi}(\omega)$, and electric quadrupole−electric dipole ROA tensors, $A_{ijl}^{\phi\psi}(\omega)$ and $\bar{A}_{ijl}^{\phi\psi}(\omega)$, are defined as

$$\alpha_{ij}^{\phi\psi}(\omega) = \sum_s \frac{\mu_i^{\phi s}\mu_j^{s\psi}}{E_{s0} - \hbar\omega} + \frac{\mu_j^{\phi s}\mu_i^{s\psi}}{E_{s0} + \hbar\omega},$$

$$G_{ij}^{\phi\psi}(\omega) = \sum_s \frac{\mu_i^{\phi s} m_j^{s\psi}}{E_{s0} - \hbar\omega} + \frac{m_j^{\phi s}\mu_i^{s\psi}}{E_{s0} + \hbar\omega},$$

$$\bar{G}_{ij}^{\phi\psi}(\omega) = \sum_s \frac{m_i^{\phi s}\mu_j^{s\psi}}{E_{s0} - \hbar\omega} + \frac{\mu_j^{\phi s} m_i^{s\psi}}{E_{s0} + \hbar\omega},$$

$$A_{ijl}^{\phi\psi}(\omega) = \sum_s \frac{\mu_i^{\phi s} Q_{jl}^{s\psi}}{E_{s0} - \hbar\omega} + \frac{Q_{jl}^{\phi s}\mu_i^{s\psi}}{E_{s0} + \hbar\omega}, \quad \text{and}$$

$$\bar{A}_{ijl}^{\phi\psi}(\omega) = \sum_s \frac{Q_{il}^{\phi s}\mu_j^{s\psi}}{E_{s0} - \hbar\omega} + \frac{\mu_j^{\phi s} Q_{il}^{s\psi}}{E_{s0} + \hbar\omega} \tag{9-25}$$

In eq 9-25, the summation over s involves all vibronic states except for the initial molecular quantum state $|0\rangle$. The matrix element $\alpha_{ij}^{\phi\psi}(\omega)$, for example, denotes the (i,j)th tensor element of the transition polarizability between $|\psi\rangle$ and $|\phi\rangle$, i.e., $\alpha_{ij}^{\phi\psi}(\omega) = \langle\phi|\alpha_{ij}(\omega)|\psi\rangle$.

9.3.1. LP-IR–vis SFG

Using Fermi's golden rule, one can obtain the IR−vis SFG intensity, which is proportional to the square of the IR−vis SFG transition amplitude in eq 9-23, as

$$I_{\text{LP-IV-SFG}} = \frac{I_{\text{IR}} I_{\text{vis}} k_3^4 N^2 L^2 (\omega_3, \omega_2, \omega_1)}{1152\pi^2 \epsilon_0^3 c} \sin^2\theta |\epsilon_{\lambda\mu\nu}\beta_{\lambda\mu\nu}^{\alpha\mu}|^2 \tag{9-26}$$

where $\epsilon_{\lambda\mu\nu}$ is the antisymmetric Levi−Civita epsilon and the subscripts λ, μ, and ν are indices for the molecular axes. Note that the rotational average of the third-rank tensor, $\langle\beta_{ijk}^{\alpha m}\rangle$, is given as $\langle\beta_{ijk}^{\alpha m}\rangle = \epsilon_{ijk}\epsilon_{\lambda\mu\nu}\beta_{\lambda\mu\nu}^{\alpha\mu}/6$ for an isotropic system. Due to the Levi−Civita epsilon, the IR−vis SFG signal is nonzero only when the antisymmetric Raman tensor elements do not vanish. It should be emphasized that the all-linearly polarized IR−vis SFG results from all-electric-dipole-field interactions, i.e., the first term in eq 9-23.

9.3.2. CP-IR IR–vis SFG

When the incident IR beam is either left- or right-CP, using the IR−vis SFG transition amplitude in eq 9-23 and performing the rotational average properly, the left-CP-IR and right-CP-IR SFG intensities were found to be

$$I_{\text{CP-IR}}(\text{L}) = \frac{I_{\text{IR}} I_{\text{vis}} k_3^4 N^2 L^2 \sin^2\theta}{64\pi^2\epsilon_0^3 c}\left\{\frac{|\epsilon_{\lambda\mu\nu}\beta_{\lambda\mu\nu}^{\alpha\mu}|^2}{36} + k_1^2\left|I_{YZYZ,\lambda\mu\nu\pi}^{(4)}\beta_{\lambda\mu\nu\pi}^{\alpha Q}\right|^2 - \frac{k_1}{3}\text{Re}[\epsilon_{\lambda\mu\nu}\beta_{\lambda\mu\nu}^{\alpha\mu} I_{YZYZ,\phi\chi\theta\rho}^{(4)}\bar{\beta}_{\phi\chi\theta\rho}^{\alpha Q}]\right\} \tag{9-27}$$

$$I_{\text{CP-IR}}(\text{R}) = \frac{I_{\text{IR}} I_{\text{vis}} k_3^4 N^2 L^2 \sin^2\theta}{64\pi^2\epsilon_0^3 c}\left\{\frac{|\epsilon_{\lambda\mu\nu}\beta_{\lambda\mu\nu}^{\alpha\mu}|^2}{36} + k_1^2\left|I_{YZYZ,\lambda\mu\nu\pi}^{(4)}\beta_{\lambda\mu\nu\pi}^{\alpha Q}\right|^2 + \frac{k_1}{3}\text{Re}[\epsilon_{\lambda\mu\nu}\beta_{\lambda\mu\nu}^{\alpha\mu} I_{YZYZ,\phi\chi\theta\rho}^{(4)}\bar{\beta}_{\phi\chi\theta\rho}^{\alpha Q}]\right\} \tag{9-28}$$

Here, the rotational averaging factor associated with the four-rank tensor is given as

$$I_{ijkl,\lambda\mu\nu\pi}^{(4)} = \frac{1}{30}(\delta_{ij}\delta_{kl} \;\; \delta_{ik}\delta_{jl} \;\; \delta_{il}\delta_{jk})\begin{pmatrix} 4 & -1 & -1 \\ -1 & 4 & -1 \\ -1 & -1 & 4 \end{pmatrix}\begin{pmatrix} \delta_{\lambda\mu}\delta_{\nu\pi} \\ \delta_{\lambda\nu}\delta_{\mu\pi} \\ \delta_{\lambda\pi}\delta_{\mu\nu} \end{pmatrix} \tag{9-29}$$

Therefore, the factor, $I_{YZYZ,\lambda\mu\nu\pi}^{(4)}$, is

$$I_{YZYZ,\lambda\mu\nu\pi}^{(4)} = \frac{1}{30}(4\delta_{\lambda\nu}\delta_{\mu\pi} - \delta_{\lambda\mu}\delta_{\nu\pi} - \delta_{\lambda\pi}\delta_{\mu\nu}) \tag{9-30}$$

In eqs 9-27 and 9-28, the first term is identical to the LP IV-SFG signal intensity. The second terms in eqs 9-27 and

9-28 corresponds to the polarizability−electric quadrupole term, $\beta^{\alpha Q}_{\lambda\mu\nu\pi}$. However, this term does not depend on the rotational direction of the circularly polarized IR beam. Only the last term in eqs 9-27 and 9-28, which is an interference term between the $\beta^{\alpha\mu}_{\lambda\mu\nu}$-induced IV-SFG field and the $\beta^{\alpha Q}_{\lambda\mu\nu\pi}$-induced IR−vis SFG field, depends on the circular polarization state of the IR beam. Thus, the circular intensity difference (CID) defined as $\Delta I \equiv I(\mathrm{L}) - I(\mathrm{R})$ is, in this case of the CP-IR IR−vis SFG, given as

$$\Delta I_{\text{CP-IR}} = -\frac{I_{\text{IR}} I_{\text{vis}} k_1 k_3{}^4 N^2 L^2 \sin^2\theta}{96\pi^2 \epsilon_0{}^3 c} \mathrm{Re}\, [\epsilon_{\lambda\mu\nu} \beta^{\alpha\mu}_{\lambda\mu\nu} I^{(4)}_{YZYZ,\phi\chi\theta\rho} \bar{\beta}^{\alpha Q}_{\phi\chi\theta\rho}] \quad (9\text{-}31)$$

This was shown to be sensitive to molecular chirality.

9.3.3. CP-vis IR–vis SFG

The third case in Figure 68 is when the incident visible beam is left- or right-CP. The left- and right-CP-visible SFG signal intensities were found to be

$$I_{\text{CP-vis}}(\mathrm{L}) = \frac{I_{\text{IR}} I_{\text{vis}} k_3{}^4 N^2 L^2 \sin^2\theta}{16\pi^2 \epsilon_0{}^3 c} \left\{ \frac{|\epsilon_{\lambda\mu\nu} \beta^{\alpha\mu}_{\lambda\mu\nu}|^2}{144} + k_2{}^2 \left| I^{(4)}_{YYXX,\lambda\mu\nu\pi} \beta^{A\mu}_{\lambda\mu\nu\pi} \right|^2 + \frac{k_2\, \mathrm{Re}[\epsilon_{\lambda\mu\nu} \beta^{\alpha\mu}_{\lambda\mu\nu} I^{(4)}_{YYXX,\phi\chi\theta\rho} \bar{\beta}^{A\mu}_{\phi\chi\theta\rho}]}{6} \right\} \quad (9\text{-}32)$$

$$I_{\text{CP-vis}}(\mathrm{R}) = \frac{I_{\text{IR}} I_{\text{vis}} k_3{}^4 N^2 L^2 \sin^2\theta}{16\pi^2 \epsilon_0{}^3 c} \left\{ \frac{|\epsilon_{\lambda\mu\nu} \beta^{\alpha\mu}_{\lambda\mu\nu}|^2}{144} + k_2{}^2 \left| I^{(4)}_{YYXX,\lambda\mu\nu\pi} \beta^{A\mu}_{\lambda\mu\nu\pi} \right|^2 - \frac{k_2 \mathrm{Re}[\epsilon_{\lambda\mu\nu} \beta^{\alpha\mu}_{\lambda\mu\nu} I^{(4)}_{YYXX,\phi\chi\theta\rho} \bar{\beta}^{A\mu}_{\phi\chi\theta\rho}]}{6} \right\} \quad (9\text{-}33)$$

Again, the first term in eqs 9-32 and 9-33 is the all-electric-dipole-allowed contribution to the IR−vis SFG signal. The second terms in these equations are related to the electric quadrupole−electric dipole ROA tensors. The third term is the interference term, and its sign depends on the circular polarization states of the incident visible beam. The CID signal in this case of the CP-visible IR−vis SFG is then

$$\Delta I_{\text{CP-vis}} = \frac{I_{\text{IR}} I_{\text{vis}} k_2 k_3{}^4 N^2 L^2 \sin^2\theta}{48\pi^2 \epsilon_0{}^3 c} \mathrm{Re}\, [\epsilon_{\lambda\mu\nu} \beta^{\alpha\mu}_{\lambda\mu\nu} I^{(4)}_{YYXX,\phi\chi\theta\rho} \bar{\beta}^{A\mu}_{\phi\chi\theta\rho}] \quad (9\text{-}34)$$

Note again that the CP-vis IR−vis SFG can provide complementary information on the molecular chirality in comparison to the other vibrational optical activity measurement techniques discussed in this subsection.

9.3.4. CP-Field-Detected IR–vis SFG

The last scheme in Figure 68 is the case when the two incident beams both are linearly polarized but the circularly polarized components of the coherently emitted IR−vis SFG field are separately detected. In this case of CP-field-detected IR−vis SFG, the two signal intensities are

$$I_{\text{CP-field}}(L) = \frac{I_{\text{IR}} I_{\text{vis}} k_3{}^4 N^2 L^2 \sin^2\theta}{16\pi^2 \epsilon_0{}^3 c} \left\{ \frac{|\epsilon_{\lambda\mu\nu} \beta^{\alpha\mu}_{\lambda\mu\nu}|^2}{144} + k_1{}^2 \hat{k}_{3Z}{}^2 \left| I^{(4)}_{XZXZ,\lambda\mu\nu\pi} \beta^{\alpha Q}_{\lambda\mu\nu\pi} \right|^2 - \frac{k_1 \hat{k}_{3Z}}{6} \mathrm{Re}[\epsilon_{\lambda\mu\nu} \beta^{\alpha\mu}_{\lambda\mu\nu} I^{(4)}_{XZXZ,\phi\chi\theta\rho} \bar{\beta}^{\alpha Q}_{\phi\chi\theta\rho}] \right\} \quad (9\text{-}35)$$

$$I_{\text{CP-field}}(L) = \frac{I_{\text{IR}} I_{\text{vis}} k_3{}^4 N^2 L^2 \sin^2\theta}{16\pi^2 \epsilon_0{}^3 c} \left\{ \frac{|\epsilon_{\lambda\mu\nu} \beta^{\alpha\mu}_{\lambda\mu\nu}|^2}{144} + k_1{}^2 \hat{k}_{3Z}{}^2 \left| I^{(4)}_{XZXZ,\lambda\mu\nu\pi} \beta^{\alpha Q}_{\lambda\mu\nu\pi} \right|^2 + \frac{k_1 \hat{k}_{3Z}}{6} \mathrm{Re}[\epsilon_{\lambda\mu\nu} \beta^{\alpha\mu}_{\lambda\mu\nu} I^{(4)}_{XZXZ,\phi\chi\theta\rho} \bar{\beta}^{\alpha Q}_{\phi\chi\theta\rho}] \right\} \quad (9\text{-}36)$$

The second terms in eqs 9-35 and 9-36 are the polarizability−electric quadrupole hyperpolarizability contributions. Again, the interference terms that are the third terms in these two equations depend on the circular polarization states of the detected IR−vis SFG field. Then, the circular intensity difference is

$$\Delta I_{\text{CP-field}} = \frac{I_{\text{IR}} I_{\text{vis}} k_1 k_3{}^4 N^2 L^2 \hat{k}_{3Z} \sin^2\theta}{48\pi^2 \epsilon_0{}^3 c} \mathrm{Re}\, [\epsilon_{\lambda\mu\nu} \beta^{\alpha\mu}_{\lambda\mu\nu} I^{(4)}_{XZXZ,\phi\chi\theta\rho} \bar{\beta}^{\alpha Q}_{\phi\chi\theta\rho}] \quad (9\text{-}37)$$

Noting that $I^{(4)}_{XZXZ,\phi\chi\theta\rho} = I^{(4)}_{YZYZ,\phi\chi\theta\rho}$, one can find that the CP-field-detected IR−vis SFG CID is linearly proportional to the circular intensity difference of the CP-IR IV-SFG.

In this subsection, theoretical descriptions of three different IR−vis SFG schemes utilizing circularly polarized beams were discussed. In addition to the chiral-sensitive all-electric-dipole-allowed IR−vis SFG method, they were shown to be useful in extracting information on the polarizability−electric quadrupole term and electric quadrupole−electric dipole ROA tensor term. Although, in this subsection, only the frequency-domain IR−vis SFG susceptibilities were briefly outlined, one can develop the theory in terms of time-domain nonlinear response functions. This was achieved for the case of the CP-IR IR−vis SFG in ref 41. In such a case when ultrafast IR and visible pulses are used to carry out these experiments, these techniques will be of use in studying ultrafast chemical and physical processes involving chiral molecules such as proteins in the future, i.e., protein folding or unfolding and chemical reaction dynamics involving chirality changes.

9.4. Nonlinear Optical Activity Four-Wave-Mixing Spectroscopy

Coherent 2D spectroscopy has been shown to be useful in quantitatively estimating interchromophore couplings and studying structural changes, e.g., peptide structures in condensed phases,[24,292,385,386,450,572−576] structural transitions of small peptides,[450] solute−solvent interaction dynamics,[17,445,577−580] ultrafast excitation migration processes in photosynthetic protein complexes,[9,581] and exciton dynamics in semiconductors.[484,582] A crucial advantage of the 2D optical spectroscopy is that it can provide far more detailed information on molecular structure since the frequencies and amplitudes of cross peaks in a two-dimensionally displayed spectrum contain vital information on couplings between different basis modes as well as on the time-dependent

Scheme 4

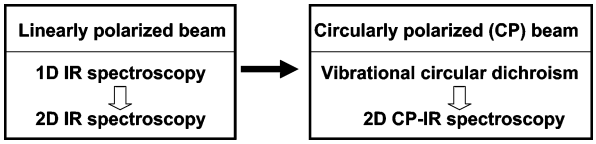

conditional probability describing the population and coherence transfer or chemical exchange process during the waiting time.[3,34]

All these 2D spectroscopic investigations utilizing the photon echo technique used linearly polarized beams. However, by noting that the optical activity is related to the differential interaction of a chiral molecule with left- and right-circularly polarized radiation during quantum excitation, novel 2D optical spectroscopy utilizing circularly polarized beams can be devised (see Scheme 4).

One of the first theoretical attempts along this line was presented in ref 42, where the so-called 2D *circularly polarized* pump−probe (CP PP) spectroscopy with a circularly polarized pump beam was theoretically proposed. The difference between the left- and right-CP PP spectra was shown to be dependent on molecular chirality. This is because the leading contributions to the difference spectrum originate from both magnetic dipole−magnetic field and quadrupole−electric field interactions and they are sensitive to the absolute configuration of chiral molecule. In general, one can selectively measure the real and imaginary parts of the self-heterodyned CP PP signal by controlling the phase of the probe beam with respect to the pump beam. The two parts then correspond to the nonlinear circular birefringent and circular dichroic responses, respectively. Later, the 2D circularly polarized photon echo spectroscopy was theoretically proposed and some numerical simulation results on polypeptides and a light-harvesting protein complex were presented. In relation to these works, the first-order terms of the nonlinear material polarization with respect to the optical wave vector were considered and shown to be sensitive to molecular chirality. It was however proven that there are direct correspondences between the linear **k**-term measurement methods and the difference signal measurement methods except for a constant factor.

In ref 42, a general CP PP spectroscopy was considered and particularly it was shown that the magnetic dipole contributions to the signal could be selectively measured by controlling the angle, θ, between the pump and probe beam propagation directions to be $\tan^{-1}(1/\sqrt{2})$. Recently, by carrying out quantum chemistry calculations of transition quadrupole moments of the amide I vibration and of the Q_y-transition of bacteriochlorophyll, it was possible to show that the 2D CP photon echo signals can be calculated and that for these cases the magnetic dipole contribution to the 2D CP photon echo is dominant.

Using the semiclassical field−matter interaction Hamiltonian,

$$H_{\mathrm{I}} = -\mu_i E_i(\mathbf{r},t) - m_i B_i(\mathbf{r},t) - Q_{ij}\nabla_j E_i(\mathbf{r},t) \quad (9\text{-}38)$$

and time-dependent perturbation theory, one could obtain the third-order polarization $\mathbf{P}^{(3)}(\mathbf{r},t)$ as[571]

$$\mathbf{P}^{(3)}(t) = \mathbf{P}_0^{(3)}(t) + \delta\mathbf{P}^{(3)}(t;m) + \delta\mathbf{P}^{(3)}(t;Q) + \ldots \quad (9\text{-}39)$$

The first term on the right-hand side of eq 9-39 represents the polarization created by the all-electric-dipole-allowed FWM process. The second and third terms are linearly proportional to the magnetic dipole and electric quadrupole moments, respectively. Due to the fact that the electric dipole−electric field interaction strength is usually 2 to 3 orders of magnitude larger than the magnetic dipole−magnetic field and the electric quadrupole-electric field interactions,[571] the first term $\mathbf{P}_0^{(3)}(t)$ is much larger than the other terms in eq 9−39. However, since $\mathbf{P}_0^{(3)}(t)$ is insensitive to molecular chirality, the 2D photon echo spectroscopy utilizing linearly polarized beams cannot provide information on the nonlinear optical activity of chiral molecules in solution. The second and third terms in eq 9−39 are, in contrast, strongly dependent on molecular chirality and on the rotational direction of the incident circularly polarized beam.

In general, most of the optical activity spectroscopies are to measure the difference of spectroscopic observables obtained by using left- and right-circularly polarized beams. By following the same convention, the nonlinear optical activity measurement spectroscopy was defined as the difference between two nonlinear optical signals obtained with left- and right-circularly polarized beams as

$$\Delta S = S_{\mathrm{L}} - S_{\mathrm{R}} \quad (9\text{-}40)$$

Here, the subscripts L and R represent the cases when the polarization states of the injected beam are left- and right-circularly polarized, respectively. Depending on specific detection method, e.g., homodyne or heterodyne, the measured signal is proportional to $|\mathbf{P}^{(3)}|^2$, Re[$\mathbf{P}^{(3)}$], or Im[$\mathbf{P}^{(3)}$]. Recently, FWM spectroscopy measuring nonlinear response function tensor elements that are not rotationally invariant within the electric dipole approximation, such as the [*XXXY*]-component, was shown to be chiral-sensitive, where they considered the linear **k**-term in the expansion of the radiation−molecule interaction Hamiltonian.[529,557] Noting that the circularly polarized beams can be written as linear combinations of two linearly polarized beams with a $\pi/2$ phase difference, i.e., $e^{(\mathrm{L})} = (\mathbf{x} + i\mathbf{y})/\sqrt{2}$ and $e^{(\mathrm{R})} = (\mathbf{x} - i\mathbf{y})/\sqrt{2}$, it was possible to show that the difference measurement method emphasized in eq 9-40 is identical to the measurement scheme utilizing polarization controlled beams by the factor of $i\sqrt{2}$ (see the Appendix in ref 45 for a detailed discussion on this equality). More specifically, from the minimal coupling Hamiltonian, the radiation−molecule interaction energy is given as

$$H_{\mathrm{I}} = -\frac{e}{mc}\mathbf{A}(\mathbf{r},t)\cdot\mathbf{p} \quad (9\text{-}41)$$

where **A** is the vector potential and **p** is the quantum mechanical momentum operator. The classical vector potential is assumed to be given as $\mathbf{A}(\mathbf{r},t) = \epsilon A_0 f(t)\cos(\mathbf{k}\cdot\mathbf{r} - \omega t)$, where ϵ is the unit vector, A_0 is the amplitude, $f(t)$ is the temporal envelope function and it is real, **k** is the wave vector, and ω is the center frequency. Then one can rewrite the interaction Hamiltonian as[583]

$$H_I = -U(\mathbf{k})\,F(t) - U(-\mathbf{k})\,F^*(t) \quad (9\text{-}42)$$

with

$$U(\mathrm{k}) = \frac{eA_0}{2mc}e^{i\mathbf{k}\cdot\mathbf{r}}(\epsilon\cdot\mathbf{p})$$

$$F(t) = f(t)e^{-i\omega t} \quad (9\text{-}43)$$

The first and second terms in eq 9-42 are known to cause absorption and stimulated emission, respectively. Expanding $e^{i\mathbf{k}\cdot\mathbf{r}}$ as $e^{i\mathbf{k}\cdot\mathbf{r}} \simeq 1 + i\mathbf{k}\cdot\mathbf{r}$ up to the first order with respect to $\mathbf{k}$, one can obtain the magnetic dipole−magnetic field and quadrupole−electric field interaction terms. In refs 529 and 557, this approach to the calculations of nonlinear response functions that are linearly proportional to $\mathbf{k}$ was used. Then, they showed that the rotationally invariant contributions from these $\mathbf{k}$-dependent terms to the polarization were found to be important and sensitive to molecular chirality. Nevertheless, this approach of measuring a particular polarization-controlled signal, such as the [*XXXY*]-tensor component of the third-order nonlinear response function, was shown to be essentially identical to the conventional difference measurement technique utilizing circularly polarized beams.[45]

Recently, circularly polarized photon echo spectroscopy employing a spectral interferometric heterodyne-detection method was considered in detail.[29,584] Particularly, the specific case when the first pulse used for this experiment is circularly polarized will be briefly discussed in this subsection. Since the angles between pulse propagation directions are close to zero, not only the magnetic dipole but also the electric quadrupole transitions can contribute to the measured CP photon echo signal. The beam propagation directions are parallel to the *Z*-axis in a space-fixed frame. The first light pulse is controlled to be either left- or right-CP, but the second and third pulses are linearly polarized along the *X*-axis and the *X*-component of the photon echo polarization vector is measured. The difference between the two signals with left- and right-CP first light pulses was then found to be given as the sum of two terms

$$\Delta S = \Delta S_{\mathrm{mag}} + \Delta S_{\mathrm{quad}} \propto \{\delta\mathbf{P}_{\mathrm{L}}^{\mathrm{PE}}(t;m) - \delta\mathbf{P}_{\mathrm{R}}^{\mathrm{PE}}(t;m)\} + \{\delta\mathbf{P}_{\mathrm{L}}^{\mathrm{PE}}(t;Q) - \delta\mathbf{P}_{\mathrm{R}}^{\mathrm{PE}}(t;Q)\} \quad (9\text{-}44)$$

where the first and second terms on the right-hand side of eq 9-44 are the magnetic dipole and electric quadrupole contributions to the CP-PE signal, respectively. Theoretical expressions of these two terms are as follows:[45]

$$\Delta S_{\mathrm{mag}}(\tau,t) = {}^{(1)}\Delta S_{\mathrm{mag}}^{\mathrm{diag}}(\tau,t) + {}^{(1)}\Delta S_{\mathrm{mag}}^{\mathrm{cross}}(\tau,t) + {}^{(2)}\Delta S_{\mathrm{mag}}(\tau,t) \quad (9\text{-}45)$$

$$\Delta S_{\mathrm{quad}}(\tau,t) = {}^{(1)}\Delta S_{\mathrm{quad}}^{\mathrm{cross}}(\tau,t) + {}^{(2)}\Delta S_{\mathrm{quad}}(\tau,t) \quad (9\text{-}46)$$

where

$${}^{(1)}\Delta S_{\mathrm{mag}}^{\mathrm{diag}}(\tau,t) = \sum_j \frac{4}{15} D_{e_je_j}^g R_{e_je_j}^g \{r_{jj}^{\mathrm{EA}}(\tau,t) + r_{jj}^{\mathrm{GB}}(\tau,t)\}$$

$${}^{(1)}\Delta S_{\mathrm{mag}}^{\mathrm{cross}}(\tau,t) = \sum_j \sum_{k\neq j} \left\{ \frac{1}{5} D_{e_ke_k}^g R_{e_je_j}^g + \frac{1}{15} D_{e_je_k}^g R_{e_je_k}^g \right\} r_{jk}^{\mathrm{GB}}(\tau,t)$$

$${}^{(2)}\Delta S_{mag}(\tau,t) = -\sum_{j,l} \left\{ \frac{1}{5} D_{f_lf_l}^{e_j} R_{e_je_j}^g + \frac{1}{15} (\mu_{f_le_j}\cdot\mu_{e_jg})(\mu_{f_le_j}\cdot\mathbf{M}_{e_jg}) \right\} r_{\mathrm{ljj}}^{\mathrm{EA}}(\tau,t)$$

$${}^{(1)}\Delta S_{\mathrm{quad}}^{\mathrm{cross}}(\tau,t) = \sum_{j,k} \frac{1}{15} \mu_{e_kg}\cdot\{\mu_{e_jg} \times (\mu_{e_kg}\cdot\tilde{Q}_{e_jg})\} r_{kj}^{\mathrm{GB}}(\tau,t)$$

$${}^{(2)}\Delta S_{\mathrm{quad}}(\tau,t) = -\sum_{j,k,l} \frac{1}{15} \mu_{f_le_j}\cdot\{\mu_{e_jg} \times (\mu_{f_le_j}\cdot\tilde{Q}_{e_jg})\} r_{\mathrm{ljj}}^{\mathrm{EA}}(\tau,t) \quad (9\text{-}47)$$

The dipole and rotational strength matrices are defined as

$$D_{e_je_k}^g \equiv \mu_{e_jg}\cdot\mu_{e_kg}$$

$$R_{e_je_k}^g \equiv \mu_{e_jg}\cdot\mathbf{M}_{e_kg} \quad (9\text{-}48)$$

where $\mathbf{m}_{ba} = -\bar{\mathbf{m}}_{ab} = i\mathbf{M}_{ba}$. Note that the diagonal elements of the $\tilde{\mathbf{D}}^g$ and $\tilde{\mathbf{R}}^g$ matrices correspond to the usual dipole and rotational strengths determining the transition probabilities of the corresponding light absorption and circular dichroism, respectively. In addition, we introduced the excited-state dipole strength as

$$D_{f_lf_l}^{e_j} \equiv \mu_{f_le_l}\cdot\mu_{f_le_j} \quad (9\text{-}49)$$

which represents the transition probability from $|e_j\rangle$ to $|f_l\rangle$ states, i.e., the electric dipole-allowed excited-state absorption.

The three line broadening functions in eq 9-47 were obtained from eqs 4-41−4-44 and are given as[238]

$$r_{jk}^{\mathrm{SE}}(\tau,T,t) = \exp\{-i\Omega_j t + i(\Omega_k - \Omega_j)T + i\Omega_k\tau\} \exp\{-\int_0^{\tau+T} d\tau_1 \int_0^{\tau_1} d\tau_2\, \xi_{e_ke_k}^*(\tau_1,\tau_2) - \int_\tau^{\tau+T+t} d\tau_1 \int_\tau^{\tau_1} d\tau_2\, \xi_{e_je_j}(\tau_1,\tau_2) + \int_0^{\tau+T} d\tau_1 \int_\tau^{\tau+T+t} d\tau_2\, \xi_{e_ke_j}(\tau_1,\tau_2)\}$$

$$r_{jk}^{\mathrm{GB}}(\tau,T,t) = \exp\{-i\Omega_j t + i\Omega_k\tau\} \exp\{-\int_0^{\tau} d\tau_1 \int_0^{\tau_1} d\tau_2\, \xi_{e_ke_k}^*(\tau_1,\tau_2) - \int_{\tau+T}^{\tau+T+t} d\tau_1 \int_{\tau+T}^{\tau_1} d\tau_2\, \xi_{e_je_j}(\tau_1,\tau_2) + \int_0^{\tau} d\tau_1 \int_{\tau+T}^{\tau+T+t} d\tau_2\, \xi_{e_ke_j}(\tau_1,\tau_2)\}$$

$$r_{lkj}^{\mathrm{EA}}(\tau,T,t) = \exp\{-i(W_1 - \Omega_j)t - i(\Omega_k - \Omega_j)T + i\Omega_j\tau\} \exp\{-\int_\tau^{\tau+T} d\tau_1 \int_\tau^{\tau_1} d\tau_2\, \xi_{e_ke_k}(\tau_1,\tau_2) - \int_{\tau+T}^{\tau+T+t} d\tau_1 \int_{\tau+T}^{\tau_1} d\tau_2\, \xi_{f_lf_l}(\tau_1,\tau_2) - \int_0^{\tau+T+t} d\tau_1 \int_0^{\tau_1} d\tau_2\, \xi_{e_je_j}^*(\tau_1,\tau_2) - \int_\tau^{\tau+T} d\tau_1 \int_{\tau+T}^{\tau+T+t} d\tau_2\, \xi_{e_kf_l}(\tau_1,\tau_2) + \int_\tau^{\tau+T} d\tau_1 \int_0^{\tau+T+t} d\tau_2\, \xi_{e_ke_j}^*(\tau_1,\tau_2) + \int_{\tau+T}^{\tau+T+t} d\tau_1 \int_0^{\tau+T+t} d\tau_2\, \xi_{f_le_j}^*(\tau_1,\tau_2)\} \quad (9\text{-}50)$$

Since the signs of rotational strength carry critical information on the relative angles between the transition electric and magnetic dipoles, the 2D CP photon echo can provide detailed information on the structure and dynamics of complex molecules with chiral properties. To demonstrate the advantages of the 2D CP photon echo technique, numerically simulated spectra of polypeptides and a light-harvesting protein complex were directly compared with their 2D PE spectra.[45]

The amide I vibrations of polypeptides were successfully described by using the fragment approximation and coupled anharmonic oscillator model. Also, theoretical procedures

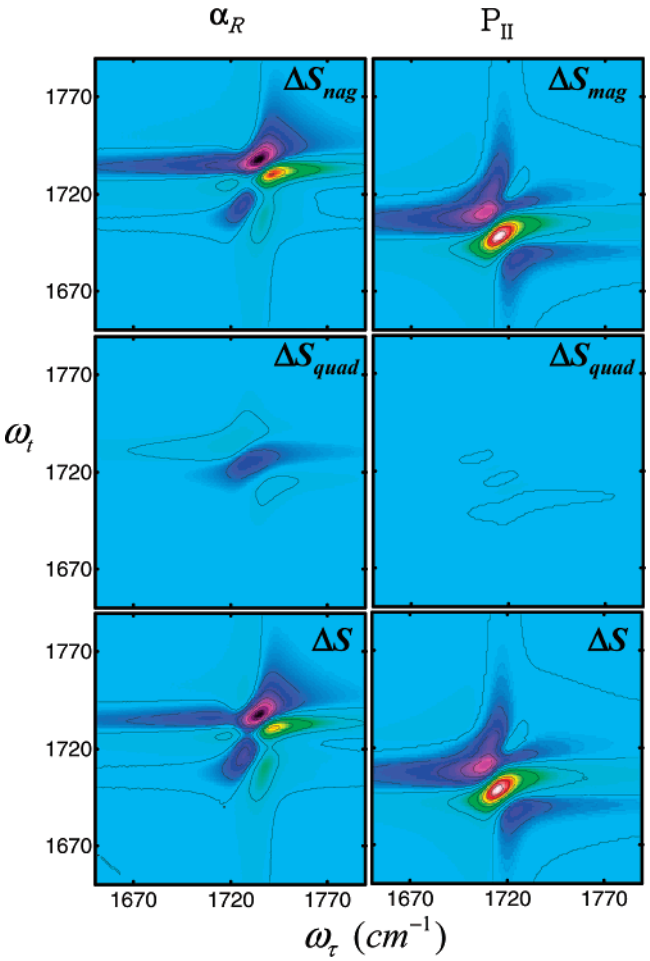

Figure 70. 2D circularly polarized IR photon echo spectra of right-handed α-helical and polyproline II dipeptides (Ac-Ala-NHMe).[45] The upper two panels show the 2D CP-IR photon echo spectra obtained by considering the magnetic dipole−magnetic field contribution in eq 9-45. The middle spectra are the quadrupole contribution to the 2D CP-IR photon echo spectra. The bottom two spectra are the total 2D spectrum.

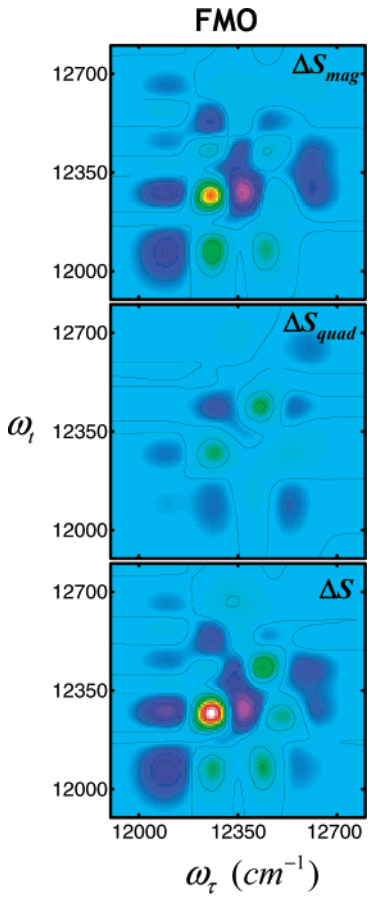

Figure 71. 2D CP-visible photon echo spectra of the FMO light-harvesting complex.[45] Parameters, other than transition magnetic and quadrupole matrix elements, used to simulate these spectra were taken from ref 10.

for calculating transition electric and magnetic dipoles of amide I vibrations have been developed (see section 9.2). However, it was still necessary to determine the transition electric quadrupoles to completely simulate the 2D CP PE spectra of polypeptides. Considering the NMA as a unit peptide, one could carry out *ab initio* calculations of transition quadrupole tensor elements associated with the amide I vibration of NMA (see ref 45 for detailed computational methods). Then, using thus calculated transition quadrupoles of NMA, it was possible to calculate the transition quadrupole moments of two amide I normal modes of dipeptide. In Figure 70, the 2D CP PE spectra of the right-handed α-helical and P_{II} dipeptides are shown. It turned out that the quadrupole contribution, ΔS_{quad}, to the total 2D CP PE signal is about an order of magnitude smaller than that from the magnetic dipole contribution, ΔS_{mag}.

Similarly, to obtain the transition quadrupole tensor of a BChl (bacteriochlorophyll), the geometry-optimized structure of a model BChl molecule was obtained with the B3LYP method and the 6-31G(d) basis set. The dipole and quadrupole moments of the ground state and the excited Q_y state were calculated by using the CIS method (configuration interaction with single excitation from a spin-restricted Hartree−Fock (RHF) reference determinant).[45] From these permanent dipole and quadrupole moments, the transition dipole and quadrupole moments can be determined by taking the differences between those of the excited and ground states. By using the calculated transition electric dipole, magnetic dipole, and quadrupole moments of the FMO complex, the 2D CP PE spectra were calculated and shown in Figure 71. For detailed discussions on the computational method as well as on the advantages of the 2D CP photon echo technique, the readers may find refs 44, 45, and 585 interesting.

As discussed and demonstrated in this section, time-resolved nonlinear optical activity measurement spectroscopy can provide valuable information on structural changes of chiral molecules in solution. It will be of great interest to measure the time-resolved 2D nonlinear optical activity snapshot spectra of folding or unfolding proteins in the future.

10. Perspectives and a Few Concluding Remarks

Natural science has been advanced in two different ways, i.e., paradigm change (conceptual development) and design of novel tools (technical development). An example for the former is the development of quantum mechanics, whereas those for the latter are the developments of X-ray crystallography and NMR spectroscopy. There is little doubt about the impact of the former on scientific advancement. However, most often we have witnessed technical breakthroughs belonging to the latter, and they sometimes opened up a new branch of scientific research. In this regard, coherent multidimensional optical spectroscopy, as a novel tool, will trigger a number of new studies and investigations in all areas of natural science.[586]

Coherent 2D vibrational and electronic spectroscopy utilizing femtosecond IR−vis laser pulses has thus been paid a lot of attention over the past decade, because it can provide detailed and highly dense information on the molecular structure of peptides and proteins, molecular interactions and dynamics, nucleic acid structures, semiconductor dynamics, chemical exchanges, population and coherence transfers in coupled multichromophore systems, intramolecular vibrational energy relaxation, hydrogen-bonging dynamics and network forming liquids, and so on. One of the most important advantages of this spectroscopic technique is its unprecedented ultrafast time resolution (∼femtosecond) so that a variety of chemical reactions and biochemical processes involving transient species can be studied. Conventional applications of time-resolved spectroscopy such as time-resolved absorption and fluorescence spectroscopy and other types of one-dimensional four-wave-mixing spectroscopy have mainly focused on measurements of the lifetime of an excited-state or of radiationless transition rates among different quantum states. In order to elucidate the entire kinetic network of reactive and product species, it was inevitable to perform quite a number of independent experiments by tuning light frequencies separately, e.g., two-color pump−probe spectroscopy, which can be quite tedious and time-consuming. Furthermore, due to time−energy uncertainty, it is not always possible to achieve both ultrafast time-resolution and high frequency-resolution simultaneously. Here, it should be emphasized that coherent multidimensional spectroscopy should be distinguished from incoherent time-frequency resolved spectroscopy such as impulsive stimulated Raman probe with ultrafast pump, IR-Raman (IR-pump with Raman detection) spectroscopy, etc. Note that the latter type of incoherent spectroscopy, for which the signal has often been presented as a multidimensional spectrum, can only provide information on incoherent population (square of wave function) relaxation. On the other hand, since the coherent 2D spectroscopy discussed in this paper utilizes femtosecond laser pulses with broad spectral bandwidths, quantum coherence states of which oscillation frequencies are within the pulse spectral bandwidth can be created simultaneously and probed in time by using yet another interrogating femtosecond laser pulse. Consequently, preservation of phase information and investigation of coherence evolution and transfer can be achieved by this technique.

One of the most important applications of such ultrafast 2D spectroscopic techniques would be to study chemical reaction dynamics in condensed phases including solutions, surfaces, and interfaces. The spatial connectivity between any two different vibrational (or electronic) degrees of freedom (chromophores) via through-bond and/or through-space interactions is the key information that can be extracted from the time-resolved multidimensional spectra. Thus, in general, by properly selecting two vibrational (electronic) degrees of freedom directly associated with reactive and product species, one can in principle follow the chemical reaction dynamics by monitoring the cross peak amplitude changes in time.

An important process involved in chemical reaction dynamics is the intramolecular energy redistribution. Ultrafast multidimensional vibrational spectroscopy detecting the coherently generated signal field will be of use to study state-to-state or mode-to-mode energy transfer pathways along the reaction coordinate. The other and directly related issue is to investigate the role of the solvent molecules in chemical reactions, which has been the central research theme of physical chemistry. However, still there is a lack of experimental means to obtain direct information on how each individual solvent molecule participates in a given chemical or biological reaction. Most previous spectroscopic investigations largely focused on how to follow the dynamics and spectral changes of probing solute mode (or state) to indirectly infer an unknown time-scale and dynamics of interacting solvent molecules. Now, it will be possible to use ultrafast 2D spectroscopy to simultaneously follow the dynamics of both solute and solvent modes (or states). Suppose that there is a characteristic vibrational chromophore in a reactive species and that its primary spectroscopic properties such as frequency (ω_{solute}) and dipole strength are strongly coupled to (or modulated by) a particular solvent mode ($\omega_{solvent}$). If the laser pulse frequencies, ω_1 and ω_2, are tuned to be resonant with ω_{solute} and $\omega_{solvent}$, i.e., $\omega_1 \approx \omega_{solute}$ and $\omega_2 \approx \omega_{solvent}$, only when the two characteristic modes are coupled (or spatially close) to each other does the 2D vibrational spectroscopic signal, i.e., cross peaks, not vanish. The cross peak at ($\omega_1 \approx \omega_{solute}$, $\omega_2 \approx \omega_{solvent}$) therefore acts like a direct reporter revealing how the solvent mode actively participates in the course of the chemical reaction. Two-dimensionally displayed spectra in time will thus give a detailed picture of the solvent dynamics during the chemical reaction such as photodissociation, photoinduced electron transfer, excited-state isomerization, proton transfers induced by a photodissociation or photoexcitation, etc.

As shown in this article, 2D spectroscopy has been proven to be quite useful in studying hydrogen-bond formation and dissociation processes, van der Waals complexation dynamics, and internal rotations within a molecule. A notable advantage of the 2D spectroscopic technique is that it does not require any external perturbation, such as T-jump, pressure-jump, concentration change, etc., to create a new nonequilibrium state. The light-excitation of a specific mode, which can be viewed as a *photoe*xcitation-labeling, can be monitored in time by examining time-dependent changes of the associated cross peaks. In the future, one could use this technique to directly follow the chemical reaction dynamics by examining the cross peak, if the chromophores properly chosen represent reactant, intermediates, and product exclusively, which enables one to determine the entire kinetic network.

Solvation dynamics has been extensively studied over the last two decades by using a variety of time-resolved spectroscopic techniques such as time-dependent fluorescence Stokes shift, three-pulse photon echo peak shift, etc. Nevertheless, it is still desired to have an experimental method capable of providing direct information on how the surrounding solvent molecules participate in the solvation dynamics and in the formation of the local structure around it. Are two different solvent modes participating in a solvation process coupled? Are there any experimental methods that can be used to study solvation dynamics by watching the vibrational dynamics of both (unreactive) solute and solvent? Noting that 2D spectroscopy can provide direct information on the coupling between two *spatially separated but coupled* modes or states, following the cross peak revealing coupling between the solute and solvent modes would provide information on solvation time-scales and

interaction strengths, i.e., the microscopic aspect of the solvation dynamics.

Although there is no coherent 2D spectroscopic investigation of coupled multichromophore systems on surfaces or at interfaces yet, it will be highly interesting to apply the technique to adsorbed molecules on surfaces or at interfaces. A few potentially useful techniques are 2D SFG spectroscopy or 2D IR−vis FWM spectroscopy. Although an example of CO molecules adsorbed on a metal surface, where CO stretching modes are coupled to each other via dipole−dipole interactions, was studied by using an IR−vis FWM technique, it will be extremely interesting to apply the full 2D spectroscopic technique to study heterogeneous adsorbed molecular systems on surfaces or at interfaces to eventually shed light on couplings, inhomogeneity, and excitation transfers within the delocalized excitonic states with respect to fractional coverage or surface concentration. Surely, an application of the surface 2D spectroscopy to study the chemical reaction dynamics on surfaces, i.e., inhomogeneous catalysis, will be extremely interesting.

One of the most important applications of ultrafast multidimensional vibrational spectroscopy is definitely on biological phenomena, as has been demonstrated over the years and outlined in section 5 of this article. In particular, 2D IR spectroscopy has already been shown to be a useful tool for determining the local structure of peptides. One can combine vibrational and electronic transition processes, e.g., triply resonant 2D vibrational spectroscopy or vibrational/electronic four-wave-mixing spectroscopy, to explore a wide range of vibrational and vibronic coupling mechanisms in biomolecules. For instance, the vibronic coupling between peptide vibrations and peptide electronic transitions would be an interesting property reflecting the three-dimensional structure of the polypeptide backbone. Alternatively, electronically resonant fifth-order Raman spectroscopy and two-color fifth-order three pulse scattering spectroscopy that directly probe the energies and dynamics of electronically excited states might be of use for such a purpose. A vibrational spectroscopic analogue of heteronuclear 2D NMR spectroscopy is dual frequency (or two-color) 2D vibrational echo spectroscopy. Perhaps, one can combine IR- and UV-excitation schemes to create a two-dimensional transient grating in the vibrational and electronic manifold, which can then be probed by using (coherent) a resonant stimulated Raman scattering process.

As emphasized in this review and by others, the key advantage of ultrafast multidimensional spectroscopy is its experimentally accessible time-scale. Although the protein folding process in nature occurs in a wide range of time scales, from picoseconds to seconds or even hours, solution NMR cannot be used to study the early part of the protein folding process due to its limited time resolution (∼milliseconds). In this respect, ultrafast multidimensional spectroscopy utilizing IR or visible pulses has a clear advantage over the other techniques. Recently, nonlinear spectroscopy utilizing circularly polarized beams was theoretically proposed and shown to be highly sensitive to molecular chirality. Noting that almost all biological molecules of interest are chiral in nature, such novel time-resolved nonlinear optical activity spectroscopy will provide critical information on structures of biomolecules from the optical activity viewpoint.

Another interesting bioapplication of ultrafast multidimensional spectroscopy is to investigate the substrate−enzyme, ligand−protein, protein−protein, ligand−DNA (or RNA), protein−DNA (or RNA) interactions. For instance, in order for a given enzyme to catalyze a biochemical reaction, the substrate (or ligand) should form a complex at the catalytic site of the enzyme. Tuning the two external field frequencies to be in resonance with the characteristic vibrational modes of the substrate and enzyme separately, one can directly measure the formation and dissociation of the ES complex. Similarly, protein−DNA (or protein−RNA) complexes, antibody−antigen complexes, etc. can be other interesting systems to be studied with ultrafast multidimensional spectroscopy.

Coherent multidimensional optical spectroscopy, even though it has a short history, has already become a well-defined and widely applicable tool, largely owing to the dramatic advancement of ultrafast laser technology as well as to high-performance computers and simulation algorithms. To make these techniques more useful and popular in the future, it will be absolutely necessary to make 2D vibrational and electronic spectrometers commercially available. In parallel, systematic computational tools and programs that can be used with ease should be developed. With this, I would like to end this review article.

11. Glossary of Acronyms

2D	two-dimensional
3D	three-dimensional
3PEPS	three-pulse photon echo peak shift
CD	circular dichroism
COSY	correlation spectroscopy
CP	circularly polarized
DFG	difference frequency generation
DFT	density functional theory
DO	diffractive optics
DOVE	doubly vibrationally enhanced
EA	excited-state absorption
Ex	excitation
FMO	Fenna−Matthews−Olson
FSS	fluorescence Stokes shift
FT	Fourier transform
FWM	four-wave mixing
GB	ground-state bleaching
IR	infrared
ISS	impulsive stimulated Raman scattering
LCAO	linear combination of atomic orbitals
LCBM	linear combination of basis modes
LP	linearly polarized
MD	molecular dynamics
ML	monolayer
NMA	*N*-methylacetamide
NMR	nuclear magnetic resonance
NOESY	nuclear Overhauser enhancement spectroscopy
OD	optical density
OHD	optical heterodyne-detected
OKE	optical Kerr effect
PE	photon echo
PEPS	photon echo peak shift
PP	pump probe
Pr	probing
QM/MM	quantum mechanical/molecular mechanical
ROA	Raman optical activity
SE	stimulated emission
SFG	sum frequency generation
TWM	three-wave mixing
UV	ultraviolet
VCD	vibrational circular dichroism
vis	visible

12. Acknowledgments

This work was supported by the creative research initiatives (CRI) program of KOSEF (MOST, Korea). The author thanks graduate students, postdoctoral research associates at the Center for Multidimensional Spectroscopy, Korea University, and collaborators, in particular Professors G. R. Fleming, J. C. Wright, A. Tokmakoff, M. D. Fayer, and Y. Tanimura.

13. References

(1) Ernst, R. R.; Bodenhausen, G.; Wokaun, A. *Nuclear Magnetic Resonance in One and Two Dimensions*; Oxford University Press: Oxford, 1987.
(2) Wuthrich, K. *NMR of proteins and nucleic acids*; John Wiley & Sons: New York, 1986.
(3) Cho, M. *Nature* **2006**, *444*, 431.
(4) Warren, W. S.; Zewail, A. H. *J. Chem. Phys.* **1981**, *75*, 5956.
(5) Fleming, G. R.; Cho, M. *Annu. Rev. Phys. Chem.* **1996**, *47*, 109.
(6) Zimdars, D.; Tokmakoff, A.; Chen, S.; Greenfield, S. R.; Fayer, M. D.; Smith, T. I.; Schwettman, H. A. *Phys. Rev. Lett.* **1993**, *70*, 2718.
(7) Cho, M.; Brixner, T.; Stiopkin, I.; Vaswani, H.; Fleming, G. R. *J. Chin. Chem. Soc.* **2006**, *53*, 15.
(8) Hamm, P.; Lim, M. H.; Hochstrasser, R. M. *J. Phys. Chem. B* **1998**, *102*, 6123.
(9) Brixner, T.; Stenger, J.; Vaswani, H. M.; Cho, M.; Blankenship, R. E.; Fleming, G. R. *Nature* **2005**, *434*, 625.
(10) Cho, M.; Vaswani, H. M.; Brixner, T.; Stenger, J.; Fleming, G. R. *J. Phys. Chem. B* **2005**, *109*, 10542.
(11) Engel, G. S.; Calhoun, T. R.; Read, E. L.; Ahn, T. K.; Mancal, T.; Cheng, Y. C.; Blankenship, R. E.; Fleming, G. R. *Nature* **2007**, *446*, 782.
(12) Woutersen, S.; Mu, Y.; Stock, G.; Hamm, P. *Chem. Phys.* **2001**, *266*, 137.
(13) Kwac, K.; Lee, H.; Cho, M. *J. Chem. Phys.* **2004**, *120*, 1477.
(14) Zheng, J.; Kwak, K.; Asbury, J. B.; Chen, X.; Piletic, I.; Fayer, M. D. *Science* **2005**, *309*, 1338.
(15) Kim, Y. S.; Hochstrasser, R. M. *Proc. Natl. Acad. Sci. U.S.A.* **2005**, *102*, 11185.
(16) Kwac, K.; Lee, C.; Jung, Y.; Han, J.; Kwak, K.; Zheng, J. R.; Fayer, M. D.; Cho, M. *J. Chem. Phys.* **2006**, *125*, 244508.
(17) Cowan, M. L.; Bruner, B. D.; Huse, N.; Dwyer, J. R.; Chugh, B.; Nibbering, E. T. J.; Elsaesser, T.; Miller, R. J. D. *Nature* **2005**, *434*, 199.
(18) Asbury, J. B.; Steinel, T.; Stromberg, C.; Corcelli, S. A.; Lawrence, C. P.; Skinner, J. L.; Fayer, M. D. *J. Phys. Chem. A* **2004**, *108*, 1107.
(19) Fecko, C. J.; Loparo, J. J.; Roberts, S. T.; Tokmakoff, A. *J. Chem. Phys.* **2005**, *122*, 054506.
(20) Tian, P.; Keusters, D.; Suzaki, Y.; Warren, W. S. *Science* **2003**, *300*, 1553.
(21) DeCamp, M. F.; Tokmakoff, A. *Opt. Lett.* **2006**, *31*, 113.
(22) DeCamp, M. F.; DeFlores, L. P.; Jones, K. C.; Tokmakoff, A. *Opt. Express* **2007**, *15*, 233.
(23) Tanimura, Y.; Mukamel, S. *J. Chem. Phys.* **1993**, *99*, 9496.
(24) Hamm, P.; Lim, M.; Hochstrasser, R. M. *J. Phys. Chem. B* **1998**, *102*, 6123.
(25) Cho, M. In *Advances in Multi-Photon Processes and Spectroscopy*; Lin, S. H., Villaeys, A. A., Fujimura, Y., Ed.; World Scientific Pulblishing Co.: Singapore, 1999.
(26) Zanni, M. T.; Hochstrasser, R. M. *Curr. Opin. Struct. Biol.* **2001**, *11*, 516.
(27) Mukamel, S. *Annu. Rev. Phys. Chem.* **2000**, *51*, 691.
(28) Cho, M. *PhysChemComm* **2002**, *5*, 40.
(29) Jonas, D. M. *Annu. Rev. Phys. Chem.* **2003**, *54*, 425.
(30) Khalil, M.; Demirdoven, N.; Tokmakoff, A. *J. Phys. Chem. A* **2003**, *107*, 5258.
(31) Wright, J. C. *Int. Rev. Phys. Chem.* **2002**, *21*, 185.
(32) Woutersen, S.; Hamm, P. *J. Phys.: Condens. Matter* **2002**, *14*, R1035.
(33) Tanimura, Y. *J. Phys. Soc. Jpn.* **2006**, *75*, 082001.
(34) Cho, M. *Bull. Kor. Chem. Soc* **2006**, *27*, 1940.
(35) Finkelstein, I. J.; Zheng, J. R.; Ishikawa, H.; Kim, S.; Kwak, K.; Fayer, M. D. *Phys. Chem. Chem. Phys.* **2007**, *9*, 1533.
(36) Zheng, J.; Kwak, K.; Fayer, M. D. *Acc. Chem. Res.* **2007**, *40*, 75.
(37) Mukamel, S. *Principles of Nonlinear Optical Spectroscopy*; Oxford University Press: Oxford, 1995.
(38) Fleming, G. R. *Chemical Applications of Ultrafast Spectroscopy*; Oxford: London, 1986.
(39) Shen, Y. R. *The Principles of Nonlinear Optics*; John Wiley & Sons: New York, 1984.
(40) Levenson, M. D.; Kano, S. S. *Introduction to Nonlinear Laser Spectroscopy*; Academic Press, Inc.: San Diego, CA, 1988.
(41) Cho, M. *J. Chem. Phys.* **2002**, *116*, 1562.
(42) Cho, M. *J. Chem. Phys.* **2003**, *119*, 7003.
(43) Cheon, S.; Cho, M. *Phys. Rev. A* **2005**, *71*, 013808.
(44) Choi, J. H.; Cho, M. *J. Phys. Chem. A* **2007**, *111*, 5176.
(45) Choi, J.-H.; Cho, M. *J. Chem. Phys.* **2007**, *127*, 024507.
(46) Fayer, M. D. *Annu. Rev. Phys. Chem.* **1982**, *33*, 63.
(47) Vohringer, P.; Arnett, D. C.; Yang, T. S.; Scherer, N. F. *Chem. Phys. Lett.* **1995**, *237*, 387.
(48) deBoeij, W. P.; Pshenichnikov, M. S.; Wiersma, D. A. *J. Chem. Phys.* **1996**, *105*, 2953.
(49) deBoeij, W. P.; Pshenichnikov, M. S.; Wiersma, D. A. *J. Phys. Chem.* **1996**, *100*, 11806.
(50) Lepetit, L.; Joffre, M. *Opt. Lett.* **1996**, *21*, 564.
(51) Likforman, J. P.; Joffre, M.; Thierry-Mieg, V. *Opt. Lett.* **1997**, *22*, 1104.
(52) Lepetit, L.; Cheriaux, G.; Joffre, M. *J. Opt. Soc. Am. B: Opt. Phys.* **1995**, *12*, 2467.
(53) Segonds, P.; Canioni, L.; LeBoiteux, S.; Joffre, M.; Bousquet, B.; Li, W.; Sarger, L. *J. Lumin.* **1997**, *72*−*4*, 849.
(54) Likforman, J. P.; Joffre, M.; ThierryMieg, V. *Opt. Lett.* **1997**, *22*, 1104.
(55) Asplund, M. C.; Zanni, M. T.; Hochstrasser, R. M. *Proc. Natl. Acad. Sci. U.S.A.* **2000**, *97*, 8219.
(56) Gallagher, S. M.; Albrecht, A. W.; Hybl, T. D.; Landin, B. L.; Rajaram, B.; Jonas, D. M. *J. Opt. Soc. Am. B* **1998**, *15*, 2338.
(57) Hybl, J. D.; Albrecht, A. W.; Gallagher Faeder, S. M.; Jonas, D. M. *Chem. Phys. Lett.* **1998**, *297*, 307.
(58) Brixner, T.; Mancal, T.; Stiopkin, I. V.; Fleming, G. R. *J. Chem. Phys.* **2004**, *121*, 4221.
(59) Brixner, T.; Stiopkin, I. V.; Fleming, G. R. *Opt. Lett.* **2004**, *29*, 884.
(60) Tekavec, P. F.; Dyke, T. R.; Marcus, A. H. *J. Chem. Phys.* **2006**, *125*, 194303.
(61) de Boeij, W. P.; Pshenichnikov, M. S.; Wiersma, D. A. *Annu. Rev. Phys. Chem.* **1998**, *49*, 99.
(62) Cho, M.; Yu, J. Y.; Joo, T. H.; Nagasawa, Y.; Passino, S. A.; Fleming, G. R. *J. Chem. Phys.* **1996**, *100*, 11944.
(63) de Boeij, W.; Pshenichnikov, M. S.; Wiersma, D. A. *Chem. Phys. Lett.* **1996**, *253*, 53.
(64) Keusters, D.; Tan, H. S.; Warren, W. S. *J. Phys. Chem. A* **1999**, *103*, 10369.
(65) Davydov, A. S. *Theory of Molecular Excitons*; Plenum: New York, 1971.
(66) Mukamel, S.; Abramavicius, D. *Chem. Rev.* **2004**, *104*, 2073.
(67) Torii, H.; Tasumi, M. *J. Chem. Phys.* **1992**, *96*, 3379.
(68) Cho, M.; Fleming, G. R. *J. Chem. Phys.* **2005**, *123*, 114506.
(69) Stiopkin, I.; Brixner, T.; Yang, M.; Fleming, G. R. *J. Phys. Chem. B* **2006**, *110*, 20032.
(70) Fleming, A. J.; Coleman, J. N.; Dalton, A. B.; Fechtenkotter, A.; Watson, M. D.; Mullen, K.; Byrne, H. J.; Blau, W. J. *J. Phys. Chem. B* **2003**, *107*, 37.
(71) Zhang, W. M.; Meier, T.; Chernyak, V.; Mukamel, S. *Philos. Trans. R. Soc. London, Ser. A: Math. Phys. Eng. Sci.* **1998**, *356*, 405.
(72) Zhang, W. M.; Meier, T.; Chernyak, V.; Mukamel, S. *J. Chem. Phys.* **1998**, *108*, 7763.
(73) Kobayashi, T. *J-aggregates*; World Scientific: Singapore, 1996.
(74) Sung, J. Y.; Silbey, R. J.; Cho, M. *J. Chem. Phys.* **2001**, *115*, 1422.
(75) Sung, J. Y.; Cho, M. *J. Chem. Phys.* **2000**, *113*, 7072.
(76) Cho, M. *J. Chem. Phys.* **2001**, *115*, 4424.
(77) Sung, J. Y.; Silbey, R. J. *J. Chem. Phys.* **2003**, *118*, 2443.
(78) Sung, J. Y.; Silbey, R. J. *J. Chem. Phys.* **2001**, *115*, 9266.
(79) Kwac, K.; Cho, M. *J. Raman Spectrosc.* **2005**, *36*, 326.
(80) Zheng, J. R.; Kwak, K.; Asbury, J.; Chen, X.; Piletic, I. R.; Fayer, M. D. *Science* **2005**, *309*, 1338.
(81) Zheng, J.; Kwak, K.; Xie, J.; Fayer, M. D. *Science* **2006**, *313*, 1951.
(82) Kwak, K.; Zheng, J. R.; Cang, H.; Fayer, M. D. *J. Phys. Chem. B* **2006**, *110*, 19998.
(83) Maroncelli, M.; Fleming, G. R. *J. Chem. Phys.* **1988**, *89*, 5044.
(84) Jimenez, R.; Fleming, G. R.; Kumar, P. V.; Maroncelli, M. *Nature* **1994**, *369*, 471.
(85) Horng, L.; Kumar, V. P.; Maroncelli, M. *Abstr. Pap. Am. Chem. Soc.* **1994**, *207*, 1.
(86) Kumar, P. V.; Maroncelli, M. *J. Chem. Phys.* **1995**, *103*, 3038.
(87) Fleming, G. R.; Joo, T.; Cho, M. *Adv. Chem. Phys.* **1997**, *101*, 141.
(88) Cho, M.; Fleming, G. R. *Adv. Chem. Phys.* **1999**, *107*, 311.
(89) Yang, S.; Cho, M. *J. Chem. Phys.* **2005**, *123*.
(90) Kinnaman, C. S.; Cremeens, M. E.; Romesberg, F. E.; Corcelli, S. A. *J. Am. Chem. Soc.* **2006**, *128*, 13334.
(91) Li, S. Z.; Schmidt, J. R.; Corcelli, S. A.; Lawrence, C. P.; Skinner, J. L. *J. Chem. Phys.* **2006**, *124*, 204110.
(92) Krimm, S.; Bandekar, J. *Adv. Protein Chem.* **1986**, *38*, 181.
(93) Torii, H.; Tasumi, M. *J. Chem. Phys.* **1992**, *97*, 92.

(94) Miyazawa, T. *J. Chem. Phys.* **1960**, *32*, 1647.
(95) Fleming, G. R.; Scholes, G. D. *Nature* **2004**, *431*, 256.
(96) Krueger, B. P.; Scholes, G. D.; Fleming, G. R. *J. Phys. Chem. B* **1998**, *102*, 5378.
(97) Jordanides, X. J.; Scholes, G. D.; Shapley, W. A.; Reimers, J. R.; Fleming, G. R. *J. Phys. Chem. B* **2004**, *108*, 1753.
(98) Hamm, P.; Lim, M.; DeGrado, W. F.; Hochstrasser, R. M. *Proc. Natl. Acad. Sci. U.S.A.* **1999**, *96*, 2036.
(99) Dybal, J.; Cheam, T. C.; Krimm, S. *J. Mol. Struct.* **1987**, *159*, 183.
(100) Torii, H.; Tasumi, M. *J. Mol. Struct.* **1993**, *300*, 171.
(101) Woutersen, S.; Hamm, P. *J. Chem. Phys.* **2001**, *115*, 7737.
(102) Hamm, P.; Woutersen, S. *Bull. Chem. Soc. Jpn.* **2002**, *75*, 985.
(103) Tominaga, K.; Yoshihara, K. *Phys. Rev. Lett.* **1995**, *74*, 3061.
(104) Tominaga, K.; Keogh, G. P.; Naitoh, Y.; Yoshihara, K. *J. Raman Spectrosc.* **1995**, *26*, 495.
(105) Tominaga, K.; Keogh, G. P.; Yoshihara, K. *J. Mol. Liq.* **1995**, *65*−*6*, 389.
(106) Tominaga, K.; Yoshihara, K. *J. Chem. Phys.* **1996**, *104*, 1159.
(107) Tominaga, K.; Yoshihara, K. *J. Chem. Phys.* **1996**, *104*, 4419.
(108) Tokmakoff, A.; Lang, M. J.; Larsen, D. S.; Fleming, G. R.; Chernyak, V.; Mukamel, S. *Phys. Rev. Lett.* **1997**, *79*, 2702.
(109) Tokmakoff, A.; Fleming, G. R. *J. Chem. Phys.* **1997**, *106*, 2569.
(110) Tokmakoff, A.; Lang, M. J.; Jordanides, X. J.; Fleming, G. R. *Chem. Phys.* **1998**, *233*, 231.
(111) Tokmakoff, A.; Lang, M. J.; Larsen, D. S.; Fleming, G. R. *Chem. Phys. Letters* **1997**, *272*, 48.
(112) Cho, M.; Blank, D. A.; Sung, J.; Park, K.; Hahn, S.; Fleming, G. R. *J. Chem. Phys.* **2000**, *112*, 2082.
(113) Blank, D. A.; Kaufman, L. J.; Fleming, G. R. *J. Chem. Phys.* **1999**, *111*, 3105.
(114) Blank, D. A.; Kaufman, L. J.; Fleming, G. R. *J. Chem. Phys.* **2000**, *113*, 771.
(115) Kaufman, L. J.; Blank, D. A.; Fleming, G. R. *J. Chem. Phys.* **2001**, *114*, 2312.
(116) Torii, H.; Tasumi, M. In *Infrared Spectroscopy of Biomolecules*; Mantsch, H. H., Chapman, D., Ed.; Wiley-Liss: New York, 1996.
(117) Cho, M.; Fleming, G. R. *J. Phys. Chem.* **1994**, *98*, 3478.
(118) Meyer, K. A.; Wright, J. C.; Thompson, D. E. *J. Phys. Chem. A* **2004**, *108*, 11485.
(119) Besemann, D. M.; Meyer, K. A.; Wright, J. C. *J. Phys. Chem. B* **2004**, *108*, 10493.
(120) Rickard, M. A.; Pakoulev, A. V.; Kornau, K.; Mathew, N. A.; Wright, J. C. *J. Phys. Chem. A* **2006**, *110*, 11384.
(121) Pakoulev, A. V.; Rickard, M. A.; Meyer, K. A.; Kornau, K.; Mathew, N. A.; Thompson, D. E.; Wright, J. C. *J. Phys. Chem. A* **2006**, *110*, 3352.
(122) Rickard, M. A.; Pakoulev, A. V.; Mathew, N. A.; Kornau, K. M.; Wright, J. C. *J. Phys. Chem. A* **2007**, *111*, 1163.
(123) Fulmer, E. C.; Ding, F.; Zanni, M. T. *J. Chem. Phys.* **2005**, *122*, 034302.
(124) Ding, F.; Fulmer, E. C.; Zanni, M. T. *J. Chem. Phys.* **2005**, *123*, 094502.
(125) Ruhman, S.; Kohler, B.; Joly, A. G.; Nelson, K. A. *IEEE J. Quantum Electron.* **1988**, *24*, 470.
(126) Ruhman, S.; Williams, L. R.; Joly, A. G.; Kohler, B.; Nelson, K. A. *J. Phys. Chem.* **1987**, *91*, 2237.
(127) Ruhman, S.; Joly, A. G.; Nelson, K. A. *J. Chem. Phys.* **1987**, *86*, 6563.
(128) Ruhman, S.; Kohler, B.; Joly, A. G.; Nelson, K. A. *Chem. Phys. Lett.* **1987**, *141*, 16.
(129) Ruhman, S.; Joly, A. G.; Nelson, K. A. *IEEE J. Quantum Electron.* **1988**, *24*, 460.
(130) Maznev, A. A.; Nelson, K. A.; Rogers, T. A. *Opt. Lett.* **1998**, *23*, 1319.
(131) Dhar, L.; Rogers, J. A.; Nelson, K. A. *Chem. Rev.* **1994**, *94*, 157.
(132) Kalpouzos, C.; Lotshaw, W. T.; McMorrow, D.; Kenney-Wallace, G. A. *J. Phys. Chem.* **1987**, *91*, 2028.
(133) Lotshaw, W. T.; McMorrow, D.; Kalpouzos, C.; Kenney-Wallace, G. A. *Chem. Phys. Lett.* **1987**, *136*, 323.
(134) McMorrow, D.; Lotshaw, W. T.; Kenney-Wallace, G. A. *IEEE J. Quantum Electron.* **1988**, *24*, 443.
(135) McMorrow, D.; Lotshaw, W. T.; Kenney-Wallace, G. A. *Chem. Phys. Lett.* **1988**, *145*, 309.
(136) Kalpouzos, C.; McMorrow, D.; Lotshaw, W. T.; Kenney-Wallace, G. A. *Chem. Phys. Lett.* **1988**, *150*, 138.
(137) Lotshaw, W. T.; McMorrow, D. *J. Chem. Phys.* **1990**, *93*, 2160.
(138) McMorrow, D.; Lotshaw, W. T. *J. Phys. Chem.* **1991**, *95*, 10395.
(139) Back, R.; Kenney-Wallace, G. A.; Lotshaw, W. T.; McMorrow, D. *Chem. Phys. Lett.* **1992**, *191*, 423.
(140) Lotshaw, W. T.; McMorrow, D.; Thantu, N.; Melinger, J. S.; Kitchenham, R. *J. Raman Spectrosc.* **1995**, *26*, 571.
(141) McMorrow, D.; Thantu, N.; Melinger, J. S.; Kim, S. K.; Lotshaw, W. T. *J. Phys. Chem.* **1996**, *100*, 10389.
(142) Righini, R. *Science* **1993**, *262*, 1386.
(143) Kinoshita, S.; Kai, Y.; Ariyoshi, T.; Shimada, Y. *Int. J. Mod. Phys. B* **1996**, *10*, 1229.
(144) Farrer, R. A.; Fourkas, J. T. *Acc. Chem. Res.* **2003**, *36*, 605.
(145) Loughnane, B. J.; Farrer, R. A.; Scodinu, A.; Fourkas, J. T. *J. Chem. Phys.* **1999**, *111*, 5116.
(146) Loughnane, B. J.; Fourkas, J. T. *J. Phys. Chem. B* **1998**, *102*, 10288.
(147) Loughnane, B. J.; Scodinu, A.; Farrer, R. A.; Fourkas, J. T.; Mohanty, U. *J. Chem. Phys.* **1999**, *111*, 2686.
(148) Loughnane, B. J.; Scodinu, A.; Fourkas, J. T. *Chem. Phys.* **2000**, *253*, 323.
(149) Loughnane, B. J.; Scodinu, A.; Fourkas, J. T. *J. Phys. Chem. B* **2006**, *110*, 5708.
(150) Scodinu, A.; Fourkas, J. T. *J. Phys. Chem. B* **2003**, *107*, 44.
(151) Zhu, X.; Farrer, R. A.; Fourkas, J. T. *J. Phys. Chem. B* **2005**, *109*, 8481.
(152) Zhu, X.; Farrer, R. A.; Gershgoren, E.; Kapteyn, H. C.; Fourkas, J. T. *J. Phys. Chem. B* **2004**, *108*, 3384.
(153) Castner, E. W.; Chang, Y. J.; Chu, Y. C.; Walrafen, G. E. *J. Chem. Phys.* **1995**, *102*, 653.
(154) Castner, E. W.; Chang, Y. J.; Melinger, J. S.; McMorrow, D. *J. Lumin.* **1994**, *60*−*1*, 723.
(155) Chang, Y. J.; Castner, E. W. *J. Chem. Phys.* **1993**, *99*, 7289.
(156) Chang, Y. J.; Castner, E. W. *J. Chem. Phys.* **1993**, *99*, 113.
(157) Chang, Y. J.; Castner, E. W. *J. Phys. Chem.* **1994**, *98*, 9712.
(158) Chang, Y. J.; Castner, E. W. *J. Phys. Chem.* **1996**, *100*, 3330.
(159) Cho, M.; Du, M.; Scherer, N. F.; Fleming, G. R.; Mukamel, S. *J. Chem. Phys.* **1993**, *99*, 2410.
(160) Cho, M. H.; Okumura, K.; Tanimura, Y. *J. Chem. Phys.* **1998**, *108*, 1326.
(161) Okumura, K.; Tokmakoff, A.; Tanimura, Y. *J. Chem. Phys.* **1999**, *111*, 492.
(162) Okumura, K.; Tanimura, Y. *J. Chem. Phys.* **1997**, *107*, 2267.
(163) Tanimura, Y.; Okumura, K. *J. Chem. Phys.* **1997**, *106*, 2078.
(164) Okumura, K.; Tanimura, Y. *J. Chem. Phys.* **1997**, *106*, 1687.
(165) Okumura, K.; Tanimura, Y. *J. Chem. Phys.* **1996**, *105*, 7294.
(166) Fourkas, J. T. *Adv. Chem. Phys.* **2001**, *117*, 235.
(167) Milne, C. J.; Li, Y. L.; Jansen, T. L. C.; Huang, L.; Miller, R. J. D. *J. Phys. Chem. B* **2006**, *110*, 19867.
(168) Cho, M. *J. Chem. Phys.* **1998**, *109*, 6227.
(169) Hahn, S.; Park, K.; Cho, M. *J. Chem. Phys.* **1999**, *111*, 4121.
(170) Saito, S.; Ohmine, I. *J. Chem. Phys.* **1998**, *108*, 240.
(171) Mukamel, S.; Khidekel, V.; Chernyak, V. *Phys. Rev. E* **1996**, *53*, R1.
(172) Saito, S.; Ohmine, I. *Phys. Rev. Lett.* **2002**, *88*.
(173) Jansen, T. L. C.; Snijders, J. G.; Duppen, K. *J. Chem. Phys.* **2000**, *113*, 307.
(174) Jansen, T. L. C.; Snijders, J. G.; Duppen, K. *J. Chem. Phys.* **2001**, *114*, 10910.
(175) Denny, R. A.; Reichman, D. R. *Phys. Rev. E* **2001**, *6306*.
(176) Denny, R. A.; Reichman, D. R. *J. Chem. Phys.* **2002**, *116*, 1979.
(177) Denny, R. A.; Reichman, D. R. *J. Chem. Phys.* **2002**, *116*, 1987.
(178) Cao, J. S.; Yang, S. L.; Wu, J. L. *J. Chem. Phys.* **2002**, *116*, 3760.
(179) Hasegawa, T.; Tanimura, Y. *J. Chem. Phys.* **2006**, *125*.
(180) Ulness, D. J.; Kirkwood, J. C.; Albrecht, A. C. *J. Chem. Phys.* **1998**, *108*, 3897.
(181) Kirkwood, J. C.; Ulness, D. J.; Albrecht, A. C.; Stimson, M. J. *Chem. Phys. Lett.* **1998**, *293*, 417.
(182) Ivanecky, J. E.; Wright, J. C. *Chem. Phys. Lett.* **1993**, *206*, 437.
(183) Brewer, R. G.; Shoemaker, R. L. *Phys. Rev. Lett.* **1971**, *27*, 631.
(184) Hochstrasser, R. M. *Chem. Phys.* **2001**, *266*, 273.
(185) Zanni, M. T.; Ge, N. H.; Kim, Y. S.; Hochstrasser, R. M. *Proc. Natl. Acad. Sci. U.S.A.* **2001**, *98*, 11265.
(186) Zanni, M. T.; Gnanakaran, S.; Stenger, J.; Hochstrasser, R. M. *J. Phys. Chem. B* **2001**, *105*, 6520.
(187) Scheurer, C.; Piryatinski, A.; Mukamel, S. *J. Am. Chem. Soc.* **2001**, *123*, 3114.
(188) Mikenda, W. *J. Mol. Struct.* **1986**, *147*, 1.
(189) Cho, M. *J. Chem. Phys.* **2003**, *118*, 3480.
(190) Ham, S.; Kim, J. H.; Lee, H.; Cho, M. *J. Chem. Phys.* **2003**, *118*, 3491.
(191) Kwac, K.; Cho, M. *J. Chem. Phys.* **2003**, *119*, 2247.
(192) Kwac, K.; Cho, M. *J. Chem. Phys.* **2003**, *119*, 2256.
(193) Kim, J. H.; Cho, M. *Bull. Korean Chem. Soc.* **2003**, *24*, 1061.
(194) Schmidt, J. R.; Corcelli, S. A.; Skinner, J. L. *J. Chem. Phys.* **2004**, *121*, 8887.
(195) Jansen, T. L.; Knoester, J. *J. Chem. Phys.* **2006**, *124*, 044502.
(196) Hayashi, T.; Zhuang, W.; Mukamel, S. *J. Phys. Chem. A* **2005**, *109*, 9747.
(197) Zanni, M. T.; Asplund, M. C.; Hochstrasser, R. M. *J. Chem. Phys.* **2001**, *114*, 4579.
(198) Woutersen, S.; Pfister, R.; Hamm, P.; Mu, Y. G.; Kosov, D. S.; Stock, G. *J. Chem. Phys.* **2002**, *117*, 6833.

(199) DeCamp, M. F.; DeFlores, L.; McCracken, J. M.; Tokmakoff, A.; Kwac, K.; Cho, M. *J. Phys. Chem. B* **2005**, *109*, 11016.
(200) Kwac, K.; Cho, M. *J. Phys. Chem. A* **2003**, *107*, 5903.
(201) Bratos, S.; Gale, G. M.; Gallot, G.; Hache, F.; Lascoux, N.; Leicknam, J. C. *Phys. Rev. E* **2000**, *61*, 5211.
(202) Gallot, G.; Lascoux, N.; Gale, G. M.; Leicknam, J. C.; Bratos, S.; Pommeret, S. *Chem. Phys. Lett.* **2001**, *341*, 535.
(203) Laenen, R.; Rauscher, C.; Laubereau, A. *Phys. Rev. Lett.* **1998**, *80*, 2622.
(204) Laenen, R.; Rauscher, C.; Laubereau, A. *J. Phys. Chem. B* **1998**, *102*, 9304.
(205) Gaffney, K. J.; Davis, P. H.; Piletic, I. R.; Levinger, N. E.; Fayer, M. D. *J. Phys. Chem. A* **2002**, *106*, 12012.
(206) Gaffney, K.; Piletic, I.; Fayer, M. D. *J. Phys. Chem. A* **2002**, *106*, 9428.
(207) Kropman, M. F.; Nienhuys, H.-K.; Woutersen, S.; Bakker, H. J. *J. Phys. Chem. A* **2001**, *105*, 4622.
(208) Gaffney, K. J.; Piletic, I. R.; Fayer, M. D. *J. Chem. Phys.* **2003**, *118*, 2270.
(209) Laenen, R.; Rauscher, C.; Simeonidis, K. *J. Chem. Phys.* **1999**, *110*, 5814.
(210) Gale, G. M.; Gallot, G.; Lascoux, N. *Chem. Phys. Lett.* **1999**, *311*, 123.
(211) Tokmakoff, A.; Fayer, M. D. *J. Chem. Phys.* **1995**, *103*, 2810.
(212) Tokmakoff, A.; Fayer, M. D. *Acc. Chem. Res.* **1995**, *28*, 437.
(213) Tokmakoff, A.; Zimdars, D.; Urdahl, R. S.; Francis, R. S.; Kwok, A. S.; Fayer, M. D. *J. Phys. Chem.* **1995**, *99*, 13310.
(214) Asbury, J. B.; Steinel, T.; Kwak, K.; Corcelli, S.; Lawrence, C. P.; Skinner, J. L.; Fayer, M. D. *J. Chem. Phys.* **2004**, *121*, 12431.
(215) Asbury, J. B.; Steinel, T.; Stromberg, C.; Corcelli, S. A.; Lawrence, C. P.; Skinner, J. L.; Fayer, M. D. *J. Phys. Chem. A* **2004**, *108*, 1107.
(216) Corcelli, S.; Lawrence, C. P.; Asbury, J. B.; Steinel, T.; Fayer, M. D.; Skinner, J. L. *J. Chem. Phys.* **2004**, *121*, 8897.
(217) Steinel, T.; Asbury, J. B.; Corcelli, S. A.; Lawrence, C. P.; Skinner, J. L.; Fayer, M. D. *Chem. Phys. Lett.* **2004**, *386*, 295.
(218) Asbury, J. B.; Steinel, T.; Kwak, K.; Corcelli, S. A.; Lawrence, C. P.; Skinner, J. L.; Fayer, M. D. *J. Chem. Phys.* **2004**, *121*, 12431.
(219) Corcelli, S. A.; Lawrence, C. P.; Asbury, J. B.; Steinel, T.; Fayer, M. D.; Skinner, J. L. *J. Chem. Phys.* **2004**, *121*, 8897.
(220) Eaves, J. D.; Loparo, J. J.; Fecko, C. J.; Roberts, S. T.; Tokmakoff, A.; Geissler, P. L. *Proc. Natl. Acad. Sci. U.S.A.* **2005**, *102*, 13019.
(221) Eaves, J. D.; Tokmakoff, A.; Geissler, P. L. *J. Phys. Chem. A* **2005**, *109*, 9424.
(222) Fecko, C. J.; Eaves, J. D.; Loparo, J. J.; Tokmakoff, A.; Geissler, P. L. *Science* **2003**, *301*, 1698.
(223) Hayashi, T.; Jansen, T. L.; Zhuang, W.; Mukamel, S. *J. Phys. Chem. A* **2005**, *109*, 64.
(224) Jansen, T. L.; Hayashi, T.; Zhuang, W.; Mukamel, S. *J. Chem. Phys.* **2005**, *123*, 114504.
(225) Loparo, J. J.; Roberts, S. T.; Tokmakoff, A. *J. Chem. Phys.* **2006**, *125*, 194521.
(226) Loparo, J. J.; Roberts, S. T.; Tokmakoff, A. *J. Chem. Phys.* **2006**, *125*, 194522.
(227) Ham, S.; Cho, M. *J. Chem. Phys.* **2003**, *118*, 6915.
(228) Torii, H.; Tasumi, M. *J. Raman Spectrosc.* **1998**, *29*, 81.
(229) Choi, J. H.; Cho, M. *J. Chem. Phys.* **2004**, *120*, 4383.
(230) Choi, J.-H.; Ham, S.; Cho, M. *J. Phys. Chem. B* **2003**, *107*, 9132.
(231) Ham, S.; Cha, S.; Choi, J.-H.; Cho, M. *J. Chem. Phys.* **2003**, *119*, 1451.
(232) Hamm, P.; Lim, M.; Hochstrasser, R. M. *J. Phys. Chem. B* **1998**, *102*, 6123.
(233) Hamm, P.; Lim, M.; DeGrado, W. F.; Hochstrasser, R. M. *J. Chem. Phys.* **2000**, *112*, 1907.
(234) Cha, S.; Ham, S.; Cho, M. *J. Chem. Phys.* **2002**, *117*, 740.
(235) Ham, S.; Cho, M. *J. Chem. Phys.* **2003**, *118*, 6915.
(236) Choi, J.-H.; Ham, S.; Cho, M. *J. Phys. Chem. B* **2003**, *107*, 9132.
(237) Cha, S. Y.; Ham, S. H.; Cho, M. *J. Chem. Phys.* **2002**, *117*, 740.
(238) Hahn, S.; Ham, S.; Cho, M. *J. Phys. Chem. B* **2005**, *109*, 11789.
(239) Ham, S.; Hahn, S.; Lee, C.; Kim, T. K.; Kwak, K.; Cho, M. *J. Phys. Chem. B* **2004**, *108*, 9333.
(240) Ge, N. H.; Hochstrasser, R. M. *PhysChemComm* **2002**, 17.
(241) Rubtsov, I. V.; Hochstrasser, R. M. *J. Phys. Chem. B* **2002**, *106*, 9165.
(242) Hahn, S.; Lee, H.; Cho, M. *J. Chem. Phys.* **2004**, *121*, 1849.
(243) Lee, K.-K.; Hahn, S.; Oh, K.-I.; Choi, J. S.; Joo, C.; Lee, H.; Han, H. Y.; Cho, M. *J. Phys. Chem. B* **2006**, *110*, 18834.
(244) Oh, K. I.; Han, J.; Lee, K. K.; Hahn, S.; Han, H.; Cho, M. *J. Phys. Chem. A* **2006**, *110*, 13355.
(245) Woutersen, S.; Hamm, P. *J. Phys. Chem. B* **2000**, *104*, 11316.
(246) Woutersen, S.; Hamm, P. *J. Chem. Phys.* **2001**, *114*, 2727.
(247) Mu, Y.; Stock, G. *J. Phys. Chem. B* **2002**, *106*, 5294.
(248) Mu, Y. G.; Kosov, D. S.; Stock, G. *J. Phys. Chem. B* **2003**, *107*, 5064.
(249) Gorbunov, R. D.; Nguyen, P. H.; Kobus, M.; Stock, G. *J. Chem. Phys.* **2007**, *126*.
(250) Kim, Y. S.; Hochstrasser, R. M. *J. Phys. Chem. B* **2005**, *109*, 6884.
(251) Kim, Y. S.; Wang, J. P.; Hochstrasser, R. M. *J. Phys. Chem. B* **2005**, *109*, 7511.
(252) Han, W. G.; Jalkanen, K. J.; Elstner, M.; Suhai, S. *J. Phys. Chem. B* **1998**, *102*, 2587.
(253) Drozdov, A. N.; Grossfield, A.; Pappu, R. V. *J. Am. Chem. Soc.* **2004**, *126*, 2574.
(254) Poon, C. D.; Samulski, E. T.; Weise, C. F.; Weisshaar, J. C. *J. Am. Chem. Soc.* **2000**, *122*, 5642.
(255) Graf, J.; Nguyen, P. H.; Stock, G.; Schwalbe, H. *J. Am. Chem. Soc.* **2007**, *129*, 1179.
(256) Jansen, T. L.; Knoester, J. *J. Phys. Chem. B* **2006**, *110*, 22910.
(257) Dreyer, J.; Moran, A. M.; Mukamel, S. *J. Phys. Chem. B* **2003**, *107*, 5967.
(258) Dreyer, J.; Moran, A. M.; Mukamel, S. *Bull. Korean Chem. Soc.* **2003**, *24*, 1091.
(259) Khalil, M.; Demirdoven, N.; Tokmakoff, A. *Phys. Rev. Lett.* **2003**, *90*, 047401(4).
(260) Demirdoven, N.; Khalil, M.; Golonzka, O.; Tokmakoff, A. *J. Phys. Chem. A* **2001**, *105*, 8030.
(261) Golonzka, O.; Khalil, M.; Demirdoven, N.; Tokmakoff, A. *Phys. Rev. Lett.* **2001**, *86*, 2154.
(262) Demirdoven, N.; Khalil, M.; Tokmakoff, A. *Phys. Rev. Lett.* **2002**, *89*, 237401.
(263) Khalil, M.; Demirdoven, N.; Tokmakoff, A. *J. Chem. Phys.* **2004**, *121*, 362.
(264) Moran, A. M.; Dreyer, J.; Mukamel, S. *J. Chem. Phys.* **2003**, *118*, 1347.
(265) Huse, N.; Bruner, B. D.; Cowan, M. L.; Dreyer, J.; Nibbering, E. T. J.; Miller, R. J. D.; Elsaesser, T. *Phys. Rev. Lett.* **2005**, *95*, 147402.
(266) Huse, N.; Heyne, K.; Dreyer, J.; Nibbering, E. T. J.; Elsaesser, T. *Phys. Rev. Lett.* **2003**, *91*, 197401.
(267) Heyne, K.; Huse, N.; Nibbering, E. T. J.; Elsaesser, T. *Chem. Phys. Lett.* **2003**, *369*, 591.
(268) Heyne, K.; Huse, N.; Nibbering, E. T. J.; Elsaesser, T. *J. Phys.: Condens. Matter* **2003**, *15*, S129.
(269) Heyne, K.; Huse, N.; Nibbering, E. T. J.; Elsaesser, T. *Chem. Phys. Lett.* **2003**, *382*, 19.
(270) Heyne, K.; Huse, N.; Dreyer, J.; Nibbering, E. T. J.; Elsaesser, T.; Mukamel, S. *J. Chem. Phys.* **2004**, *121*, 902.
(271) Fujii, Y.; Yamada, H.; Mizuta, M. *J. Phys. Chem.* **1988**, *92*, 6768.
(272) Rubtsov, I. V.; Wang, J. P.; Hochstrasser, R. M. *Proc. Natl. Acad. Sci. U.S.A.* **2003**, *100*, 5601.
(273) Rubtsov, I. V.; Wang, J.; Hochstrasser, R. M. *J. Chem. Phys.* **2003**, *118*, 7733.
(274) Rubtsov, I. V.; Kumar, K.; Hochstrasser, R. M. *Chem. Phys. Lett.* **2005**, *402*, 439.
(275) Rubtsov, I. V.; Wang, J. P.; Hochstrasser, R. M. *J. Phys. Chem. A* **2003**, *107*, 3384.
(276) Naraharisetty, S. R. G.; Kurochkin, D. V.; Rubtsov, I. V. *Chem. Phys. Lett.* **2007**, *437*, 262.
(277) Kurochkin, D. V.; Naraharisetty, S. R. G.; Rubtsov, I. V. *J. Phys. Chem. A* **2005**, *109*, 10799.
(278) Kubelka, J.; Hofrichter, J.; Eaton, W. A. *Curr. Opin. Struct. Biol.* **2004**, *14*, 76.
(279) Searle, M. S.; Ciani, B. *Curr. Opin. Struct. Biol.* **2004**, *14*, 458.
(280) Choi, J. H.; Hahn, S.; Cho, M. *Int. J. Quantum Chem.* **2005**, *104*, 616.
(281) Barber-Armstrong, W.; Donaldson, T.; Wijesooriya, H.; Silva, R. A. G. D.; Decatur, S. M. *J. Am. Chem. Soc.* **2004**, *126*, 2339.
(282) Decatur, S. M. *Biopolymers* **2000**, *54*, 180.
(283) Decatur, S. M. *Acc. Chem. Res.* **2006**, *39*, 169.
(284) Silva, R. A. G. D.; Barber-Armstrong, W.; Decatur, S. M. *J. Am. Chem. Soc.* **2003**, *125*, 13674.
(285) Keiderling, T. A.; Huang, R.; Kubelka, J.; Hilario, J.; Barber-Armstrong, W.; Silva, R. A. G. D.; Decatur, S. M.; Bour, P. *Biophys. J.* **2003**, *84*, 482A.
(286) Huang, R.; Krejtschi, C.; Hauser, K.; Kim, J.; Keiderling, T. A. *Biophys. J.* **2007**, 208A.
(287) Mukherjee, P.; Krummel, A. T.; Fulmer, E. C.; Kass, I.; Arkin, I. T.; Zanni, M. T. *J. Chem. Phys.* **2004**, *120*, 10215.
(288) Keiderling, T. A.; Kubelka, J.; Silva, R. A. G. D.; Bour, P.; Decatur, S. M. *Biophys. J.* **2001**, *80*, 407A.
(289) Bour, P.; Kubelka, J.; Keiderling, T. A. *Biopolymers* **2000**, *53*, 380.
(290) Schweitzer-Stenner, R. *Vib. Spectrosc.* **2006**, *42*, 98.
(291) Fang, C.; Hochstrasser, R. M. *J. Phys. Chem. B* **2005**, *109*, 18652.
(292) Fang, C.; Wang, J.; Kim, Y. S.; Charnley, A. K.; Barber-Armstrong, W.; Smith, A. B., III; Decatur, S. M.; Hochstrasser, R. M. *J. Phys. Chem. B* **2004**, *108*, 10415.
(293) Gnanakaran, S.; Hochstrasser, R. M.; Garcia, A. E. *Proc. Natl. Acad. Sci. U.S.A.* **2004**, *101*, 9229.

(294) Yang, S.; Cho, M. *J. Phys. Chem. B* **2007**, *111*, 605.
(295) Lee, C.; Cho, M. *J. Phys. Chem. B* **2004**, *108*, 20397.
(296) Cheatum, C. M.; Tokmakoff, A.; Knoester, J. *J. Chem. Phys.* **2004**, *120*, 8201.
(297) Demirdoven, N.; Cheatum, C. M.; Chung, H. S.; Khalil, M.; Knoester, J.; Tokmakoff, A. *J. Am. Chem. Soc.* **2004**, *126*, 7981.
(298) Susi, H.; Timashef, S. N.; Stevens, L. *J. Biol. Chem.* **1967**, *242*, 5460.
(299) Chirgadz, Y. N.; Shestopa, B. V.; Venyamin, S. Y. *Biopolymers* **1973**, *12*, 1337.
(300) Jackson, M.; Haris, P. I.; Chapman, D. *Biochim. Biophys. Acta* **1989**, *998*, 75.
(301) Paul, C.; Wang, J.; Wimley, W. C.; Hochstrasser, R. M.; Axelsen, P. H. *J. Am. Chem. Soc.* **2004**, *126*, 5843.
(302) Hahn, S.; Kim, S.-S.; Lee, C.; Cho, M. *J. Chem. Phys.* **2005**, *123*, 084905.
(303) Kubelka, J.; Keiderling, T. A. *J. Am. Chem. Soc.* **2001**, *123*, 12048.
(304) Kubelka, J.; Keiderling, T. A. *J. Am. Chem. Soc.* **2001**, *123*, 6142.
(305) Mikhonin, A. V.; Myshakina, N. S.; Bykov, S. V.; Asher, S. A. *J. Am. Chem. Soc.* **2005**, *127*, 7712.
(306) Kuznetsov, S. V.; Hilario, J.; Keiderling, T. A.; Ansari, A. *Biochemistry* **2003**, *42*, 4321.
(307) Bour, P.; Keiderling, T. A. *J. Phys. Chem. B* **2005**, *109*, 5348.
(308) Bour, P.; Keiderling, T. A. *THEOCHEM* **2004**, *675*, 95.
(309) Hilario, J.; Keiderling, T. A. *Biophys. J.* **2002**, *82*, 298A.
(310) Silva, R. A. G. D.; Sherman, S. A.; Keiderling, T. A. *Biopolymers* **1999**, *50*, 413.
(311) Zhao, C.; Polavarapu, P. L.; Das, C.; Balaram, P. *J. Am. Chem. Soc.* **2000**, *122*, 8228.
(312) Kubelka, J.; Keiderling, T. A. *Biophys. J.* **2001**, *80*, 302A.
(313) Hilario, J.; Kubelka, J.; Syud, F. A.; Gellman, S. H.; Keiderling, T. A. *Biopolymers* **2002**, *67*, 233.
(314) Hilario, J.; Kubelka, J.; Keiderling, T. A. *J. Am. Chem. Soc.* **2003**, *125*, 7562.
(315) Smith, A. W.; Cheatum, C. M.; Chung, H. S.; Demirdoven, N.; Khalil, M.; Knoester, J.; Tokmakoff, A. *Biophys. J.* **2004**, *86*, 619A.
(316) Bour, P.; Keiderling, T. A. *J. Phys. Chem. B* **2005**, *109*, 23687.
(317) Huang, R.; Setnicka, V.; Thomas, C. L.; Etienne, M. A.; Hammer, R. P.; Keiderling, T. A. *Biophys. J.* **2005**, *88*, 159A.
(318) Setnicka, V.; Huang, R.; Thomas, C. L.; Etienne, M. A.; Kubelka, J.; Hammer, R. P.; Keiderling, T. A. *J. Am. Chem. Soc.* **2005**, *127*, 4992.
(319) Smith, A. W.; Chung, H. S.; Ganim, Z.; Tokmakoff, A. *J. Phys. Chem. B* **2005**, *109*, 17025.
(320) Streicher, W. W.; Makhatadze, G. I. *J. Am. Chem. Soc.* **2006**, *128*, 30.
(321) Wang, J.; Chen, J.; Hochstrasser, R. M. *J. Phys. Chem. B* **2006**, *110*, 7545.
(322) Kim, J.; Huang, R.; Kubelka, J.; Bour, P.; Keiderling, T. A. *J. Phys. Chem. B* **2006**, *110*, 23590.
(323) Wang, J. P.; Chen, J. X.; Hochstrasser, R. M. *J. Phys. Chem. B* **2006**, *110*, 7545.
(324) Huang, R.; Wu, L.; Keiderling, T. A. *Biophys. J.* **2007**, 377A.
(325) Xu, Y.; Wang, T.; Gai, F. *Chem. Phys.* **2006**, *323*, 21.
(326) Xu, Y.; Oyola, R.; Gai, F. *J. Am. Chem. Soc.* **2003**, *125*, 15388.
(327) Searle, M. S.; Platt, G. W.; Bofill, R.; Simpson, S. A.; Ciani, B. *Angew. Chem., Int. Ed.* **2004**, *43*, 1991.
(328) Ciani, B.; Jourdan, M.; Searle, M. S. *J. Am. Chem. Soc.* **2003**, *125*, 9038.
(329) Arrondo, J. L. R.; Blanco, F. J.; Serrano, L.; Goni, F. M. *FEBS Lett.* **1996**, *384*, 35.
(330) Wang, T.; Xu, Y.; Du, D. G.; Gai, F. *Biopolymers* **2004**, *75*, 163.
(331) Smith, A. W.; Tokmakoff, A. *J. Chem. Phys.* **2007**, *126*, 045109.
(332) Toniolo, C.; Benedetti, E. *Trends Biochem. Sci.* **1991**, *16*, 350.
(333) Bolin, K. A.; Millhauser, G. L. *Acc. Chem. Res.* **1999**, *32*, 1027.
(334) Millhauser, G. L.; Stenland, C. J.; Hanson, P.; Bolin, K. A.; vandeVen, F. J. M. *J. Mol. Biol.* **1997**, *267*, 963.
(335) De Guzman, R. N.; Wu, Z. R.; Stalling, C. C.; Pappalardo, L.; Borer, P. N.; Summers, M. F. *Science* **1998**, *279*, 384.
(336) Hashimoto, Y.; Kohri, K.; Kaneko, Y.; Morisaki, H.; Kato, T.; Ikeda, K.; Nakanishi, M. *J. Biol. Chem.* **1998**, *273*, 16544.
(337) Enkhbayar, P.; Hikichi, K.; Osaki, M.; Kretsinger, R. H.; Matsushima, N. *Proteins: Struct., Funct., Bioinf.* **2006**, *64*, 691.
(338) Shea, J. E.; Brooks, C. L. *Annu. Rev. Phys. Chem.* **2001**, *52*, 499.
(339) Nagaraj, R.; Balaram, P. *Acc. Chem. Res.* **1981**, *14*, 356.
(340) Toniolo, C.; Polese, A.; Formaggio, F.; Crisma, M.; Kamphuis, J. *J. Am. Chem. Soc.* **1996**, *118*, 2744.
(341) Yoder, G.; Polese, A.; Silva, R. A. G. D.; Formaggio, F.; Crisma, M.; Broxterman, Q. B.; Kamphuis, J.; Toniolo, C.; Keiderling, T. A. *J. Am. Chem. Soc.* **1997**, *119*, 10278.
(342) Mammi, S.; Rainaldi, M.; Bellanda, M.; Schievano, E.; Peggion, E.; Broxterman, Q. B.; Formaggio, F.; Crisma, M.; Toniolo, C. *J. Am. Chem. Soc.* **2000**, *122*, 11735.
(343) Pengo, P.; Pasquato, L.; Moro, S.; Brigo, A.; Fogolari, F.; Broxterman, Q. B.; Kaptein, B.; Scrimin, P. *Angew. Chem., Int. Ed.* **2003**, *42*, 3388.
(344) Maekawa, H.; Toniolo, C.; Moretto, A.; Broxterman, Q. B.; Ge, N.-H. *J. Phys. Chem. B* **2006**, *110*, 5834.
(345) Maekawa, H.; Toniolo, C.; Broxterman, Q. B.; Ge, N. H. *J. Phys. Chem. B* **2007**, *111*, 3222.
(346) Torres, J.; Briggs, J. A. G.; Arkin, I. T. *J. Mol. Biol.* **2002**, *316*, 365.
(347) Torres, J.; Briggs, J. A. G.; Arkin, I. T. *J. Mol. Biol.* **2002**, *316*, 375.
(348) Jacobs, H. *Immunol. Today* **1997**, *18*, 565.
(349) Manolios, N. *Immunol. Cell Biol.* **1995**, *73*, 544.
(350) Mukherjee, P.; Kass, I.; Arkin, I. T.; Zanni, M. T. *J. Phys. Chem. B* **2006**, *110*, 24740.
(351) Mukherjee, P.; Kass, I.; Arkin, I. T.; Zanni, M. T. *Proc. Natl. Acad. Sci. U.S.A.* **2006**, *103*, 3528.
(352) Fang, C.; Senes, A.; Cristian, L.; DeGrado, W. F.; Hochstrasser, R. M. *Proc. Natl. Acad. Sci. U.S.A.* **2006**, *103*, 16740.
(353) MacKenzie, K. R.; Prestegard, J. H.; Engelman, D. M. *Science* **1997**, *276*, 131.
(354) Volkov, V. V.; Chelli, R.; Righini, R. *J. Phys. Chem. B* **2006**, *110*, 1499.
(355) Simons, K.; Toomre, D. *Nat. Rev. Mol. Cell Biol.* **2000**, *1*, 31.
(356) Pilet, J.; Brahms, J. *Biopolymers* **1973**, *12*, 387.
(357) Liquier, J.; Akhebat, A.; Taillandier, E.; Ceolin, F.; Dinh, T. H.; Igolen, J. *Spectrochim. Acta, Part A: Mol. Biomol. Spectrosc.* **1991**, *47*, 177.
(358) Urpi, L.; Ridoux, J. P.; Liquier, J.; Verdaguer, N.; Fita, I.; Subirana, J. A.; Iglesias, F.; Huynhdinh, T.; Igolen, J.; Taillandier, E. *Nucleic Acids Res.* **1989**, *17*, 6669.
(359) Lindqvist, M.; Graslund, A. *J. Mol. Biol.* **2001**, *314*, 423.
(360) Zhong, W. X.; Gulotta, M.; Goss, D. J.; Diem, M. *Biochemistry* **1990**, *29*, 7485.
(361) Semenov, M.; Bolbukh, T.; Maleev, V. *J. Mol. Struct.* **1997**, *408*, 213.
(362) Hirakawa, A. Y.; Okada, H.; Sasagawa, S.; Tsuboi, M. *Spectrochim. Acta, Part A: Mol. Biomol. Spectrosc.* **1985**, *41*, 209.
(363) Szczesniak, M.; Leszczynski, J.; Person, W. B. *J. Am. Chem. Soc.* **1992**, *114*, 2731.
(364) Nowak, M. J.; Lapinski, L.; Fulara, J. *Spectrochim. Acta, Part A: Mol. Biomol. Spectrosc.* **1989**, *45*, 229.
(365) Sheina, G. G.; Stepanian, S. G.; Radchenko, E. D.; Blagoi, Y. P. *J. Mol. Struct.* **1987**, *158*, 275.
(366) Pilet, J.; Leng, M. *Proc. Natl. Acad. Sci. U.S.A.—Biol. Sci.* **1982**, *79*, 26.
(367) Taboury, J. A.; Taillandier, E. *Nucleic Acids Res.* **1985**, *13*, 4469.
(368) Szczesniak, M.; Szczepaniak, K.; Kwiatkowski, J. S.; Kubulat, K.; Person, W. B. *J. Am. Chem. Soc.* **1988**, *110*, 8319.
(369) Dhaouadi, Z.; Ghomi, M.; Austin, J. C.; Girling, R. B.; Hester, R. E.; Mojzes, P.; Chinsky, L.; Turpin, P. Y.; Coulombeau, C.; Jobic, H.; Tomkinson, J. *J. Phys. Chem.* **1993**, *97*, 1074.
(370) Banyay, M.; Sarkar, M.; Graslund, A. *Biophys. Chem.* **2003**, *104*, 477.
(371) Kyogoku, Y.; Lord, R. C.; Rich, A. *Proc. Natl. Acad. Sci. U.S.A.* **1967**, *57*, 250.
(372) Kyogoku, Y.; Lord, R. C.; Rich, A. *J. Am. Chem. Soc.* **1967**, *89*, 496.
(373) Toyama, A.; Takeuchi, H.; Harada, I. *J. Mol. Struct.* **1991**, *242*, 87.
(374) Maevsky, A. A.; Sukhorukov, B. I. *Nucleic Acids Res.* **1980**, *8*, 3029.
(375) Audet, P.; Simard, C.; Savoie, R. *Biopolymers* **1991**, *31*, 243.
(376) Loprete, D. M.; Hartman, K. A. *Biochemistry* **1993**, *32*, 4077.
(377) Perno, J. R.; Cwikel, D.; Spiro, T. G. *Inorg. Chem.* **1987**, *26*, 400.
(378) Lee, C.; Park, K. H.; Cho, M. *J. Chem. Phys.* **2006**, *125*, 114508.
(379) Lee, C.; Cho, M. *J. Chem. Phys.* **2006**, *125*, 114509.
(380) Lee, C.; Park, K. H.; Kim, J. A.; Hahn, S.; Cho, M. *J. Chem. Phys.* **2006**, *125*, 114510.
(381) Lee, C.; Cho, M. *J. Chem. Phys.* **2007**, *126*, 145102.
(382) Liquier, J.; Taillandier, E. In *Infrared Spectroscopy of Biomolecules*; Mantsch, H. H., Chapman, D., Ed.; Wiley-Liss: New York, 1996.
(383) Tsuboi, M. In *Applied Spectroscopy Reviews*; Brame, E. G., Jr., Ed.; Marcel Dekker: New York, 1969.
(384) Tsuboi, M., Takahashi, S. *Physico-Chemical Properties of Nucleic Acids*; Duchesne, J., Ed.; Academic: London, 1973.
(385) Krummel, A. T.; Mukherjee, P.; Zanni, M. T. *J. Phys. Chem. B* **2003**, *107*, 9165.
(386) Krummel, A. T.; Zanni, M. T. *J. Phys. Chem. B* **2006**, *110*, 13991.
(387) Howard, F. B.; Frazier, J.; Miles, H. T. *Proc. Natl. Acad. Sci. U.S.A.* **1969**, *64*, 451.
(388) Moroni, F.; Famulari, A.; Raimondi, M. *J. Phys. Chem. A* **2001**, *105*, 1169.
(389) Dickerson, R. E. *Methods Enzymol.* **1992**, *211*, 67.
(390) Asensio, A.; Kobko, N.; Dannenberg, J. J. *J. Phys. Chem. A* **2003**, *107*, 6441.
(391) Florian, J.; Leszczynski, J. *J. Am. Chem. Soc.* **1996**, *118*, 3010.

(392) Kurita, N.; Danilov, V. I.; Anisimov, V. M. *Chem. Phys. Lett.* **2005**, *404*, 164.
(393) Richardson, N. A.; Wesolowski, S. S.; Schaefer, H. F. *J. Phys. Chem. B* **2003**, *107*, 848.
(394) Shishkin, O. V.; Sponer, J.; Hobza, P. *J. Mol. Struct.* **1999**, *477*, 15.
(395) Shukla, M. K.; Leszczynski, J. *J. Phys. Chem. A* **2002**, *106*, 4709.
(396) Sponer, J.; Leszczynski, J.; Hobza, P. *J. Phys. Chem.* **1996**, *100*, 1965.
(397) Reichardt, C. *Solvents and Solvent Effects in Organic Chemistry*, 3rd ed.; Wiley-VCH: Weinheim, 2003.
(398) Vinogradov, S. N.; Linnell, R. H. *Hydrogen Bonding*; Van Nostrand Reinhold: New York, 1971.
(399) Nibbering, E. T. J.; Elsaesser, T. *Chem. Rev.* **2004**, *104*, 1887.
(400) Kwac, K.; Cho, M. *J. Raman Spectrosc.* **2005**, *36*, 326.
(401) Asbury, J. B.; Steinel, T.; Stromberg, C.; Gaffney, K. J.; Piletic, I. R.; Fayer, M. D. *J. Chem. Phys.* **2003**, *119*, 12981.
(402) Asbury, J. B.; Steinel, T.; Stromberg, C.; Gaffney, K. J.; Piletic, I. R.; Goun, A.; Fayer, M. D. *Phys. Rev. Lett.* **2003**, *91*, 237402.
(403) Asbury, J. B.; Steinel, T.; Fayer, M. D. *J. Lumin.* **2004**, *107*, 217.
(404) Pimentel, G. C.; McClellan, A. L. *The Hydrogen Bond*; W. H. Freeman: San Francisco, CA, 1960.
(405) Bakker, H. J.; Neinhuys, H. K.; Gallot, G.; Lascoux, N.; Gale, G. M.; Leicknam, J. C.; Bratos, S. *J. Chem. Phys.* **2002**, *116*, 2592.
(406) Gale, G. M.; Gallot, G.; Hache, F.; Lascoux, N.; Bratos, S.; Leicknam, J. C. *Phys. Rev. Lett.* **1999**, *82*, 1068.
(407) Laenen, R.; Gale, G. M.; Lascoux, N. *J. Phys. Chem. A* **1999**, *103*, 10708.
(408) Amir, W.; Lascoux, N.; Gallot, G.; Gale, G.; Pommeret, S.; Leicknam, J. C.; Bratos, S. *J. Phys. IV* **2002**, *12*, 381.
(409) Gallot, G.; Bratos, S.; Pommeret, S.; Lascoux, N.; Leicknam, J. C.; Kozinski, M.; Amir, W.; Gale, G. M. *J. Chem. Phys.* **2002**, *117*, 11301.
(410) Bakker, H. J.; Nienhuys, H. K.; Gallot, G.; Lascoux, N.; Gale, G. M.; Leicknam, J. C.; Bratos, S. *J. Chem. Phys.* **2002**, *116*, 2592.
(411) Bakker, H. J.; Woutersen, S.; Nienhuys, H. K. *Chem. Phys.* **2000**, *258*, 233.
(412) Woutersen, S.; Emmerichs, U.; Bakker, H. J. *J. Chem. Phys.* **1997**, *107*, 1483.
(413) Lock, A. J.; Woutersen, S.; Bakker, H. J. *J. Phys. Chem. A* **2001**, *105*, 1238.
(414) Nienhuys, H.-K.; Woutersen, S.; van Santen, R. A.; Bakker, H. J. *J. Chem. Phys.* **1999**, *111*, 1494.
(415) Woutersen, S.; Bakker, H. J. *Nature (London)* **1999**, *402*, 507.
(416) Woutersen, S.; Bakker, H. J. *Phys. Rev. Lett.* **1999**, *83*, 2077.
(417) Woutersen, S.; Emmerichs, U.; Bakker, H. J. *Science* **1997**, *278*, 658.
(418) Woutersen, S.; Emmerichs, U.; Nienhuys, H.-K.; Bakker, H. J. *Phys. Rev. Lett.* **1998**, *81*, 1106.
(419) Lawrence, C. P.; Skinner, J. L. *J. Chem. Phys.* **2002**, *117*, 5827.
(420) Lawrence, C. P.; Skinner, J. L. *J. Chem. Phys.* **2002**, *117*, 8847.
(421) Lawrence, C. P.; Skinner, J. L. *J. Chem. Phys.* **2003**, *118*, 264.
(422) Piryatinski, A.; Lawrence, C. P.; Skinner, J. L. *J. Chem. Phys.* **2003**, *118*, 9664.
(423) Piryatinski, A.; Lawrence, C. P.; Skinner, J. L. *J. Chem. Phys.* **2003**, *118*, 9672.
(424) Laenen, R.; Rausch, C.; Laubereau, A. *Phys. Rev. Lett.* **1998**, *80*, 2622.
(425) Laenen, R.; Rausch, C.; Laubereau, A. *J. Phys. Chem. B* **1998**, *102*, 9304.
(426) Laenen, R.; Rauscher, C.; Laubereau, A. *J. Phys. Chem. A* **1997**, *101*, 3201.
(427) Laenen, R.; Rauscher, C.; Laubereau, A. *Chem. Phys. Lett.* **1998**, *283*, 7.
(428) Laenen, R.; Simeonidis, K.; Laubereau, A. *J. Phys. Chem. B* **2002**, *106*, 408.
(429) Luzar, A. *J. Chem. Phys.* **2000**, *113*, 10663.
(430) Møller, K. B.; Rey, R.; Hynes, J. T. *J. Phys. Chem. A* **2004**, *108*, 1275.
(431) Rey, R.; Møller, K. B.; Hynes, J. T. *J. Phys. Chem. A* **2002**, *106*, 11993.
(432) Staib, A.; Hynes, J. T. *Chem. Phys. Lett.* **1993**, *204*, 197.
(433) Esisenberg, D.; Kauzmann, W. *The structure and properties of water*; Oxford University Press: New York, 1969.
(434) Franks, F. *Water, a Comprehensive Treatise*; Plenum: New York, 1972.
(435) Luzar, A.; Chandler, D. *Nature* **1996**, *379*, 55.
(436) Marx, D.; Tuckerman, M. E.; Hutter, J.; Parrinello, M. *Nature* **1999**, *397*, 601.
(437) Graener, H.; Seifert, G.; Laubereau, A. *Phys. Rev. Lett.* **1991**, *66*, 2092.
(438) Stenger, J.; Madsen, D.; Hamm, P.; Nibbering, E. T. J.; Elsaesser, T. *Phys. Rev. Lett.* **2001**, *87*, 027401.
(439) Moller, K. B.; Rey, R.; Hynes, J. T. *J. Phys. Chem. A* **2004**, *108*, 1275.
(440) Lawrence, C. P.; Skinner, J. L. *J. Chem. Phys.* **2002**, *117*, 8847.
(441) Torre, R.; Bartolini, P.; Righini, R. *Nature* **2004**, *428*, 296.
(442) Stenger, J.; Madsen, D.; Hamm, P.; Nibbering, E. T. J.; Elsaesser, T. *J. Phys. Chem. A* **2002**, *106*, 2341.
(443) Hansen, J.; McDonald, I. *Theory of Simple Liquids*; Academic Press: London, 1976.
(444) McQuarrie, D. A. *Statistical Mechanics*; Harper & Row: New York, 1976.
(445) Zheng, J.; Kwak, K.; Chen, X.; Asbury, J. B.; Fayer, M. D. *J. Am. Chem. Soc.* **2006**, *128*, 2977.
(446) Chung, H. S.; Khalil, M.; Smith, A. W.; Ganim, Z.; Tokmakoff, A. *Proc. Natl. Acad. Sci. U.S.A.* **2005**, *102*, 612.
(447) Chung, H. S.; Khalil, M.; Tokmakoff, A. *J. Phys. Chem. B* **2004**, *108*, 15332.
(448) Chung, H. S.; Khalil, M.; Tokmakoff, A. *Biophys. J.* **2004**, *86*, 526A.
(449) Ballew, R. M.; Sabelko, J.; Gruebele, M. *Nature Struct. Biol.* **1996**, *3*, 923.
(450) Kolano, C.; Helbing, J.; Kozinski, M.; Sander, W.; Hamm, P. *Nature* **2006**, *444*, 469.
(451) Hybl, J. D.; Albrecht, A. W.; Faeder, S. M. G.; Jonas, D. M. *Chem. Phys. Lett.* **1998**, *297*, 307.
(452) Hybl, J. D.; Christophe, Y.; Jonas, D. M. *Chem. Phys.* **2001**, *266*, 295.
(453) Hybl, J. D.; Faeder, S. M. G.; Albrecht, A. W.; Tolbert, C. A.; Green, D. C.; Jonas, D. M. *J. Lumin.* **2000**, *87*−*9*, 126.
(454) Hybl, J. D.; Ferro, A. A.; Jonas, D. M. *J. Chem. Phys.* **2001**, *115*, 6606.
(455) Hybl, J. D.; Yu, A.; Farrow, D. A.; Jonas, D. M. *J. Phys. Chem. A* **2002**, *106*, 7651.
(456) Stolow, A.; Jonas, D. M. *Science* **2004**, *305*, 1575.
(457) Yang, M.; Fleming, G. R. *J. Chem. Phys.* **1999**, *110*, 2983.
(458) Fleming, G. R.; Yang, M.; Agarwal, R.; Prall, B. S.; Kaufman, L. J.; Neuwahl, F. V. R. *Bull. Korean Chem. Soc.* **2003**, *24*, 1081.
(459) Prall, B. S.; Parkinson, D. Y.; Yang, M.; Ishikawa, N.; Fleming, G. R. *J. Chem. Phys.* **2004**, *120*, 2537.
(460) Yang, M.; Fleming, G. R. *J. Chem. Phys.* **2000**, *113*, 2823.
(461) Agarwal, R.; Yang, M.; Xu, Q. H.; Fleming, G. R. *J. Phys. Chem. B* **2001**, *105*, 1887.
(462) Cho, M. H.; Brixner, T.; Stiopkin, I.; Vaswani, H.; Fleming, G. R. *J. Chin. Chem. Soc.* **2006**, *53*, 15.
(463) Zigmantas, D.; Read, E. L.; Mancal, T.; Brixner, T.; Gardiner, A. T.; Cogdell, R. J.; Fleming, G. R. *Proc. Natl. Acad. Sci. U.S.A.* **2006**, *103*, 12672.
(464) van Amerongen, H.; Valkunas, L.; van Grondelle, R. *Photosynthetic Excitons*; World Scientific: Singapore, 2000.
(465) Fenna, R. E.; Matthews, B. W. *Nature* **1975**, *258*, 573.
(466) Matthews, B. W.; Fenna, R. E. *Acc. Chem. Res.* **1980**, *13*, 309.
(467) Tronrud, D. E.; Schmid, M. F.; Matthews, B. W. *J. Mol. Biol.* **1986**, *188*, 443.
(468) Matthews, B. W.; Fenna, R. E.; Bolognesi, M. C.; Schmid, M. F.; Olson, J. M. *J. Mol. Biol.* **1979**, *131*, 259.
(469) Ana, C.-A.; Robert, E. B.; James, P. A. *Photosynth. Res.* **2003**, *V75*, 49.
(470) Li, Y. F.; Zhou, W. L.; Blankenship, R. E.; Allen, J. P. *J. Mol. Biol.* **1997**, *271*, 456.
(471) Camara-Artigas, A.; Blankenship, R. E.; Allen, J. P. *Photosynth. Res.* **2003**, *75*, 49.
(472) Li, Y.-F.; Zhou, W.; Blankenship, R. E.; Allen, J. P. *J. Mol. Biol.* **1997**, *271*, 456.
(473) Kwac, K.; Cho, M. *J. Phys. Chem. A* **2003**, *107*, 5903.
(474) Yang, M.; Fleming, G. R. *Chem. Phys.* **2002**, *282*, 163.
(475) Pisliakov, A. V.; Mancal, T.; Fleming, G. R. *J. Chem. Phys.* **2006**, 124.
(476) McLuskey, K.; Prince, S. M.; Cogdell, R. J.; Isaacs, N. W. *Biochemistry* **2001**, *40*, 8783.
(477) Novoderezhkin, V.; Wendling, M.; van Grondelle, R. *J. Phys. Chem. B* **2003**, *107*, 11534.
(478) Cheng, Y. C.; Silbey, R. J. *Phys. Rev. Lett.* **2006**, *96*, 028103.
(479) Sumi, H. *J. Phys. Chem. B* **1999**, *103*, 252.
(480) Mukai, K.; Abe, S.; Sumi, H. *J. Phys. Chem. B* **1999**, *103*, 6096.
(481) Scholes, G. D.; Fleming, G. R. *J. Phys. Chem. B* **2000**, *104*, 1854.
(482) Jang, S. J.; Newton, M. D.; Silbey, R. J. *Phys. Rev. Lett.* **2004**, *92*, 218301.
(483) Borca, C. N.; Zhang, T. H.; Li, X. Q.; Cundiff, S. T. *Chem. Phys. Lett.* **2005**, *416*, 311.
(484) Li, X.; Zhang, T.; Borca, C. N.; Cundiff, S. T. *Phys. Rev. Lett.* **2006**, *96*, 057406.
(485) Yang, L. J.; Schweigert, I. V.; Cundiff, S. T.; Mukamel, S. *Phys. Rev. B* **2007**, *75*, 125302.
(486) Kuznetsova, I.; Thomas, P.; Meier, T.; Zhang, T.; Li, X.; Mirin, R. P.; Cundiff, S. T. *Solid State Commun.* **2007**, *142*, 154.
(487) Chemla, D. S.; Shah, J. *Nature* **2001**, *411*, 549.

(488) Haug, H.; Koch, S. W. *Quantum Theory of the Optical and Electronic Properties of Semiconductors*; World Scientific: Singapore, 2004.
(489) Leo, K.; Wegener, M.; Shah, J.; Chemla, D. S.; Gobel, E. O.; Damen, T. C.; Schmittrink, S.; Schafer, W. *Phys. Rev. Lett.* **1990**, *65*, 1340.
(490) Wegener, M.; Chemla, D. S.; Schmittrink, S.; Schafer, W. *Phys. Rev. A* **1990**, *42*, 5675.
(491) Bott, K.; Heller, O.; Bennhardt, D.; Cundiff, S. T.; Thomas, P.; Mayer, E. J.; Smith, G. O.; Eccleston, R.; Kuhl, J.; Ploog, K. *Phys. Rev. B* **1993**, *48*, 17418.
(492) Wang, H. L.; Ferrio, K.; Steel, D. G.; Hu, Y. Z.; Binder, R.; Koch, S. W. *Phys. Rev. Lett.* **1993**, *71*, 1261.
(493) Hu, Y. Z.; Binder, R.; Koch, S. W.; Cundiff, S. T.; Wang, H.; Steel, D. G. *Phys. Rev. B* **1994**, *49*, 14382.
(494) Shacklette, J. M.; Cundiff, S. T. *Phys. Rev. B* **2002**, *66*, 045309.
(495) Weiss, S.; Mycek, M. A.; Bigot, J. Y.; Schmittrink, S.; Chemla, D. S. *Phys. Rev. Lett.* **1992**, *69*, 2685.
(496) Koch, M.; Feldmann, J.; Vonplessen, G.; Gobel, E. O.; Thomas, P.; Kohler, K. *Phys. Rev. Lett.* **1992**, *69*, 3631.
(497) Lyssenko, V. G.; Erland, J.; Balslev, I.; Pantke, K. H.; Razbirin, B. S.; Hvam, J. M. *Phys. Rev. B* **1993**, *48*, 5720.
(498) Cundiff, S. T.; Koch, M.; Knox, W. H.; Shah, J.; Stolz, W. *Phys. Rev. Lett.* **1996**, *77*, 1107.
(499) Euteneuer, A.; Finger, E.; Hofmann, M.; Stolz, W.; Meier, T.; Thomas, P.; Koch, S. W.; Ruhle, W. W.; Hey, R.; Ploog, K. *Phys. Rev. Lett.* **1999**, *83*, 2073.
(500) Chen, X.; Walecki, W. J.; Buccafusca, O.; Fittinghoff, D. N.; Smirl, A. L. *Phys. Rev. B* **1997**, *56*, 9738.
(501) Zwanzig, R. *Phys. Rev.* **1961**, *124*, 983.
(502) Mori, H. *Prog. Theor. Phys.* **1965**, *33*, 423.
(503) Yang, M.; Fleming, G. R. *Chem. Phys.* **2002**, *275*, 355.
(504) Hyeon-Deuk, K.; Tanimura, Y.; Cho, M. *J. Chem. Phys.* **2007**, *127*.
(505) Redfield, A. G. *Adv. Magn. Reson.* **1965**, *1*, 1.
(506) Pollard, W. T.; Felts, A. K.; Friesner, R. A. *Adv. Chem. Phys.* **1996**, *93*, 77.
(507) Kuhn, O.; Sundstrom, V. *J. Chem. Phys.* **1997**, *107*, 4154.
(508) Kuhn, O.; Sundstrom, V. *J. Phys. Chem. B* **1997**, *101*, 3432.
(509) Park, K.; Cho, M. *J. Chem. Phys.* **1998**, *109*, 10559.
(510) Park, K.; Cho, M. H.; Hahn, S.; Kim, D. *J. Chem. Phys.* **1999**, *111*, 4131.
(511) Zhao, W.; Wright, J. C. *Phys. Rev. Lett.* **1999**, *83*, 1950.
(512) Zhao, W.; Wright, J. C. *J. Am. Chem. Soc.* **1999**, *121*, 10994.
(513) Kwak, K.; Cha, S.; Cho, M. H.; Wright, J. C. *J. Chem. Phys.* **2002**, *117*, 5675.
(514) Cho, M.; Hess, C.; Bonn, M. *Phys. Rev. B* **2002**, *65*, 205423.
(515) Bonn, M.; Hess, C.; Miners, J. H.; Heinz, T. F.; Bakker, H. J.; Cho, M. *Phys. Rev. Lett.* **2001**, *86*, 1566.
(516) Hess, C.; Cho, M.; Bonn, M. *Surf. Sci.* **2002**, *502*, 123.
(517) Mahan, G. D.; Lucas, A. A. *J. Chem. Phys.* **1978**, *68*, 1344.
(518) Scheffler, M. *Surf. Sci.* **1979**, *81*, 562.
(519) Cho, M. *Phys. Rev. A* **2000**, *6102*, 023406.
(520) Hess, C.; Bonn, M.; Funk, S.; Wolf, M. *Chem. Phys. Lett.* **2000**, *325*, 139.
(521) Jakob, P.; Persson, B. N. J. *J. Chem. Phys.* **1998**, *109*, 8641.
(522) Andrews, D. L.; Thirunamachandran, T. *J. Chem. Phys.* **1977**, *67*, 5026.
(523) Craig, D. P.; Thirunamachandran, T. *Molecular Quantum Electrodyanmics: An Introduction to Radiation Molecule Interactions*; Dover Publications, Inc.: New York, 1998.
(524) Giordmaine, J. A. *Phys. Rev.* **1965**, *138*, 1599.
(525) Fischer, P.; Hache, F. *Chirality* **2005**, *17*, 421.
(526) Fischer, P.; Wiersma, D. S.; Righini, R.; Champagne, B.; Buckingham, A. D. *Phys. Rev. Lett.* **2000**, *85*, 4253.
(527) Belkin, M. A.; Kulakov, T. A.; Ernst, K.-H.; Yan, L.; Shen, Y. R. *Phys. Rev. Lett.* **2000**, *85*, 4474.
(528) Belkin, M. A.; Han, S. H.; Wei, X.; Shen, Y. R. *Phys. Rev. Lett.* **2001**, *87*, 113001.
(529) Abramavicius, D.; Mukamel, S. *J. Chem. Phys.* **2005**, *122*, 134305.
(530) Cho, M. *J. Chem. Phys.* **2000**, *112*, 9978.
(531) Cheon, S.; Lee, H.; Choi, J.-H.; Cho, M. *J. Chem. Phys.* **2007**, *126*, 054505.
(532) Hahn, S.; Kwak, K.; Cho, M. *J. Chem. Phys.* **2000**, *112*, 4553.
(533) Nafie, L. A. *Annu. Rev. Phys. Chem.* **1997**, *48*, 357.
(534) Tinoco, I. *Adv. Chem. Phys.* **1962**, *4*, 113.
(535) Berova, N.; Nakanishi, K.; Woody, R. W. *Circular Dichroism: Principles and Applications*; Wiley-VCH: New York, 2000.
(536) Woody, R. W. *J. Chem. Phys.* **1968**, *49*, 4797.
(537) Rosenfeld, L. Z. *Phys.* **1928**, *52*, 161.
(538) Nafie, L. A.; Cheng, J. C.; Stephens, P. J. *J. Am. Chem. Soc.* **1975**, *97*, 3842.
(539) Nafie, L. A.; Keiderling, T. A.; Stephens, P. J. *J. Am. Chem. Soc.* **1976**, *98*, 2715.
(540) Pancoska, P.; Baumruk, V.; Keiderling, T. A. *Biophys. J.* **1994**, *66*, A393.
(541) Bour, P.; Keiderling, T. A. *J. Am. Chem. Soc.* **1993**, *115*, 9602.
(542) Keiderling, T. A.; Pancoska, P.; Baumruk, V.; Urbanova, M.; Gupta, V. P.; Dukor, R. K.; Huo, D. F. *Mol. Model.* **1994**, *576*, 61.
(543) Wang, L. J.; Yang, L. G.; Keiderling, T. A. *Biophys. J.* **1994**, *67*, 2460.
(544) Pancoska, P.; Bitto, E.; Janota, V.; Keiderling, T. A. *Faraday Discuss.* **1994**, 287.
(545) Silva, R. A. G. D.; Kubelka, J.; Bour, P.; Decatur, S. M.; Keiderling, T. A. *Proc. Natl. Acad. Sci. U.S.A.* **2000**, *97*, 8318.
(546) Zhao, C.; Polavarapu, P. L.; Das, C.; Balaram, P. *J. Am. Chem. Soc.* **2000**, *122*, 8228.
(547) Schweitzer-Stenner, R. *J. Phys. Chem. B* **2004**, *108*, 16965.
(548) Shanmugam, G.; Polavarapu, P. L. *J. Am. Chem. Soc.* **2004**, *126*, 10292.
(549) Baumruk, V.; Keiderling, T. A. *J. Am. Chem. Soc.* **1993**, *115*, 6939.
(550) Keiderling, T. A. *Curr. Opin. Chem. Biol.* **2002**, *6*, 682.
(551) Barron, L. D.; Bogaard, M. P.; Buckingham, A. D. *J. Am. Chem. Soc.* **1973**, *95*, 603.
(552) Wilson, G.; Hecht, L.; Barron, L. D. *Biochemistry* **1996**, *35*, 12518.
(553) Barron, L. D.; Hecht, L.; Blanch, E. W.; Bell, A. F. *Prog. Biophys. Mol. Biol.* **2000**, *73*, 1.
(554) McColl, I. H.; Blanch, E. W.; Hecht, L.; Kallenbach, N. R.; Barron, L. D. *J. Am. Chem. Soc.* **2004**, *126*, 5076.
(555) Zhu, F.; Isaacs, N. W.; Hecht, L.; Barron, L. D. *J. Am. Chem. Soc.* **2005**, *127*, 6142.
(556) Kapitan, J.; Baumruk, V.; Bour, P. *J. Am. Chem. Soc.* **2006**, *128*, 2438.
(557) Abramavicius, D.; Mukamel, S. *J. Chem. Phys.* **2006**, *124*, 034113.
(558) Voronine, D. V.; Abramavicius, D.; Mukamel, S. *J. Chem. Phys.* **2006**, *125*.
(559) Besley, N. A.; Hirst, J. D. *J. Am. Chem. Soc.* **1999**, *121*, 9636.
(560) Kurapkat, G.; Kruger, P.; Wollmer, A.; Fleischhauer, J.; Kramer, B.; Zobel, E.; Koslowski, A.; Botterweck, H.; Woody, R. W. *Biopolymers* **1997**, *41*, 267.
(561) Hirst, J. D.; Hirst, D. M.; Brooks, C. L. *J. Phys. Chem. A* **1997**, *101*, 4821.
(562) Choi, J.-H.; Kim, J. S.; Cho, M. *J. Chem. Phys.* **2005**, *122*, 174903.
(563) Stephens, P. J. *J. Phys. Chem.* **1987**, *91*, 1712.
(564) Holzwarth, G.; Chabay, I. *J. Chem. Phys.* **1972**, *57*, 1632.
(565) Belkin, M. A.; Shen, Y. R. *Phys. Rev. Lett.* **2003**, *91*, 213907.
(566) Belkin, M. A.; Shen, Y.-R.; Harris, R. A. *J. Chem. Phys.* **2004**, *120*, 10118.
(567) Ji, N.; Shen, Y. R. *J. Am. Chem. Soc.* **2004**, *126*, 15008.
(568) Zhu, X. D.; Suhr, H.; Shen, Y. R. *Phys. Rev. B* **1987**, *35*, 3047.
(569) Guyotsionnest, P.; Hunt, J. H.; Shen, Y. R. *Phys. Rev. Lett.* **1987**, *59*, 1597.
(570) Shen, Y. R. *Nature* **1989**, *337*, 519.
(571) Loudon, R. *The Quantum Theory of Light*; Clarendon Press: Oxford, 1983.
(572) Demirdoven, N.; Cheatum, C. M.; Chung, H. S.; Khalil, M.; Knoester, J.; Tokmakoff, A. *J. Am. Chem. Soc.* **2004**, *126*, 7981.
(573) Hamm, P.; Lim, M.; DeGrado, W. F.; Hochstrasser, R. M. *Proc. Natl. Acad. Sci. U.S.A.* **1999**, *96*, 2036.
(574) Maekawa, H.; Toniolo, C.; Moretto, A.; Broxterman, Q. B.; Ge, N.-H. *J. Phys. Chem. B* **2006**, *110*, 5834.
(575) Mukherjee, P.; Kass, I.; Arkin, I. T.; Zanni, M. T. *J. Phys. Chem. B* **2006**, *110*, 24740.
(576) Woutersen, S.; Hamm, P. *J. Chem. Phys.* **2001**, *115*, 7737.
(577) Eaves, J. D.; Loparo, J. J.; Fecko, C. J.; Roberts, S. T.; Tokmakoff, A.; Geissler, P. L. *Proc. Natl. Acad. Sci. U.S.A.* **2005**, *102*, 13019.
(578) Kim, Y. S.; Hochstrasser, R. M. *Proc. Natl. Acad. Sci. U.S.A.* **2005**, *102*, 11185.
(579) Zheng, J.; Kwak, K.; Asbury, J. B.; Chen, X.; Piletic, I.; Fayer, M. D. *Science* **2005**, *309*, 1338.
(580) Huse, N.; Bruner, B. D.; Cowan, M. L.; Dreyer, J.; Nibbering, E. T. J.; Miller, R. J. D.; Elsaesser, T. *Phys. Rev. Lett.* **2005**, *95*.
(581) Cho, M.; Vaswani, H. M.; Brixner, T.; Stenger, J.; Fleming, G. R. *J. Phys. Chem. B* **2005**, *109*, 10542.
(582) Zhang, T.; Borca, C. N.; Li, X.; Cundiff, S. T. *Opt. Express* **2005**, *13*, 7432.
(583) Schatz, G. C.; Ratner, M. A. *Quantum Mechanics in Chemistry*; Prentice Hall: Englewood Cliffs, NJ, 1993.
(584) Brixner, T.; Stiopkin, I. V.; Fleming, G. R. *Opt. Lett.* **2004**, *29*, 884.
(585) Choi, J.-H.; Cho, M. *Chem. Phys.* **2007**, *341*, 57.
(586) Hochstrasser, R. M. *Proc. Natl. Acad. Sci. U.S.A.* **2007**, *104*, 14189.

CR078377B